



NKS-317  
ISBN 978-87-7893-397-3

---

# Analysis of Debris Bed Formation, Spreading, Coolability, and Steam Explosion in Nordic BWRs

Pavel Kudinov<sup>1</sup>  
Alexander Konovalenko<sup>1</sup>  
Dmitry Grishchenko<sup>1</sup>  
Sergey Yakush<sup>2</sup>  
Simone Basso<sup>1</sup>  
Nazar Lubchenko<sup>3</sup>  
Aram Karbojian<sup>1</sup>

<sup>1</sup>Division of Nuclear Power Safety (NPS)  
Royal Institute of Technology (KTH), Stockholm, Sweden

<sup>2</sup>Institute for Problems in Mechanics of the Russian Academy of Science  
Moscow, Russia

<sup>3</sup>Massachusetts Institute of Technology  
Cambridge, Massachusetts, USA

November 2014

## Abstract

The work is motivated by the need to assess effectiveness of severe accident management strategy adopted in Nordic type BWRs with melt ejection from the vessel into a deep water pool below the vessel. In this work we address phenomena relevant to the debris bed formation, coolability and steam explosion experimentally and analytically.

A new series of DEFOR-A (Agglomeration) tests have been carried out in order to clarify the effect of the melt jet velocity on the particle size distribution and fraction of agglomeration. Ablation and plugging of the melt release nozzle is also addressed in this work.

DECOSIM code was further developed to address debris bed coolability in post-dryout regime. An analytical model is proposed based on the analysis of DECOSIM calculations for prediction of the maximum temperature of the debris if the size of the dry zone is known. A model for prediction of particulate debris spreading has been implemented in the DECOSIM code. The code has been further validated against latest COOLOCE data for multidimensional debris bed configurations.

A scaling approach for prediction of particulate debris spreading has been proposed in this work based on the PDS-C experimental data. A universal semi-empirical closure has been developed for prediction of debris spreading mass flux.

An approach to steam explosion sensitivity analysis using TEXAS code has been developed. Obtained database of the impulse and maximum pressure as a function of TEXAS input parameters is used for development of the computationally efficient surrogate model.

## Key words

Nordic BWR, severe accident, debris bed formation, coolability, steam explosion



# **Analysis of Debris Bed Formation, Spreading, Coolability, and Steam Explosion in Nordic BWRs**

**Final Report from the NKS-R DECOSE activity**

**(Contract: NKS\_R\_2012\_100)**

*Pavel Kudinov<sup>1</sup>, Alexander Konovalenko<sup>1</sup>, Dmitry Grishchenko<sup>1</sup>,  
Sergey Yakush<sup>2</sup>, Simone Basso<sup>1</sup>, Nazar Lubchenko<sup>3</sup>, Aram Karbojian<sup>1</sup>*

<sup>1</sup>Division of Nuclear Power Safety (NPS), Royal Institute of Technology (KTH), Stockholm

<sup>2</sup>Institute for Problems in Mechanics of the Russian Academy of Sciences, Moscow, Russia

<sup>3</sup>Massachusetts Institute of Technology, Cambridge, Massachusetts, USA

June, 2014  
Stockholm



## Contents

<b>CONTENTS .....</b>	<b>3</b>
<b>LIST OF FIGURES.....</b>	<b>5</b>
<b>LIST OF TABLES.....</b>	<b>8</b>
<b>1 INTRODUCTION.....</b>	<b>11</b>
1.1 MOTIVATION AND BACKGROUND .....	11
<b>2 INVESTIGATION OF MELT JET FRAGMENTATION, DEBRIS BED FORMATION AND MELT-STRUCTURE-COOLANT INTERACTIONS IN DEFOR-A FACILITY.....</b>	<b>14</b>
2.1 GOALS AND TASKS .....	14
2.2 EXPERIMENTAL FACILITY.....	16
2.3 RESULTS AND DISCUSSION .....	21
2.3.1 <i>DEFOR-A10-A21 experimental conditions and parameters</i> .....	21
Test matrix 21	
DEFOR tests with conical sample .....	25
DEFOR tests with sample plate .....	28
2.3.2 <i>Melt pouring</i> .....	37
DEFOR tests without sample .....	37
DEFOR tests with conical sample .....	40
DEFOR tests with sample plate .....	43
2.3.3 <i>Posttest debris analysis</i> .....	49
Comparison of the DEFOR-A10,A11 tests with FARO tests and previous DEFOR test series .....	49
Debris bed formation and agglomeration .....	53
Particle size distribution .....	59
2.3.4 <i>Posttest analysis of the samples</i> .....	61
Tests with conically shaped samples .....	61
Tests with sample plate .....	67
2.4 SUMMARY OF DEFOR EXPERIMENTS .....	74
<b>3 DECOSIM CODE DEVELOPMENT AND VALIDATION AGAINST THE EXPERIMENTAL RESULTS PRODUCED IN COOLOCE AND POMEKO-HT FACILITIES. ....</b>	<b>76</b>
3.1 OVERVIEW OF DECOSIM CODE .....	76
3.2 GOVERNING EQUATIONS AND NUMERICAL SOLVER .....	77
3.3 SEARCH ALGORITHM FOR DETERMINATION OF COOLABILITY BOUNDARY .....	83
3.4 DECOSIM SIMULATIONS OF COOLOCE EXPERIMENTS .....	89
3.4.1 <i>Parameters of DECOSIM Simulations</i> .....	89
3.5 SUMMARY OF RESULTS .....	90
3.6 DISCUSSION OF RESULTS .....	96
3.7 SIMULATION OF POST-DRYOUT DEBRIS BED .....	99
3.8 IMPLEMENTATION OF PARTICLE SPREADING MODEL.....	105
<b>4 INVESTIGATION OF PARTICULATE DEBRIS SPREADING.....</b>	<b>108</b>
4.1 PARTICULATE DEBRIS SPREADING: EXPERIMENTS AND SCALING APPROACH.....	108
4.1.1 <i>Introduction</i> .....	108
4.2 EXPERIMENTAL APPROACH .....	111
4.2.1 <i>PDS-C Experimental setup</i> .....	111

<i>Superficial Gas Velocities in PDS-C Facility</i> .....	113
4.2.2 <i>Estimation of particulate flow rate</i> .....	117
4.2.3 <i>Test conditions and results</i> .....	118
4.3 SCALING APPROACH.....	121
4.4 SUMMARY.....	124
4.5 INVESTIGATION OF PARTICULATE DEBRIS SPREADING: POSSIBLE EFFECT OF THE HEATERS AND THERMOCOUPLES IN COOLOCE FACILITY .....	126
4.6 GOALS AND TASKS .....	126
4.7 EXPERIMENTAL APPROACH AND PROCEDURE .....	126
4.7.1 <i>Experimental facility</i> .....	126
PDS-C test section .....	126
Mockup of the COOLOCE heaters and TCs .....	128
Debris simulants: properties and characterization.....	132
Experimental procedure .....	136
4.8 RESULTS AND OBSERVATIONS .....	138
4.8.1 <i>Fluidization velocities of the zirconium-silicate bed</i> .....	140
4.8.2 <i>Summary and Outlook</i> .....	140
<b>5 APPLICATION OF MC3D AND TEXAS-V TO ANALYSIS OF STEAM EXPLOSION IN A BWR CONTAINMENT .....</b>	<b>142</b>
5.1 TEXAS-V CODE .....	144
5.2 SEIM FRAMEWORK .....	151
5.2.1 <i>Surrogate model</i> .....	153
5.2.2 <i>Implementation of the reversed analysis and results</i> .....	154
5.3 SENSITIVITY STUDY OF TEXAS-V .....	157
5.3.1 <i>Choice and classification of input parameters</i> .....	157
5.3.2 <i>Implementation and results</i> .....	158
5.4 SUMMARY AND OUTLOOK.....	164
<b>6 SUMMARY AND OUTLOOK .....</b>	<b>165</b>
<b>7 NOMENCLATURE.....</b>	<b>169</b>
<b>8 ACKNOWLEDGEMENT .....</b>	<b>170</b>
<b>9 DISCLAIMER .....</b>	<b>170</b>
<b>10 REFERENCES .....</b>	<b>171</b>
<b>APPENDIX 1.....</b>	<b>179</b>

## List of Figures

Figure 1: DEFOR experimental facility: a – common setup for DEFOR-A01-11;15, b – common setup for DEFOR-A12-14;16 and c - DEFOR-A17-21. ....	16
Figure 2: DEFOR catchers with debris: a – side view; b – top view .....	17
Figure 3: DEFOR-A experimental setup without (a), with conical shell (b) and horizontal plate as sample. ....	18
Figure 4: Common for DEFOR-A12 and A13 tests assembly (by example of the A12 test): general view (a), funnel (b) and melt granulation device (c-e) bottom, top and inside views respectively.....	26
Figure 5: Design and instrumentation of the test sample in A12 (top) and A13 (bottom) tests .....	27
Figure 6: Setup of TCs inside the test sample common for A12 and A13 tests: a – B2 and B3 TCs; b – C1-C3 TCs; c – TCs feeding through screws fixed in the sample wall.....	28
Figure 7: Melt delivery setup with vertically extended column (a) and typical dimensions of the lead plate (sample) and its holder (b). ....	29
Figure 8: Experimental facility: general view (a), melt delivery setup (b), view on the extended column cross section and gap filling (c) and lead plate holder (d).....	30
Figure 9: DEFOR-A17 (a) and A18 (b) sample plates with nozzles plugged by the air-pressurized rubber balloon. ....	31
Figure 10: DEFOR-A17 sample: drawing and TC positioning (a) and actual bottom side of the plate (b). ....	32
Figure 11: DEFOR-A18 sample: drawing and TC positioning (a) and actual bottom side of the plate (b). ....	33
Figure 12: DEFOR-A19 sample: drawing and TC positioning (a) and actual bottom side of the plate (b). ....	34
Figure 13: DEFOR-A20 sample: drawing and TC positioning (a) and actual bottom side of the plate (b). ....	35
Figure 14: DEFOR-A21 sample: drawing and TC positioning (a) and actual bottom side of the plate (b). ....	36
Figure 15: Melt pouring in A10 (a), A11 (b) and A15 (c) tests .....	37
Figure 16: Three phase melt-water-steam dynamics recorded in A11 test at the top catcher by fast camera (170 fps). ....	38
Figure 17: Melt release in A12 test (time stamp in the images is relative to the start of melt release from the test sample).....	41
Figure 18: Melt release in A13 test (time stamp in the images is relative to the start of melt release from the test sample) (frame 308). ....	42
Figure 19: Snapshots of the melt release recorded by the main view camera (25 fps) in at 1.6 s after the release of the melt through nozzle outlets: a) A17 b) A18. ....	43
Figure 20: Snapshots of the melt release recorded by the close-up view camera (50 fps) in A17 (a-c) and A18 (d-f) tests. ....	44
Figure 21: Snapshots of the melt release recorded by the high-speed camera (160 fps) in A17 (a-e) and A18 (f-j) tests. ....	45
Figure 22: DEFOR-A19: snapshots of the melt release recorded by the main view camera (25 fps) .....	46
Figure 23: DEFOR-A20: snapshots of the melt release recorded by the main view camera (25 fps) .....	47
Figure 24: DEFOR-A21: snapshots of the melt release recorded by the main view camera (25 fps) .....	48

Figure 25: Comparison of the agglomerated debris fraction obtained in DEFOR-A10,A11 to previously performed DEFOR-A and DEFOR-S experiments ..... 50

Figure 26: Comparison of the particle size distributions from DEFOR-A tests to DEFOR-A tests (only data from the bottom catcher is plotted) ..... 51

Figure 27: Comparison of the particle size distributions of DEFOR-A tests to FARO experiments ..... 52

Figure 28: Comparison of the particle size distributions of DEFOR-A tests to FARO experiments ..... 53

Figure 29: Spatial distribution of debris: top view of the catchers. .... 55

Figure 30: Debris from DEFOR-A15 test found in catcher 1. .... 56

Figure 31: Debris from DEFOR-A15 test found in catcher 2 (a) and catcher 3 (b). .... 56

Figure 32: Debris from DEFOR-A15 test found in catcher 4. .... 57

Figure 33: Debris bed agglomeration fraction as function of water pool depth for A1:9, S8, S19 (a) and A10:21 (b) tests. .... 58

Figure 34: Measured total debris bed porosity as function of water pool depth in DEFOR-A10:21 tests. .... 59

Figure 35: Cumulative mass fraction for the debris in DEFOR-A1:9 (a) and DEOFR-A10:21 (b) tests. For comparison, the data from FARO tests and averaged DEFOR curves for corresponding series of tests are provided. .... 60

Figure 36: Debris bed solidified inside the sample in A12 (left) and A13 (right) tests ..... 62

Figure 37: Test sample of A13 test after cutting: nozzle and ablation hole ..... 63

Figure 38: Test sample wall ablation in A13 ..... 64

Figure 39: Test sample after cutting (left – A12, right – A13) ..... 65

Figure 40: Test sample after cutting, comparison of surface erosion A12 at the top part of the image and A13 in the lower part ..... 66

Figure 41: Ingots collected in DEFOR-A12-A14 and A16 tests..... 66

Figure 42: A17 (a) and A18 (b) samples after the interaction, view on the inner surface ..... 68

Figure 43: Sample wall melting dynamics in A18 test ..... 69

Figure 44: Lead sample radial ablation (crust being removed)..... 70

Figure 45: The temperature recordings inside the sample in A19 to A21 test (zoom) ..... 71

Figure 46: Averaged radial and axial ablation rates in A19-11 tests ..... 73

Figure 47: Bisection search algorithm for the dryout boundary. .... 85

Figure 48: Grid convergence results: dependence of dryout heat release rate on cell size..... 88

Figure 49: Comparison of calculated dryout heat power as function of system pressure (cylindrical debris bed) with COOLOCE experiments. .... 93

Figure 50: Comparison of calculated dryout heat power as function of system pressure (conical debris bed) with COOLOCE experiments. .... 93

Figure 51: Dependence of ratio DHF/DHF<sub>0</sub> on the slope angle. .... 98

Figure 52: Computational domain and numerical grid used for simulations of conical (a) and mound-shaped (b) debris bed. .... 100

Figure 53: Time histories of the maximum temperature of solid particles in conical (a) and mound-shaped (b) debris bed ..... 101

Figure 54: Void fraction (left) and solid particle temperature (right) in the post-dryout cone-shaped debris bed ( W = 200 W/kg, D<sub>p</sub> = 2 mm) at time 4000 s..... 102

Figure 55: Void fraction (left) and solid particle temperature (right) in the post-dryout mound-shaped debris bed ( W = 250 W/kg, D<sub>p</sub> = 3 mm) at time 4000 s..... 102

Figure 56: Void fraction (left) and vapor temperature (right) distributions along the axis of symmetry for the cases where temperature stabilization was obtained (see Table 13)..... 102

Figure 57: Dependence of the critical temperature on the relative size of dry zone..... 104

Figure 58: Self-levelling of debris bed (volume fraction of particles,  $d=1\text{mm}$ ,  $W=160\text{ W/kg}$ ) ..... 106

Figure 59: Maximum temperatures of solid particles. Solid lines: no spreading, dashed lines: spreading ..... 106

Figure 60: Illustration of self-leveling process ..... 108

Figure 61. The slope angle of the heap is changed only in the section where gas flow rate was provided (between the two vertical dashed lines). ..... 110

Figure 62: Examples showing post-processing technique applied to the video recorded during experiment PDS-C8..... 112

Figure 63: Normalized superficial velocity of the steam as function of debris bed length with particles of different sizes: a) for 1 mm particles; b) for 3.43 mm particles. The green and blue points show air velocities reachable in PDS-2 and PDS-C facilities respectively..... 116

Figure 64: Particulate flow rate per unit width as function of heap slope angle obtained from different PDS experiments with stainless steel spheres and cylinders..... 119

Figure 65: Example of the analytical fit applied to experimental closures for SS 3x3 mm cylindrical particles: experimental points (black dots) and fit surface (colormap)..... 120

Figure 66: Schematic of the balance between main forces acting on a particle in the debris bed. .... 121

Figure 67: Non-dimensional representation of experimental closure curves. The red curves represent SS 3x3 mm cylinders while the blue are for SS 6 mm spheres. The black curve indicates the universal non-dimensional closure..... 123

Figure 67: PDS-C drawings: air injection chamber (a) and acrylic body (b)..... 128

Figure 68: PDS-C facility: Manufactured (a) and installed (b)..... 128

Figure 69: PDS-C test section (a) and its spreading plate (b). ..... 129

Figure 70: Schematics (a) and photographic image (b) of the heaters and TCs used in COOLOCE-1 facility [1]. Schematics of the pins arrangement in COOLOCE mockup: plate (c) and holes (d) dimensions together with pitch sizes..... 130

Figure 71: COOLOCE heaters and TCs mockup: top (a) and side (b) views; pins holding plate with inner (c) and outer (d) perforated surfaces as well net protecting the particle through flow. .... 131

Figure 72: Properties (a) and image (b) of the 0.8-1.0 mm zirconium-silicate Alpine Powerbeads provided by supplier [4]. ..... 133

Figure 73: Original (a), filtered and color inverted (b) images of the beads..... 134

Figure 74: Size distribution of the zirconium-silicate beads..... 135

Figure 75: Results from the tests with zirconium-silicate beads: 3 tests with mockup and 10 tests w/o mockup are grouped in 4 groups. The error bars correspond to the tripled standard deviation  $\pm 3\sigma$  of the characteristic self-leveling time..... 139

Figure 76: Trailing edge breakup vs leading edge breakup mechanisms..... 146

Figure 77: Top level of the SEIM framework ..... 151

Figure 78: SM development methodology ..... 153

Figure 79: SEIM framework implementation (a – deterministic output; b – failure probability; c – failure domain; d - example of failure domain in terms of three selected parameters for 300 mm jet diameter) ..... 156

Figure 80: Explosion impulse predicted by TEXAS-V as a function of triggering time..... 159

Figure 81: Morris diagrams for explosion impulse (a – 300 mm jet diameter; b – 500 mm jet diameter)..... 161

Figure 82: Cumulative density function for explosion impulse: a – 140 mm jet diameter; b – 500 mm jet diameter..... 162

## List of Tables

Table 1: Ranges of the DEFOR-A tests parameters.....	20
Table 2: Summary of the DEFOR-A10-A21 tests conditions and main results .....	22
Table 3: Relevant experimental parameters for DEFOR-A tests comparison to selected DEFOR-A tests .....	49
Table 4: Test sample and debris properties in DEFOR-A12-A14 and A16 tests .....	61
Table 5: Onset of sample melting according to embedded TCs in A19 .....	72
Table 6: Onset of sample melting according to embedded TCs in A20 .....	72
Table 7: Onset of sample melting according to embedded TCs in A21 .....	72
Table 8: Parameters used in DECOSIM simulations of COOLOCE experiments. ....	89
Table 9: DECOSIM simulations of COOLOCE experiments: cylindrical debris bed with impermeable walls.....	91
Table 10: DECOSIM simulations of COOLOCE experiments with conical debris bed. ....	92
Table 11: DECOSIM simulations of COOLOCE-10 experiments, cylindrical debris bed with open side wall.....	95
Table 12: DECOSIM simulations of COOLOCE-12 experiments, conical debris bed with on cylindrical base.....	95
Table 13: DECOSIM simulations of post-dryout debris beds. ....	100
Table 14: Particles properties .....	112
Table 15: Steam generating debris bed properties. ....	113
Table 16: Minimum bed fluidization velocities by air and steam for the stainless steel 3x3 mm in size cylindrical particles. ....	114
Table 17 Experimental matrix.....	118
Table 16: Experimental procedure for preparation of the tests with and w/o mockup. ....	136
Table 17: Experimental procedures for running the tests with and w/o mockup.....	137
Table 18: Results from tests with- and without COOLOCE heaters/TCs mockup performed in PDS-C facility on self-leveling of the 0.8-1 mm zirconium-silicate beads. ....	138
Table 19: Minimum fluidization velocities of the zirconium-silicate beds by air and steam.	140
Table 20: List of TEXAS-V parameters used in sensitivity study .....	158
Table 21: List of scenario dependent parameters used in the sensitivity study .....	160
Table 22: List of scenario independent parameters used in the sensitivity study .....	160

## Executive Summary

The work is motivated by the need to assess effectiveness of severe accident management strategy adopted in Nordic type BWRs. It is assumed that core melt ejected from the vessel will fragment, quench and form a coolable debris bed in a deep water pool below the vessel. However, there is a risk that formed debris bed will not be coolable. It is also possible that energetic steam explosion will occur in the process of melt fragmentation in the pool. The goal of the project is to reduce uncertainties in assessment of (i) debris bed properties and coolability, (ii) steam explosion impact. To achieve the project goal, experimental and analytical research program is carried out.

In this work we continue further experimental investigation of the debris bed formation phenomena and resulting properties of the debris bed using new melt simulant ( $ZrO_2-WO_3$ ) at higher temperatures. We consider the effects of the melt material, melt superheat, initial jet velocity on the (i) fraction of agglomerated debris, (ii) particle size distribution, (iii) ablation and plugging of the nozzle for the melt release. Several DEFOR-A (Debris Bed Formation – Agglomeration) tests have been carried out with the new corium simulant material and a mockup of the melt releasing nozzle. In the previous work we considered melt released above water level (DEFOR-A10 - A13). In this work we report results of the tests that have been carried out with melt release under water (DEFOR-A14 - A21). We found that the difference between the particle size distributions obtained in the tests with melt release above water level is minor, while on average slightly larger particles are obtained in the tests with melt release under water. There is no visible effect of the initial jet velocity on debris agglomeration. Results of the tests confirmed that melt superheat has major impact on the fraction of agglomerated debris and on the intensive ablation of the nozzle sample made of lower melting temperature metals.

DECOSIM code has been developed for analysis of porous debris coolability. In this work we the code was further developed to address debris bed coolability in post-dryout regime. The DECOSIM was further validated against new COOLOCE data for different configurations: (i) cylindrical debris bed with open side walls (COOLOCE-10), (ii) conical bed on a cylindrical base (COOLOCE-12). An analytical model is proposed based on the analysis of DECOSIM calculations for prediction of the maximum temperature of the debris if the size of the dry zone is known. Excellent agreement with the DECOSIM data is demonstrated. The model for

prediction of particulate debris spreading was implemented in the DECOSIM code allowing calculations of the debris bed spreading phenomena with possible feedbacks between dryout and spreading effectiveness.

Boiling and two-phase flow inside the bed is a source of mechanical energy which can help to spread the debris bed by so called “self-leveling” phenomenon. However, to be effective in providing a coolable geometrical configuration, self-leveling time scale has to be smaller than the time scale for drying out and onset of re-melting of the bed. In this work a new scaling approach for particulate debris spreading has been proposed. Based on the scaling and on the PDS-C experimental data a universal semi-empirical closure has been developed for prediction of particulate debris spreading. Validity of the closure for arbitrary shaped and multi-size particles to be confirmed in the future PDS-C tests.

In this work we present an approach developed for analysis of steam explosion sensitivity to the uncertain modeling and scenario parameters using TEXAS-V code. First results indicate that the most influential parameters are water level and water temperature. More work is necessary for selection and justification of the parameter ranges and clarification of their potential inter-dependencies. Obtained database of impulse and pressure as a function of the TEXAS input parameters is used for development of the surrogate model. Further work will be directed towards: (i) the sensitivity study aiming to cover completely all cases of melt ejection mode and vessel failure scenarios; (ii) refinement and generalization of the surrogate model; (iii) development of a robust approach to identification and classification of the failure domain in multidimensional space of input parameters and scenario parameters.

# 1 Introduction

## 1.1 *Motivation and background*

In this work we continue research work which was presented in the previous NKS report [35]. The project is motivated by Severe Accident (SA) Mitigation Strategy adopted in several designs of light water reactors (LWR) and specifically in Nordic type BWRs. The LWR SA management strategy considered hereafter is based on ex-vessel melt coolability in the reactor cavity filled up with water. It is assumed in the design that, in case of severe core melt accident, reactor pressure vessel (RPV) lower head can fail and molten core materials (corium) can be poured into a several meters deep reactor cavity filled with water. It is assumed further that decay heat can be removed from the debris bed by natural circulation. However, coolability of such bed is contingent upon the properties of the debris bed, such as particle size distribution, porosity and geometrical configuration of the bed. A tall, mound shape debris bed can be hardly coolable, while the same mass of the debris can be easily cooled if the bed is spread uniformly over the area of the reactor cavity [7], [10].

Generally, the SA management strategy has to be proven robust (insensitive to scenarios and conditions of melt release from the vessel). Yet, there is apparent significant influence of the accident scenario on the success of the SA management strategy. Specifically, melt release mode defines conditions and effectiveness of melt fragmentation, spreading and thus coolability. There are several characteristic modes of vessel failure and melt release that might result in completely different ex-vessel melt configurations. It is instructive to note that even within one scenario of accident progression the melt is expected to be released in more than one shot with different (a) sizes of the vessel breach, (b) different melt compositions (oxidic or metallic), (c) melt superheats. Respective configuration of the debris bed can be completely fragmented particles (small vessel breach, small superheat of the melt), mixture of liquid and solid particles promoting formation of non-coolable “cakes” (medium size breach) and mostly liquid melt (large size breach, large melt superheat). A prove of the robustness of the management strategy implies systematic and consistent analysis of different scenarios of melt release modes, their consequences for the ex-vessel melt arrest and coolability and associated epistemic and aleatory uncertainties. It is expected that some melt release scenarios will result in formation of non-coolable debris configurations threatening containment integrity.

Although the strategy of melt quenching in a pool is known for decades and has been a subject for intensive research since '80s, the main questions persist: whether or not decay heated porous debris bed can be cooled by natural circulation in the reactor cavity pool; and is there a threat to containment integrity due to energetic steam explosion, which can occur during melt pouring into water.

The APRI (Accident Phenomena of Risk Importance) research program was initiated at the Royal Institute of Technology (KTH) to help bring to the resolution the long standing severe accident issues: ex-vessel coolability and steam explosion for the Swedish-type BWRs. Advanced experimental infrastructure for tests with high melting temperature core melt simulant materials was developed at the division of Nuclear Power Safety (NPS) during last two decades with continuous support from Swedish nuclear power utility and safety authority. The focus of the previous APRI-7 (2009-2011) and current APRI-8,9 (2012-2017) at NPS-KTH is development of understanding and predictive capabilities for the debris bed formation and coolability phenomena in the process of melt pouring into coolant.

The research program on debris bed formation (DEFOR) carried out in the framework of APRI projects includes experimental studies [28], [29], [30], [22], [32], [34], [21], [35], [37], [38], [12], [33] in the DEFOR facility and comprehensive analytical research [49], [35], [36], [13], [26], [23], [48], [51], [24], [50], [14], [27], [38], [39], [16], [25]. Sophisticated experimental techniques and multiphysics computational approaches were developed over the last years to understand and model the process of particle bed formation when a melt jet is released in a pool of water. The pool depth and water subcooling can be varied and so can be the melt jet height and the volume discharged into the water pool. The melt materials and compositions employed can be varied also, e.g. ceramic and glass type melts at temperatures up to 1500°C with different melt viscosities can be employed.

COOLOCE facility at VTT [1], [2] has been used in the past for analysis of debris bed coolability. As a pool type facility, it can be used not only for analysis of coolability of different 2D and 3D geometries of the debris bed, but also for investigation of particulate debris spreading. However, there is a concern if presence of the vertical heaters and thermocouples can affect spreading of the bed.

In this work we clarify the concerns about the effect of the heaters and thermocouples on particulate debris spreading using PDS-C (particulate debris spreading closures) experiment at KTH with the same particles and mockups of heaters and thermocouples used in the COOLOCE facility.

DECOSIM is a thermo-hydraulic code developed at KTH for simulation of debris bed formation and coolability [48], [49], [35]. In the framework of this work, validation of DECOSIM code is being performed against the COOLOCE data. The work is concerned with further development of the code for prediction of (i) debris coolability in post-dryout regime, and (ii) debris bed spreading.

## **2 Investigation of Melt Jet Fragmentation, Debris Bed Formation and Melt-Structure-Coolant Interactions in DEFOR-A Facility**

### **2.1 Goals and Tasks**

The goal of the research project is to provide experimental data and develop analytical methods and approaches which can be used to facilitate technical decision making on development of general severe accident mitigation strategy for LWR in case of corium melt release through a breach in lower head into the flooded drywell. The emphasis is thus on the interaction of the melt with vessel lower head and debris bed formation.

The main tasks of the research project are to produce experimental data, and to develop and validate analytical models for assessment of:

- i. Effectiveness of liquid melt jet fragmentation and debris bed formation in different conditions of
  - i. melt release (jet diameter, free fall height etc.)
  - ii. melt superheat
  - iii. water subcooling
  - iv. and water pool depth
- ii. Radial, axial ablation and plugging of the nozzle (sample) for melt release.

In the following we provide the main results of the 4 new tests of the DEFOR-A series A10-A21. The review of the previous DEFOR-A01-09 tests can be found in [31], [32] and [33].

The DEFOR-A10 - A21 tests have been performed with new simulant material ( $ZrO_2-WO_3$ ). Its application was mainly motivated by the need for the improvement of the melt fragmentation visualization: used in previous DEFOR-A tests mixture of  $Bi_2O_3-WO_3$  as corium melt simulant produced an opaque cloud when interacting with water. The cloud was hindering observations of the melt jet fragmentation process and prevented observation of the debris bed formation. Results of DEFOR-A10 – A13 tests have been presented in [35].

Primary tasks of the DEFOR-A10-A21 tests are as follows:

- i. Validate prototypic behavior of the new simulant material in terms of melt jet fragmentation and debris bed formation:
  - compare experimental data on debris bed agglomeration and melt jet fragmentation with previous DEFOR-A and DEFOR-S test results obtained with already validated  $\text{Bi}_2\text{O}_3\text{-WO}_3$  simulant,
  - compare experimental particle size distribution with FARO tests results obtained on prototypic oxidic corium.
- ii. Assess the effect of the melt jet free fall height on the particle size distribution.
- iii. Assess the effect of the direct melt release into water (through a submerged conical or bottom-flat shell) on the melt fragmentation and debris bed formation.
- iv. Study axial and radial ablation of the immersed in water nozzle (sample) upon melt release.
- v. Investigate possibility of melt freezing inside the sample and late nozzle plugging.

Task (i) and (ii) were addressed in the A10 and A11 tests respectively; remaining tasks (iii-v) were evaluated in tests A12 - A21.

## 2.2 Experimental Facility

DEFOR (Debris Bed Formation) facility was developed for studies of melt fragmentation, particle and debris bed formation and agglomeration in deep water pool.

The installation consists of (i) an induction furnace for melt generation, (ii) a funnel for melt deliver, (iii) a test section with optional metallic sample, and (iv) external water heating system. The scheme of the installation is given in the Figure 1a and Figure 3a. The furnace is composed of a (i) SiC crucible inductively heated with a 45kW medium-frequency (up to 30 kHz) generator and (ii) an opened housing connected to a tilting mechanism for crucible leaning and melt delivery into the funnel.

The furnace can provide melting of corium simulant materials at temperatures up to 1600°C and melt volume up to 10 liters. It is equipped with three bottom thermocouples and one lateral thermocouple for temperature control.

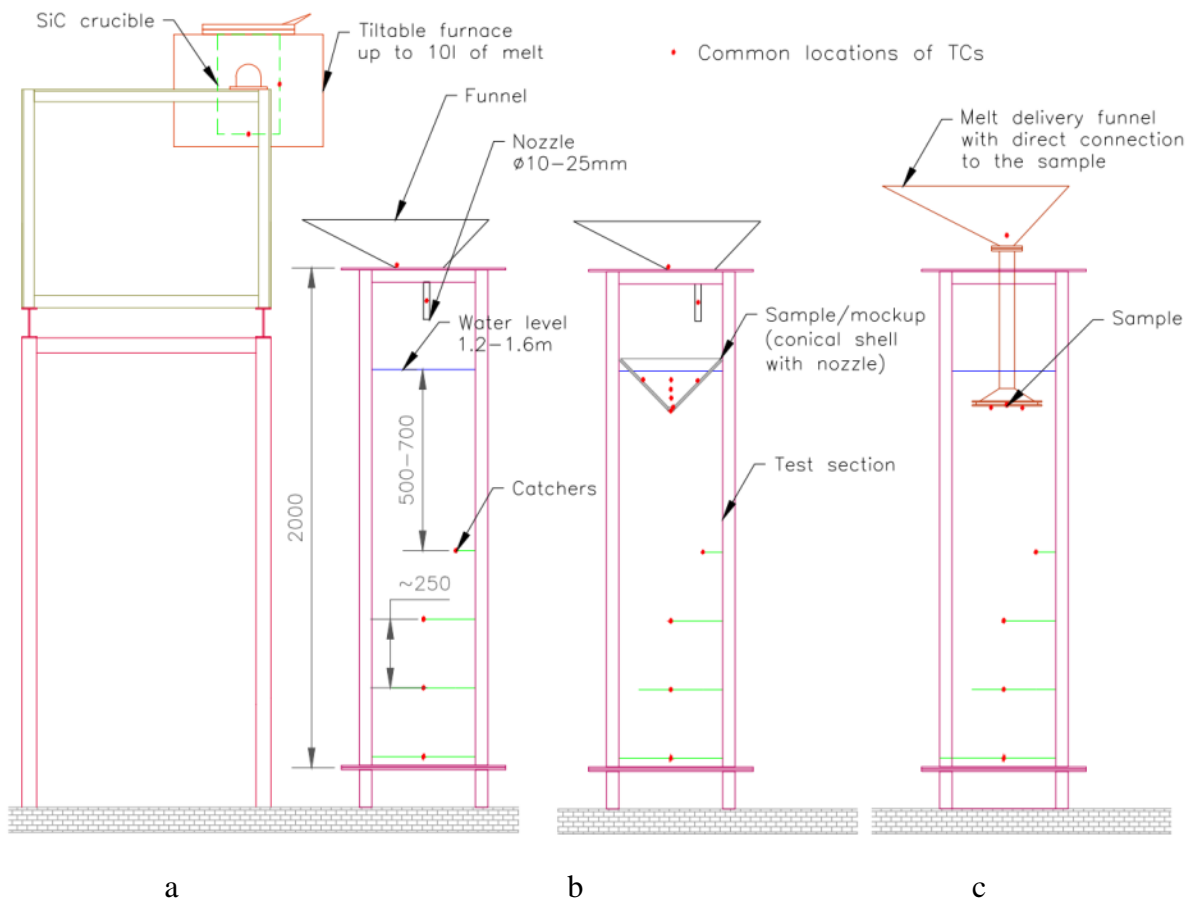


Figure 1: DEFOR experimental facility: a – common setup for DEFOR-A01-11;15, b – common setup for DEFOR-A12-14;16 and c - DEFOR-A17-21.

The funnel is equipped with nozzle which allows jet diameters from 10 to 25 mm. A K-type thermocouple is positioned inside the nozzle for the temperature measurement of the delivered melt.

The DEFOR test section is a vertical 2.0 m tank with approximately rectangular cross section 0.5x0.5 m filled up with tap water. The water for the tests is heated in an external tank to a predefined temperature and is poured into the test section shortly before the melt delivery.

Visual observation of the melt release and melt-coolant interaction is performed through a number of rectangular Plexiglas windows installed on lateral sides of the test section. Commonly up to five cameras are used to record the melt-coolant interaction, including a number of high-speed cameras with up to 735 frames per second.



a



b

Figure 2: DEFOR catchers with debris: a – side view; b – top view

Inside the test section 4 debris catchers are positioned at different elevations (Figure 2). Vertical location of the catcher can be adjusted according to test requirements. Each catcher is covering one of four quadrants of the test vessel cross section and collects melt fragments ejected from the jet. This allows assessment of the water pool depth on debris bed formation: agglomeration

and local particle size distribution. The water pool depth and depth of the top catcher are chosen to ensure complete breakup of the melt jet. This is required to avoid the possible effect of the catchers on jet fragmentation and breakup length.

The water temperature inside the test section is measured along the walls at several elevations; the debris temperature is measured on every catcher by 2 thermocouples installed in the vicinity of the jet. In addition several TCs can be placed above the water level. The exact positioning and number of thermocouples varies from test to test.

The installation is placed inside a concrete containment for personnel safety (danger of steam explosion, melt splashes etc.) and is controlled remotely.

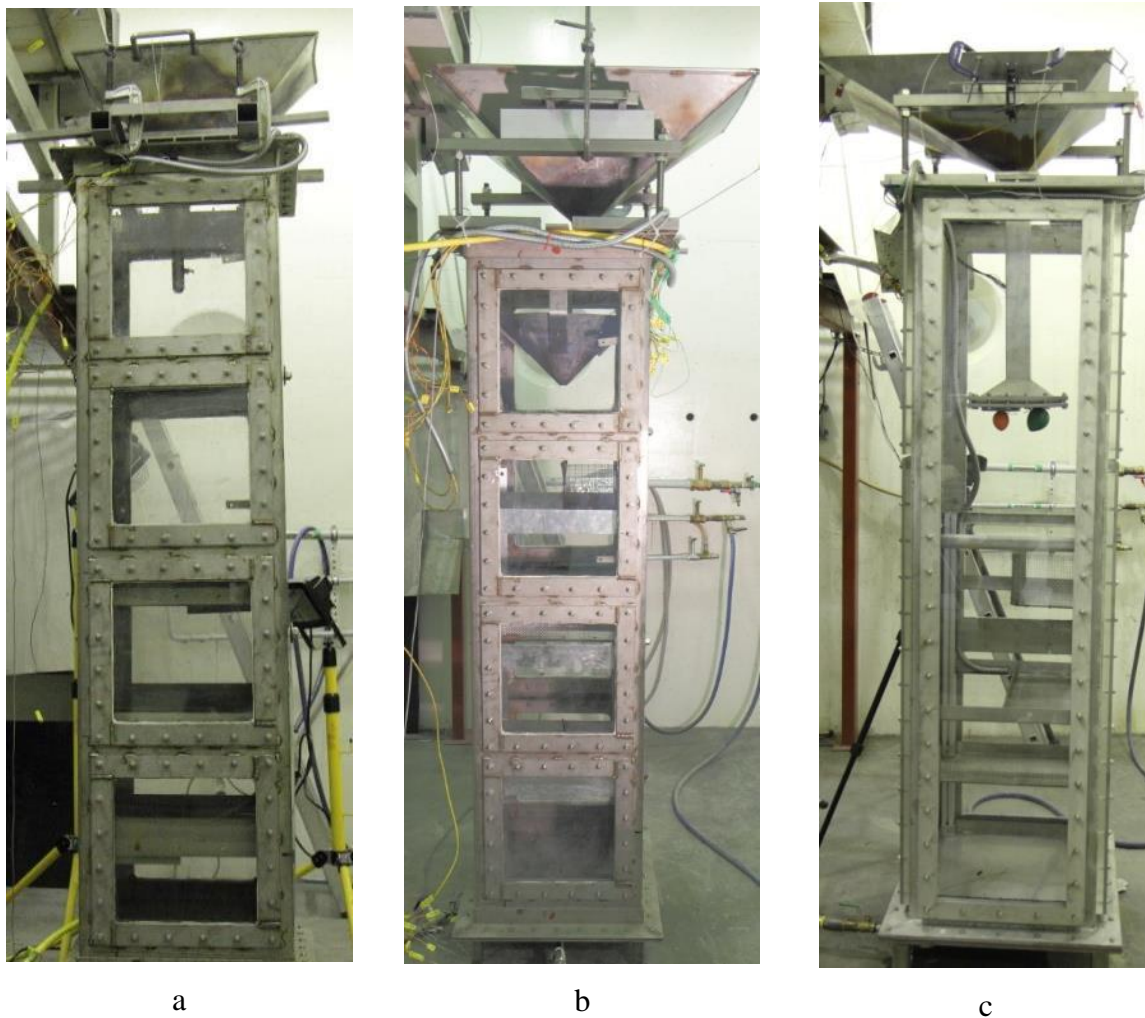


Figure 3: DEFOR-A experimental setup without (a), with conical shell (b) and horizontal plate as sample.

In the DEFOR-A12-14;16 configuration (Figure 1b and Figure 3b) a test sample is installed at the top of the water pool to study (i) wall and nozzle ablation during melt release and (ii) effect of melt release directly into water on resulting debris size distribution and agglomeration. The test sample is designed as a conical shell with 90 degree angle and with single hole at the bottom (apex). Being partially immersed into water and provided 45° inclination angle of the lateral surface allows efficient heat removal due to intense natural convection flows increasing the critical heat flux limit in comparison with a not-inclined (horizontal) surface.

In the DEFOR-A17-A21 tests the experimental configuration (Figure 1c and Figure 3c) differs by following:

- New DEFOR test section has been designed and manufactured providing following advantages:
  - Larger windows from all four sides for a better visual observation.
  - Rigid construction preventing wall vibrations.
- The geometry of the sample used.

The geometry of the sample in DEFOR-A17-A21 tests is chosen to be a flat horizontal plate. The reasons for sample geometry change are following. Physical phenomenon that has not been observed in previous tests and that is considered to be one of important modes of wall failure is nozzle ablation. Another issue requiring clarification are conditions of the nozzle plugging. It was assumed that nozzle length to diameter ratio is one of the key parameters affecting nozzle plugging. With this regard the following additional goals have been identified:

- To provide conditions at which nozzle ablation and plugging could be studied experimentally.
- To clarify importance of the nozzle diameter for plugging.
- To confirm the influence of the mockup on the melt fragmentation, agglomeration and debris bed formation phenomena.
- To provide experimental data for model development and validation.

The material of the sample (lead) has melting temperature (327°C) lower than that of the melt (870°C or 1231°C), but higher than Leidenfrost temperature to allow for dryout on the wall. The difference between melting temperatures of the melt simulant and the sample material is 540°C for Bi<sub>2</sub>O<sub>3</sub>-WO<sub>3</sub> and 1000°C for ZrO<sub>2</sub>-WO<sub>3</sub> eutectic mixtures respectively.

After each test the debris beds from every catcher undergo systematic analysis for debris bed topology, total porosity, agglomerated vs non-agglomerated mass, mass of cake and particle size distribution. The obtained data is then plotted as a function of catcher depth and compared to other tests in terms of the melt superheat, water subcooling, melt release conditions and melt material.

Ranges of varied experimental parameters of the whole DEFOR-A series are summarized in Table 1.

Table 1: Ranges of the DEFOR-A tests parameters

Parameter	Unit	Range
<b>Test section parameters</b>		
Pool depth: $H_{pool}$	m	1.1-1.75
Water temperature	°C	70 – 93
Debris catchers	-	4 catchers installed at different elevations inside the test section
<b>Melt parameters</b>		
Material and melting temperature	-	ZrO <sub>2</sub> -WO <sub>3</sub> (eutectic), 1231°C; Bi <sub>2</sub> O <sub>3</sub> -WO <sub>3</sub> (eutectic), 870°C
Melt superheat	°C	50-200
Melt volume	liters	3-6
Jet free fall height: $H_j$	m	0.2-0.9
Jet diameter: $D_{jet}$	mm	10 – 25
<b>Sample parameters</b>		
Sample geometry	-	Conical shell with a nozzle at the tip of the cone or flat plate with single or multiple nozzles.
Initial conditions inside the sample	-	Wet (filled with water through open nozzle);
Sample material and melting temperature	°C	Lead, 327°C
Base diameter of the sample	mm	400 mm
Free volume inside the sample	liters	8.4
Water pool depth in the sample:	mm	150
Water pool volume	liters	3,5
Sample wall thickness	mm	5 – 20
Sample nozzle diameter	mm	5 – 30

## **2.3 Results and Discussion**

### **2.3.1 DEFOR-A10-A21 experimental conditions and parameters**

#### **Test matrix**

All experimental conditions and main observation on all twelve recently performed DEFOR-A10-A21 tests are summarized in Table 2. Three tests A10, A11 and A15 have been performed in the same manner as previously performed A1-A9 [31]. In the rest nine tests the melt was poured through a nozzle manufactured in the Pb-plate (sample). In any case as presented below the resulting particle size distribution and agglomeration fraction are not affected by this experimental condition.

Note, that in some cases the melt was released directly under water, i.e. when sample is emerged under water surface. In this case the initial melt velocity is smaller than in in jet free fall cases. A slight influence on resulting particle size distribution can be expected.

The increased free fall height has been established by decreasing the water level in the DEFOR test section by 50 cm. This also required shifting of the debris catchers with respect to the water surface, except for the top one, which position (depth with respect to the free surface) has been preserved.

Table 2: Summary of the DEFOR-A10-A21 tests conditions and main results

Parameter	A10	A11	A12	A13	A14	A15	A16	A17	A18	A19	A20	A21
Melt material	ZrO <sub>2</sub> WO <sub>3</sub>											
Eutectic melt composition (mass fraction, %)	16.4-83.6	16.4-83.6	16.4-83.6	16.4-83.6	16.4-83.6	16.4-83.6	16.4-83.6	16.4-83.6	16.4-83.6	16.4-83.6	16.4-83.6	16.4-83.6
Eutectic temperature, °C	1231	1231	1231	1231	1231	1231	1231	1231	1231	1231	1231	1231
<b>Melt parameters</b>	<b>A10</b>	<b>A11</b>	<b>A12</b>	<b>A13</b>	<b>A14</b>	<b>A15</b>	<b>A16</b>	<b>A17</b>	<b>A18</b>	<b>A19</b>	<b>A20</b>	<b>A21</b>
Initial melt volume, liters	3	3	3	3	4	2	4	5	5	5	5	5
Initial melt mass, kg	20.6	20.6	20.6	20.6	27.5	13.8	27.5	34.3	34.3	34.3	34.3	34.3
Melt mass delivered into water, kg	17.08	13.39	15.32	6.74	21.16	3.5	18.95	24.39	22.76	30.55	26.24	3.43
Maximal melt temperature in the funnel $T_{max}$ , °C	1371	1333	1345	1293	1467	1231	1348	1462	1420	1545	1518	1517
Melt superheat, °C	150	102	114	62	196	~0	117	231	189	314	287	286
$T_{max} - T_{sample\ melting}$ , °C	-	-	1018	966	1140	-	1021	1135	1093	1218	1191	1190
<b>Pool parameters and experimental conditions</b>	<b>A10</b>	<b>A11</b>	<b>A12</b>	<b>A13</b>	<b>A14</b>	<b>A15</b>	<b>A16</b>	<b>A17</b>	<b>A18</b>	<b>A19</b>	<b>A20</b>	<b>A21</b>
Jet free fall height, m	0.2	0.7	0.13	0.13	0.20	0.2	0.2	-	-	-	-	-
Initial water temperature, °C	75	75	75	75	81	81	72	82	81	86	80	85
Water pool depth $H_{pool}$ , m	1.52	1.1	1.85	1.85	1.75	1.80	1.65	1.65	1.65	1.44	1.65	1.5
Jet diameter $D_{jet}$ , mm	20	20	20	20	20	20	20	-	-	-	-	-
$H_{pool}/D_{jet}$	75	55	75*	150*	115*	90	110*	82.5	82.5	48	55	50
Estimated melt jet velocity near water surface, m/s	~2	~4	~1	~1	-	~2	-	-	-	-	-	-

NKS-DECOSE Report-1/2013

Estimated melt jet velocity near Pb-plate surface, m/s	~1	~1	~1	~1	~1	~1	~1	-	-	-	-	-	
Release time, s	-	-	10	10	9.6	-	9.5	10	10	10	10	12	
Pouring time, s	13	12	22	6.6	11	9.6	22.7	10	13	10	15	13	
<b>Debris catchers</b>	<b>A10</b>	<b>A11</b>	<b>A12</b>	<b>A13</b>	<b>A14</b>	<b>A15</b>	<b>A16</b>	<b>A17</b>	<b>A18</b>	<b>A19</b>	<b>A20</b>	<b>A21</b>	
Catchers location (elevation / depth from Pb plate), cm	C1:	90 / 65	45 / 65	120 / 50	120 / 50	90 / 55	90 / 65	120 / 30	82.5 / 56	82.5 / 56	82.5/61	82.5/61	90 / 60
	C2:	60 / 95	30 / 80	80 / 90	80 / 90	60 / 85	60 / 95	80 / 70	55 / 83.5	55 / 83.5	55/88.5	55/88.5	60 / 90
	C3:	30 / 125	15 / 95	40 / 130	40 / 130	30 / 115	30 / 125	40 / 110	27.5 / 111	27.5 / 111	27.5/116	27.5/116	30 / 120
	C4:	0 / 155	0 / 110	0 / 170	0 / 170	0 / 145	0 / 155	0 / 150	0 / 138.5	0 / 138.5	0/143.5	0/143.5	0 / 150
<b>Pb-plate mockup / sample</b>	<b>A10</b>	<b>A11</b>	<b>A12</b>	<b>A13</b>	<b>A14</b>	<b>A15</b>	<b>A16</b>	<b>A17</b>	<b>A18</b>	<b>A19</b>	<b>A20</b>	<b>A21</b>	
Geometry	-	-	Con. shell	Con. shell	Con. shell	-	Con. shell	Plate	Plate	Plate	Plate	Plate	
Initial conditions inside the mockup <sup>***</sup>	-	-	Wet	Wet	Dry	-	Dry	Dry	Dry	Dry	Dry	Dry	
Material and melting temperature, °C	-	-	Pb, 327										
T <sub>simulant melting</sub> - T <sub>Pb melting</sub> , °C	-	-	904	904	904	904	904	904	904	904	904	904	
Base inner diameter, mm	-	-	400	400	400	-	400	-	-	-	-	-	
Wall thickness, mm	-	-	10	5	15	-	10	10 / 40	20 / 30	20	30	25	
Outlet(s) diameter $D_{out}$ , mm	-	-	20	10	15	-	15	20 / 20	20 / 20	30	30	30	
Outlet(s) height $L_{out}$ , mm	-	-	14.1	7.1	21.2	-	14.1	10 / 40	20 / 30	20	30	25	
$L/D_{jet}$	-	-	0.707	0.707	1.41	-	0.943	0.5 / 2	1 / 1.5	0.67	1	0.833	
Capacity, liters	-	-	8.60	8.59	8.57	-	8.62	-	-	-	-	-	
Water pool depth inside the mockup, mm	-	-	150	150	-	-	-	-	-	-	-	-	
Water pool volume inside the mockup, liters	-	-	3.53	3.53	0	-	0	0	0	0	0	0	

NKS-DECOSE Report-1/2013

Main observations	A10	A11	A12	A13	A14		A16	A17	A18	A19	A20	A21
Nozzle: -plugging -ablation	-	-	late no	early no	late no	-	early no	no / no wall failure / axial	late / axial late / axial	no rad/axial	no rad/axial	no rad/axial
Wall: -ablation	-	-	no	no	no	-	no	10 mm	10 mm	15 mm	10 mm	15 mm
Impingement point: -ablation	-	-	no	yes/plug.	complete	-	protected	-	-	-	-	-
Ingot: -type -mass, kg	-	-	hollow 2.35	solid 5.7	solid 1	-	solid 10	no 0	plug <0.5	crust <0.5	crust <0.5	crust <0.5
	A10: No sample, release of Ø20 jet into water from 20 cm height											
	A11: No sample, release of Ø20 jet into water from 70 cm height											
	A12: Wet conical shell, thick wall, complete release of the melt, late plugging, formation of a hollow ingot with two large cavities											
	A13: Wet conical shell, thin wall, melt through around the impingement point, plugging and formation of a solid massive ingot											
	A14: Dry conical shell, intermediate wall thickness, catastrophic melt through of the wall, formation of a small solid ingot											
	A16: Dry conical shell, thick wall, protective plate under impingement point, plugging, solid massive ingot											
	A17.1: Flat sample, thick wall, catastrophic melt through of the wall probably due to a cavity in the sample, not complete plugging											
	A17.2: Flat sample, thin wall, catastrophic melt through of the wall											
	A18.1: Flat sample, thick wall, late plugging, wall ablation around 10 mm											
	A18.2: Flat sample, thin wall, late plugging, wall ablation around 10 mm											
	A19: Flat sample, thin wall, no plugging, wall ablation up to 15 mm, nozzle radial ablation >25 mm											
	A20: Flat sample, thin wall, no plugging, wall ablation around 10 mm at the periphery and up to 30 mm around the nozzle, nozzle radial ablation 40-50 mm											
	A21: Flat sample, intermediate wall thickness, no plugging, wall ablation around 15 mm at the periphery and up to 25 mm around the nozzle, nozzle radial ablation 40 mm											

\*Estimated with respect to the diameter of the mockup nozzle and its elevation.

\*\*Duration of melt release from the mockup of the Pb-plate.

\*\*\*Wet: filled with water through open nozzle, Dry: nozzle plugged with fusible diaphragm.

## **DEFOR tests with conical sample**

The common for DEFOR-A12 and A13 test assembly is demonstrated in Figure 4. Note that water is not yet supplied into the DEFOR test section, its level is supposed to reach  $\sim 2/3$  of the test sample cone height. The sample is placed inside the DEFOR test section and fixed by four stainless steel 10 mm thick holders (Figure 4c). The nozzle of the sample is aligned with the test section vertical axis. The funnel for delivery of melt into the sample is placed above it in a way that the jet is shifted from the center of the sample and melt impingement point is on the underwater part of the sample conical wall.

In the Figure 5 the detailed designs of two samples manufactured for A12 and A13 tests respectively are provided. Main difference in samples geometry is in the nozzle diameter and wall thickness. Other geometrical parameters have been preserved the same. For A12 test the test sample has been manufactured with thick 10 mm walls and large 20 mm nozzle diameter (the same as used in the funnel for melt delivery). Such configuration is expected to be more resistant to the wall ablation while enlarged nozzle diameter should provide easier melt release decreasing the duration of melt residence time in the sample and thus decreasing possibility of nozzle plugging. For A13 test, sample has been manufactured with thinner 5 mm walls and decreased 10 mm nozzle diameter. Such configuration favors longer melt residence time, provides decreased sample to melt mass ratio speeding up sample heat up during interaction. Also thinner wall is more susceptible to onset of dryout.

Following some of the LWR designs (which implies wet cavity) the test sample is partially immersed into water (including melt impingement point). Water reaches 150 mm level measured from the sample nozzle outlet and is 130 mm away from the funnel nozzle outlet.

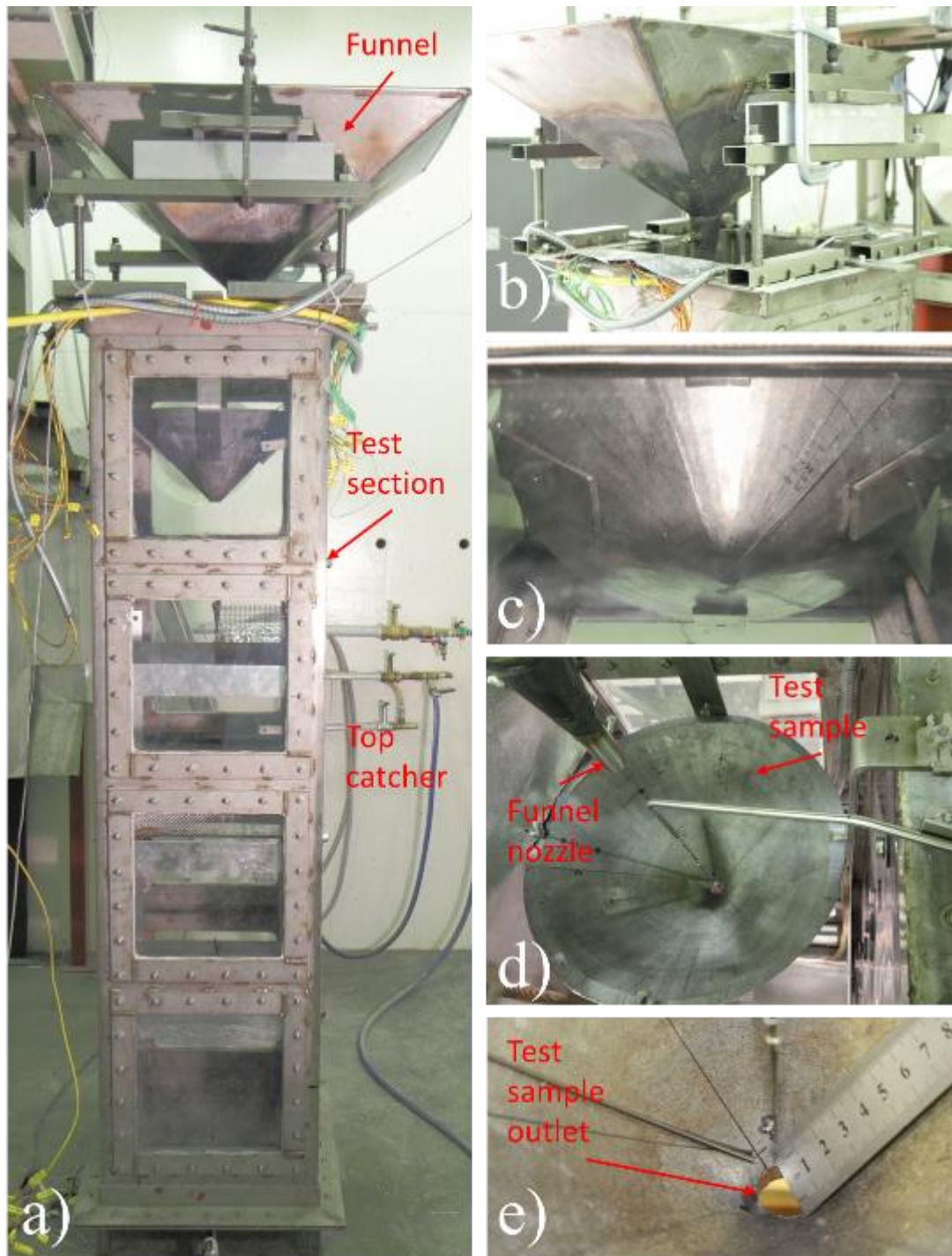


Figure 4: Common for DEFOR-A12 and A13 tests assembly (by example of the A12 test): general view (a), funnel (b) and melt granulation device (c-e) bottom, top and inside views respectively.

Several groups of thermocouples have been installed in the sample: around melt impingement point, around nozzle outlet and inside the water pool along the vertical axis. The junctions of the outside superficial TCs have been peened into the conical sample as close as possible to the

surface, while the inside TCs have been flushed to the surface (see below Figure 6 for illustrations). The bodies of the TCs have been secured by feeding through rivets or screws fixed around the circumference of the sample above the water level.

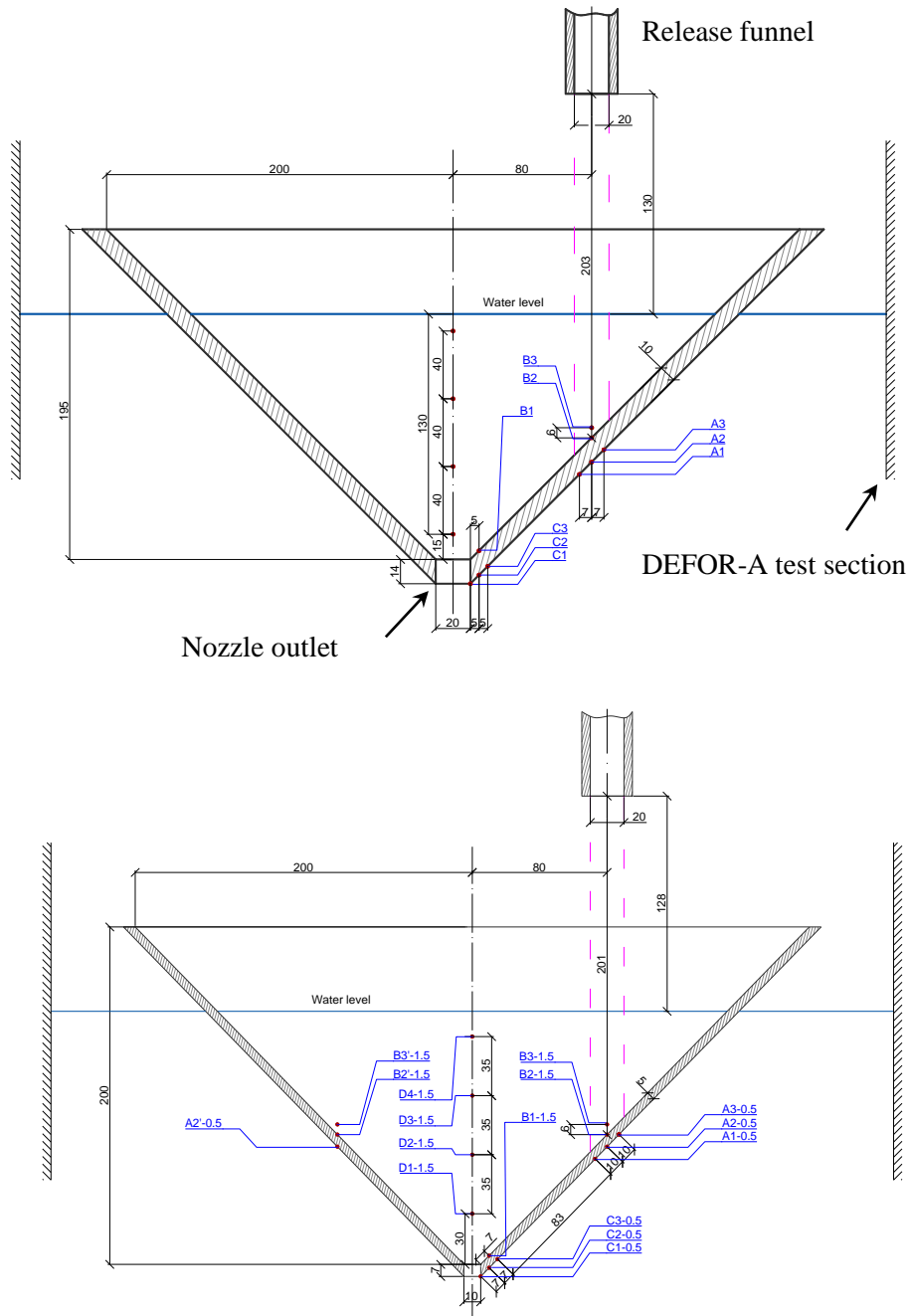


Figure 5: Design and instrumentation of the test sample in A12 (top) and A13 (bottom) tests

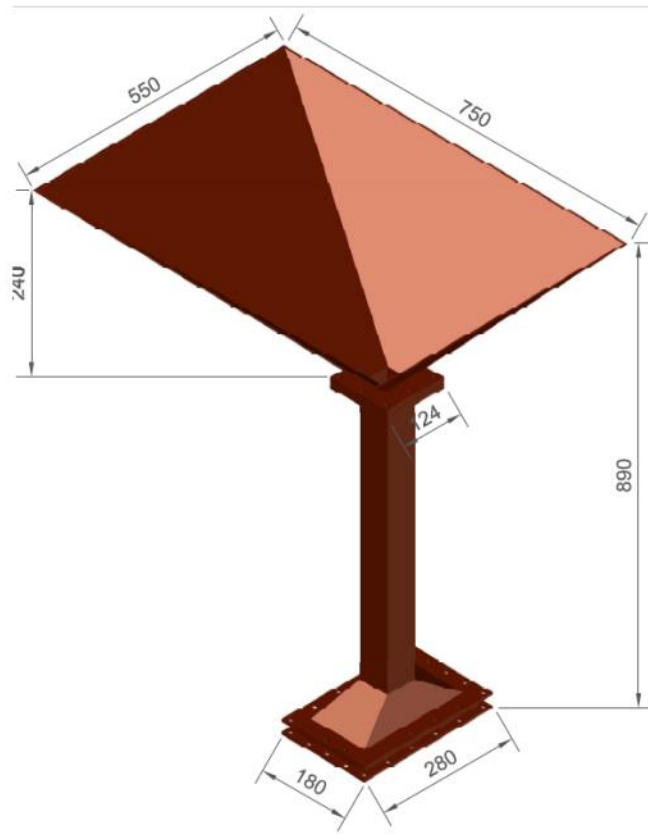


Figure 6: Setup of TCs inside the test sample common for A12 and A13 tests: a – B2 and B3 TCs; b – C1-C3 TCs; c – TCs feeding through screws fixed in the sample wall.

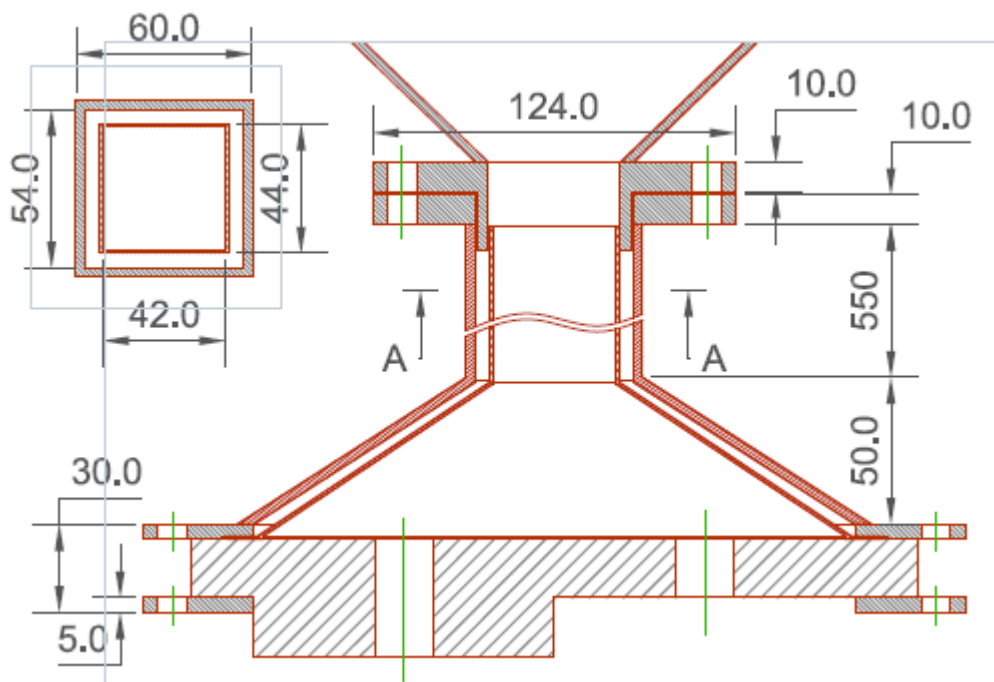
The TCs flushed to the outer surface are  $\varnothing 0.5$  mm and those in direct contact with the melt are  $\varnothing 1.5$  mm. Notice that B3 thermocouple is bended 6 mm upward from the surface to measure the temperature of the impinging jet. Also notice that in A13 test 3 TCs: B2', B3' and A2' have been added symmetrically to B2, B3 and A2 for comparison.

### **DEFOR tests with sample plate**

In the DEFOR-A17-A21 series of the tests the flat sample geometry has been used. For such geometry a special melt delivery setup and funnel have been designed and manufactured. As shown in Figure 7 and Figure 8 the setup consists of funnel, vertically extended column having double wall and filled by insulation material, sample plate and its holder.



a



b

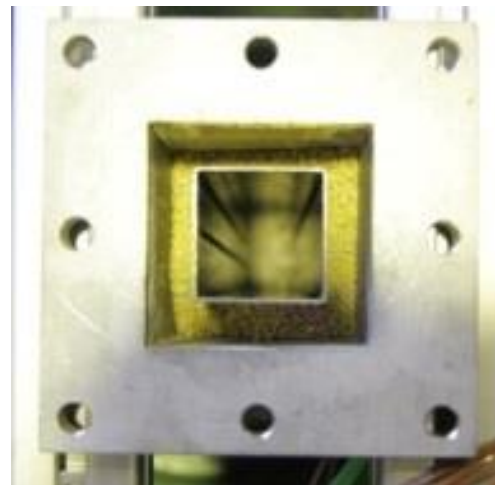
Figure 7: Melt delivery setup with vertically extended column (a) and typical dimensions of the lead plate (sample) and its holder (b).



a



b



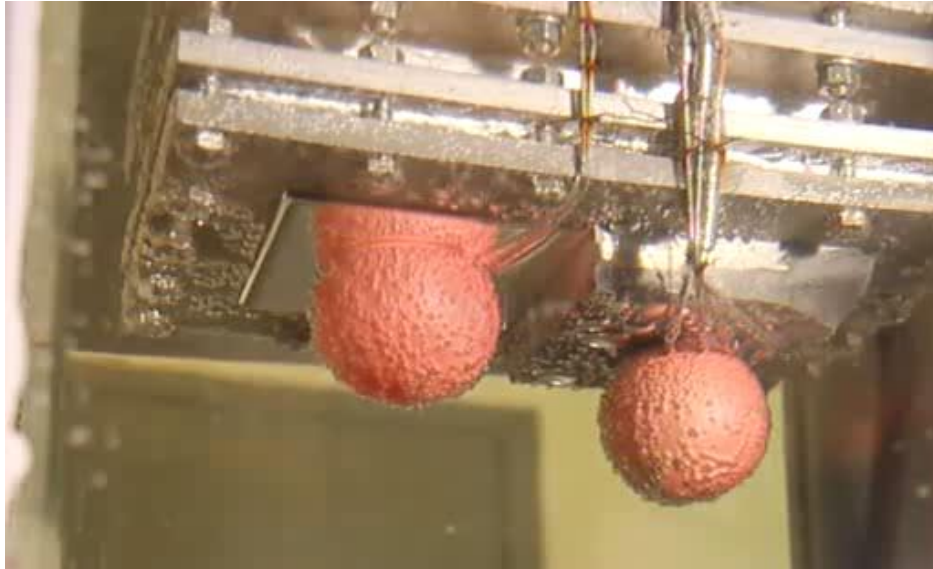
c



d

Figure 8: Experimental facility: general view (a), melt delivery setup (b), view on the extended column cross section and gap filling (c) and lead plate holder (d).

In order to prevent the contact between water and melt inside the melt delivery column above the plate the plate nozzle outlet is usually tightly plugged by an air-pressurized rubber balloon (Figure 8a, Figure 9).



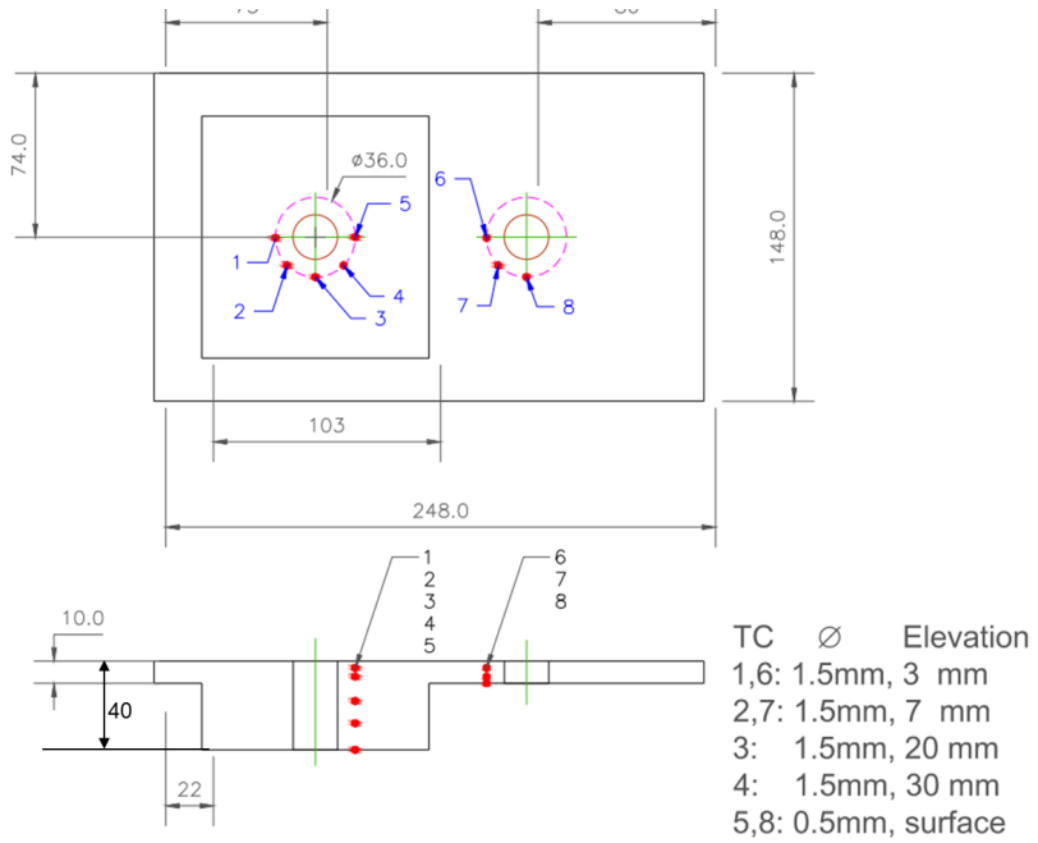
a)



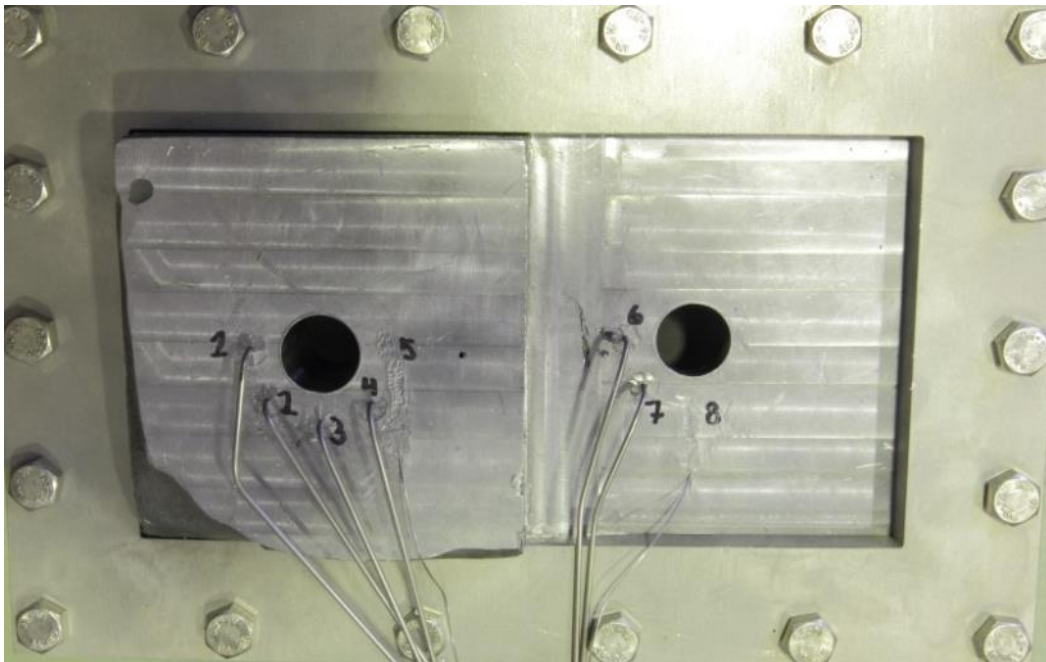
b)

Figure 9: DEFOR-A17 (a) and A18 (b) sample plates with nozzles plugged by the air-pressurized rubber balloon.

The samples in DEFOR-A17-A21 are made of lead by the casting process with predefined positioning of the thermocouples. The Omega made K-type TCs with nominal 0.5, 1.0 and 1.5 mm thickness have been used. The dimensions and TC positioning (a) as well as plate bottom images (b) are shown in Figure 10 through Figure 14 for A17-A21 tests respectively.

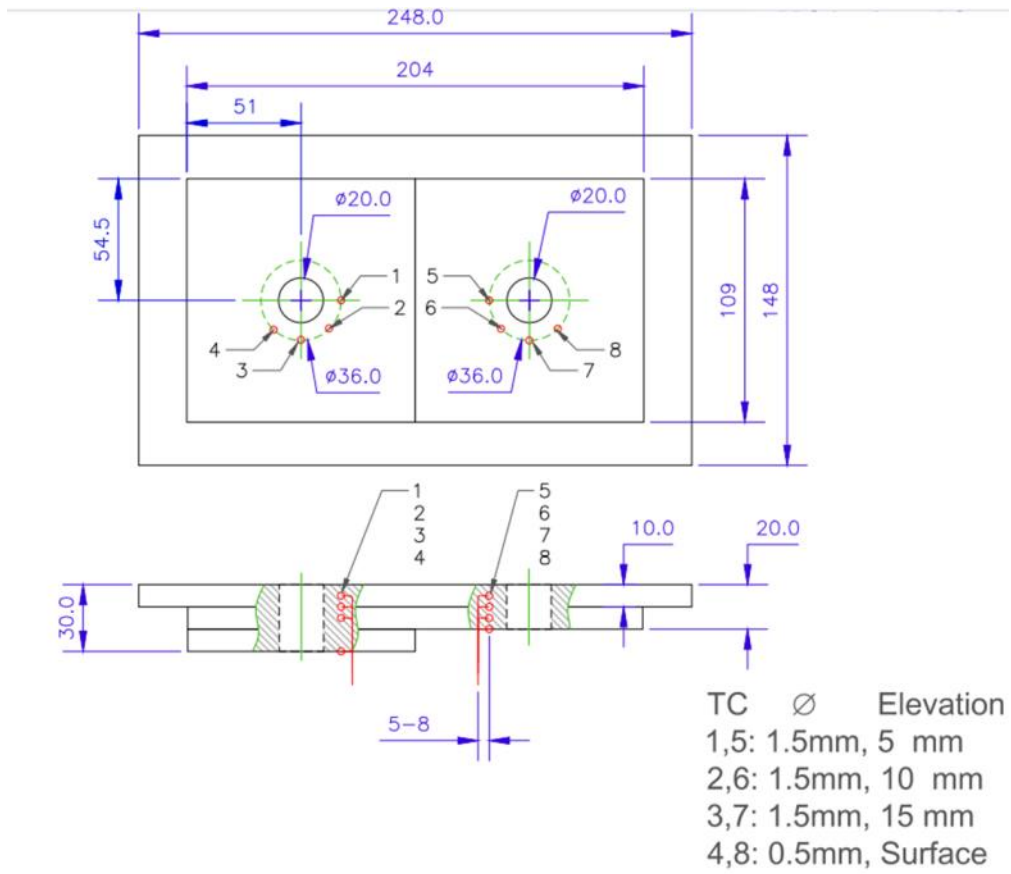


a)

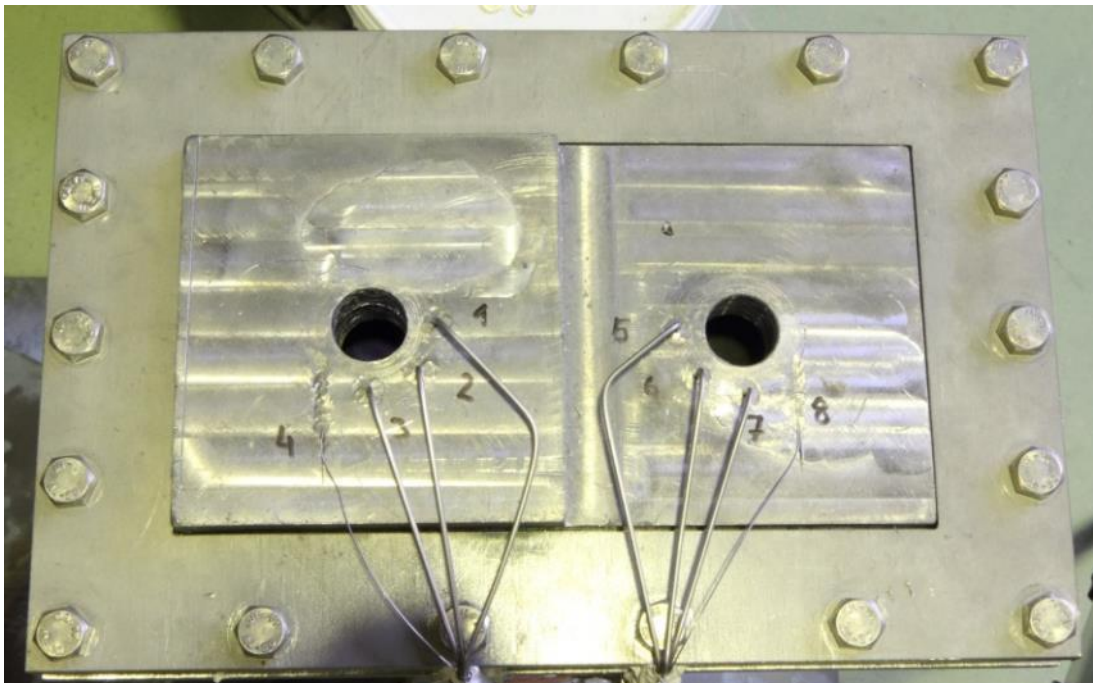


b)

Figure 10: DEFOR-A17 sample: drawing and TC positioning (a) and actual bottom side of the plate (b).

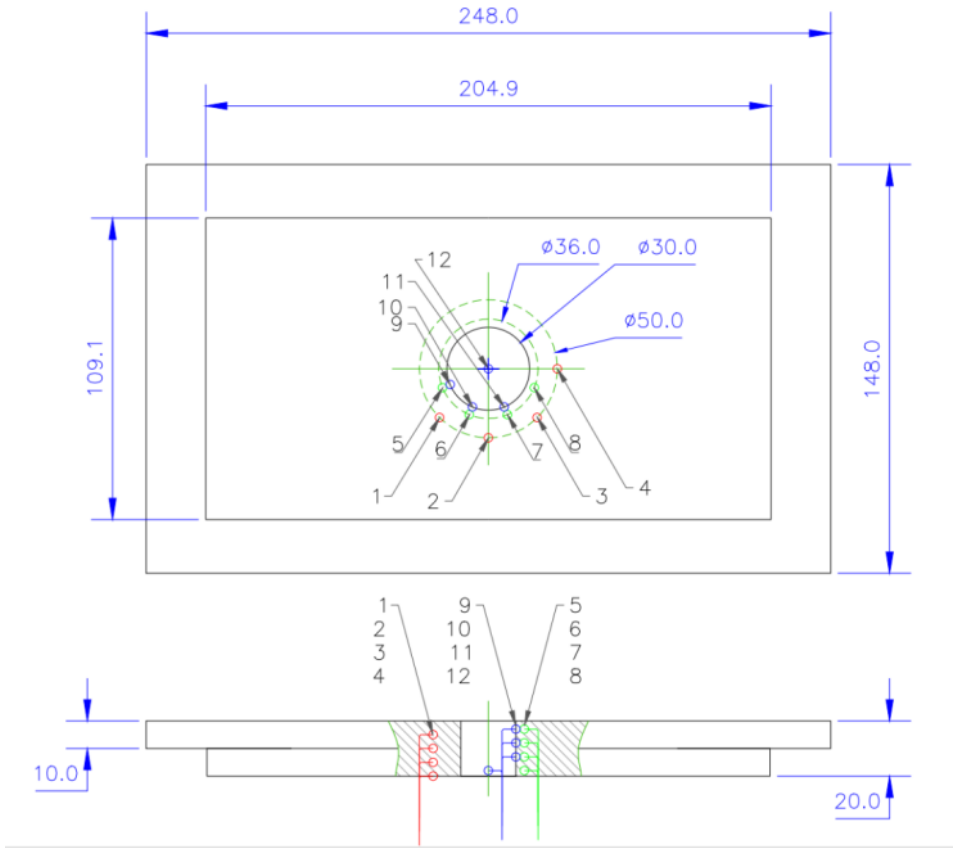


a)

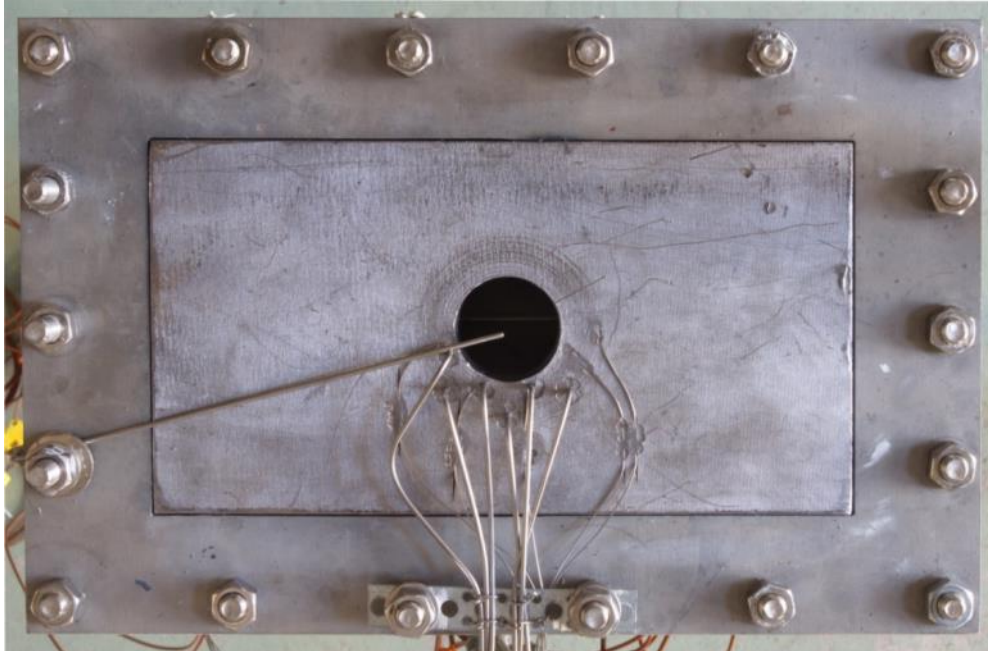


b)

Figure 11: DEFOR-A18 sample: drawing and TC positioning (a) and actual bottom side of the plate (b).



a)



b)

Figure 12: DEFOR-A19 sample: drawing and TC positioning (a) and actual bottom side of the plate (b).

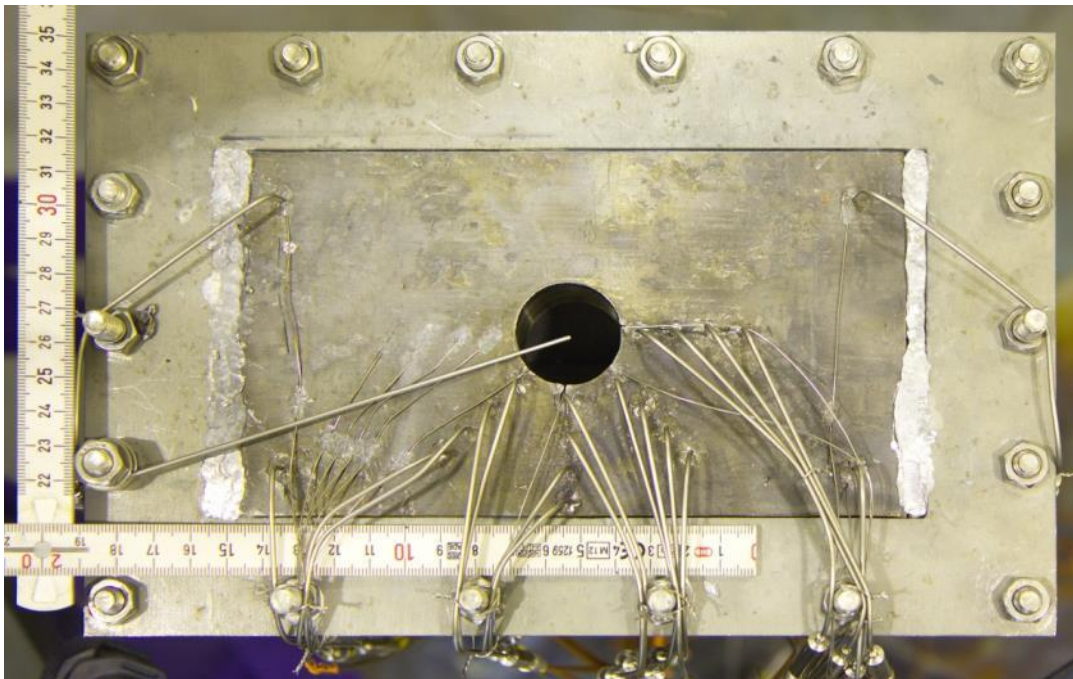
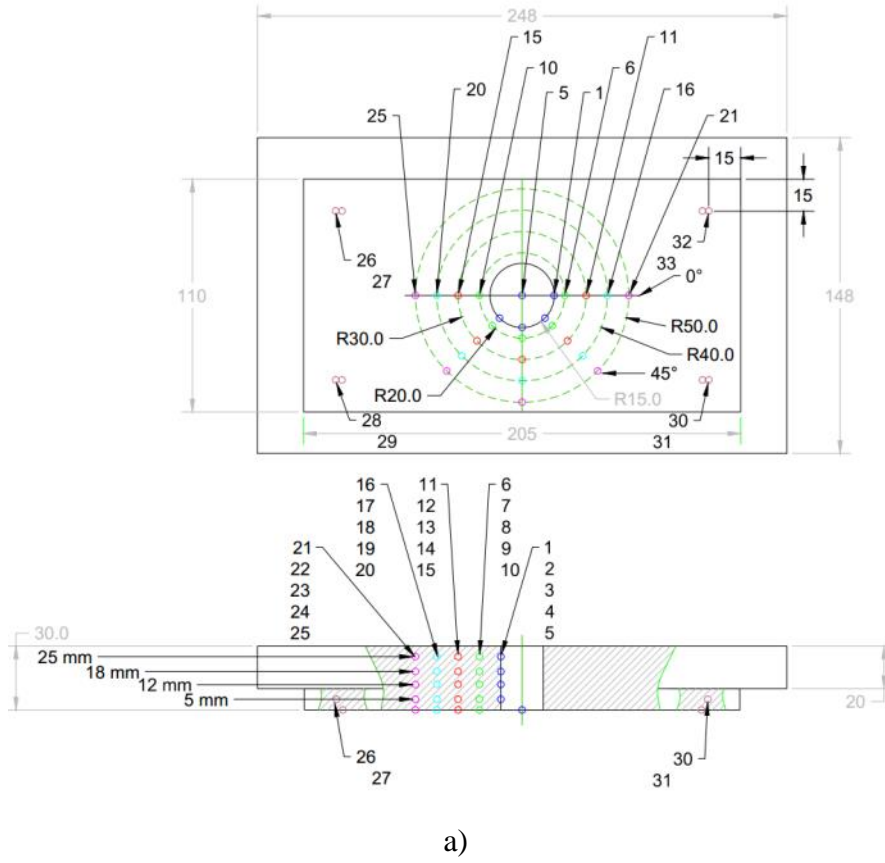
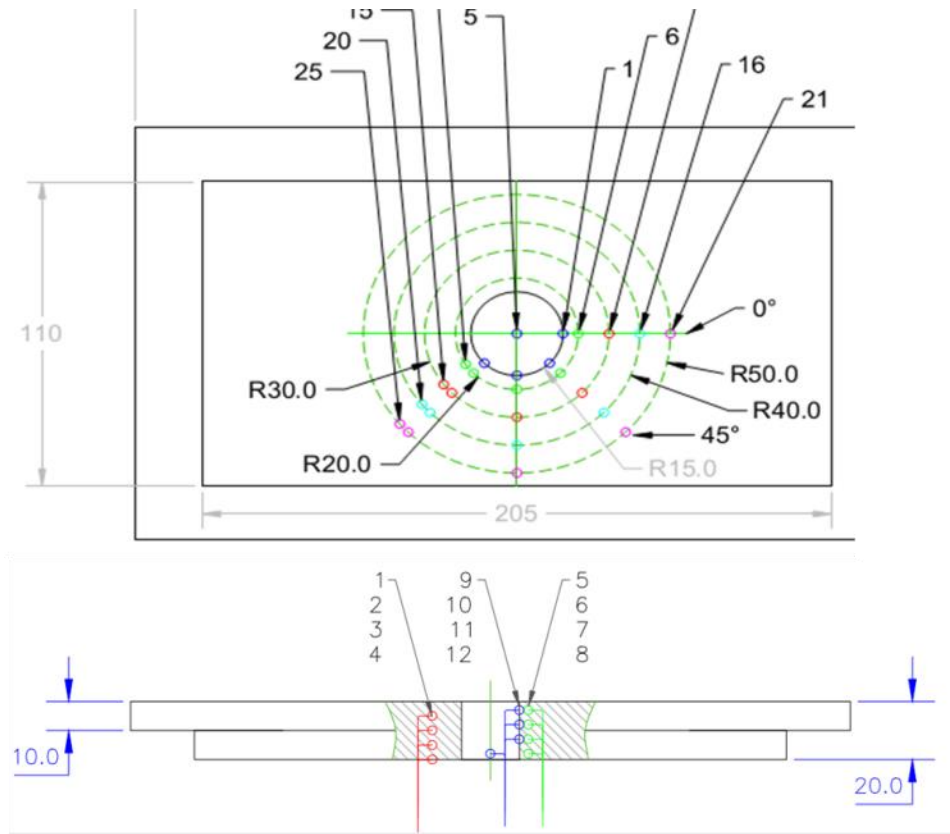
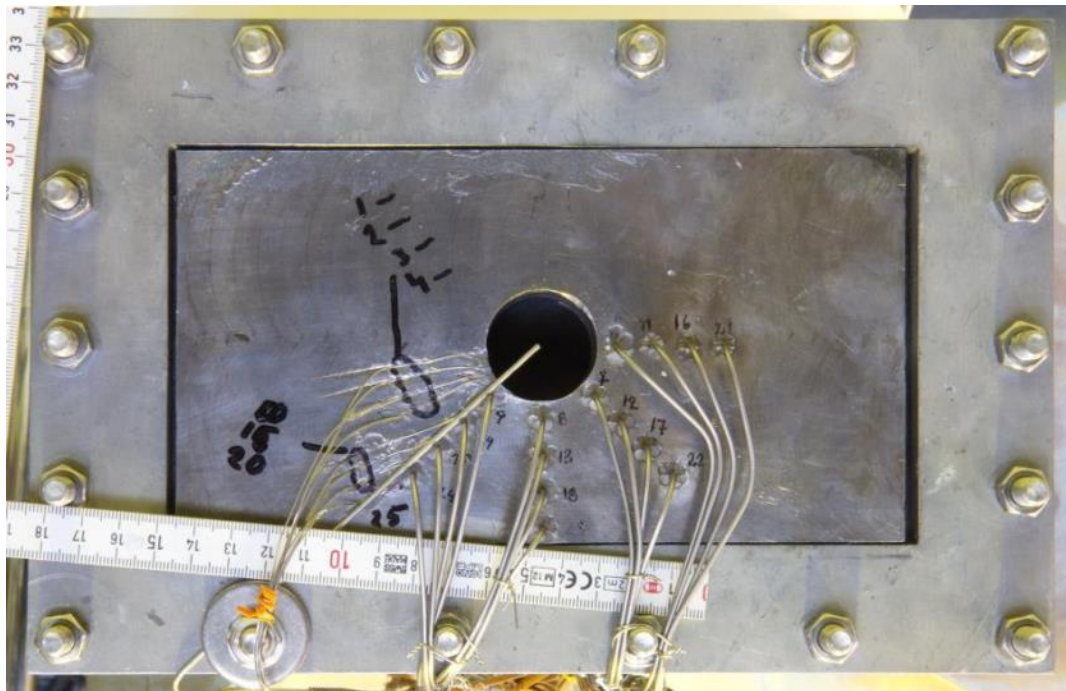


Figure 13: DEFOR-A20 sample: drawing and TC positioning (a) and actual bottom side of the plate (b).



a)



b)

Figure 14: DEFOR-A21 sample: drawing and TC positioning (a) and actual bottom side of the plate (b).

### 2.3.2 Melt pouring

In this subsection the details on melt pouring in DEFOR tests are provided. A typical melt pouring conditions are discussed and corresponding illustrations are provided for the selected experiments out of each following categories:

- Tests without sample
- Tests with sample having the geometry as:
  - Conical;
  - Plate.

The complete characteristics of the melt pouring conditions for each test can be found in Table 2 in subsection 2.3.1.

#### DEFOR tests without sample

In A10-12 tests melt release took around 12-13 sec in A10-A11 and 9.6 in A12. Out of 20.6 kg of the initial melt charge, in A10 test 17.08 kg of melt has been delivered into water, in the A11 this value has been somewhat smaller 13.39 kg. The difference can be attributed to the lower melt superheat in the A11 test.

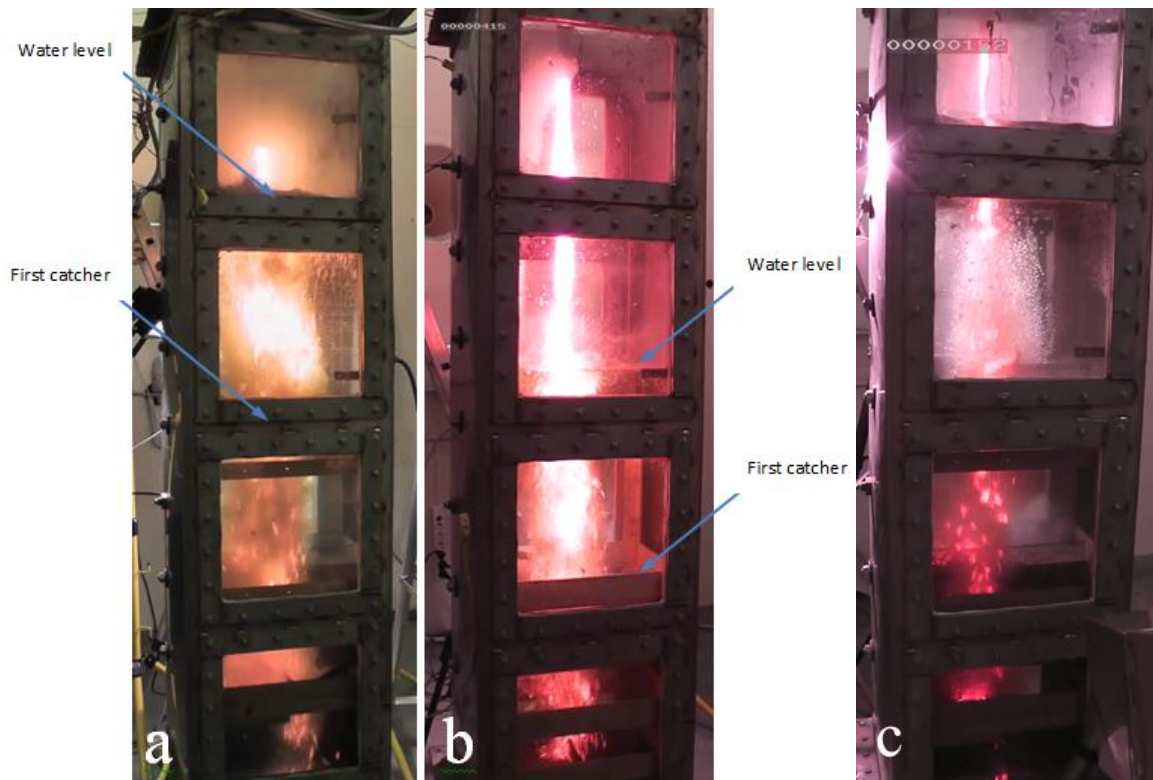


Figure 15: Melt pouring in A10 (a), A11 (b) and A15 (c) tests

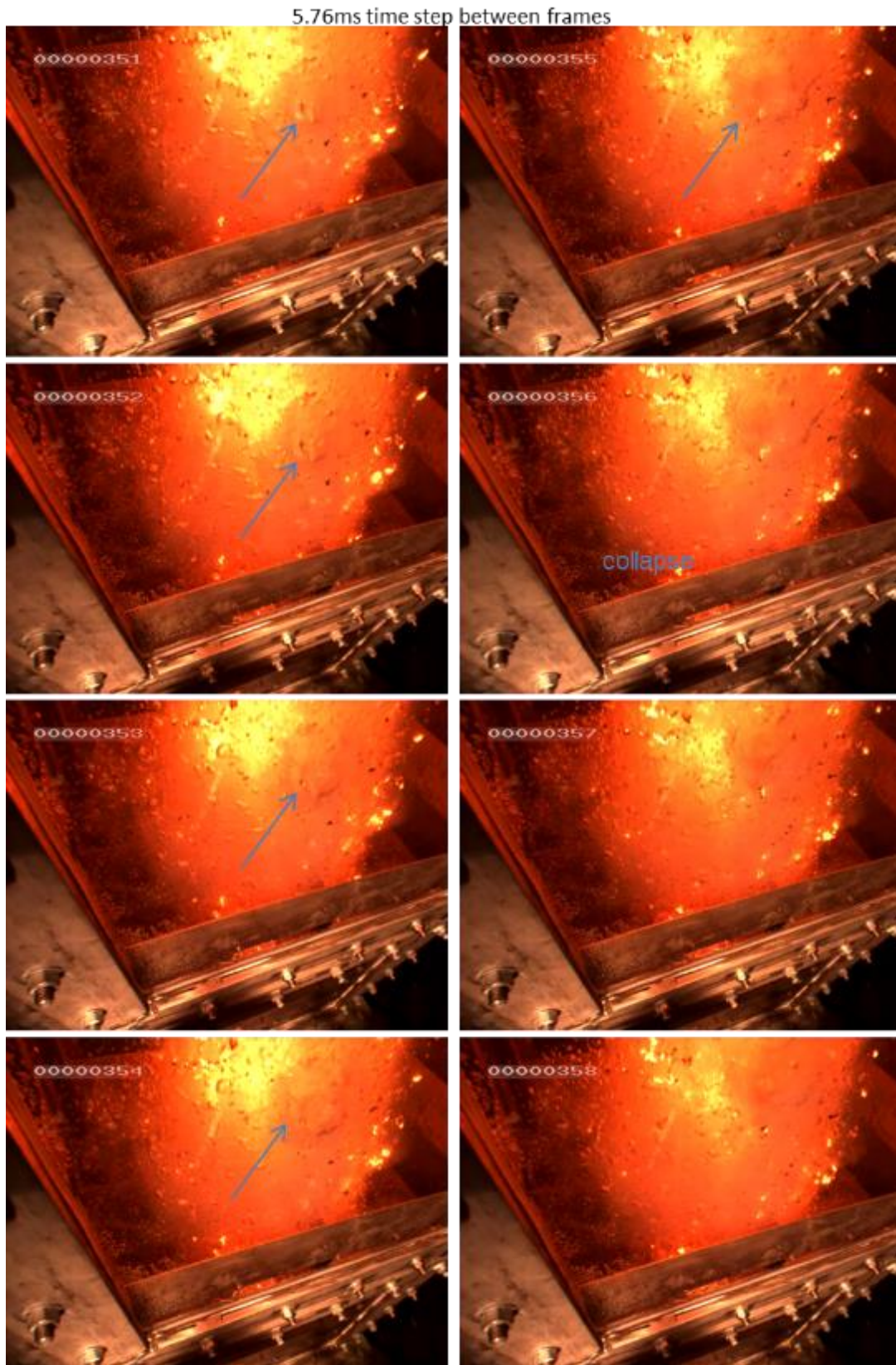


Figure 16: Three phase melt-water-steam dynamics recorded in A11 test at the top catcher by fast camera (170 fps).

Note that due to different melt masses delivered into the test section, the melt to water mass ratio has been preserved almost the same in both tests: 0.044 in A10 and 0.049 in A11. This allowed for similar temperature evolution of the bulk water during melt release providing similar values of water temperature after the test 91 and 89 °C respectively.

Comparison of melt delivery into water for A10, A11 and A12 is provided in the Figure 15. In both snapshots a straight and coherent jet can be seen above the water level as well as its fast break up and fragmentation upon entrance into water.

The melt front velocity at the initial water level (estimated assuming free fall acceleration from the nozzle outlet) is at least 2.0 and 3.7 m/sec for A10 and A11 tests respectively. The corresponding jet diameter (by mass conservation) is ~2 and ~1.5 cm. Thus, expected jet breakup level is above the level of the top catcher in both tests.

During the pouring process, considerable vibrations of the DEFOR test section walls have been observed. The periodic “bulging” of the test section walls is attributed to the effect of dynamic growth and collapse of the vapor bubbles, phenomena common for boiling or steam injection into subcooled water.

Improved visualization due to application of the new melt simulant allows verification of this hypothesis. The dynamics of bubble growth and collapse is shown in the Figure 16. Growth of a bubble starts around a hot fragment or next to the melt puddle where local water temperature is close to the saturation point. Once the buoyancy exceeds surface tension forces that keep the bubble attached to the heat source, the bubble starts to move upward. Small bubbles merge together into large bubbles. Since the heat source is no more supplying energy to the bubble, the steam rapidly cools down. Due to subcooled state of surrounding water the condensation process rapidly develops leaving virtually an empty bubble at absolute pressure close to zero. Driven by the surrounding pressure the bubble collapses. Converging flow of water develops a pressure pike behind the moving interface.

By video recordings we could estimate that characteristic time of steam bubble collapse is quite short while the size is quite large (~10 ms and ~10 cm respectively). During the rapid bubble collapse, water is accelerated inwards at the velocity of about 10 m/s and collides closing the void left from the condensed steam.

It is instructive to note that dynamics of individual bubbles growth/collapse events in rather confined geometry of the DEFOR test section are affected by neighboring bubble growth/collapse events and thus become correlated.

### **DEFOR tests with conical sample**

Application of the lead (Pb) sample has significantly affected the duration of the melt release. Out of initial 20.6 kg of the load, in A12 test 15.32 kg of melt has been delivered into the water (including 2.35 kg solidified inside the sample) within 34 sec – duration almost 3 times longer than in previous A10 and A11 tests (12-13 sec). In contrast, in the A13 test melt delivery has been interrupted 6.3 seconds later after the start of the release. Mass of solidified inside the sample melt is 5.7 kg and only a small portion of 1.04 kg has been collected from the catchers. About 12.1 kg of melt was found in the melt delivery funnel. The difference between melt delivery in A12 and A13 is surely due to the low melt superheat in the A13 test (64 °C) resulting in early plugging of the sample. It is interesting to note that despite lower melt superheat in A13 test melting through of the test sample wall occurred providing additional opening for the melt release.

At the very beginning of the melt release the jet released from the test sample is slightly inclined due to horizontal momentum obtained by the flow inside the sample (see for example Figure 17a and Figure 18a for A12 and A13 tests respectively). Later the release stabilizes, forming vertical coherent jet, slightly pulsating in case of the A13 test due to smaller jet diameter.

In A12 test the melt-water interactions are more intense compared to the A10 test. Periodic bulging (notice red arrow in the Figure 17a and Figure 17b) and even shaking of the DEFOR test section has been observed. Such behavior can be attributed to the effect of the test sample which partially confines the water pool in the test section. Nucleate boiling regime has been established below the melt impingement point at 1.38 sec after the melt release from the sample, no film boiling could be seen on the video footages. After the 34 sec of the release the test sample has been plugged.

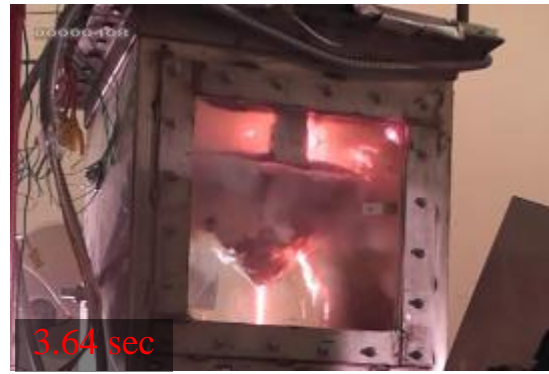


Figure 17: Melt release in A12 test (time stamp in the images is relative to the start of melt release from the test sample)

In the A13 tests the melt-water interaction has been more moderate (Figure 18a and Figure 18f) in terms of bulging and shaking of the test section, which is attributed to the decreased instantaneous amount of melt in the premixture. After around 1.02 sec (from the start of the melt release from the sample) film boiling is established below the melt impingement point. Just 0.44 sec later a melt splash is observed inside the sample (Figure 18b) followed by (at 1.46 sec) melt through of the sample wall (Figure 18c). The melt jet released through the ablated hole in lateral direction is disturbed by rising convective flows and by the evolution of the melting-through geometry (Figure 18d and Figure 18f). Melt release continued only for 6.26 sec. At first the lateral jet has been plugged (at 5.58 sec) and shortly after that, the melt release from the sample nozzle was stopped.



a)



e)



b)



c)



d)



f)

Figure 18: Melt release in A13 test (time stamp in the images is relative to the start of melt release from the test sample) (frame 308).

## DEFOR tests with sample plate

In the DEFOR-A17-A18 tests with a sample plate there are two nozzles. Therefore, the melt pouring is established through both of them at the beginning of the melt release. The sample plates in A19-A21 tests have only one nozzle. In the following set of figures (Figure 19 through Figure 24) the snapshots of the underwater melt pouring are presented.

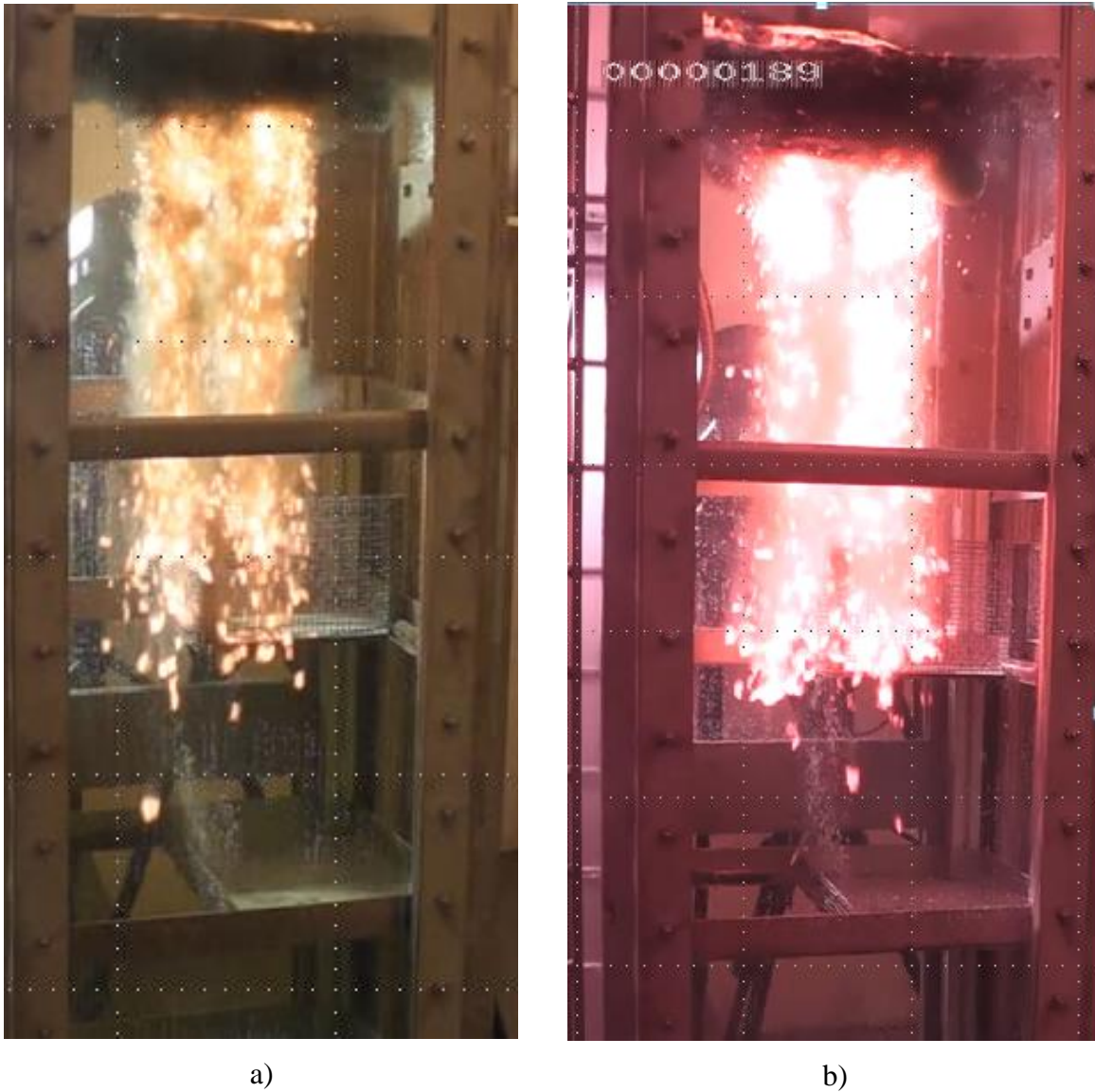
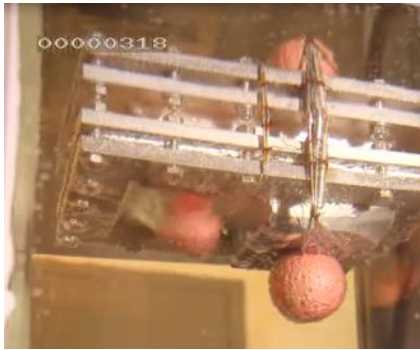


Figure 19: Snapshots of the melt release recorded by the main view camera (25 fps) in at 1.6 s after the release of the melt through nozzle outlets: a) A17 b) A18.



a) start of melt release



d) start of melt release



b) ~1s



e) ~1s



c) ~1.5s



f) ~2s

Figure 20: Snapshots of the melt release recorded by the close-up view camera (50 fps) in A17 (a-c) and A18 (d-f) tests.

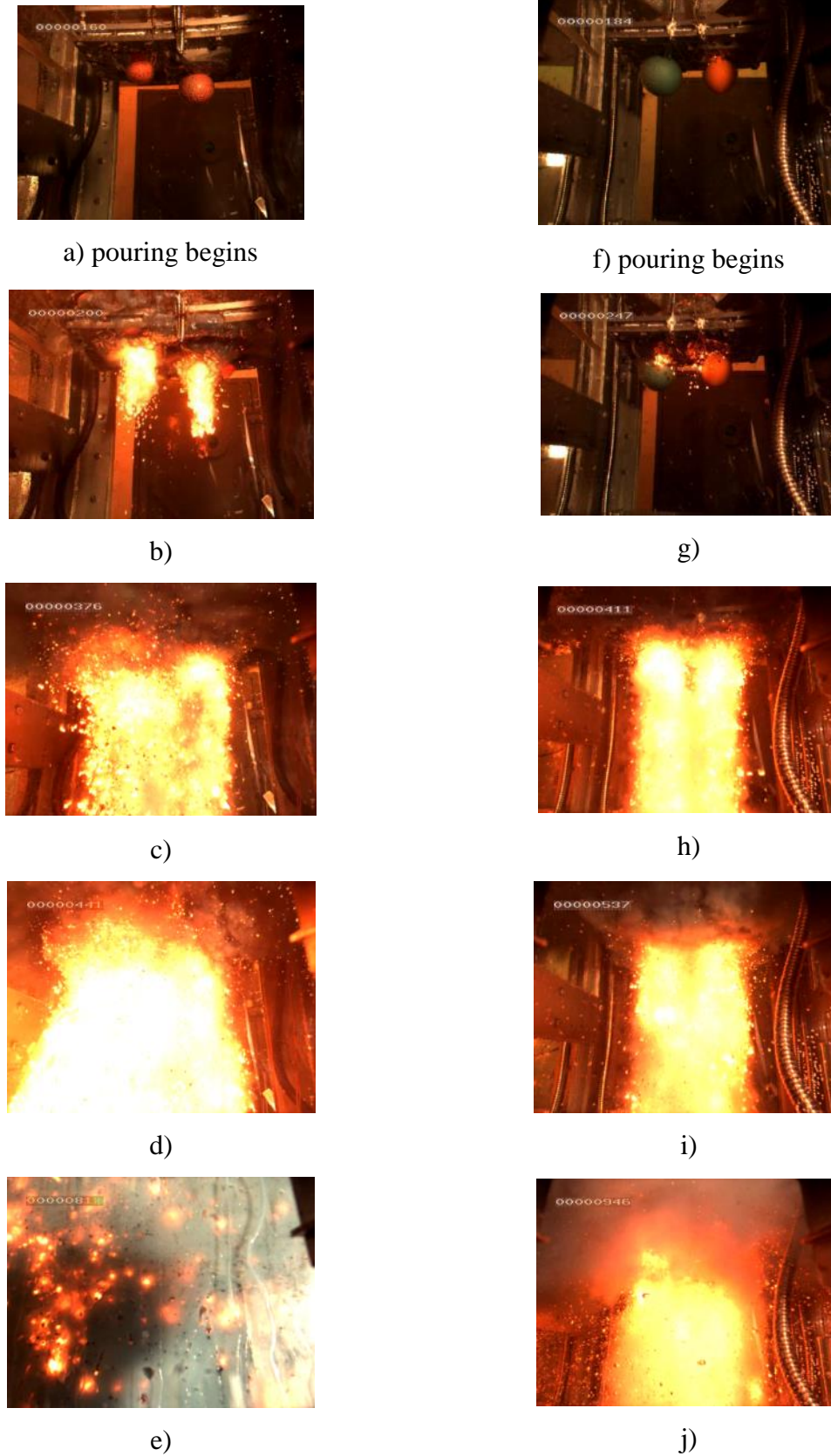


Figure 21: Snapshots of the melt release recorded by the high-speed camera (160 fps) in A17 (a-e) and A18 (f-j) tests.



90.76s

91.00s

91.48s

91.64s



91.96s

92.44s

92.96s

94.32s

Figure 22: DEFOR-A19: snapshots of the melt release recorded by the main view camera (25 fps)

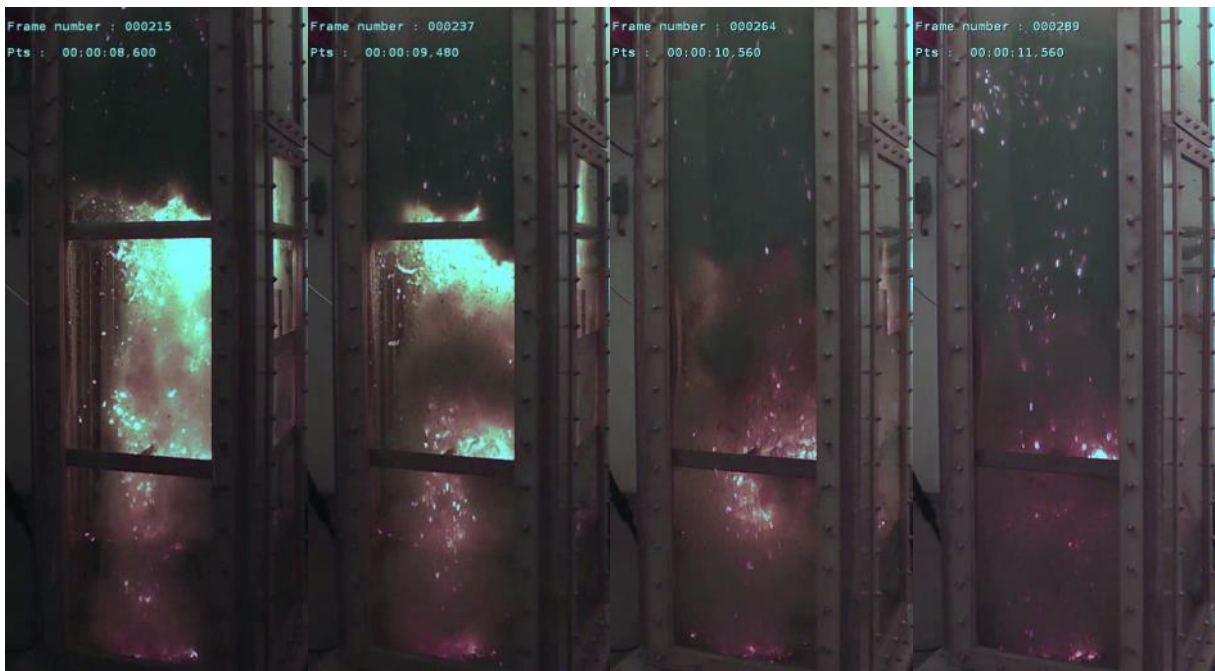


4.52s

5.52s

6.48s

7.56s



8.6s

9.48s

10.56s

11.56s

Figure 23: DEFOR-A20: snapshots of the melt release recorded by the main view camera (25 fps)

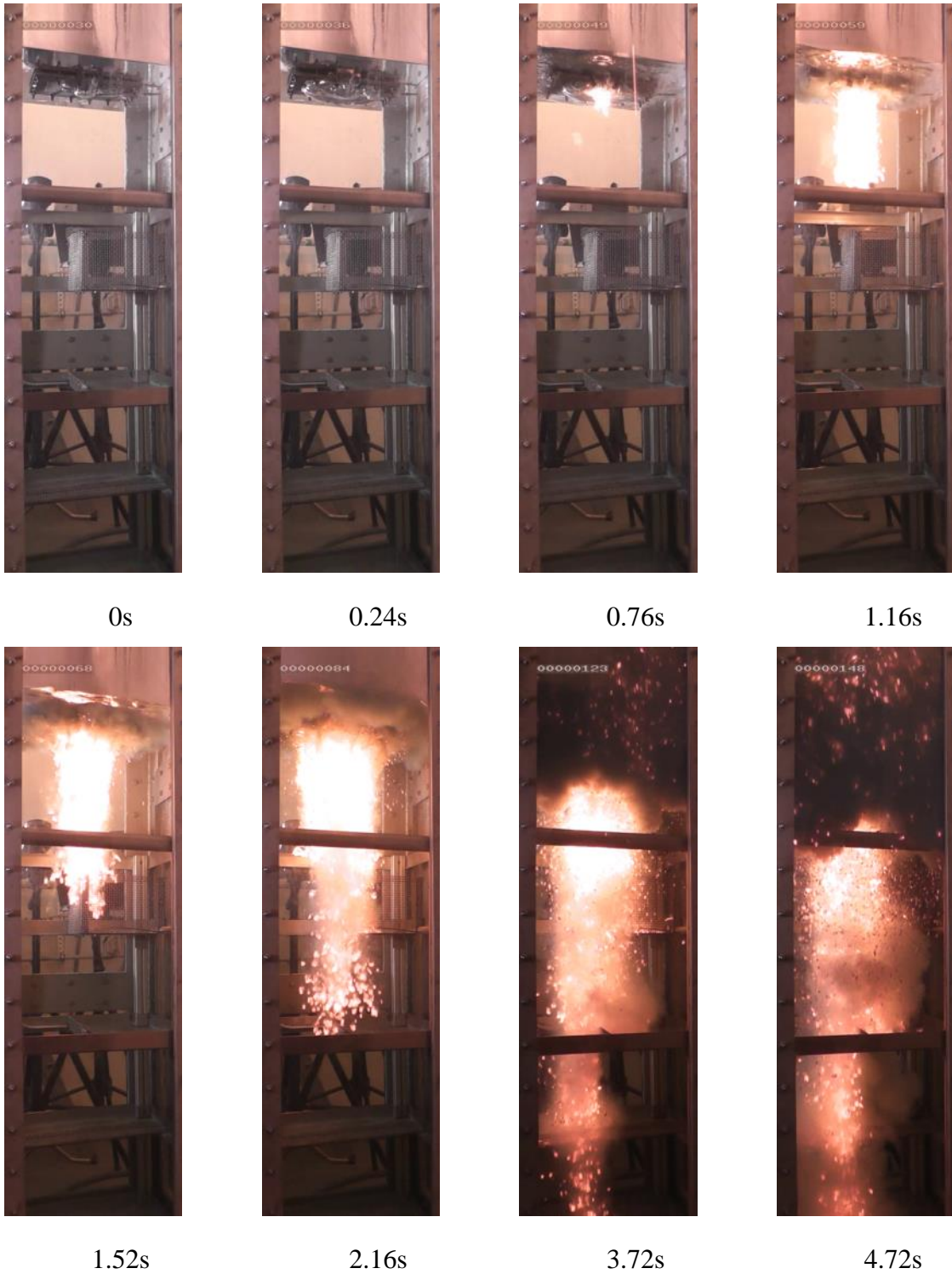


Figure 24: DEFOR-A21: snapshots of the melt release recorded by the main view camera (25 fps)

### 2.3.3 Posttest debris analysis

In this subsection the results from the analysis of the debris from DEFOR-A10:21 test series are discussed. At first, a detailed comparison of the DEFOR-A10;A11 tests versus FARO experiments is provided. Then, the results from all DEFOR-A10-A21 tests are presented and discussed in terms of debris bed fraction of agglomeration and particle size distribution in the following subsections.

#### Comparison of the DEFOR-A10,A11 tests with FARO tests and previous DEFOR test series

In Figure 25 we compare mass fraction of agglomerated debris as a function of the pool depth in the A10 and A11 tests to those obtained in the previous DEFOR-A and DEFOR-S experiments performed with another melt simulant material ( $\text{Bi}_2\text{O}_3\text{-WO}_3$ ). In terms of the melt superheat and jet diameter the A10 and A11 tests can be compared to DEFOR-A7, A2, and A6.

For the sake of clarity in Table 3 we provide relevant tests conditions. Note that exact value of water subcooling is of minor importance until thermal stresses start to induce solid particle fracture. For simplicity we can consider tests to be similar if subcooling is below 30 °C.

In the Figure 25 one can see that agglomeration curve of DEFOR-A10 test lies in between the curves of A7 and A2 tests being slightly closer to A2. This behavior agrees well with both melt superheat (A10 - 150 °C, A7 - 200 °C and A2 - 110 °C) and jet diameter (A10 – 20 mm, A7 – 25 mm and A2 – 20 mm).

Table 3: Relevant experimental parameters for DEFOR-A tests comparison to selected DEFOR-A tests

DEFOR test	Jet diameter, mm	Melt superheat, °C	Melt temperature, °C	Water subcooling, °C	Water pool depth, cm	Simulant
A10	20	150	1371	25	152	ZrO <sub>2</sub> -WO <sub>3</sub>
A11	15	102	1333	25	110	ZrO <sub>2</sub> -WO <sub>3</sub>
A7	25	206	1076	17	142	Bi <sub>2</sub> O <sub>3</sub> -WO <sub>3</sub>
A2	20	103	973	7	152	Bi <sub>2</sub> O <sub>3</sub> -WO <sub>3</sub>
A6	12	136	1006	27	152	Bi <sub>2</sub> O <sub>3</sub> -WO <sub>3</sub>

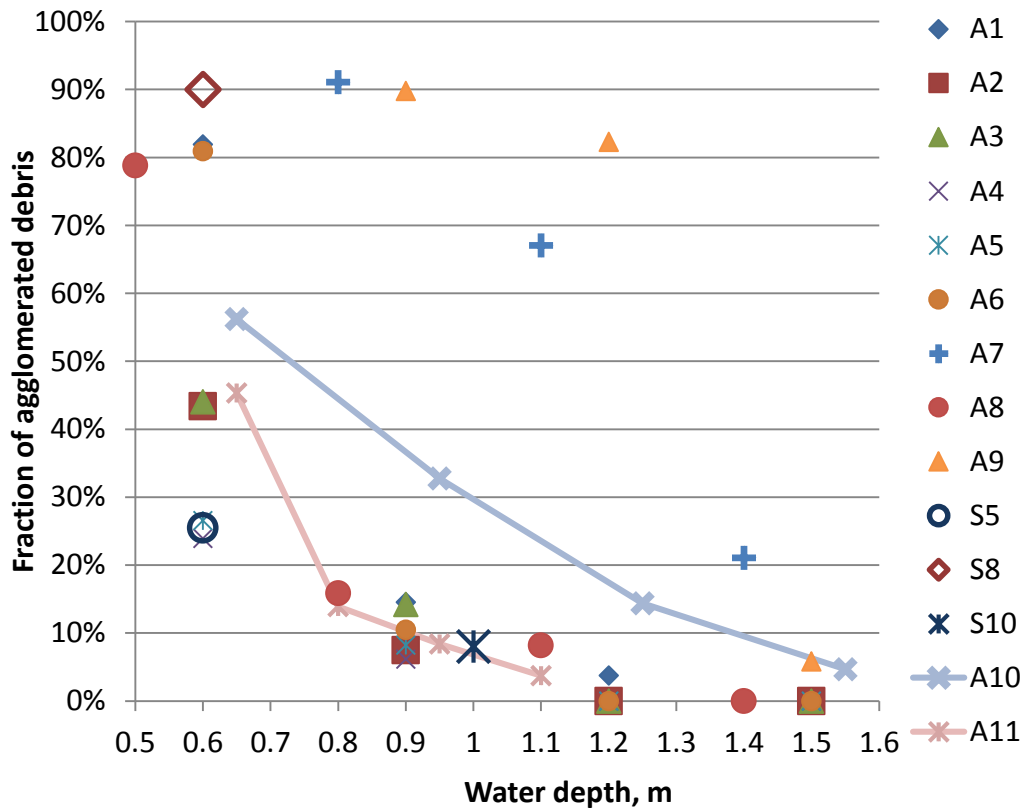


Figure 25: Comparison of the agglomerated debris fraction obtained in DEFOR-A10,A11 to previously performed DEFOR-A and DEFOR-S experiments

Direct comparison of A2,6,7 with A11 test is less straightforward due to higher velocity of the jet at the entrance into the water in A11 test. Therefore, we have chosen the jet diameter at the water level as the main similarity parameter. In terms of water subcooling and jet diameter at the water level, the closest to the A11 test is DEFOR-A6. It has slightly higher agglomeration on the top catcher which can be attributed to the higher melt superheat and experimental uncertainty due to proximity of the first catcher to the inherently instable position of the jet leading edge in this test. With respect to other catchers DEFOR-A6 is in a good agreement with the A11 test.

From the above considerations we can conclude that behavior of the new simulant material in terms of agglomeration reasonably agrees with results from the previous DEFOR-A tests series.

In the following analysis we will compare the particle size distributions. The representative particle size distribution that describes accomplished melt fragmentation should be taken from the catcher with the smallest fraction of the agglomerates, in other words the one obtained from

the debris bed collected at the bottom of the DEFOR test section. In Figure 26 one can see that particle size distribution measured in new tests shows significantly higher fraction of larger particles compared to any of the previous DEFOR-A tests. Such important difference cannot be attributed to the differences in experimental conditions and can be explained only by application of different simulant melts.

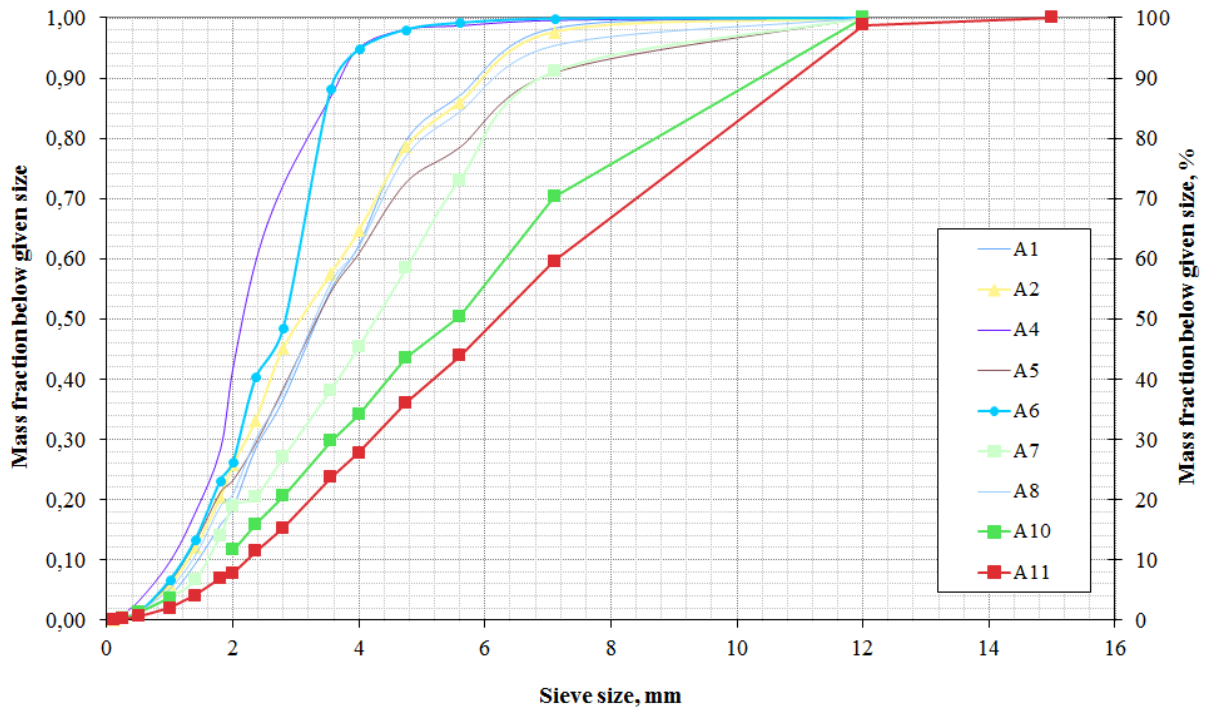


Figure 26: Comparison of the particle size distributions from DEFOR-A tests to DEFOR-A tests (only data from the bottom catcher is plotted)

In the Figure 27 we provide comparison of the ranges of particle size distributions from the A10-11 tests against FARO L28, L31 experiments performed with prototypical corium melts. One can see a very good agreement between new DEFOR-A and FARO data. Some difference still remain but it can be attributed to such features of FARO tests as different initial jet diameter (50 – 100 mm) and agglomeration of the debris that alter the resulting particle size distribution (with the exception of FARO L31).

Note that debris bed in FARO L31 has been divided into 3 parts and sieved separately; the top and bottom parts distribution appeared to cover the full range of all FARO debris size distributions coming from non-explosive tests; in the figure the L31(top) and L31(bot) are used to span the range of FARO debris size distributions.

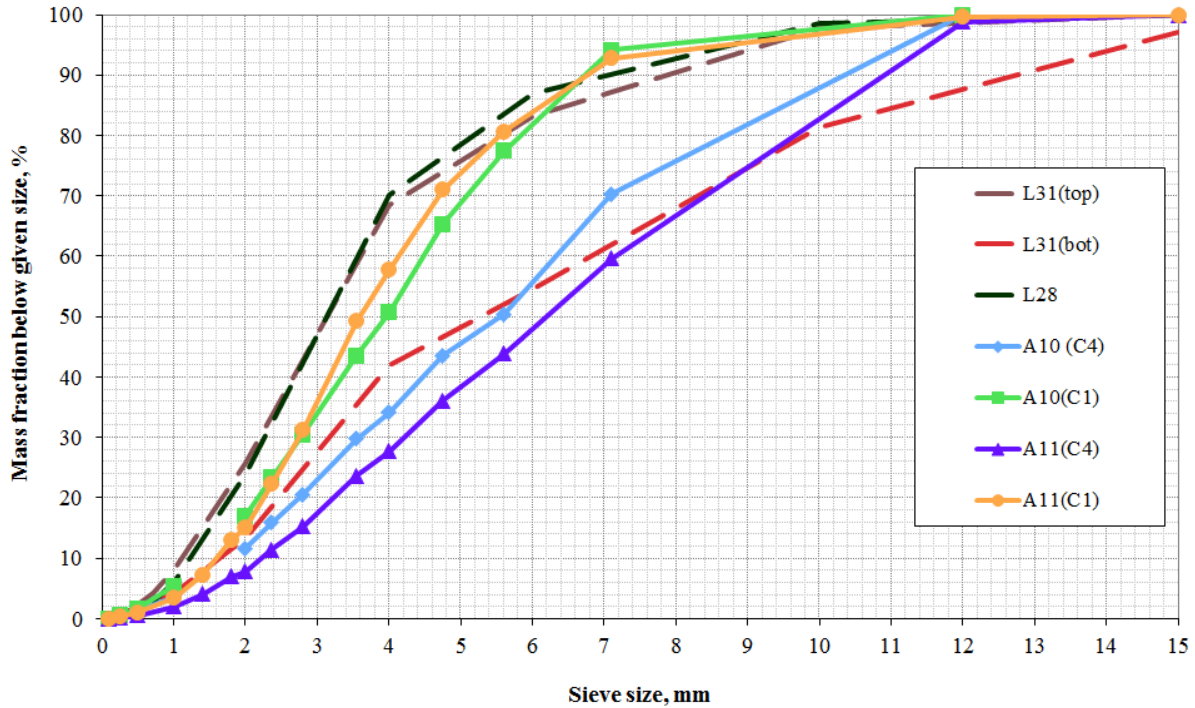


Figure 27: Comparison of the particle size distributions of DEFOR-A tests to FARO experiments

For the sake of clarity we provide the comparison of previous DEFOR-A to FARO tests in Figure 28. Previous DEFOR-A test series is also in a good overall agreement with FARO results. However, the DEFOR-A particle size distribution is closer to L28 data with smaller fraction of large particles, which could be reasonable given smaller jet diameters used in DEFOR-A tests.

Overall, from the comparison between DEFOR-A01-09, DEFOR-A10-13 and FARO data we can conclude that the influence of jet diameter and free fall height on the particle size distribution is less important than the influence of melt material. Indeed the difference between FARO vs DEFOR-A10-13 and FARO vs DEFOR-A01-09 is smaller than the difference between DEFOR-A01-09 vs DEFOR-A10-13, although melt pouring conditions in DEFOR-A are much closer to each other (10-25 mm jet diameter and 20-70 cm jet free fall height) and quite different from FARO conditions (50-100 mm jet diameter and ~1-2 m jet free fall height).

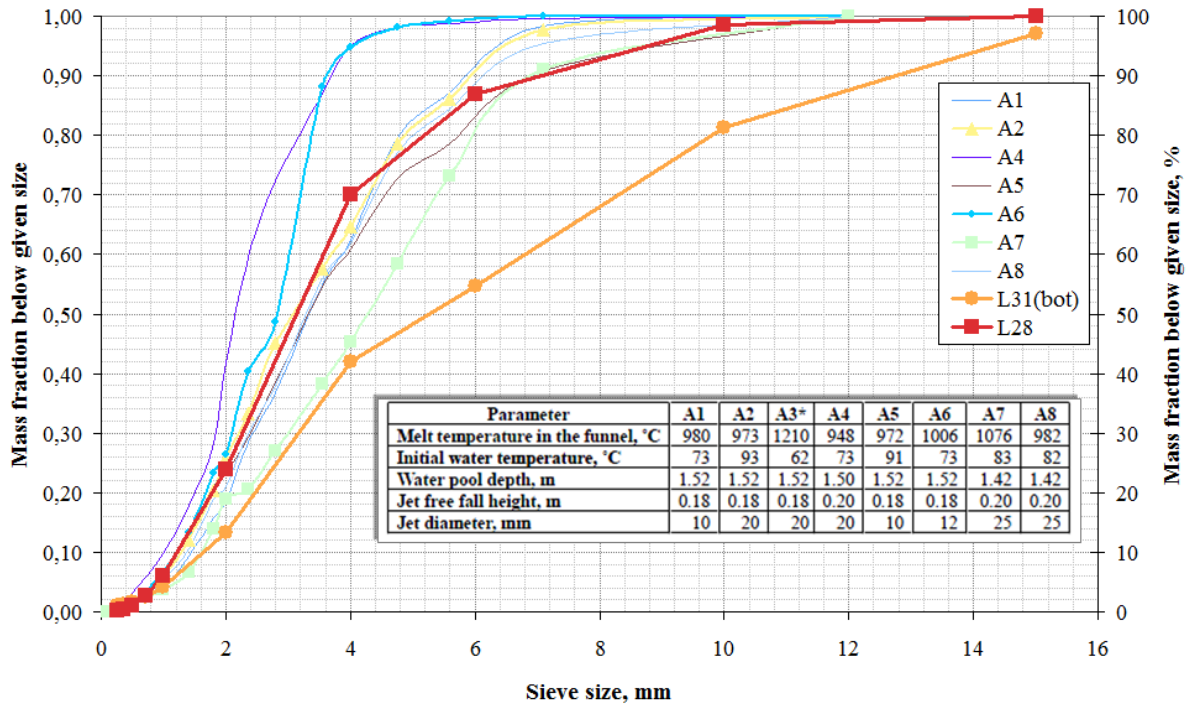


Figure 28: Comparison of the particle size distributions of DEFOR-A tests to FARO experiments

### Debris bed formation and agglomeration

Top view on the debris collected in the catchers in successful DEFOR-A tests is shown in Figure 29. In most of the cases the spatial distribution of the debris is symmetrical with respect to center. In some tests melt has been delivered off the center and, therefore, distribution is non-symmetrical.

Example of the closer view on the agglomerated debris is shown in Figure 30 for DEFOR-A15 test. It is instructive to note that even if there is a massive cake which takes up to 80-90% of the total melt mass in the catcher, there is always some amount of fragmented debris. There are two typical configurations with respect to the positions of the cake and fragmented debris:

- One is when a layer of fragmented debris is located under the cake.
- Another typical configuration is when cake is located at the bottom, directly touching the catcher plate and there is a layer of fragmented debris atop. Similar configuration was also observed in FARO test (Magallon, 2006).

For example, in a single test such as DEFOR-A15 large cake has been found in the first catcher with 82% agglomeration (Figure 30), smaller cake with smaller agglomeration (52%) fraction in the seconds catcher (Figure 31a), small agglomeration (10%) in third catcher (Figure 31b) and finally 0% agglomeration in the bottom catcher (Figure 32).

The dependencies of the mass fraction of agglomerated debris on the pool depth are presented in Figure 33a and Figure 33b corresponding for DEFOR-A1:9 and DEFOR-A10:21 tests respectively. It is instructive to note that obtained dependencies are quite consistent with each other and despite the fact that there are some stochastic variations of the mass fraction of debris collected in each catcher in different tests.

Data from the DEFOR-S5, S8 and S10 tests (Kudinov et al., 2010) also presented in Figure 33a for comparison. Analysis of presented data suggests that fraction of agglomerated debris decreases rapidly with the depth of the coolant. Data on fraction of agglomerated debris from the DEFOR-A tests also agrees well with the previously obtained results in the DEFOR-S experiments where smaller amount of melt (about 1.0 liter) was used (Kudinov et al., 2010).

The data from DEFOR-S (Kudinov et al., 2010) and DEFOR-A tests suggest that influence of water subcooling on the fraction of agglomerated debris can be non-monotone. Specifically, at high subcooling of water (50°C and higher) melt droplets are quenched rapidly, which effectively prevents formation of debris agglomerates even in a relatively shallow (~0.6 m) pool (Kudinov et al., 2010). Particle cooling efficiency decreases along with decreasing subcooling of water, thus higher fraction of agglomerated debris is expected at higher water temperature. On the other hand, at very low subcooling a moderate increase of subcooling (e.g. from 9°C in A5 to 27°C in A1) can lead to increase of the fraction of agglomerated debris. Two experiments performed at similar conditions (A1, A6) with relatively small jet diameter (10 mm and 12 mm respectively), subcooling of water ~27 K, and melt superheat around 110°C and 136°C respectively resulted in quite high mass fraction of agglomerated debris in the first catcher (~80%).

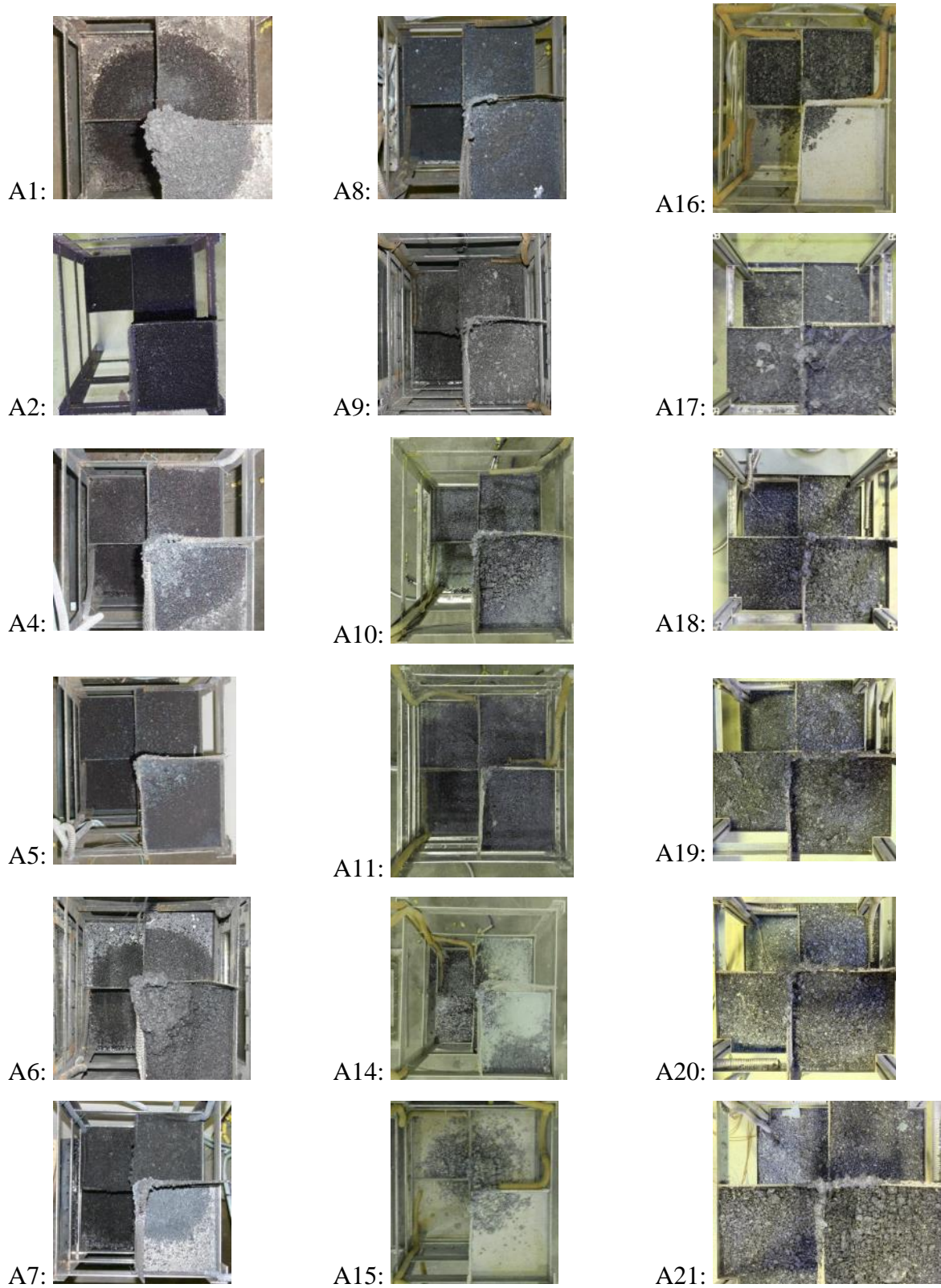


Figure 29: Spatial distribution of debris: top view of the catchers.



Figure 30: Debris from DEFOR-A15 test found in catcher 1.

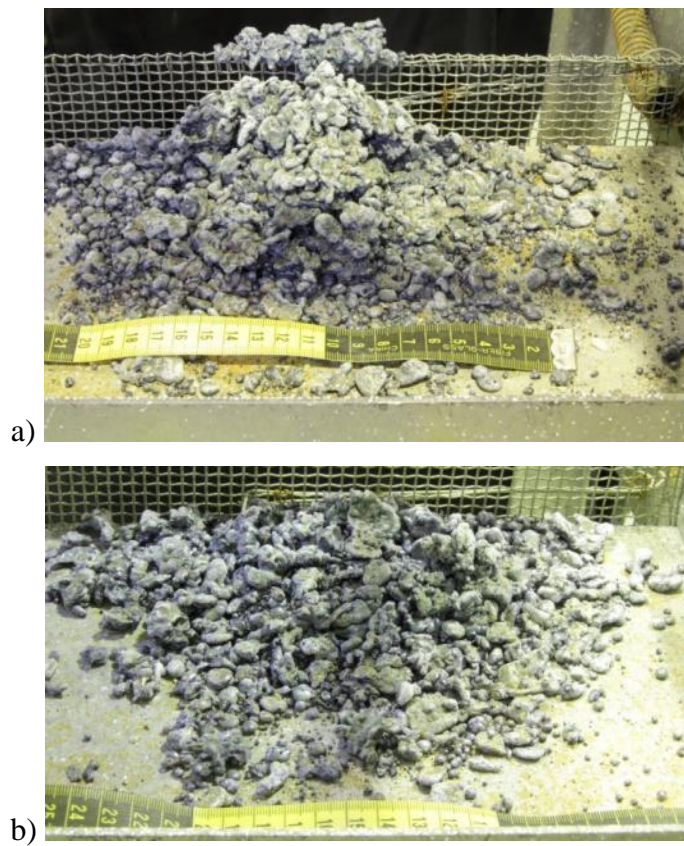
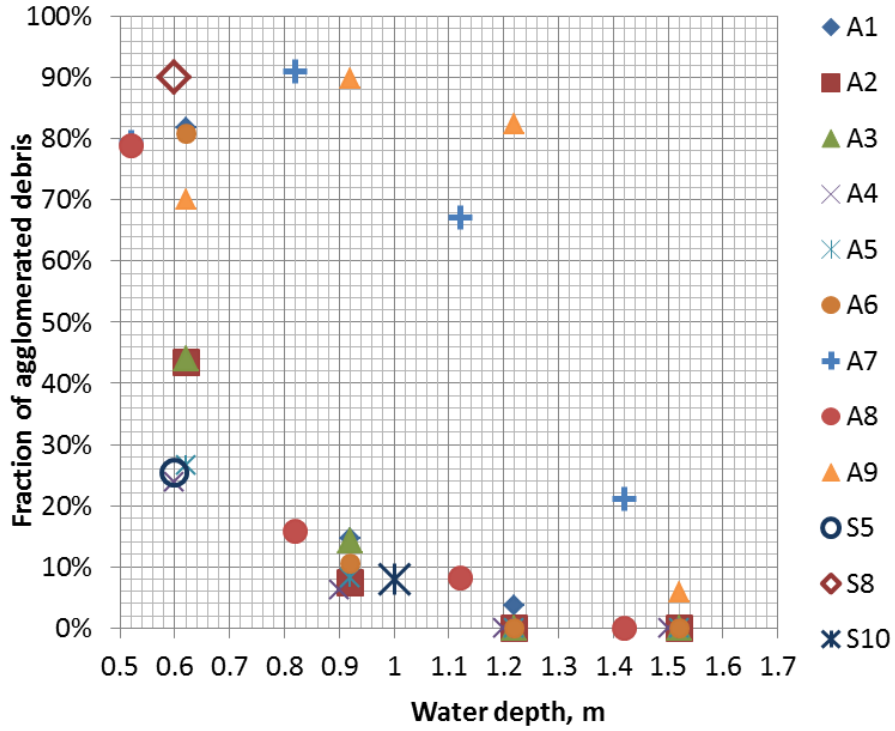


Figure 31: Debris from DEFOR-A15 test found in catcher 2 (a) and catcher 3 (b).

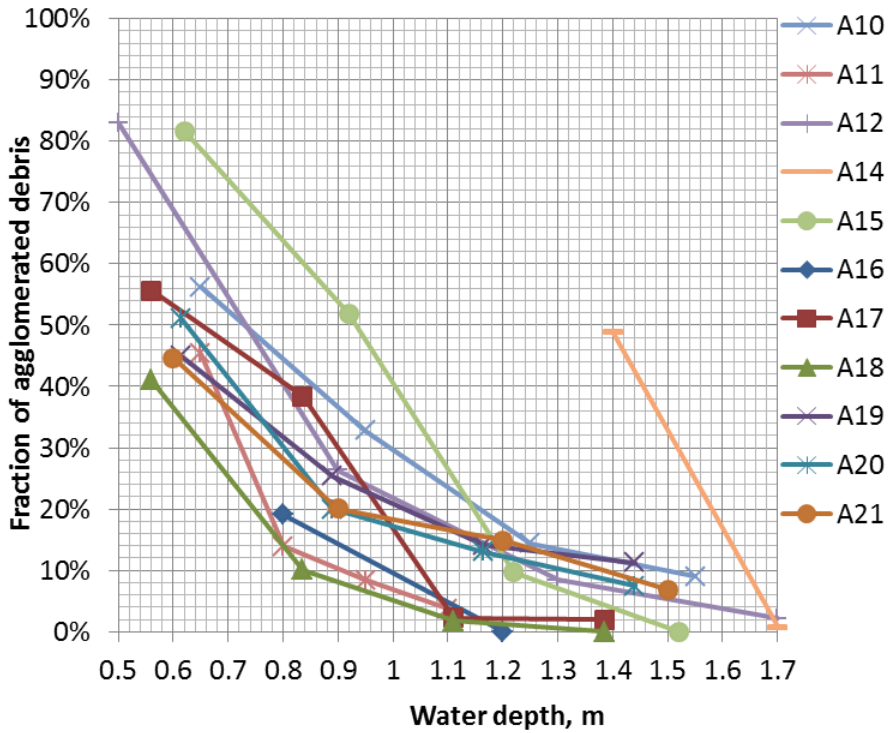


Figure 32: Debris from DEFOR-A15 test found in catcher 4.

In addition to agglomeration mass fraction the total (sum of open and closed porosity) debris bed porosity have been measured in the latest DEFOR-A10:21 tests. The measurements have been performed by 2D laser scanning technique. Despite high accuracy of such measurements the final experimental error greatly depends on the total amount of debris per catcher. The analysis of the data revealed no dependence of the total porosity on water pool depth as seen from Figure 34. The typical value of the total porosity is about 40-55% which is within experimental error also shown in Figure 34.



a)



b)

Figure 33: Debris bed agglomeration fraction as function of water pool depth for A1:9, S8, S19 (a) and A10:21 (b) tests.

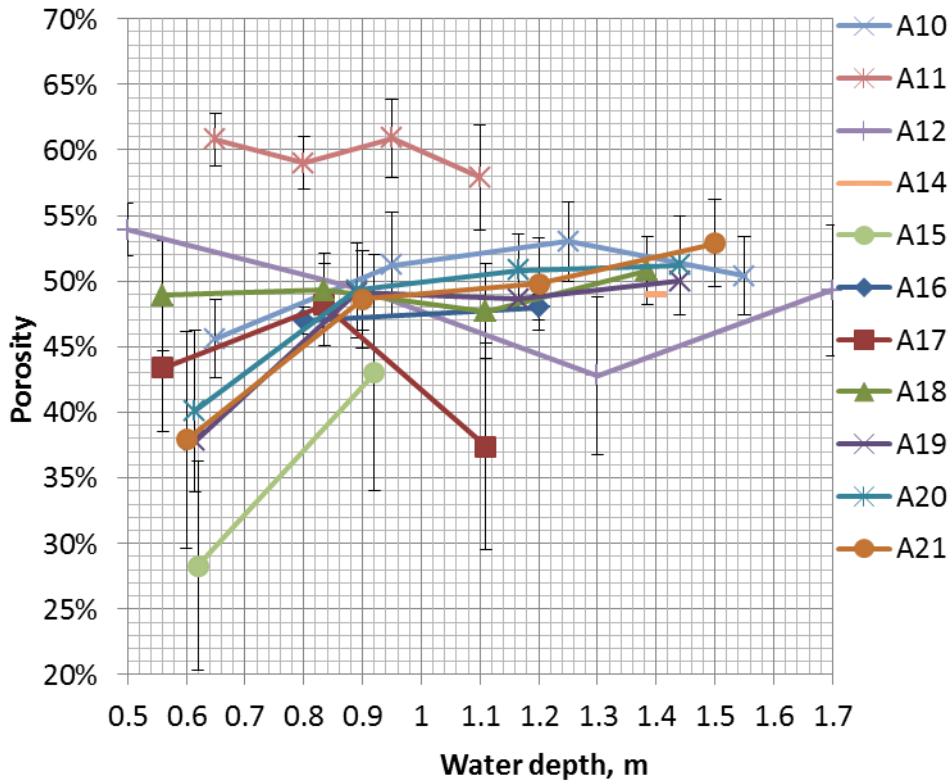


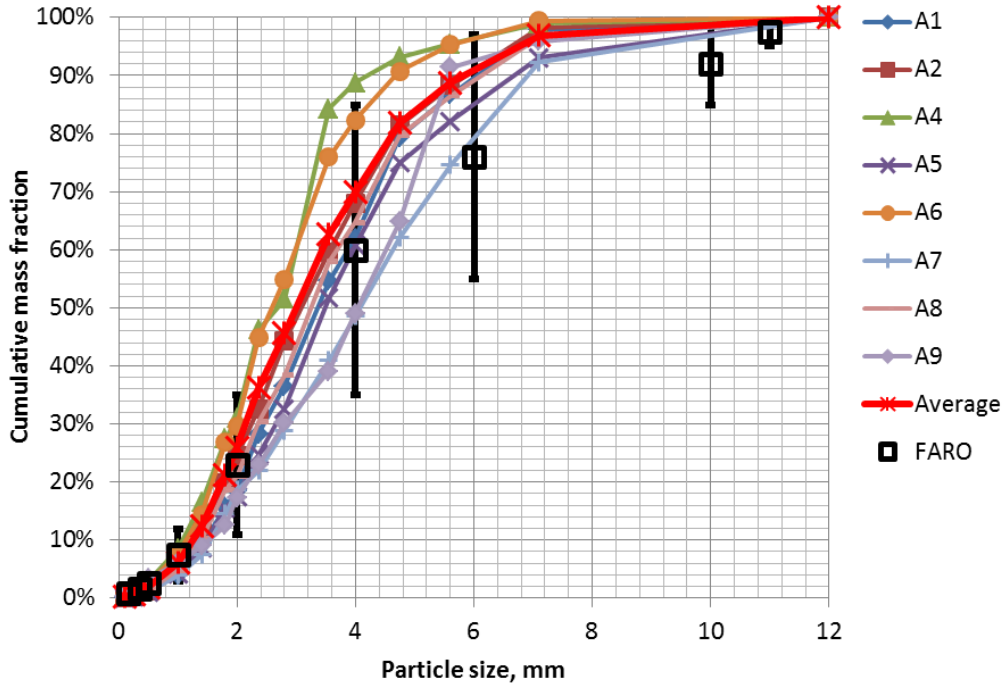
Figure 34: Measured total debris bed porosity as function of water pool depth in DEFOR-A10:21 tests.

## Particle size distribution

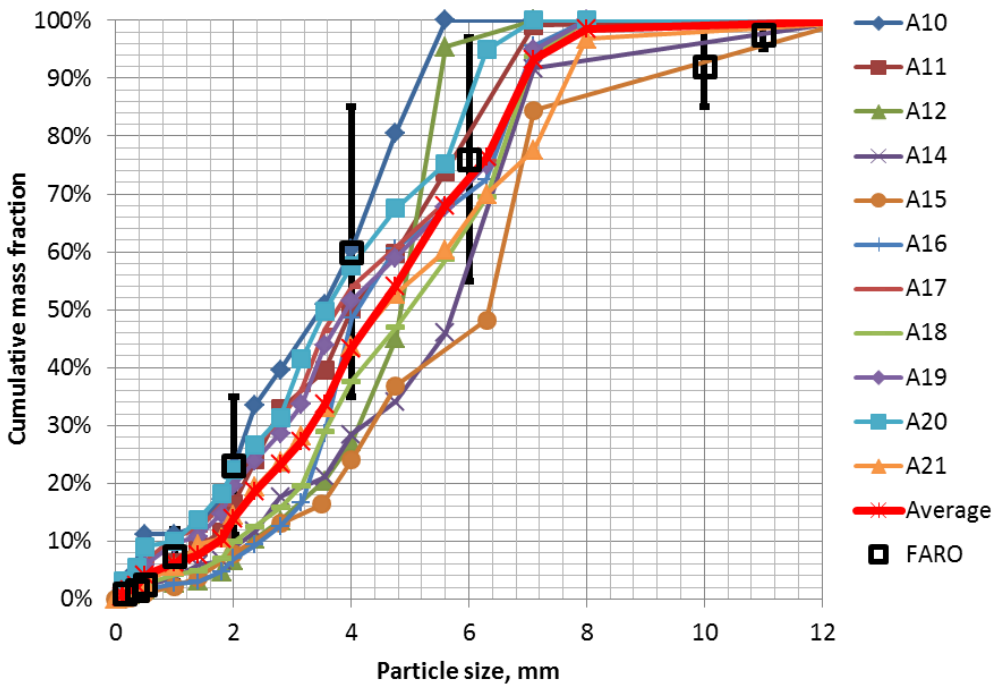
The particle size distributions were obtained by sieving the debris on a set of sieves. Particles from catchers where fraction of agglomerated debris was significant (typically in the first or upper catcher) were not used for sieving. Distributions from the tests with higher melt superheat are located slightly below the average, corresponding to on average larger particles. It is instructive to note that at least some of the variations in measured size distributions can be attributed to the fact that quenched in water ceramic particles are quite fragile and some of them might break during the sieving process. Also it would be quite natural to expect some variations due to the inherent uncertainties in such quite complex experiment with high temperature melt-coolant interactions.

The resulting size distributions are presented as cumulative mass fraction dependence on particle size shown in Figure 35. For comparison, previously obtained result from DEFOR-A1-A9 test series (Kudinov et al., 2013) is provided in Figure 35a. Despite small deviations results

from DEFOR-A10:21 tests (Figure 35b) are very similar to previously obtained data and even lie within uncertainty of the FARO measurements.



a)



b)

Figure 35: Cumulative mass fraction for the debris in DEFOR-A1:9 (a) and DEOFR-A10:21 (b) tests. For comparison, the data from FARO tests and averaged DEFOR curves for corresponding series of tests are provided.

## 2.3.4 Posttest analysis of the samples

### Tests with conically shaped samples

Results of post-test analysis of the test sample (conical shell geometry) and debris solidified inside it are summarized in Table 4. This analysis is based on visual inspection of the sample and solidified melt in the sample. After every test the test sample is removed from the test section, dried, photographed and then cut into two pieces. The section is obtained along the vertical axis of the sample in a way preserving intact the ingot inside it. The cutting is done along the melt impingement point. The following objectives are perused:

- Assessment of the sample nozzle ablation;
- Assessment of the sample wall ablation;
- Analysis of the ingot, in terms of its mass and morphology.

Table 4: Test sample and debris properties in DEFOR-A12-A14 and A16 tests

Parameter	A12	A13	A14	A16
Nozzle diameter, mm	20	10	15	15
Wall thickness, mm	10	5	15	10
Melt superheat	114	62	196	117
Delivered melt, kg	15.32	6.74	21.16	18.95
Debris mass, kg	2.35	5.446	<1	10
Debris characteristics	hollow ingot with large multiple cavities	Cake-like ingot, with shrinkage cavities	Thick crust surrounding ablated region and sample nozzle	Ingot with a crust on top separated by a gap.
Nozzle ablation	no	no	no	no
Nozzle plugging	yes	yes	yes	yes
Wall ablation under jet impingement point	Up to 1.5 mm	~1x4 cm melt through, severe erosion of the internal surface	~4x6 cm melt through, severe erosion of the internal surface	Protected by SS plate
Area of the ablated hole, cm <sup>2</sup>	-	~4	~20	-

In both experiments (A12 and A13) considerable amount of melt has been solidified inside the test sample. However in A13 the amount of the remaining melt was more than twice bigger than in A12. The posttest photographs of the test sample before cutting are shown in Figure 36. In A12 test melt pool has been established inside the sample, resulting in a smooth flat crust formation on the top upon solidification. A shrinking cavity crack can be seen at the top of it.

Comparison of its mass to overall volume indicates that obtained ingot is a hollow shell. In contrast the morphology of debris bed in A13 test is completely different. One can see a rough surface looking like an agglomerated cake with a column of solidified melt under the jet impingement location. The formation of the 10 cm stalagmite-like structure is due to low melt superheat and mushy, high viscosity melt flow at the end of the melt release.

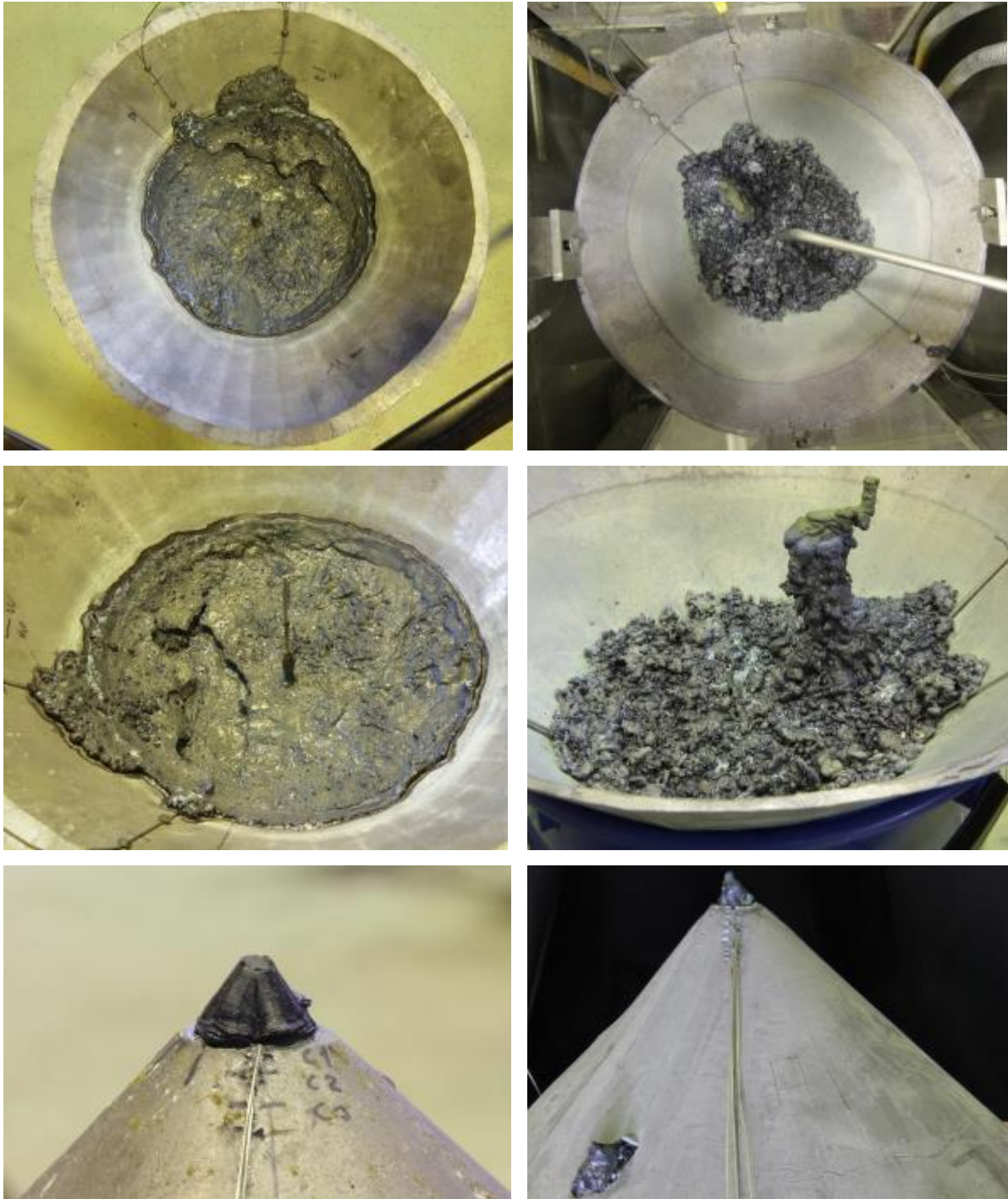


Figure 36: Debris bed solidified inside the sample in A12 (left) and A13 (right) tests

In both A12 and A13 tests the sample nozzle was plugged at the end of the melt release from the sample. In A13 test the wall of the sample was melted-through and the opening was also plugged by the melt. The location of the wall melt-through is shifted by few centimeters aside from the jet impingent point (Figure 36, Figure 37, Figure 38). In Figure 38 severe erosion in the vicinity of the melt impingement point and melt through of the wall are clearly visible.



Figure 37: Test sample of A13 test after cutting: nozzle and ablation hole

The results of the sample cutting are provided in Figure 39. Remarkably, no ablation of the sample nozzle was observed in A12 and A13 tests Figure 39. It is instructive to note the tightness of the plug in A12 test. Similar plugging occurred in A13-A14 and A16 tests, but the plug was shattered during cutting. The ingots from these four tests are shown in Figure 41. Such crystallization without shrinkage cavity is possible if continuous supply of liquid melt can compensate for shrinkage. According to the video observation, formation of the plug is a relatively fast phenomenon. In A13 test it took less than 7 seconds to completely block the flow, while solidification of the bulk melt in the sample continued for the following several minutes. It is important to clarify how much sample nozzle plugging by solidified melt depends on the geometrical characteristics of the nozzle and on the melt flow rate. This should help to clarify if continuous melt release out of the sample can be interrupted while superheated melt is still being supplied into it.



Figure 38: Test sample wall ablation in A13

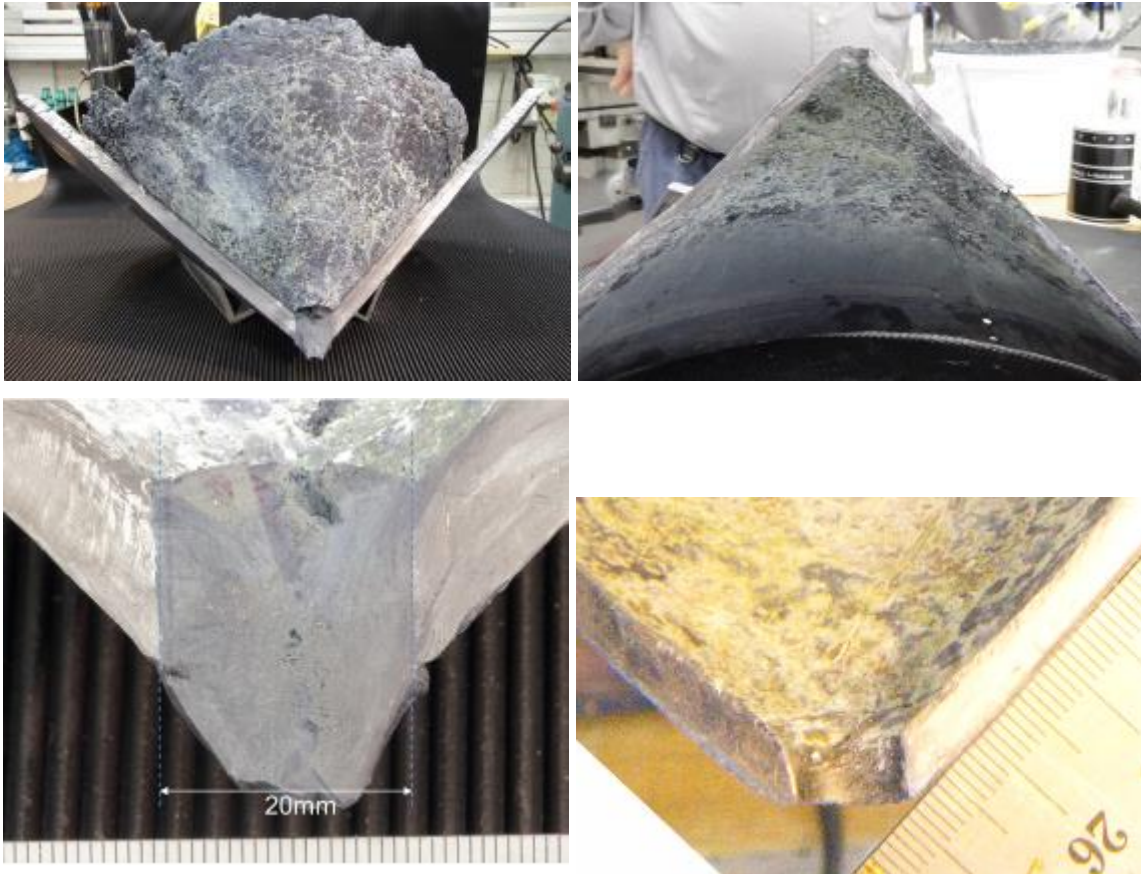


Figure 39: Test sample after cutting (left – A12, right – A13)

In general, ablation of the internal surface of the test sample in A13 test is much more pronounced than in A12 (Figure 40). These observations can be explained using below equations for the heat flux through the sample wall:

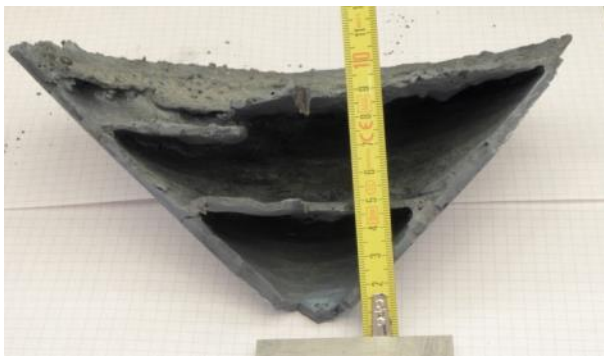
$$Q_{MG3} = k_{wall} \frac{(T_{wall\_sol} - T_{water\_sat})}{\Delta_{wall}} = 35.3 \cdot \frac{227}{0.01} = 0.8 \text{ MW/m}^2$$

$$Q_{MG4} = 35.3 \cdot \frac{227}{0.005} = 1.6 \text{ MW/m}^2$$

The heat flux through the sample wall in A12 test is twice smaller than in A13 test. Dryout heat flux on such inclined surface can be estimated about 1 MW/m<sup>2</sup>, thus the heat flux in A13 exceeded the dryout heat flux, leading to burnout of the wall with subsequent ablation of the opening.



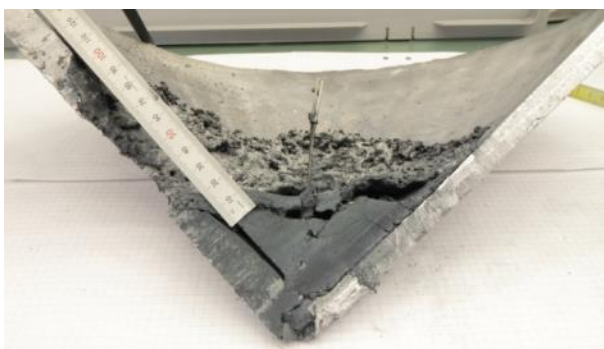
Figure 40: Test sample after cutting, comparison of surface erosion A12 at the top part of the image and A13 in the lower part



A12



A13



A14



A16

Figure 41: Ingots collected in DEFOR-A12-A14 and A16 tests.

Note, that plugging of the nozzle (Figure 41), being apparently unavoidable event even in case of the complete melt release (see DEFOR-A12 ingot), can be result of small nozzle outlet diameter, when finite crust thickness is sufficient to block the nozzle or significantly decrease its effective diameter.

## **Tests with sample plate**

### ***DEFOR-A17 and A18 tests***

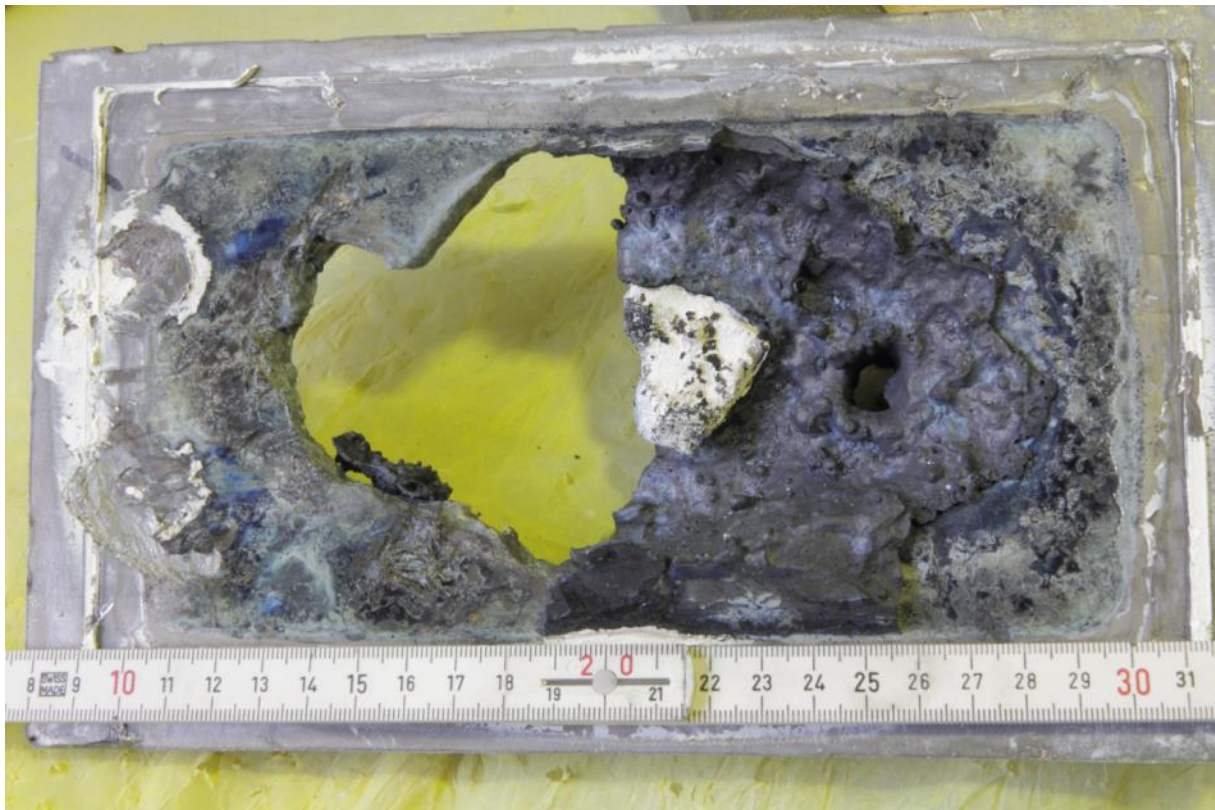
Physical phenomenon that has not been observed in previous tests and that is considered to be one of important modes of sample failure is nozzle ablation. Another issue requiring clarification are conditions of the nozzle plugging. It was assumed that nozzle length to diameter ratio is one of the key parameters affecting nozzle plugging.

With this regard the following goals for A17 and A18 tests have been identified:

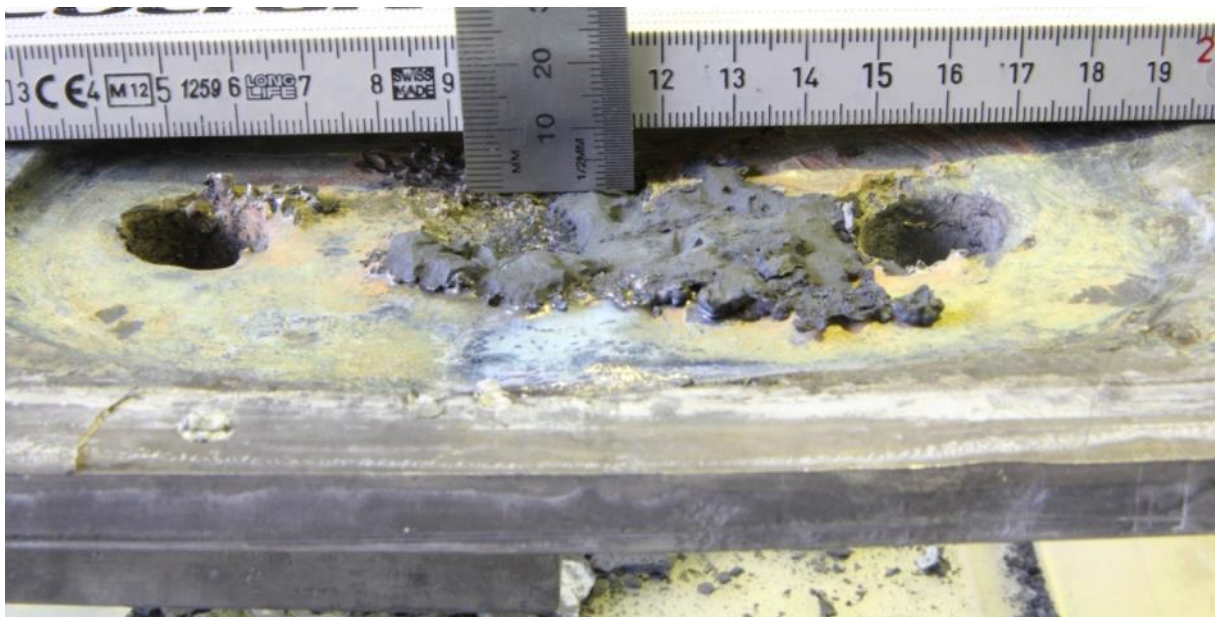
- To provide conditions at which nozzle ablation and plugging could be studied experimentally.
- To clarify importance of the nozzle diameter for plugging.
- To provide experimental data for model development and validation.

The maximum melt temperature measured in the funnel in A17 and A18 tests was 1462°C and 1420°C respectively, corresponding melt superheat was 231K and 189K. This partially clarifies the reason of sample catastrophic melt through in A17 test in which the highest melt superheat so far has been established. The photographs of the samples after the interaction are demonstrated in the Figure 42.

Severe wall ablation in A17 and nozzle plugging in A18 have been observed. The A18 plate with 20 and 30 mm thick wall ablated partially with erosion depth of about 10 mm in the plate's middle. Extrapolating the readings of embedded into the A18 sample TCs towards lead melting point (327°C) one can obtain evolution of the sample melting front in time Figure 43.



a



b

Figure 42: A17 (a) and A18 (b) samples after the interaction, view on the inner surface

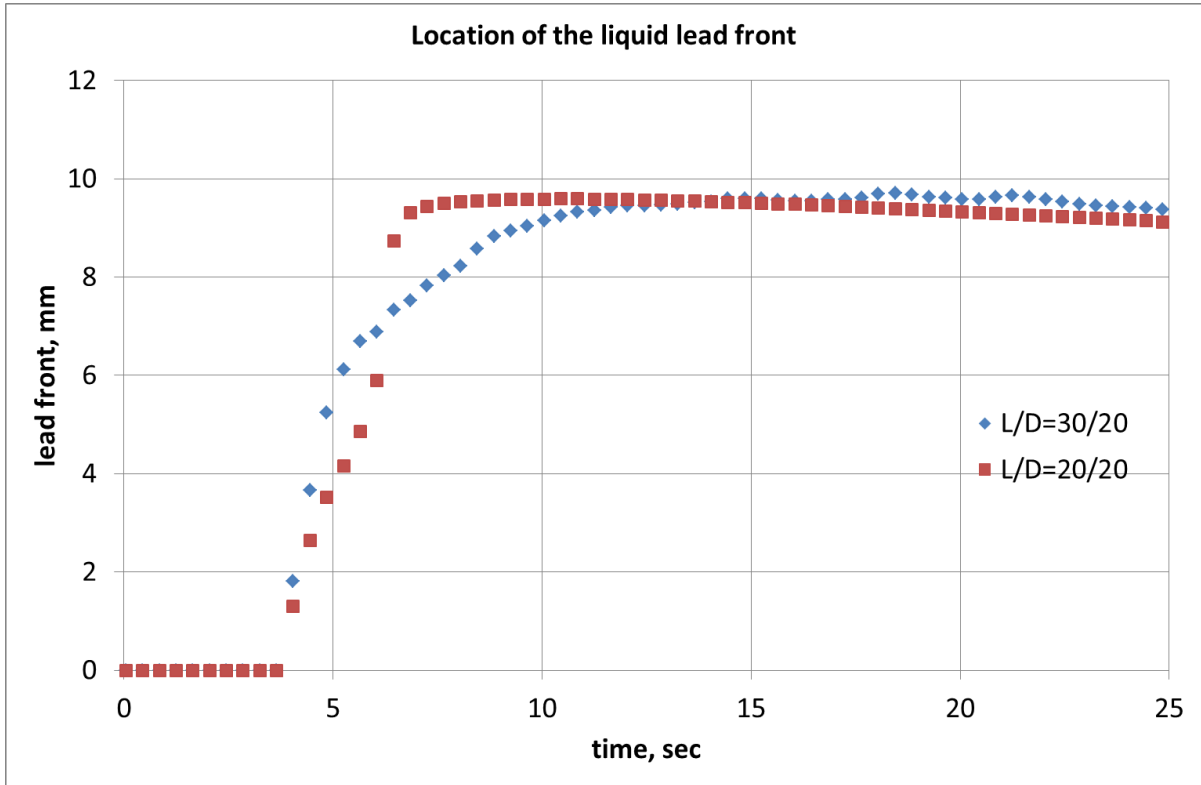


Figure 43: Sample wall melting dynamics in A18 test

- The data is in a good agreement with the posttest analysis indicating almost 10 mm of the final ablation depth. It also indicates that ablation of the thin part of the sample wall (20 mm) progressed a little faster than that of the thick one (30 mm).

Due to severe ablation of the lead plate the only solidified crust remained inside the funnel and the column. The remaining nozzle in A17 test was not plugged. On contrary, small amount of the melt solidified over the sample top surface in A18 causing complete plugging of both the nozzles.

After removal of the solidified crust from the Pb plate and nozzle outlets no clear signs of radial ablation inside the nozzles were found. One of the nozzles in A17 is lost due to wall ablation. It is not clear whether or not the radial ablation took place there or it was axial ablation and thinning of the wall. It was suggested that absence of radial nozzle ablation is caused by its rather small nozzle diameter. In this case radial divergence becomes prevailing over heat transfer and establishes logarithmic temperature profile within the sample:

$$\frac{\partial Q_N}{\partial t} = \lambda_{lead} \bar{V} T = \lambda_{lead} \frac{T_{r1} - T_{r2}}{\ln\left(\frac{r_2}{r_1}\right)} - \text{steady state conduction in cylindrical coordinates.}$$

$$\frac{\partial Q_N}{\partial t} = \lambda_{lead} \bar{V} T = \lambda_{lead} \frac{T_{r1} - T_{r2}}{r_2 - r_1} - \text{steady state conduction in Cartesian coordinates.}$$

***DEFOR-A19-A21 tests***

Experimental observation and accurate measurement of the radial and axial nozzle ablation was defined as the main objective of this test series. In order to minimize the possibility of the nozzle plugging it was suggested to increase the nozzle diameter.

The following goals have been identified for these tests:

- To provide experimental data for assessment of the heat fluxes in radial and axial direction.
- To provide experimental data assessment of the radial and axial ablation rate.

Judging from the video footage, the melt release through the lead samples in A19 - A21 tests took about 10 to 15 sec instead of expected 20 sec indicating important radial ablation of the nozzle. This value is also in agreement with temperature data. Posttest observation of the samples further revealed their axial (wall/vertical) ablation and melt through around periphery. This phenomenon is attributed to the specific flow pattern established inside the melt distributor due to the protective plate that directed the incoming melt towards the plate periphery prior to its passage through the nozzle.

The actual melt superheat measured inside the funnel was 314K, 287K and 286K in A19, A20 and A21 respectively. The photos of samples from A19-11 tests are given in the Figure 44.

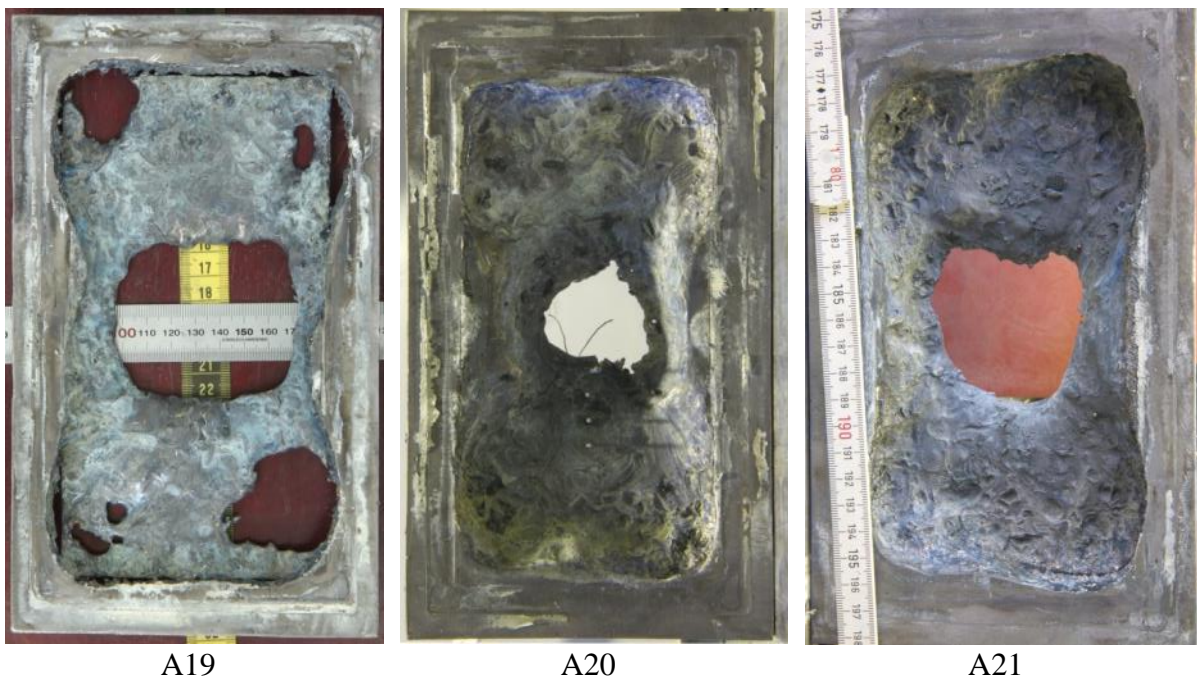


Figure 44: Lead sample radial ablation (crust being removed)

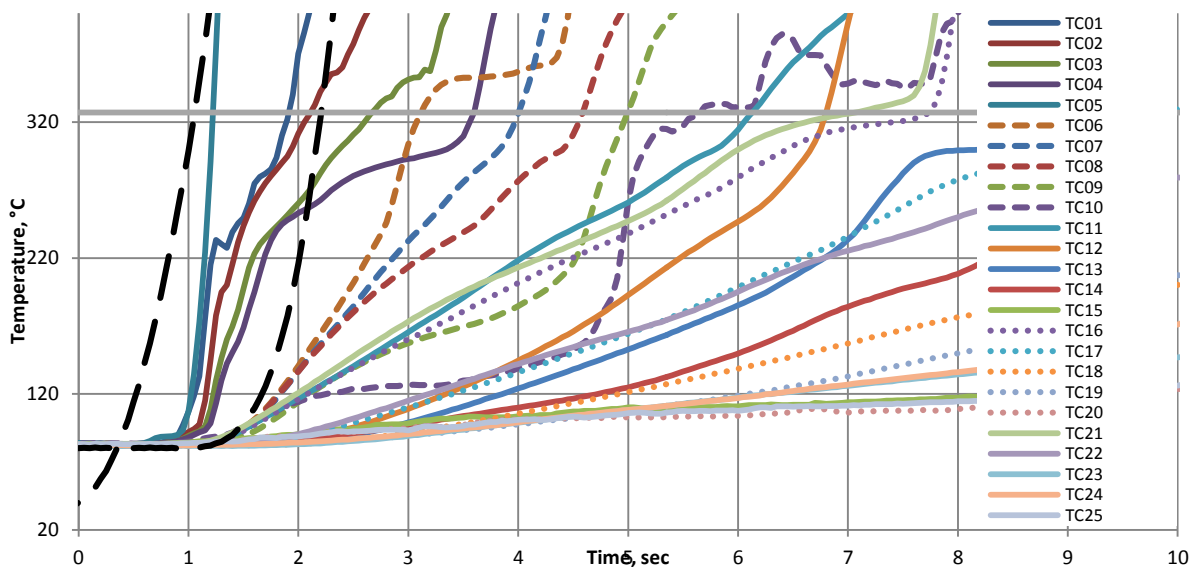
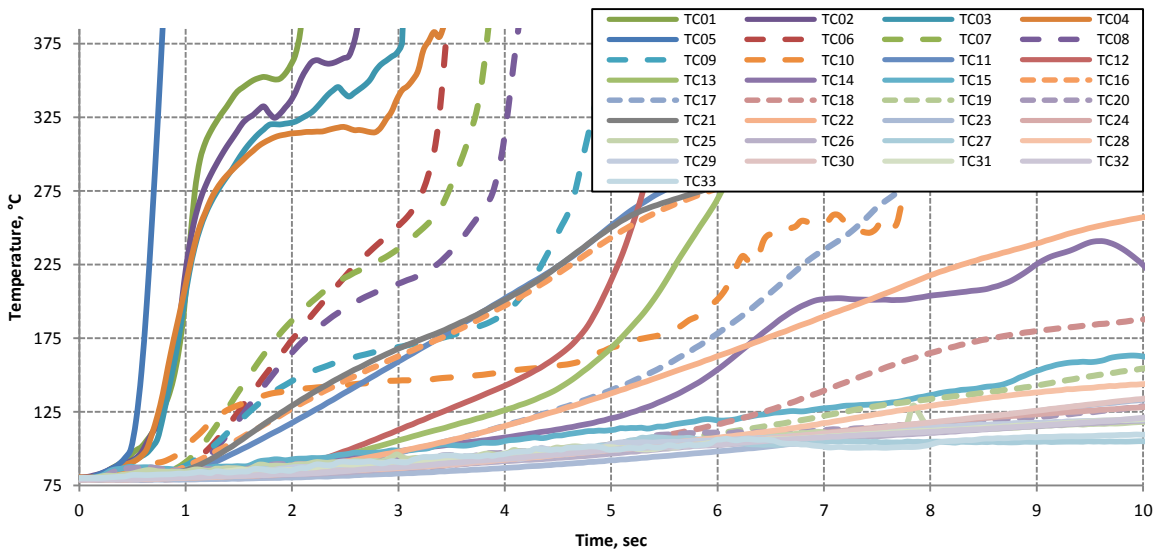
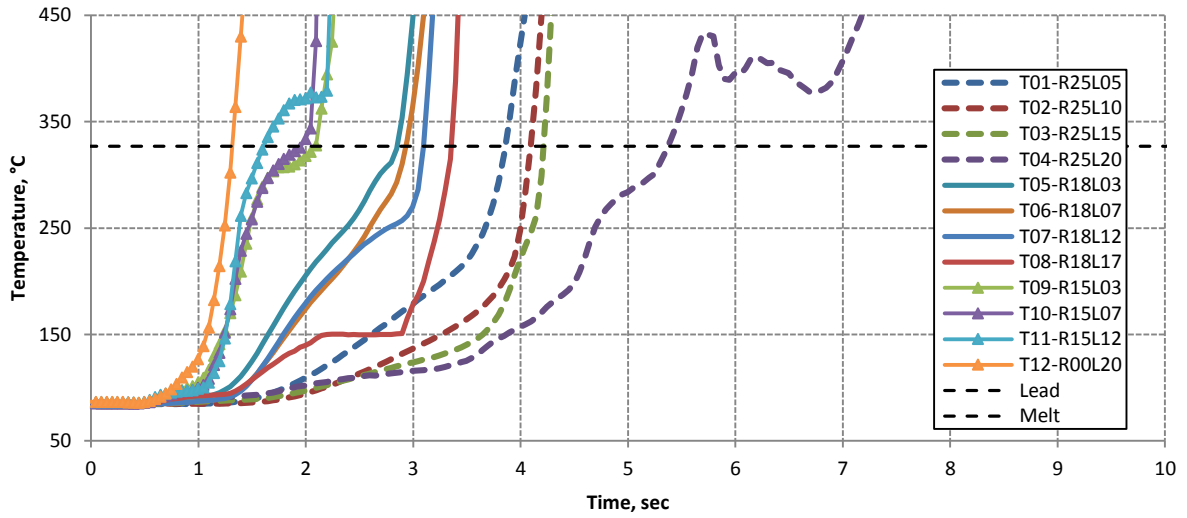


Figure 45: The temperature recordings inside the sample in A19 to A21 test (zoom)

Consistent temperature readings were obtained allowing assessment of the sample ablation dynamics and transient heat fluxes. The readings from the TCs in A19-11 are given in the Figure 45. In the following tables we provide the time values for every TC in A19-11 tests when the corresponding temperature reading reaches the melting point of lead. Note that some timing is not consistent. This is due to different azimuthal locations of the TCs in the same radial group in conjunction with non-axisymmetric character of the interaction. The zero time in the below tables was defined as the start of the melt release from the funnel for consistency. However, an actual onset of the melt / sample interaction could be taken as time of melt arrival to the nozzle outlet, its value is marked with bold font in the below tables.

Table 5: Onset of sample melting according to embedded TCs in A19

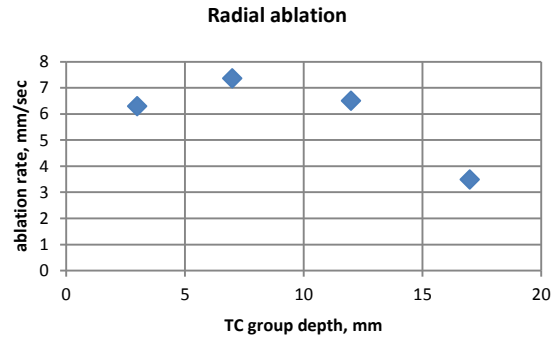
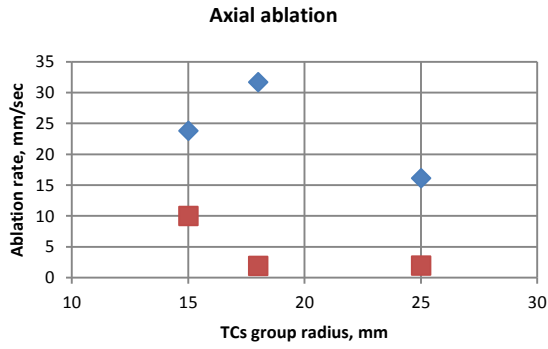
Depth of the TC from the top surface, mm	Time, sec		
	R25	R18	R15
-3 mm		2.87	2.07
-5 mm	3.87		
-7 mm		2.92	1.97
-10 mm	4.07		
-12 mm		3.12	1.62
-15 mm	4.22		
-17 mm		3.37	
-20 mm	5.37		<b>1.32</b>

Table 6: Onset of sample melting according to embedded TCs in A20

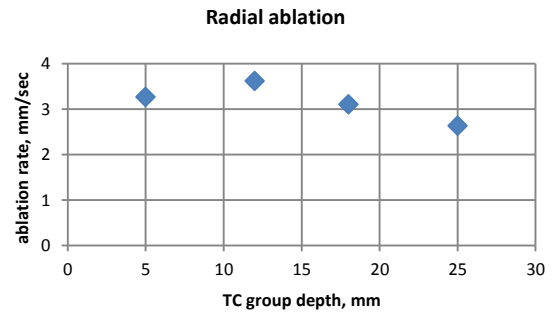
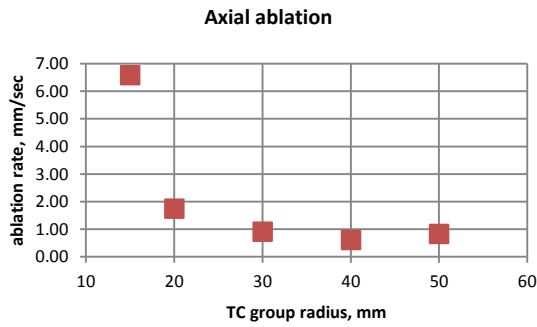
Depth of the TC from the top surface, mm	Time, sec					
	R87	R50	R40	R30	R20	R15
-5 mm	-	6.61	8.81	6.01	3.41	1.31
-12 mm	-	-	9.01	5.51	3.71	1.66
-18 mm	-	-	-	6.86	4.01	2.16
-25 mm	-	-	-	-	4.81	2.91
-30 mm	-	-	-	-	8.36	<b>0.76</b>

Table 7: Onset of sample melting according to embedded TCs in A21

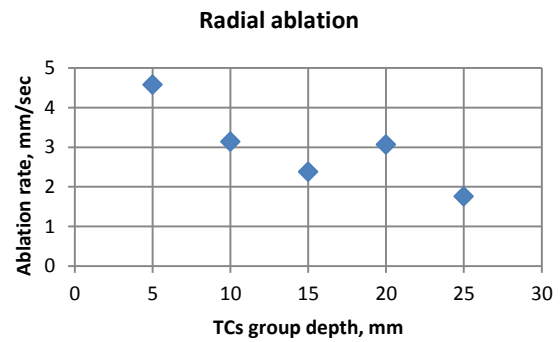
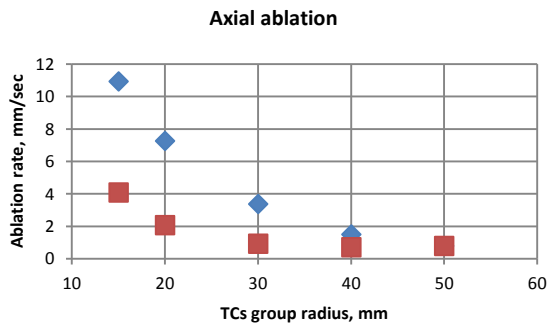
Depth of the TC from the top surface, mm	Time, sec				
	R50	R40	R30	R20	R15
-5 mm	7.075	7.725	6.125	3.125	1.925
-10 mm	-	9.925	6.825	4.025	2.125
-15 mm	-	-	9.275	4.575	2.675
-20 mm	-	-	8.875	4.975	3.575
-25 mm	-	-	9.475	5.675	<b>1.225</b>
-27 mm (TC26-C)					2.225



A19



A20



A21

Figure 46: Averaged radial and axial ablation rates in A19-11 tests (the axial ablation graphs contain curves estimated from the top layer (in red) and averaged over the sample thickness (in blue))

A simplified analysis of the readings allows estimation of the ablation rates in axial and radial directions as it is demonstrated in the Figure 46. While the data obtained is not perfectly consistent due to asymmetric manner of and mutual effect of axial and radial ablation the obtained measurements do provide valuable data.

## 2.4 Summary of DEFOR Experiments

A series of DEFOR-A10-A21 tests have been carried out in order to investigate and clarify important physical phenomena for different failure and ablation modes of the reactor vessel wall. The data can be used for development and validation of the models for assessments of the wall effectiveness and robustness. In the following we summarize main experimental findings:

- Confirmatory A10, A11 tests provided reference data on the properties of the debris bed (such as particle, size distribution, debris bed porosity and agglomeration) with  $ZrO_2-WO_3$  simulant material and different jet velocities. The data is in good agreement with the previous DEFOR-A1-A9 and FARO tests results and is used for comparison with the other DEFOR-A tests where a mockup of the wall (sample) was implemented. On average, larger particles were obtained with  $ZrO_2-WO_3$  melt than with  $Bi_2O_3-WO_3$  in DEFOR-A. Particle size distributions in DEFOR-A series are closer to the size distributions in FARO tests with on average larger particles. While the difference between particle sizes in A10 and A11 tests with free falling jets is not important, there is a tendency for larger particle sizes in those tests with samples where melt was released under water with initially smaller jet velocity. Yet, the difference is not dramatic. Initial jet velocity also seems to have no visible effect on the fraction of agglomerated debris.
- Investigation of the phenomena relevant to main failure modes of the sample such as nozzle plugging, wall and nozzle ablation provided useful data and insights. Melt superheat was shown as a driving parameter of melt interaction with sample material.
- Minor or no ablation of the inner surface of the sample wall and nozzle was observed in several DEFOR-A with sample tests with relatively low melt superheat and low melt mass flow rates.
- Ablation of the mockup wall under the jet impingement point even at moderate melt superheat can be significant. At such superheat there can be no nozzle ablation or even plugging of the nozzle can be observed (see A13, A14).
- Plugging of the nozzle has been observed in most of the DEFOR tests with sample. Ultimately, nozzle plugging was observed even in the case with considerable axial ablation. A correlation between nozzle plugging and the L/D ratio cannot be clearly based on the results of the tests. Melt superheat seems to play more important role given specific test conditions.
- Significant axial ablation of the sample wall was observed near the nozzle inlet in the last series of DEFOR-A tests.
- None or small radial ablation of the nozzle was obtained in the tests with 20 mm nozzle diameters, even in severe axial ablation and melt through of the walls was observed. When nozzle diameter was increased to 30 mm (A19-A21), radial ablation was even more significant than axial one. More detailed analytical investigation of the influence of nozzle

diameter on the radial ablation might be necessary. Temperature readings from the TCs embedded in the mockup provide unique data on the transient development of the ablation in the wall mockup.

### **3 DECOSIM Code Development and Validation Against the Experimental Results Produced in COOLOCE and POMECO-HT Facilities.**

#### **3.1 Overview of DECOSIM Code**

DECOSIM is a thermohydraulic code being developed at KTH for simulation of debris bed formation and coolability [48], [49], [35]. In the framework of DECOSE project, validation of DECOSIM code is being performed against the existing COOLOCE data.

DECOSIM has been developed to take into account not only the flows in the porous medium, but also natural convection flows in the pool, where turbulence models and discrete particle models apply [50], [51]. In this work, only a subset of all models was used: the space beyond the debris bed was filled with an artificial porous medium with low drag, so that the flow in the whole computational domain was calculated from the filtration equations. Also, saturated conditions are assumed in the debris bed and above it, so that the governing equations to be solved are the continuity equations for each phase.

Under the assumption of saturated conditions, the criterion employed to detect the local dryout is based on the analysis of the void fraction distribution, rather than the temperature field. A special algorithm for finding the dryout boundary has been developed and implemented in DECOSIM. For each given shape and properties of the debris bed (input parameters), a set of calculations was carried out in which the specific heat power released in the porous material was varied. First, two values of the specific heat power were set by the user, the higher of which results in the dryout, and the lower of which corresponds to steady-state cooling (no dryout). Then, the next value of the specific heat power was taken as the arithmetic mean of the two powers, and simulation was run with this new power to find out if dryout occurs or not. Depending on the outcome of the simulation, either the lower, or the upper boundary of the heat power interval was set to the last heat power, and the procedure was repeated. This algorithm is similar to the well-known bisection algorithm for finding the root of a function, the iterations are repeated until the upper and lower boundaries of the interval become close enough (i.e., their difference become smaller than some prescribed tolerance).

To speed up calculations, the intermediate solutions were not run to convergence; rather, empirical rules based on the observations of the behavior of the maximum void fraction in the debris bed were formulated and implemented in the code to decide if dryout is going to occur or not. This enabled the dryout boundary to be found much more efficiently than in the original version of the algorithm where all intermediate solutions were run to convergence.

It should be noted that the capability to solve the energy equations for the liquid and gas phases has been recently implemented in DECOSIM, together with the solver for heat transfer in the solid phase. These new capabilities will be utilized in the further validation studies, including the simulations of debris bed coolability in an initially subcooled water pool.

### 3.2 Governing Equations and Numerical Solver

Consider a debris bed submerged in a water pool. Transient distributions are sought for the volume fractions  $\alpha_i$ , superficial velocities  $\mathbf{j}_i$  of liquid and gas phases (subscripts  $L$  and  $G$ , respectively), and pressure  $P$ .

The phase continuity and momentum equations are

$$\frac{\partial \rho_G \alpha_G}{\partial t} + \nabla(\rho_G \mathbf{j}_G) = \Gamma, \quad \frac{\partial \rho_L \alpha_L}{\partial t} + \nabla(\rho_L \mathbf{j}_L) = -\Gamma \quad (3.1)$$

$$-\nabla P + \rho_G \mathbf{g} = \frac{\mu_G}{KK_{rG}} \mathbf{j}_G + \frac{\rho_G}{\eta \eta_{rG}} |\mathbf{j}_G| \mathbf{j}_G \quad (3.2)$$

$$-\nabla P + \rho_L \mathbf{g} = \frac{\mu_L}{KK_{rL}} \mathbf{j}_L + \frac{\rho_L}{\eta \eta_{rL}} |\mathbf{j}_L| \mathbf{j}_L \quad (3.3)$$

Here,  $\mathbf{g}$  is the gravity acceleration,  $\rho_i$  and  $\mu_i$  are the densities and viscosities of the liquid and gas phases ( $i = L, G$ ). The right-hand sides of Eqs. (3.2) and (3.3) contain the phase drag due to porous medium with linear and quadratic terms (with the absolute,  $K$ ,  $\eta$ , and relative,  $K_{ri}$ ,  $\eta_{ri}$ , permeabilities and passabilities). Commonly, saturated conditions are assumed in the debris bed, with the volumetric evaporation rate being  $\Gamma = Q/\Delta H_{ev}$ , where  $Q$  is the heat release rate per unit volume of debris bed,  $\Delta H_{ev}$  is the latent heat of evaporation (i.e., decay heat goes to water evaporation). Under this assumption, the fluid properties  $\rho_i$  and  $\mu_i$  are functions of the

pressure  $P$ . The properties of water in liquid and vapor states (densities  $\rho_i$ , enthalpies  $h_i$ , viscosities  $\mu_i$ , thermal conductivities  $\lambda_i$ ) as functions of pressure and temperature are implemented as polynomials according to IAPWS-IF97 formulation (“Steam tables”) [58].

The drag force due to solid debris (see the first and second terms on the right-hand sides of Eqs. (3.3) is characterized by the permeability  $K$  and passability  $\eta$  depending on the properties of the porous medium. For monodisperse spherical particles, these are related to the porosity  $\varepsilon$  and particle diameter  $d$  [58]:

$$K = \frac{\varepsilon^3 d^2}{150(1-\varepsilon)^2}, \quad \eta = \frac{\varepsilon^3 d}{1.75(1-\varepsilon)} \quad (3.4)$$

These relations can also be used for particles of arbitrary shapes, provided that  $d$  is substituted by a properly averaged effective mean particle diameter. The relative permeabilities  $K_{ri}$  and passabilities  $\eta_{ri}$  are functions of the void fraction  $\alpha$ , they are commonly described by power-law relations:

$$\begin{aligned} K_{rL} &= (1-\alpha)^{nL}, & \eta_{rL} &= (1-\alpha)^{mL} \\ K_{rG} &= \alpha^{nG}, & \eta_{rG} &= \alpha^{mG} \end{aligned} \quad (3.5)$$

In Reed’s model [59], the interphase drag is neglected, the exponents in the relative permeabilities are  $nL = nG = 3$ , and those in the relative passabilities are  $mL = mG = 5$ .

In order to be able to calculate the post-dryout state of debris bed, full energy formulation must be employed, rather than the model of saturated water-vapor mixture which is sufficient for modelling the pre-dryout stage. Therefore, energy equations for the liquid and vapor phases, as well as for the solid particles of debris bed material were added to the model and implemented in DECOSIM. Namely, the energy equations are

$$\varepsilon \rho_i \alpha_i \frac{d_i h_i}{dt} = \varepsilon \alpha_i \frac{d_i P}{dt} + \nabla (\varepsilon \alpha_i \lambda_i \nabla T_i) + \Gamma_i (h_i^l - h_i) + \gamma_i \dot{Q}_{si} + \dot{Q}_i^l \quad (3.6)$$

$$(1-\varepsilon) \rho_s C_s \frac{\partial T_s}{\partial t} = \nabla (\lambda_{eff} \nabla T_s) + \dot{Q}_d - \dot{Q}_{sl} - \dot{Q}_{sv} \quad (3.7)$$

The evaporation rate  $\Gamma = \Gamma_v = -\Gamma_l$  is determined by the heat balance at the interphase surface

$$\Gamma = - \frac{\dot{Q}_l^l + \dot{Q}_v^l + \dot{Q}_w^l}{h_v^l - h_l^l} \quad (3.8)$$

where the heat fluxes to the interface are

$$\dot{Q}_l^I = A\beta_l(T^I - T_l), \dot{Q}_v^I = A\beta_v(T^I - T_v), \dot{Q}_w^I = (1 - \gamma_l)\dot{Q}_{sl} \quad (3.9)$$

where the interface temperature  $T^I$  is equal to the saturation temperature at the local pressure (pure vapor is assumed in the bubbles), i.e.,  $T^I = T_{sat}(P)$ . The phase enthalpies at the interface are taken according to the direction of phase transition:

$$h_l^I = \begin{cases} h_l, & \Gamma > 0 \\ h_{l,sat}, & \Gamma \leq 0 \end{cases}, \quad h_v^I = \begin{cases} h_v, & \Gamma < 0 \\ h_{v,sat}, & \Gamma \geq 0 \end{cases} \quad (3.10)$$

In the numerator of Eq. (3.8),  $Q_w^I$  is the heat flux from the solid particles which goes directly to the interface when the liquid becomes superheated. The fraction of heat from solid particles which goes to heating of liquid phase,  $\gamma_l$ , is assumed to vary linearly from 1 for saturated liquid to 0 when the liquid superheat reaches the maximum allowable value  $\Delta T_{max} = 5 \text{ K}$ :

$$\gamma_l = \begin{cases} 1, & T_l \leq T_{sat} \\ \frac{T_l - T_{sat}}{\Delta T_{max}}, & T_{sat} \leq T_l \leq T_{sat} + \Delta T_{max} \\ 0, & T_l > T_{sat} + \Delta T_{max} \end{cases} \quad (3.11)$$

In the bubble regime ( $\alpha_v \leq 0.3$ ), the specific interphase surface area and heat transfer coefficients for the liquid and vapor phases in Eq. (3.9) are evaluated from

$$A = \varepsilon \frac{6\alpha_v}{D_b}, \quad \beta_l = \frac{\lambda_l}{D_b} (2 + 0.6 \text{Re}_{b,l}^{1/2} \text{Pr}_l^{1/3}), \quad (3.12)$$

$$\beta_v = 2 \frac{\lambda_v}{D_b}, \quad \text{Re}_{b,l} = \frac{\rho_l |U_l - U_v| D_b}{\mu_l}$$

The bubble diameter  $D_b$  is evaluated from

$$D_b = 1.35 \left( \frac{\sigma}{g(\rho_l - \rho_v)} \right)^{1/2} \quad (3.13)$$

The Reynolds number  $\text{Re}_{b,l}$  is based on the relative velocity magnitude and properties of the continuous phase (liquid).

For higher void fractions ( $0.3 \leq \alpha_v \leq 1$ ), annular regime is assumed, with water being the wetting phase in direct contact with the solid particles, in which case the specific interface area and heat transfer coefficients are

$$A = \varepsilon \frac{4\alpha_v^{1/2}}{D_p}, \quad \beta_l = \frac{\text{Nu}_l \lambda_l}{D_p}, \quad \beta_v = \frac{\text{Nu}_v \lambda_v}{D_p} \quad (3.14)$$

The Nusselt numbers for the gas phase is calculated as  $\text{Nu}_v = 2 + 0.6 \text{Re}_r^{1/2} \text{Pr}_v^{1/3}$ , where  $\text{Re}_r$  is the Reynolds number based on the relative velocity of the phases. For the liquid, a constant Nusselt number  $\text{Nu}_l = 10$  is assumed.

The source terms  $\dot{Q}_{si}$  describing heat transfer from the solid particles to the liquid and gas phases are evaluated as

$$\dot{Q}_{sl} = \chi \cdot A_s \beta_{sl} (T_s - T_l), \quad \dot{Q}_{sv} = (1 - \chi) \cdot A_s \beta_{sv} (T_s - T_v) \quad (3.15)$$

where  $A_s$  is the specific surface area of porous particles (per unit of total volume),  $\beta_{si}$  are the heat transfer coefficients for the liquid and vapor phases, respectively. It is assumed that, as long as the void fraction  $\alpha_v$  is below the critical value  $\alpha_{dry} \approx 0.95$ , all particles are covered with liquid water, so that all heat is transferred only to the liquid phase ( $\dot{Q}_{sv} = 0$ ). For higher void fractions, some part of the particle surface becomes dry, and direct heating of vapor by particles commences. A simple linear ramping of the heat transfer coefficients is applied at  $\alpha \geq \alpha_{dry}$ , so that  $\dot{Q}_{sl} = 0$  at  $\alpha_v = 1$  (this provides physically sound reduction to the case of single-phase vapor exchanging heat with the porous particles in the post-dryout conditions):

$$\chi = \min \left( \frac{1 - \alpha}{1 - \alpha_{dry}}, 1 \right) \quad (3.16)$$

The specific surface area in Eq. (3.15) is  $A_s = 6(1 - \varepsilon) / D_p$ , the vapor heat transfer coefficient is

$$\beta_{sv} = \frac{\lambda_v}{D_p} \left( 2 + 0.6 \text{Re}_{p,v}^{1/2} \text{Pr}_v^{1/3} \right), \quad \text{Re}_{p,v} = \frac{\rho_v U_v D_p}{\mu_v} \quad (3.17)$$

The heat transfer coefficient between liquid and solid particles depends on the particle superheat with respect to the saturation temperature  $T_s - T_{sat}$ . When the wall temperature is lower than  $T_s$ , the heat flux from particles to liquid is obtained from Eq. (3.15), with the heat transfer coefficient

$$\beta_{sl} = \frac{\lambda_l}{D_p} \left( 2 + 0.6 \text{Re}_{p,l}^{1/2} \text{Pr}_l^{1/3} \right) \quad (3.18)$$

When the wall temperature is above  $T_s$ , the heat flux is obtained from  $\dot{Q}_{sl} = \chi \cdot A_s \beta_{sl} (T_s - T_{sat})$  with the heat transfer coefficient depending on the boiling regime (“boiling curve”). Nucleate boiling occurs for superheats below the critical value  $0 \leq T_s - T_{sat} \leq \Delta T_{nucl}$ , the heat transfer coefficient is described by Roshenow’s correlation

$$\beta_{sl} = \mu_l \Lambda \left[ \frac{g(\rho_l - \rho_v)}{\sigma} \right]^{1/2} \left[ \frac{C_l}{C_{sf} \Lambda Pr_l^{1.7}} \right]^3 (T_s - T_{sat})^2 \quad (3.19)$$

where  $\Lambda = h_{v,sat} - h_{l,sat}$ ,  $C_l$  is the specific heat capacity of liquid, while  $C_{sf} = 0.006 - 0.013$  is a constant depending of the surface-fluid combination; in the calculations it was assumed that  $C_{sf} = 0.01$ .

For film boiling at high superheat,  $T_s - T_{sat} \geq \Delta T_{film}$ , Bromley’s correlation is applied, with the convective heat transfer coefficient

$$\beta_{sl}^{conv} = 0.67 \left[ \frac{\lambda_v^3 \rho_v g (\rho_l - \rho_v) (\Lambda + 0.4 C_{pv} (T_s - T_{sat}))}{D_p \mu_v (T_s - T_{sat})} \right]^{1/4} \quad (3.20)$$

The radiative heat transfer coefficient becoming important at high debris temperature is

$$\beta_{sl}^{rad} = \varepsilon_p \sigma_{SB} \frac{T_s^4 - T_{sat}^4}{T_s - T_{sat}} \quad (3.21)$$

where  $\varepsilon_p$  is the particle surface emissivity,  $\sigma_{SB} = 5.67 \cdot 10^{-8} \text{ W/m}^2\text{K}^4$  is the Stefan-Boltzmann constant. The total heat transfer coefficient  $\beta_{sl}$  is obtained from

$$\beta_{sl}^{4/3} = (\beta_{sl}^{conv})^{4/3} + \beta_{sl}^{rad} \beta_{sl}^{1/3} \quad (3.22)$$

In the intermediate region  $\Delta T_{nucl} \leq T_s - T_{sat} \leq \Delta T_{film}$ , linear interpolation is performed between  $\beta_{sl}$  evaluated from Eq. (3.19) with  $T_s - T_{sat} = \Delta T_{nucl}$ , and  $\beta_{sl}$  obtained from Eqs. (3.20)–(3.22) with  $T_s - T_{sat} = \Delta T_{film}$ . The boundaries of the nucleate and film boiling regimes were set to  $\Delta T_{nucl} = 20 \text{ K}$  and  $\Delta T_{film} = 120 \text{ K}$ .

The decay heat power in the solid material energy equation (3.7) is expressed in terms of the specific decay heat power as  $\dot{Q}_d = (1 - \varepsilon) \rho_s W$ . A simple model is employed for the effective heat conductivity of porous medium:  $\lambda_{eff} = (1 - \varepsilon) \lambda_s$ .

In DECOSIM, all transport equations are discretized on a staggered orthogonal grid in the 2D axisymmetric geometry. On each time step, the momentum equations are solved first to find out the preliminary velocity components of each phase. The velocity corrections are expressed in terms of pressure and volume fraction corrections, with the phase change terms taken into account implicitly. They are then substituted into the phase continuity and energy equation which are solved in a fully coupled manner by an efficient ILUT-preconditioned PGMRES solver from SPARSKIT package. Global iterations are performed on each time step until convergence with prescribed accuracy is reached. The time step is varied adaptively, depending on convergence success or failure.

DECOSIM has been validated with respect to various separate effects, including two-phase drag in porous media and coolability of flat and axisymmetric (cone-shaped) ex-vessel debris beds in configurations. The models and closures involved are similar to those of WABE/MEWA code [60] with which some cross-code verifications have been carried out. At the moment, no reactor-scale experiments are available to enable integral validation of this (or similar) codes.

### **3.3 Search Algorithm for Determination of Coolability Boundary**

To study the debris bed coolability, an algorithm for automatic search for the dryout boundary is required. A straightforward algorithm is the following: the heat release rate (HRR) is gradually increased with some step, and for each HRR transient simulation is run for a long enough time period. The minimum HRR causing the dryout is considered to be the boundary. The dryout criterion is based on the monitoring the void fraction in the debris bed. Dryout was detected if the void fraction in any cell of the grid reached the critical value (0.95–0.975), after that the heat release rate was ramped to zero because evaporation becomes inefficient for such high void fractions.

This approach has several drawbacks. Firstly, it requires long and useless calculations far from dryout, when the flow reaches the steady state. Secondly, it can miss the dryout HRR, since the time between the HRR increase and actual dryout can be very long, especially for a flat layer (see [61]). Thirdly, the accuracy of the dryout boundary detection is of the order of HRR step, and to increase the accuracy it is required to use smaller steps in HRR and, therefore, more simulations are required.

To improve the efficiency, an algorithm was proposed which makes possible an automatic search of the dryout boundary. Its main idea is to vary the HRR using the bisection algorithm and use certain semi-empirical criteria to determine whether the current state of the debris bed is likely to lead to steady state cooling, or to dryout. In what follows, the algorithm is described in detail.

The debris bed is initially filled with water in the saturated conditions. The heat released in the porous material causes the production of water vapor, which results in the development of water and vapor flows. The void fraction in the bed increases gradually, and, finally, two scenarios are possible: either the debris bed is coolable (steady-state conditions are attained), or dryout can occur at some point. Theoretically, the final state can only be checked in an infinitely long calculation (because the time to dryout can be quite long and is not known beforehand). To make the algorithm efficient, criteria were proposed for the following:

1. Convergence of all fields (velocities, pressure, volume fractions) in the debris bed to steady-state distributions with some tolerance.
2. The maximum void fraction in the debris bed.

These criteria were chosen as they are close to the physical meaning of steady-state cooling and dryout. Other criteria checked during the coolability simulations are the convergence of all fields on the whole grid, which happened to give almost the same results as that inside the bed, and the average void fraction.

After some trial runs, the following parameters were chosen for the search:

1. To check if the fields converged to some steady state, they were averaged over the last ten steps in order to reduce the effect of possible fluctuations of the numerical nature. The averaged values were compared every 10 seconds. Then, for each of the seven monitored variables the maximum change was found and normalized. For normalization, the pressure and volume fractions were divided by the maximum value of the corresponding field in the bed; the velocity components were divided by the absolute values of the superficial velocity vector. The highest value of the normalized increments was compared to the steady state criterion (SSC); if it happened to be lower than SSC, the debris bed was assumed to be in its steady state.

The SSC was chosen after several runs on the test problems. It strongly depends on the time between criterion checks, since the larger is the time interval the smaller should be the criterion. It should be noted that high SSC ( $10^{-3}$  or higher) leads to significant misses of the dryout, especially for flat debris bed. Very low SSC ( $10^{-6}$  and lower) leads to high computation time, and sometimes the problem doesn't converge to meet such an accuracy criterion at all. After all trials, the following formula was chosen for the SSC:

$$SSC = \min \left( 10^{-4}, 10^{-5} \cdot \frac{HRR \text{ Dry} - HRR \text{ Wet}}{\text{target HRR accuracy}} \right)$$

where HRR Dry and HRR Wet are the currently available boundaries of the Dryout HRR (DHRR).

2. The maximum void fraction (AMax) is a very useful criterion for the assessment of the states close to DHRR. It was shown that, for example, for a flat debris bed without bottom water injection the maximum void fraction for steady-state cooling is approximately equal to 0.8. Any higher values lead to gradual increase in the void fraction and, finally, to dryout. For non-flat configurations, or in the presence of water inflow from below, the maximum void fraction in the coolable state can reach 1.0, but it very quickly increases with the increase in HRR. Thus, the value of 0.95 was chosen as the critical value, indicating dryout in the bed.

Another important issue is to determine if the state became coolable after the HRR has been decreased. Simulations show that decrease of the AMax below 0.92 from the dryout state always indicate rewetting and show that current HRR corresponds to coolable state. But this criterion is not very efficient since the process of rewetting may take very long time, and it is hard to determine if the state is coolable or not since the fields are not converged to the steady state. To prevent this, after 500 s the current HRR is decreased, however, no conclusion is made about the state of the bed.

The full algorithm based on these two criteria is shown in Figure 47. The input data for the algorithm are the initial heat release rate, and the wet-state HRR (optional). In the initial state, DECOSIM runs until the steady state is reached, or dryout occurs. If the steady state is reached, the current value of HRR is considered as “wet” and the HRR is increased by a factor of 1.3. This multiplier was chosen since large HRR increase can lead to states far from the wet state, which converge very slowly, while small multipliers lead to slow convergence if the initial HRR is far below the dryout boundary.

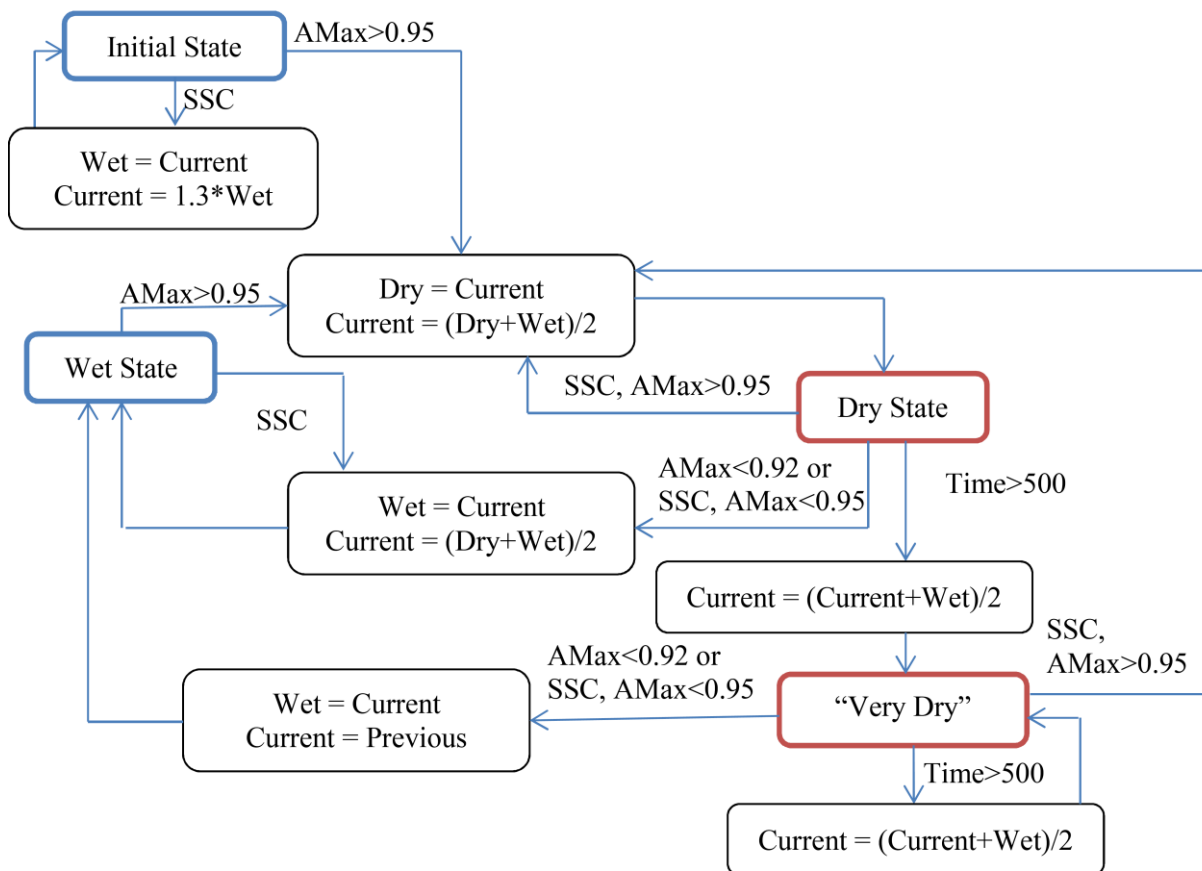


Figure 47: Bisection search algorithm for the dryout boundary.

After the first dryout has occurred, the main part of bisection algorithm is executed, in which there are two known states corresponding to coolable and non-coolable bed, and their arithmetic mean is used as the next current HRR to be checked. After each change of wet and dry limits, their difference is compared with the user-defined target HRR accuracy. Once the difference becomes smaller than the prescribed HRR accuracy, the average of the wet and dry-state HRR is taken as the coolability boundary.

Before the algorithm was applied to real problems, its sensitivity to computational parameters was studied in test calculations. There are three main parameters of the algorithm which may affect the final result: the steady state criterion, dryout and ramping void fractions, and initial values of heat release rate.

All data given below are obtained for the conical COOLOCE configuration with system pressure of 1.1 bar using Reed's model [59]. The grid had 31×57 cells, and the cell size was 1.0×1.0 cm. It should be noted that the method was also tested on many other configurations, including real pool simulations with different particle diameters, porosities, system pressure, and shape of the bed.

Before the algorithm was applied to validation simulations, its sensitivity to computational parameters was studied in the test calculations. There are three main parameters of the algorithm which may affect the final result: the steady state criterion, dryout and ramping void fractions, and initial values of heat release rate.

All data given below are obtained for the conical COOLOCE configuration with system pressure of 1.1 bar using Reed's model. The grid had 31×57 cells, and the cell size was 1.0 cm×1.0 cm. It should be noted that the method was also tested on many other configurations, including real pool simulations with different particle diameters, porosities, system pressure, and shape of the bed.

#### Dependence on Steady State Criterion (SSC)

The dependence on SSC is non-monotonic and is significantly affected by all input parameters and starting HRR values. There were found many parameters and starting points for calculations which misinterpreted the state as steady using the criterion  $10^{-2} - 10^{-3}$ . It was shown that, in

order to obtain the boundary with precision  $\sim 1\%$ , it is enough to take steady state criterion equal to  $10^{-4}$ .

#### Dependence on dryout and ramping void fractions

The results of changing the void fractions are shown in the figure. As was noted above, the maximum void fraction in the bed at steady state increases quickly with increase of the HRR. One can see from the table that the difference in results is higher than target HRR accuracy, however, it is still quite small.

Dryout void fraction	Ramping void fraction	DHRR, W/kg
0.93	0.965	199.5
0.95	0.975	200.8
0.97	0.985	201.8

#### Dependence on initial HRR

The algorithm is almost insensitive to the initial heat release rates. The results are shown in the table; one can see that their difference is less than target HRR accuracy.

Initial HRR, W/kg	Initial wet HRR, W/kg	DHRR, W/kg
250	130	200.8
223	115	200.6
220	190	200.8
240	170	200.9

#### Grid convergence

The grid convergence was also checked on the conical COOLOCE configuration with system pressure of 1.1 bar using Reed model. The grid was uniform in first 5 cases (see the Table below), the values of DHRR are shown in Figure 48.

Cell size, cm	Grid size	Grid Type	DHRR, W/kg
2.0	16×29	uniform	216.1
1.0	31×57	uniform	200.8
0.70	45×85	uniform	189.8
0.40	77×143	uniform	184.7
0.20	154×286	uniform	183.4
2.0-0.70	31×40	non-uniform, 1/3 dense	192.9

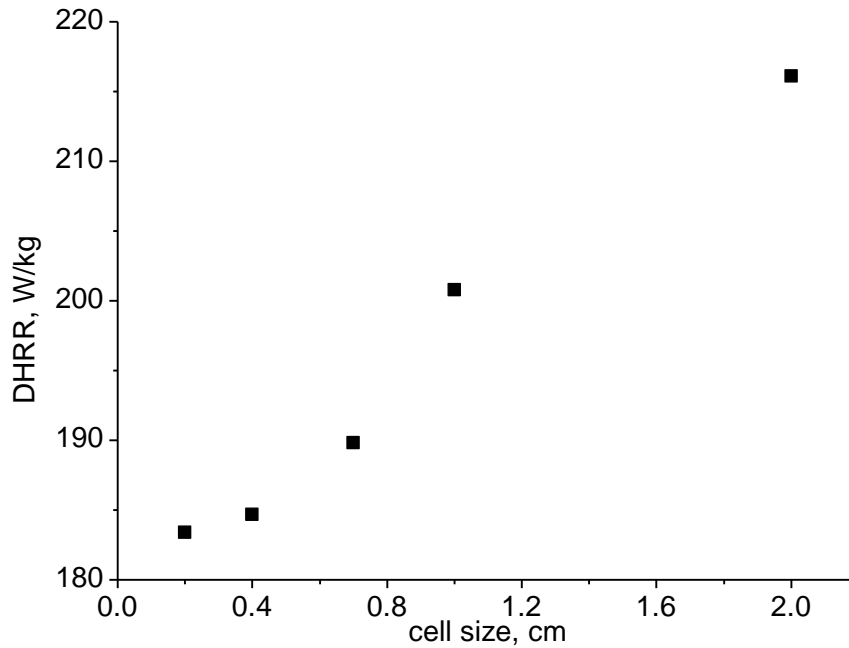


Figure 48: Grid convergence results: dependence of dryout heat release rate on cell size.

One can see that the difference in DHRR values obtained on grids with cell sizes 0.70 cm and 0.20 cm (the finest grid) is within 4%. However, simulations on the finest grid and require too much computational time because of large number of cells. To reduce the computational cost, a non-uniform grid was used with the refined area near the tip of the cone, since this region determines the coolability of the debris bed. The dryout heat release rate obtained on this grid is almost the same as on third grid, at the same time, the number of cells is three times smaller.

### 3.4 DECOSIM Simulations of COOLOCE Experiments

#### 3.4.1 Parameters of DECOSIM Simulations

In the current validation studies, the data from the COOLOCE experiments performed at VTT in 2010-2013 (see [1], [2], [64], [65], [67], [68], [69]) were used. Simulations were carried with Reed's model [59] for the phase drag in the porous medium. Parameters of the calculations are listed in Table 8.

Table 8: Parameters used in DECOSIM simulations of COOLOCE experiments.

<b>Fixed Parameters</b>	
Water pool geometry	Radius: 0.306 m
	Height: 0.57 m
Cylindrical Geometry (COOLOCE-3,4,5) (impermeable side wall)	Height: 0.27 m
	Diameter: 0.31 m
	Surface area: 0.07548 m <sup>2</sup>
	Volume: 0.02038 m <sup>3</sup>
Conical Geometry (COOLOCE-6,7)	Height: 0.27 m
	Diameter: 0.50 m
	Volume: 0.01767 m <sup>3</sup>
Cylindrical Geometry (COOLOCE-10) (open side wall)	Height: 0.27 m
	Diameter: 0.305 m
	Surface area: 0.0730 m <sup>2</sup>
	Volume: 0.0197 m <sup>3</sup>
Cone on Cylindrical Base Geometry (COOLOCE-12)	Height of conical part: 0.135 m
	Height of cylindrical part: 0.135 m
	Diameter of cylindrical part: 0.250 m
	Volume: 0.00884 m <sup>3</sup>
Friction model	Reed
<b>Variable Parameters</b>	
System pressure	$P_{\text{sys}}$ : 1.1-6.95 bar
Particle diameters	$d$ : 0.8–1.07 mm
Porosity	$\varepsilon$ : 37–40%

The system pressure was varied in accordance with the conditions of each COOLOCE experiment. The debris bed porosity and mean particle diameter, however, were varied in order to take into account the existing uncertainties in the properties of the debris bed. The debris bed particles used in the COOLOCE tests were spherical beads of Zirconium silicate whose sizes vary between 0.8 mm to 1 mm. The porosity of the debris bed reported by VTT was 37%. However, measurements performed in POMECO-FL facility for the same particles gave a higher value of porosity close to 40%, while the mean particle diameter determined from the particle size distribution analysis was higher than 0.8 mm, see Figure 75.

In the current simulations, the baseline debris bed properties were taken to be the lowest values of particle diameter  $d = 0.8$  mm and porosity  $\varepsilon = 37\%$ . It was obtained that this case gives underestimates the dryout boundary in comparison with the COOLOCE experiments. Therefore, simulations were repeated with the porosity determined from POMECO-FL tests (40%) and the particle diameter 0.89 mm, as well as for the porosity reported by VTT (37%) and particle diameter 1.07 mm. In the latter cases, the effective particle diameter was found from the best agreement of DHF predictions from one-dimensional debris bed model with COOLOCE experiments performed for cylindrical debris bed.

Simulations of COOLOCE-10 and COOLOCE-12 experiments were carried out for the particle diameter 0.9 mm and porosity 40%.

### **3.5 Summary of Results**

The simulation cases and the results obtained for cylindrical debris bed are summarized in Table 9 (for cylindrical debris bed with impermeable side walls) and Table 10 (for conical debris bed). For the conical debris bed, simulations have only been performed so far for two combinations of particle diameter and porosity, and only one point was obtained for the third combination.

The respective dependencies of the calculated dryout heat power on the system pressure are plotted in Figure 49 (for cylindrical debris bed, presented as the dryout heat flux DHF,  $W/m^2$ ) and Figure 50 (for conical debris bed). On the same graphs, results of numerical simulations by MEWA code reported in [70] are plotted for comparison, with the respective particle diameters and porosities indicated in the legends. Note that in [70] MEWA simulations of the cylindrical

debris bed were carried out with Reed's model for the drag in porous medium [59], the same as used in the current DECOSIM simulations. However, for the conical debris beds, the model by Tung and Dhir [71] with the modifications for small particles proposed in [72] was used; this model takes into account the interphase drag which is neglected in Reed's drag model [59].

Table 9: DECOSIM simulations of COOLOCE experiments: cylindrical debris bed with impermeable walls.

Case No.	Experiment	Pressure $P_{\text{sys}}$ , bar	Experimental dryout power, kW	Calculated dryout power, kW	Comments
1	COOLOCE-3	1.1	19.0	11.5	$d = 0.8 \text{ mm}$ , $\varepsilon = 37\%$
	COOLOCE-3R		20.4	19.0	$d = 0.89 \text{ mm}$ , $\varepsilon = 40\%$
					19.2
2	COOLOCE-4	1.6	23.4	14.7	$d = 0.8 \text{ mm}$ , $\varepsilon = 37\%$
				22.8	$d = 0.89 \text{ mm}$ , $\varepsilon = 40\%$
				23.0	$d = 1.07 \text{ mm}$ , $\varepsilon = 37\%$ $\varepsilon = 37\%$
3	COOLOCE-4	1.9	26.1	16.0	$d = 0.8 \text{ mm}$ , $\varepsilon = 37\%$
	COOLOCE-4bR	1.95	26.2	24.8 24.9	$d = 0.89 \text{ mm}$ , $\varepsilon = 40\%$ $d = 1.07 \text{ mm}$ , $\varepsilon = 37\%$
4	COOLOCE-5	3.0	31.9	20.1	$d = 0.8 \text{ mm}$ , $\varepsilon = 37\%$
				30.6	$d = 0.89 \text{ mm}$ , $\varepsilon = 40\%$
				30.6	$d = 1.07 \text{ mm}$ , $\varepsilon = 37\%$
5	COOLOCE-5	4.0	34.6	23.1	$d = 0.8 \text{ mm}$ , $\varepsilon = 37\%$
				34.8	$d = 0.89 \text{ mm}$ , $\varepsilon = 40\%$
				34.7	$d = 1.07 \text{ mm}$ , $\varepsilon = 37\%$
6	COOLOCE-5	4.95	37.2	25.5	$d = 0.8 \text{ mm}$ , $\varepsilon = 37\%$
				38.1	$d = 0.89 \text{ mm}$ , $\varepsilon = 40\%$
				37.9	$d = 1.07 \text{ mm}$ , $\varepsilon = 37\%$
7	COOLOCE-5	6.95	42.3	29.6	$d = 0.8 \text{ mm}$ , $\varepsilon = 37\%$
				43.8	$d = 0.89 \text{ mm}$ , $\varepsilon = 40\%$
				43.4	$d = 1.07 \text{ mm}$ , $\varepsilon = 37\%$ $\varepsilon = 37\%$

Experimental data from COOLOCE tests are presented in Figure 49 and Figure 50 by the black points. Also, in Figure 49, an experimental point is plotted (green dot) corresponding to the measurement of dryout heat flux in POMECO-HT experiment [63] performed for the same spherical beads as in COOLOCE experiments.

Table 10: DECOSIM simulations of COOLOCE experiments with conical debris bed.

Case No.	Experiment	Pressure $P_{\text{sys}}$ , bar	Experimental dryout power, kW	Calculated dryout power, kW	Comments
8	COOLOCE-6	1.1	26.0	18.0 27.8 28.1	$d = 0.8 \text{ mm}, \varepsilon = 37\%$ $d = 0.89 \text{ mm}, \varepsilon = 40\%$ $d = 1.07 \text{ mm}, \varepsilon = 37\%$
9	COOLOCE-7	1.6	31.8	22.6 34.0 –	$d = 0.8 \text{ mm}, \varepsilon = 37\%$ $d = 0.89 \text{ mm}, \varepsilon = 40\%$ $d = 1.07 \text{ mm}, \varepsilon = 37\%$
10	COOLOCE-7	2.0	36.0	25.5 38.2 –	$d = 0.8 \text{ mm}, \varepsilon = 37\%$ $d = 0.89 \text{ mm}, \varepsilon = 40\%$ $d = 1.07 \text{ mm}, \varepsilon = 37\%$
11	COOLOCE-7	3.0	42.9	31.5 46.7 –	$d = 0.8 \text{ mm}, \varepsilon = 37\%$ $d = 0.89 \text{ mm}, \varepsilon = 40\%$ $d = 1.07 \text{ mm}, \varepsilon = 37\%$

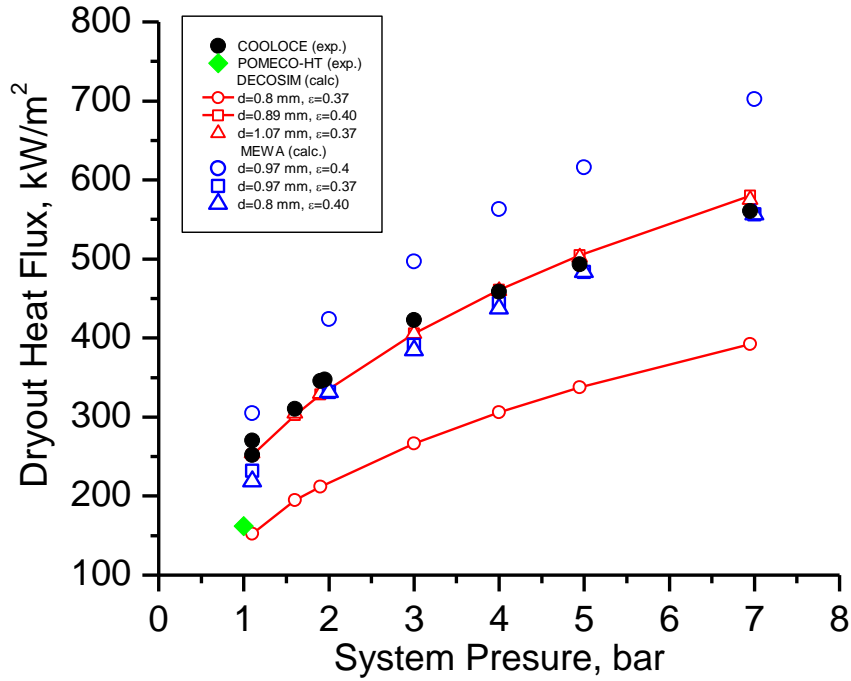


Figure 49: Comparison of calculated dryout heat power as function of system pressure (cylindrical debris bed) with COOLOCE experiments.

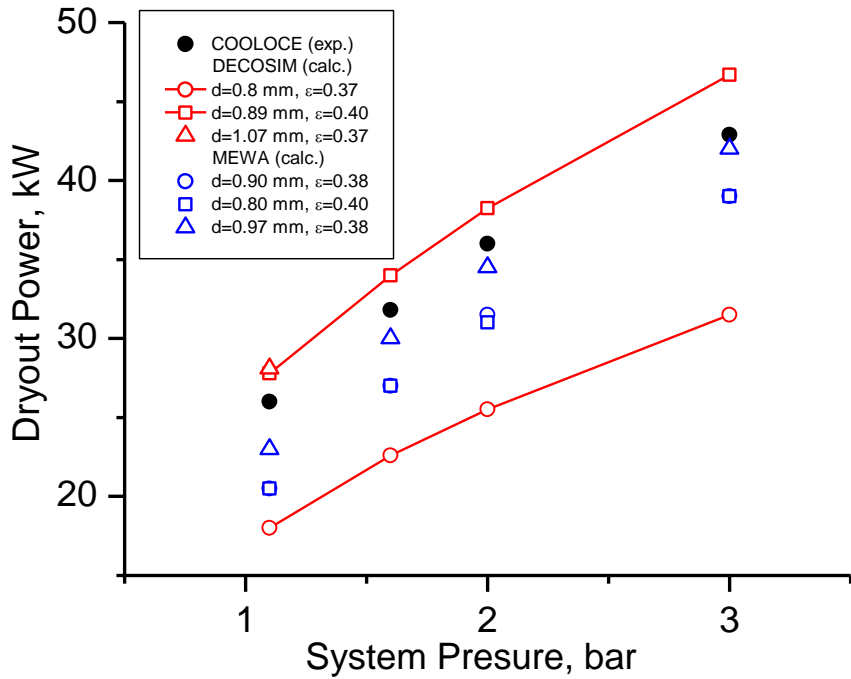


Figure 50: Comparison of calculated dryout heat power as function of system pressure (conical debris bed) with COOLOCE experiments.

In Table 11, results of DECOSIM simulations for cylindrical debris bed with open side walls are presented together with the corresponding data of COOLOCE-10 experiments. In order to evaluate the effect of side flooding on the dryout power, simulations were also performed on exactly the same numerical mesh, but with impermeable side walls (similar to the conditions of experiments and calculations presented in Table 9). The reason for performing this second set of simulations was that the pressures in COOLOCE-10 experiments were different from those in the experiments from Table 9, so that some form of interpolation would be required to obtain the ratio of dryout powers for open and impermeable side walls. Thus, in Table 11 for each experiment two values of dryout power are given, as well as their ratio  $r = W_{\text{open}} / W_{\text{imper.}}$ .

One can see that simulations gave overestimated values for the dryout power in comparison with the experiments, especially taking into account that experimental values are the control powers which include not only the power necessary to boil water, but also the losses which are estimated to be about 10-20% of the control power.

No doubt, better agreement can be achieved by taking lower porosity and particle diameters (e.g., porosities of 37% and particle diameters of 0.87 mm are quoted in [68], [69], and the dryout boundary is known to be very sensitive to these parameters for sub-mm particles). However, of much higher interest is the accuracy of prediction of the ratio of powers with open and impermeable walls  $r = W_{\text{open}} / W_{\text{imper.}}$ .

The corresponding values are presented in Table 11 for DECOSIM simulations; also, similar values are evaluated from the results of COOLOCE-10 experiment (with open walls) and those presented in Table 9 (with impermeable walls). One can see that simulations give the value of approximately  $r=1.45$ , while in the experiments the average ratio is close (albeit, somewhat higher),  $r=1.5$ . This ratio is very important in the context of development of a surrogate model for debris bed coolability because it essentially depends on the debris bed geometry, namely, for a cylindrical bed, on the diameter-to-height ratio.

Table 11: DECOSIM simulations of COOLOCE-10 experiments, cylindrical debris bed with open side wall.

Case No.	Experiment	Pressure $P_{sys}$ , bar	Experimental dryout power, kW	Calculated dryout power, kW	Comments
1	COOLOCE-10a	1.3	34.1 $r=1.55$	39.0 (open) 26.8 (imper.) $r=1.46$	$d = 0.9 \text{ mm}$ , $\varepsilon = 40\%$
2	COOLOCE-10b	2.0	40.1 $r=1.53$	50.6 (open) 35.6 (imper.) $r=1.42$	$d = 0.9 \text{ mm}$ , $\varepsilon = 40\%$
3	COOLOCE-10c	3.0	46.2 $r=1.45$	55.5 (open) 39.6 (imper.) $r=1.40$	$d = 0.9 \text{ mm}$ , $\varepsilon = 40\%$

Table 12, results of DECOSIM simulations for a cone-on-base shaped debris bed are presented, with corresponding data from COOLOCE-12 experiments [69]. One can see that the results are in very good agreement, although, reservations on the experimental power and high sensitivity of the results to porosity and particle diameter (see discussion of results presented in Table 11) must be kept in mind.

Table 12: DECOSIM simulations of COOLOCE-12 experiments, conical debris bed with on cylindrical base.

Case No.	Experiment	Pressure $P_{sys}$ , bar	Experimental dryout power, kW	Calculated dryout power, kW	Comments
1	COOLOCE-12a	1.085	17.05	14.1	$d = 0.9 \text{ mm}$ , $\varepsilon = 40\%$
2	COOLOCE-12b	1.98	19.65	19.1	$d = 0.9 \text{ mm}$ , $\varepsilon = 40\%$
3	COOLOCE-12c	2.95	22.95	23.1	$d = 0.9 \text{ mm}$ , $\varepsilon = 40\%$
4	COOLOCE-12d	3.81	25.59	26.0	$d = 0.9 \text{ mm}$ , $\varepsilon = 40\%$

### 3.6 Discussion of Results

The following conclusions can be derived from the experimental and simulation results presented in Figure 49 and Figure 50.

There is a clear discrepancy between the experimental dryout heat fluxes obtained in COOLOCE and POMECO-HT facilities at the atmospheric pressure. The dryout heat flux of  $270 \text{ kW/m}^2$  was measured in COOLOCE facility at the system pressure 1.1 bar (see [64], [70]), while in POMECO-HT facility a significantly lower value of DHF  $161.8 \text{ kW/m}^2$  was obtained [63] for the same material, though at a slightly lower system pressure 1.0 bar (see experimental point in Figure 49). The difference is of the order of  $100 \text{ kW/m}^2$ , or about 40% of the higher DHF value. The following possible reasons for this discrepancy can be named:

1. Difference in the system pressures (1.1 vs 1.0 bar). Judging from the experimental behavior of DHF as a function of system pressure, as well as simulations presented in Figure 49, this can be ruled out as the factor responsible for the difference in DHFs (e.g., two-fold increase in DHF can be reached only by increasing the system pressure from 1 to 5 bars).
2. Differences in debris bed properties. Experiments in both facilities were carried out with similar (although, technically, not the same) particles, Zirconium-silicate beads, which are analyzed in Section 4.7.1. The particles were purchased from the same manufacturer [4]. The size distributions analyzed by VTT and KTH teams turned out to be somewhat different, see Figure 75, with the average particles size estimated by VTT and KTH are 0.97 and 0.95 mm respectively, with the standard deviation 0.07 mm. The porosity estimated (although not measured directly) by VTT was 0.37 [1], whereas in the POMECO-HT facility the porosity obtained from the measured filled volume, density of material and the weight of the bed was found to be 0.371 [63]. The figures quoted imply that the properties of debris beds in both facilities were close enough and, per se, cannot be the main reason for the difference in measured DHFs.
3. Differences in geometry and heater arrangement. In COOLOCE facility, the debris bed was cylindrical (0.31 m in diameter, top surface area  $0.07548 \text{ m}^2$ , height 0.27 m, total volume 20 litres) and immersed in a water pool. In POMECO-HT facility, the debris bed was square in plan (0.2 m side, top surface area  $0.04 \text{ m}^2$ , height 0.25 m, total volume 10 litres), its side walls were thermally insulated. Therefore, the geometries seem to be comparable. However, the heaters in COOLOCE facility are 6.3 mm thicker and are

oriented vertically, with the top 40 mm of the bed being unheated. In POMECO-HT, on the contrary, the heaters are 3mm thick and horizontal. It is estimated that the heaters occupy 2.5% of debris bed volume in COOLOCE, and 0.7% in POMECO-HT. It can be argued that vertical heaters can effectively create local “channels” in the debris bed providing pathways for vapor evacuation from the bed, which can explain higher dryout heat fluxes observed in COOLOCE facility. Also, effects of anisotropy of debris bed properties due to the presence of heaters are not clear at the moment.

The simulations carried out by DECOSIM code with the porosity 37% and effective particle diameter 0.8 mm determined from POMECO-FL experiments gave the dryout heat flux at the atmospheric pressure close to that measured in POMECO-HT facility (see the bottom curve in Figure 49). This might imply that the experimental conditions in POMECO-HT were close to those assumed in simulations (homogeneous debris bed with uniform heating of the material over the volume).

The dependence of DHF on system pressure from COOLOCE experiments can be reproduced quite accurately if either the effective particle diameter or debris bed porosity is increased. For a cylindrical debris bed, good agreement is achieved in DECOSIM simulations for the particle diameter 0.89 mm and porosity 0.4, see Figure 49. The results obtained are consistent with MEWA simulation results reported in [70] where larger particle diameters and porosities were found to be necessary to reproduce the experimental data on DHF.

For the conical debris bed, DECOSIM simulations with the baseline parameters (particle diameters of 0.8 mm and porosity 37%) underestimate the dryout heat flux, see Figure 50. On the other hand, simulations with the particle diameter 0.89 mm and porosity 0.4 overestimate the dryout heat flux by about 8%.

It is interesting to note that, despite the difficulty in predicting the absolute values of dryout heat flux due to high sensitivity of results to the values of debris bed porosity and particle diameter, the relative improvement of debris bed coolability for conical debris bed in comparison with flat (or cylindrical, behaving effectively as a flat) debris bed is captured quite well in the simulations. As an example, consider the results of recent DECOSIM simulations [73] performed for prototypic reactor conditions, rather than for small-scale COOLOCE experiments. As the reference case, the following parameters were taken:  $d = 1.5$  mm,  $\varepsilon = 0.4$

pressure above the water level 1 bar, hydrostatic head of water at the cone tip 0.602 bar, mass of melt released is  $M = 256$  t. Calculations were carried out in a cylindrical pool of the diameter  $D_p = 12$  m, the density of corium was taken  $\rho = 8285.1$  kg/m<sup>3</sup>. The slope angle of the bed  $\theta$  was varied from zero to 45°, and depending on the slope angle, the debris bed was either conical (for large enough  $\theta$ ), or was comprised of a cone on a cylindrical base.

In Figure 51, the ratio of the dryout heat fluxes DHF for a conical debris bed, and the dryout heat flux for a flat debris bed with the same properties,  $DHF_0$ , is plotted. This ratio characterizes the relative improvement of coolability of non-flat debris bed due to side ingress of water into the bed. On the same graph, points are shown for the slope angle  $\theta = 47^\circ$  of four COOLOCE experiments corresponding to system pressures of 1.1, 1.6, 1.9, and 3.0 bar. In the latter case, the experimental value of dryout heat flux for the cylindrical bed was taken as  $DHF_0$ . One can see that the agreement is quite reasonable, which can be regarded as partial validation of DECOSIM code and, as well, as an indication that the relative increase in DHF due to shape effects are captured correctly.

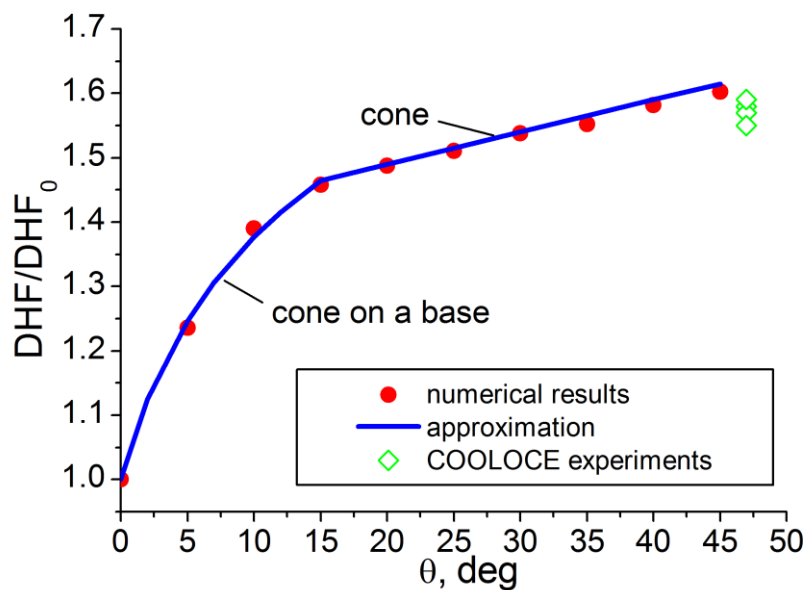


Figure 51: Dependence of ratio  $DHF/DHF_0$  on the slope angle.

### **3.7 Simulation of Post-dryout Debris Bed**

Once some zone in a debris bed dries out, the temperature of solid material starts to grow due to the continuing decay heat release. However, there are heat transfer mechanisms which provide cooling to the solid particles even in the absence of water evaporation. Among them is heat transfer to the gas phase, heat conduction in the particulate debris, radiative heat transfer (which can become effective at high enough temperatures of the solid material). These heat transfer mechanisms can provide stabilization of solid material temperature at some level above the water saturation temperature. Therefore, an important question concerning the post-dryout behavior of debris bed is whether the temperature in the dry zone can reach some critical levels at which remelting of debris and thermal attack on the basemat of reactor containment can occur.

Post-dryout behavior of debris beds was studied on the basis of numerical simulations by DECOSIM code; also, an analytical model for post-dryout debris bed heat transfer was developed [74]. Two debris bed geometries were studied in simulations by DECOSIM code: a mound-shaped debris bed and a conical bed, resting on the basemat of a water pool of 9 m in diameter. The computational domain was 6 m high, on its top boundary a constant system pressure  $P_{\text{sys}} = 3$  bar was maintained. The conical debris bed was of height  $H = 3$  m, the diameter of its base was 6 m. The mound-shaped debris bed was of the height 2.5 m, the diameter of its base was 6 m, and that of the top was 2 m. For each geometry, several cases were calculated, with the main variable parameters being the mean particle diameter  $D_p$  ranging from 1 to 3 mm, and the specific decay heat power  $W$  ranging from 150 to 250 W/kg. The simulation matrix is summarized in Table 13, with the case acronyms comprised of geometry (C is for conical, M is for mound-shaped debris bed), particle diameter  $d^*$  (in millimeters), and decay heat specific power  $W^*$  (in W/kg).

Numerical grids used in the simulations had 30 cells in the radial direction (uniform grid, 15 cm cells) and 51 cells in the vertical direction (non-uniform, with the minimum cell size of 7 cm near the top boundary of the debris bed). The computational domain and numerical grids are shown in Figure 52, with the debris bed shape shown by the white line.

Table 13: DECOSIM simulations of post-dryout debris beds.

Case	$D_p$ , mm	W, W/kg	$T_{s,max}$ , K	$T_{s,max}$ - $T_{sat}$ , K	$Z_{bot}/Z_{top}$ , m	$\xi$ , [-]
Conical, H = 3 m						
C-d1-W150	1	150	1334.0 <sup>a</sup>	947.0 <sup>a</sup>	0.3/2.8	0.89
C-d2-W150	2		559.8	173.4	1.8/2.8	0.36
C-d1-W200	1	200	1699.1 <sup>a</sup>	1311.7 <sup>a</sup>	0.05/2.8	0.89
C-d2-W200	2		781.5	395.0	1.37/2.8	0.51
C-d3-W200	3		512.5	126.1	2.1/2.8	0.25
Mound-shaped, H = 2.5 m						
M-d1-W150	1	150	1300.0 <sup>a</sup>	912.5 <sup>a</sup>	0.23/2.4	0.90
M-d2-W150	2		476.7	89.9	1.95/2.45	0.20
M-d1-W200	1	200	1646.5 <sup>a</sup>	1258.9 <sup>a</sup>	0.05/2.4	0.98
M-d2-W200	2		654.9	268.5	1.4/2.45	0.43
M-d3-W200	3		419.0	32.4	2.30/2.45	0.06
M-d1-W250	1	250	1978.7 <sup>a</sup>	1590.3 <sup>a</sup>	0/2.4	1
M-d2-W250	2		994.5	608.1	1.0/2.45	0.59
M-d3-W250	3		546.6	160.2	1.70/2.45	0.31

<sup>a</sup> Temperature stabilization did not occur, values at time 4000 s are given

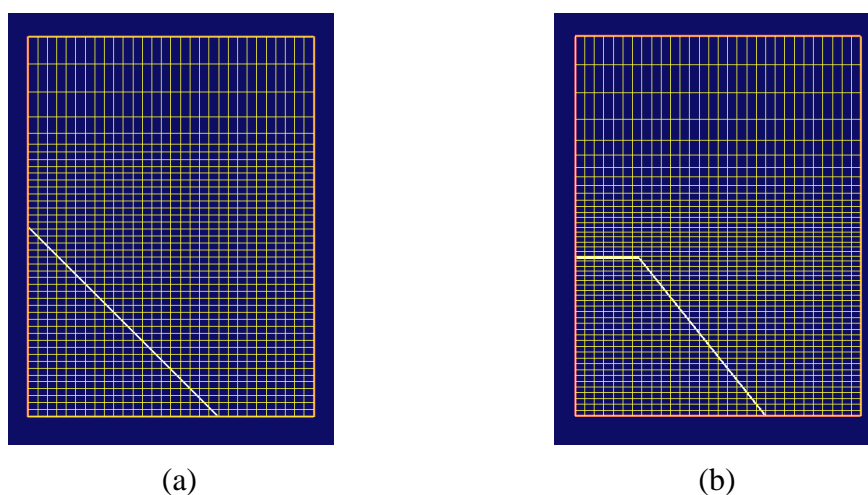


Figure 52: Computational domain and numerical grid used for simulations of conical (a) and mound-shaped (b) debris bed.

Simulations started from the initial conditions of quenched debris bed, the initial temperatures of the solid material and water in the pool were set to the local saturation temperature, and the initial void fraction was set to zero. Calculations were carried out for the period of 5000 s which was sufficient for the establishment of steady-state temperature in the dryout zone in most of the cases where stabilization was observed.

In Figure 53, the time histories of the maximum temperature of the solid material are shown for the cases presented in Table 13, the cases where temperature stabilization occurred are shown in bold. It can be seen that the time of dryout occurrence (visible as the time at which the temperature curve deviates from the initial saturation temperature) is of the order of few minutes and is determined by the decay heat. In all the cases with particle diameters of 3 mm, temperature stabilization occurred, while for the smallest particles (1 mm) steady temperature rise is observed at a rate proportional to specific power  $W$ .

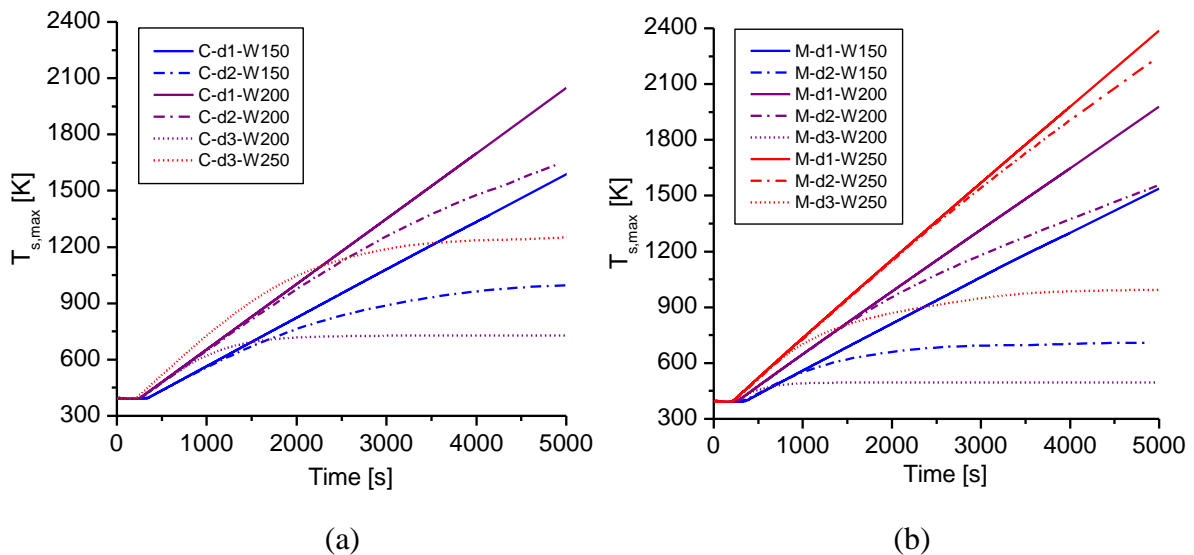


Figure 53: Time histories of the maximum temperature of solid particles in conical (a) and mound-shaped (b) debris bed

Typical spatial distributions of the void fraction and temperature of the solid material in post-dryout conical and mound-shaped debris beds are shown in Figure 54 and Figure 55, respectively. In Figure 56, the vertical distributions of void fraction (left) and vapor temperature (right) on the axis of symmetry are shown for all the cases from Table 13 in which stabilization of the dry zone was obtained. One can see that the temperature distribution in the dry zone is nearly linear, the fact which will be used in the following section to derive an analytical model for the dry zone.

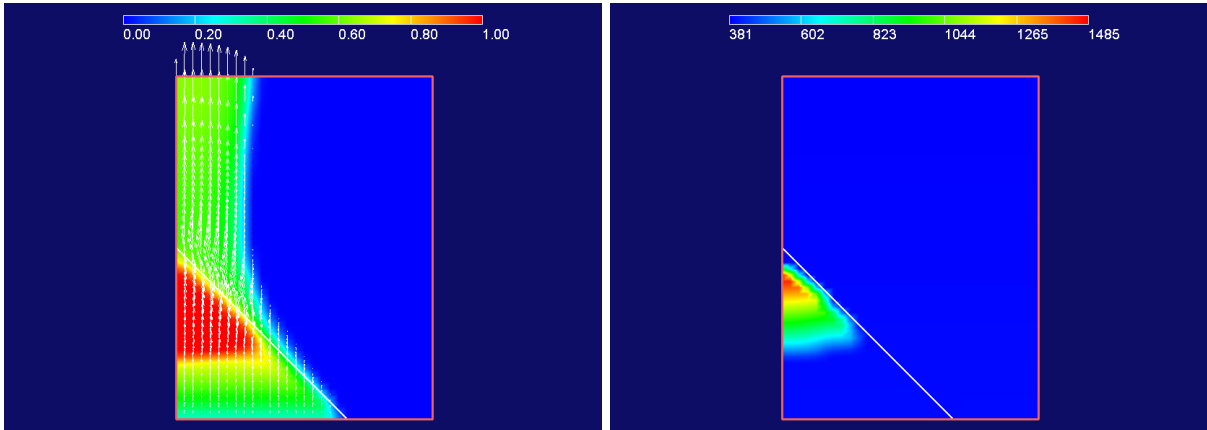


Figure 54: Void fraction (left) and solid particle temperature (right) in the post-dryout cone-shaped debris bed ( $W = 200 \text{ W/kg}$ ,  $D_p = 2 \text{ mm}$ ) at time 4000 s

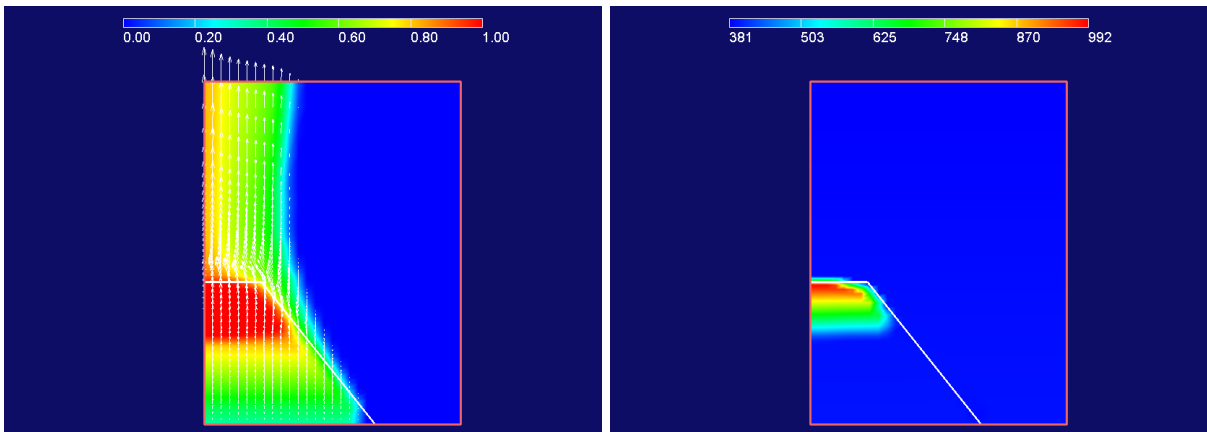


Figure 55: Void fraction (left) and solid particle temperature (right) in the post-dryout mound-shaped debris bed ( $W = 250 \text{ W/kg}$ ,  $D_p = 3 \text{ mm}$ ) at time 4000 s

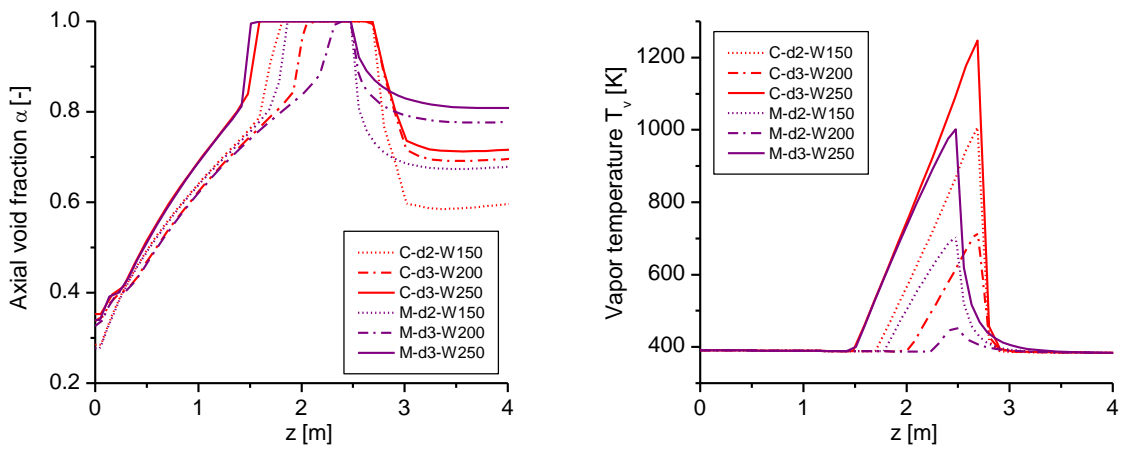


Figure 56: Void fraction (left) and vapor temperature (right) distributions along the axis of symmetry for the cases where temperature stabilization was obtained (see Table 13)

The vertical distributions of void fractions on the axis of symmetry presented in Figure 56, were used to determine the vertical coordinates of the top and bottom boundaries of the dry zone ( $Z_{top}$  and  $Z_{bot}$ , respectively), as well as the fraction of debris bed height occupied by the dry zone  $\xi = (Z_{top} - Z_{bot})/H$ .

The numerical results obtained by DECOSIM indicate that in the cases where dryout occurs in the debris bed

- Dryout zone is located in the top part of the debris bed;
- Vapor flows through the dry zone vertically upwards;
- Temperatures of solid particles and vapor increase in the vertical direction almost linearly, the difference between them being few degrees;
- Maximum temperatures of solid particles and vapor are attained in the top part of the dry zone;
- Vapor cooling is capable of stabilization of solid material temperature, provided that its flowrate through the dry zone is sufficient.

These observations imply that the dry zone has relatively simple structure which can be described by an analytical model.

In the model, one-dimensional mass and energy conservation equations were formulated for the single-phase vapor flow in the dry zone, with the mass flux determined by the total evaporation rate in the wet zone underneath the dry one. Steady-state solution was considered, and the maximum temperature reached at the top boundary of the debris bed was found. The analytical model allows one to obtain a formulas relating the critical fraction of debris bed taken by the dry zone  $\xi_*$  to the critical maximum temperature  $T_*$  (for example, the temperature at which oxidation starts, or melting temperature of the material):

$$T_* = T_{sat} + \frac{\Lambda}{C_p} \frac{\xi_*}{1 - \xi_*} \quad \text{or} \quad \xi_* = \frac{C_p (T_* - T_{sat})}{\Lambda + C_p (T_* - T_{sat})}$$

The function  $T_*(\xi_*)$  is plotted in Fig. 6 by the solid line, the saturation temperature taken equal  $T_{sat} = 390$  K. The dashed lines correspond to two characteristic values of the critical temperature. It follows from Figure 57 that the material in the dry zone can be reheated to the

temperature of 1500 K at which zirconium oxidation begins if the dry zone takes at least half the height of the debris bed. Corium remelting temperature 2800 K can be reached if the dry zone takes at least 70% of the debris bed height. This last case corresponds to massive dryout of the debris bed. Temperature escalation in smaller dry zones will be stabilized due to large flowrate of vapor generated under the dry material which is sufficient to remove the decay heat from the porous material.

The points in Figure 57 correspond to the results of numerical simulations carried out by DECOSIM for conical and mound-shaped debris beds (see Table 13). Evidently, the analytical formula predicts quite well the maximum temperature rise in the debris bed. Importantly, the results in Figure 57 are practically independent of debris bed shape and involve only few parameters, which reduce the uncertainties in the estimation of post-dryout behavior of debris beds. In the further work, relationship between the relative size of the dry zone and debris bed properties has to be obtained in order to apply the theory presented in the current work in the context of surrogate model for debris bed coolability and analysis of severe accidents risks.

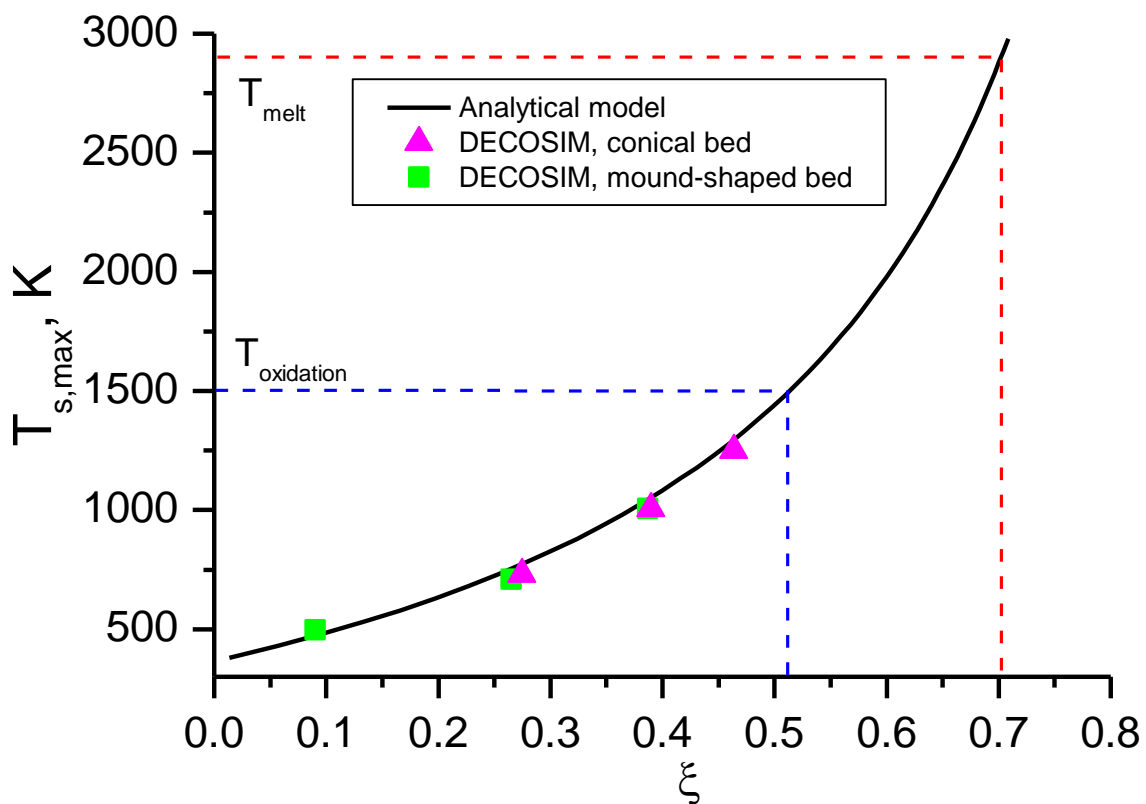


Figure 57: Dependence of the critical temperature on the relative size of dry zone

### **3.8 Implementation of Particle Spreading Model**

In PDS-C experiments (see Section 4.5), a correlation for the particle flux as a function of local slope angle, gas flowrate, and debris bed properties was obtained in the non-dimensional form. These correlations were implemented in DECOSIM in order to enable simulations of debris beds with evolving (due to particle spreading) geometry.

A subroutine for dynamic redistribution of particles was implemented in DECOSIM. On each time step, particle fluxes are evaluated at the boundaries between the top surface of debris bed, and particulate matter is redistributed accordingly along the debris bed top, ensuring proper emptying/filling of top cells and packing to provide the given debris bed porosity

Implementation of particle spreading algorithm in DECOSIM was verified against the 1D numerical model which solves the equation for debris bed height which is, essentially, a debris mass conservation equation. In these verification studies, to provide compatible spreading conditions, two-phase flow simulations were switched off in DECOSIM, and the superficial vapor velocity at the debris bed top was obtained from the (constant) volumetric evaporation rate and current debris bed height:  $U_g = \Gamma h / \rho_v$ , where  $\Gamma$  is the volumetric evaporation rate,  $h$  is the local height,  $\rho_v$  is the vapor density. Good agreement between the maximum debris bed heights as functions of time calculated by DECOSIM and that from 1D model was demonstrated, as well as the shapes of debris bed at selected times were found to practically coincide. In Figure 58, the results of DECOSIM simulations of debris bed spreading are presented, demonstrating the change in debris bed shape with time.

Few preliminary fully coupled DECOSIM simulations of debris bed were performed in which the superficial gas velocity and gas parameters involved in the correlation for the lateral particle flux were obtained from the two-phase flow model. Simulations were carried out with and without particle spreading taken into account, with the following parameters:

- Conical debris bed, slope angle 30°
- Total mass of corium 143 t.
- Relocation time 1.5 h (used for specific decay heat power calculation).
- Porosity 40%.
- Particle diameter of 1, 1.5, and 2.0 mm.

Maximum temperatures of solid material were compared in the cases with and without particle spreading, see Figure 59.

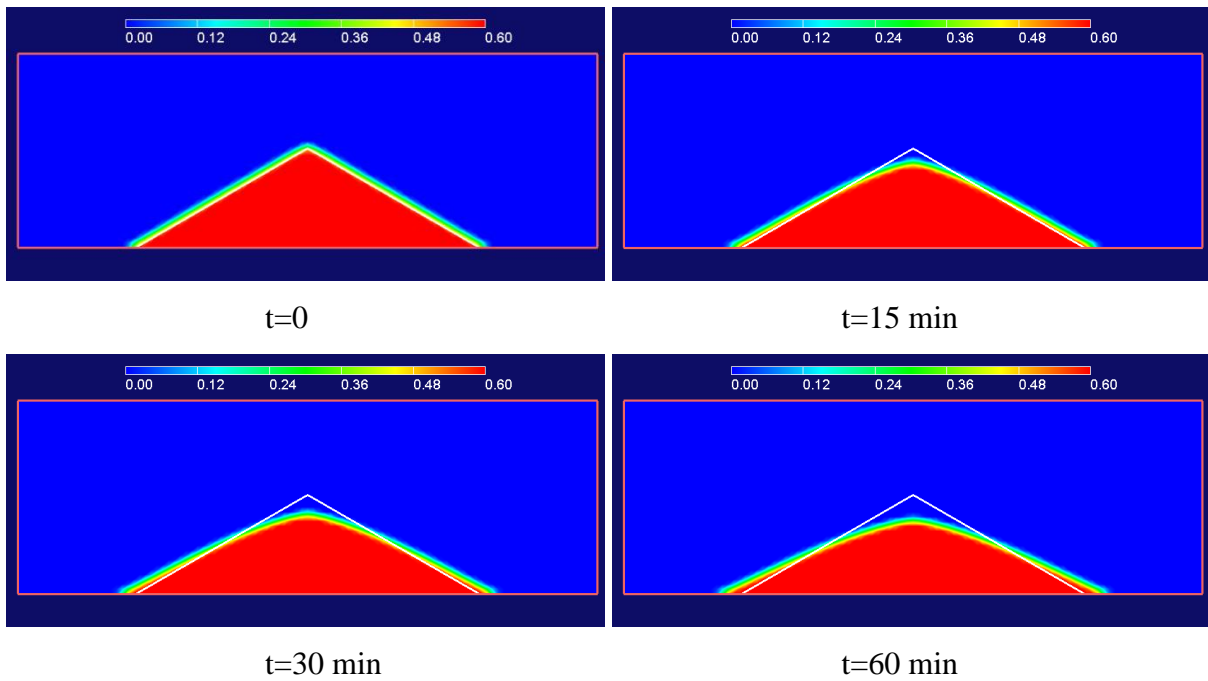


Figure 58: Self-levelling of debris bed (volume fraction of particles,  $d=1$  mm,  $W=160$  W/kg)

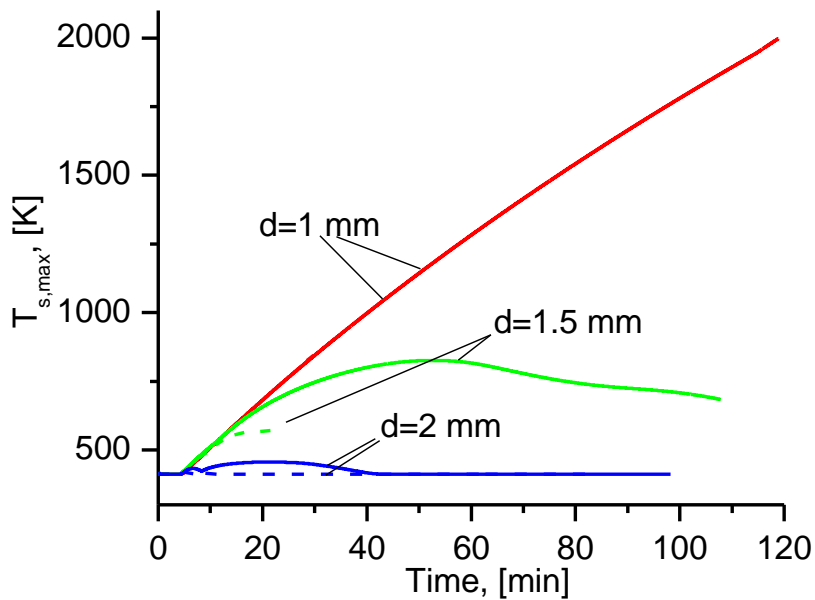


Figure 59: Maximum temperatures of solid particles. Solid lines: no spreading, dashed lines: spreading

The following conclusions can be drawn:

- For 1 mm particles, debris bed is non-coolable, temperature escalation is observed with or without particle spreading.
- For 1.5 mm particles temperature stabilization is observed, for spreading debris bed (dashed lines) the maximum temperature is stabilized at a lower level.
- For 2 mm particles, debris bed is coolable, regardless of particle spreading.

Further studies are necessary in order to quantify the effect of the dry zone on debris bed spreading and coolability.

## 4 Investigation of particulate debris spreading

### 4.1 Particulate Debris Spreading: Experiments and Scaling Approach

#### 4.1.1 Introduction

A pool of water under reactor vessel is employed in several designs of light water reactors (LWR) to provide long term cooling of core melt materials released from reactor pressure vessel (RPV) in the case of a severe accident (SA). It is assumed that corium will be fragmented and quenched in the pool, forming porous debris bed. It is assumed further that decay heat can be removed from the debris bed by natural circulation. However, coolability of such bed is contingent upon its properties such as particle size distribution, porosity and geometrical configuration. A tall, mound shape debris bed can be hardly coolable, while the same debris can be easily cooled if the bed is spread uniformly over the area of the reactor cavity [74].

Boiling and two-phase flow inside the bed is a source of mechanical energy which can move the particles flattening the debris bed. This process is called “self-leveling” phenomenon [82],[83],[84],[85],[86], see Figure 60. However, to be effective in providing a coolable geometrical configuration, the characteristic self-leveling time scale has to be smaller than the time scale for drying out and onset of re-melting of the bed.

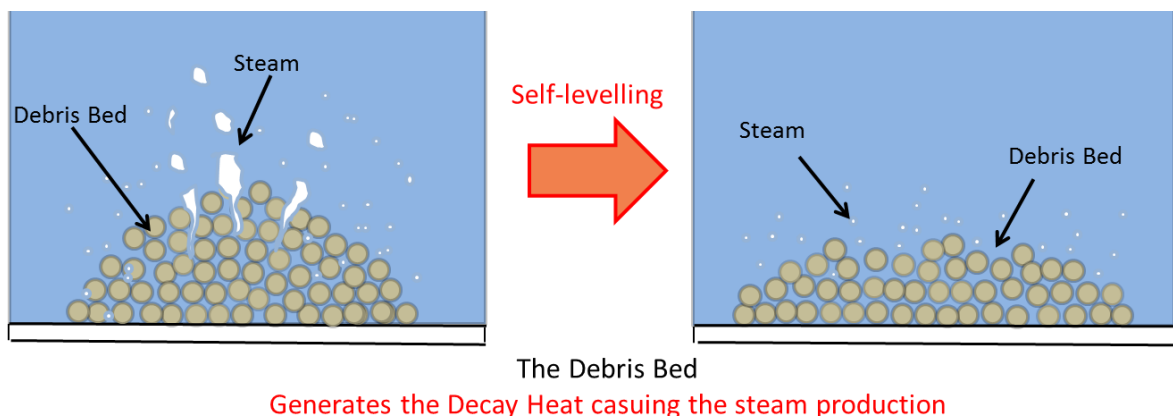


Figure 60: Illustration of self-leveling process

Particulate debris self-leveling is also an important factor for debris coolability in postulated core-disruptive accident in a sodium-cooled fast reactors [82],[83],[84],[85],[86],[87],[88],[89]. Phenomena of particulate debris spreading were studied mostly experimentally in the past [83],[84],[85],[86]. Depressurized water boiling technique was used by Zhang et al.[83] to study the influence of such parameters as particle size, density, etc. However, the effective steam generation rate in the tests was almost two orders of magnitude smaller than in prototypic accident conditions and most of the tests were carried out with low density particles. Only two tests were carried out with 0.5 mm spheres of stainless steel and lead. Cheng et al.[85] carried out a series of experiments with nitrogen percolation in order to achieve more prototypical gas superficial velocities. Cheng et al.[84] proposed an empirical correlation for the ratio of the instantaneous slope angle of a conical heap to the initial angle. However, it is not clear how such empirical correlation for evolution of a conical heap shape can be extrapolated and applied to prototypical accident conditions.

In our previous study [90], [35] we used different PDS (Particulate Debris Spreading) facilities with gas injection provided at the bottom of the debris bed in order to study spreading phenomena at prototypic gas velocities. Two most important observations from the PDS tests [90], [35] are:

1. Local slope angle of the debris bed depends on local gas velocity. For instance, Figure 61 shows debris bed shape after gas injection was provided in the central section (indicated by two vertical dashed lines). Remarkably, the slope angle changed only in this middle section, while initial slope angle remained in the other parts of the bed.
2. The bulk volume of the debris bed is immovable. The particles are moving only in the topmost layer of the bed. The moving layer thickness is order of few particle diameters.

Such behavior was insensitive to the facility scale, mass of the debris, and gas flux up to the point where whole bed becomes fluidized and put into motion.

Local nature of gas-coolant-particle interactions and the fact only thin top layer of particles is responsible for spreading suggests that experiments in reduced size laboratory facilities (such as PDS) can capture key physical phenomena. The data produced in such tests are in-principle scalable to the prototypic accident conditions if the particle properties (such as size distribution, morphology, density etc.) are similar to those of corium debris and gas velocity is properly scaled.

Experimental closures for the particle mass flow rate per unit width of the bed (referred as “particulate flow rate” for the sake of brevity) as a function of local slope angle and gas velocity have been obtained [90] at different test conditions and particle types. Using such closures an approach to predicting spreading dynamics of a debris bed with arbitrary initial shape was proposed [90]. However, when dimensional variables are used a separate set of experiments is necessary in order to build a closure for each type of particles (morphology, size distribution, material).

Therefore, the goal of this paper is to develop scaling approach to express closures in non-dimensional form, which would be universal for different sorts of particle and gas flow conditions.

In the second section of the paper we describe the experimental set-up, results on particulate debris spreading tests, and general form of the closure. Finally, in third section of the paper we introduce dimensionless variables and propose a universal form for the correlation describing the particulate flow rate.

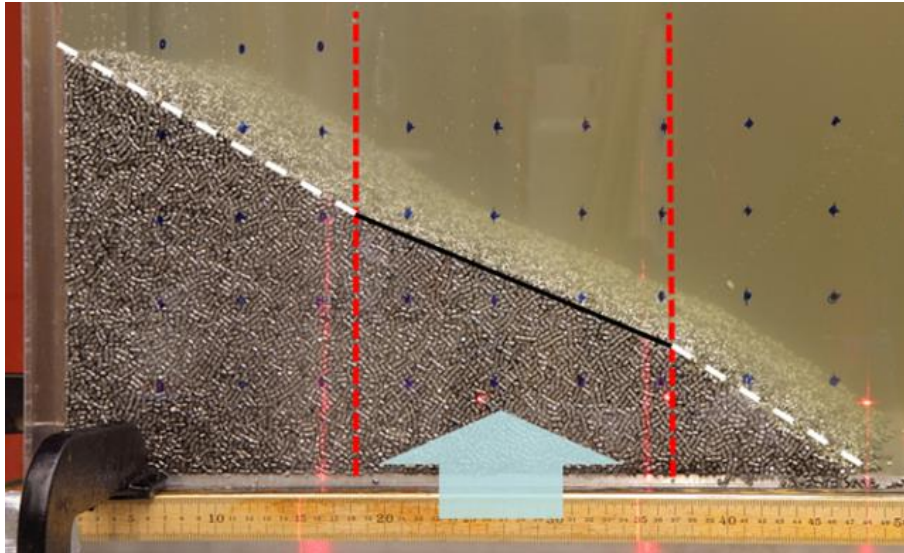


Figure 61. The slope angle of the heap is changed only in the section where gas flow rate was provided (between the two vertical dashed lines).

## 4.2 Experimental Approach

### 4.2.1 PDS-C Experimental setup

Particulate Debris Spreading Closures (PDS-C) experimental set-up is designed to simulate phenomena of particulate debris spreading under water caused by upward two phase (water and gas) flow. The PDS is composed of a vertical rectangular tank made of acrylic glass with internal dimensions 405x72x915 mm (length L, gap width W, height H), gas injection chamber 405x72 mm connected to the compressed air supply system. The video camera is used to record evolution of the heap shape in each experiment.

The gas injection chamber is positioned at the bottom of the tank under the particulate bed. Compressed air at pressure up to 2 bar is supplied through the chamber. The top of the plate is perforated with 287 (7x41) orifices 1.5 mm in diameter and 10 mm pitch. The plate can provide uniform and constant in time air injection with up to 70 L/s total flow rate, which corresponds to gas velocity of 2.4 m/s. The gas flow rate is controlled by the valve and measured by an in-line flow meter Omega FL-505.

Volume of particles used in each test is about 8.5 liters. Two types of particles material were used in this test series: stainless steel 3x3 mm cylinders and 6 mm spheres. The properties of the particles are summarized in Table 14.

The experimental procedure for a typical PDS-C test consists of the following steps:

1. Particles are loaded into the facility test.
2. The test section is filled with water up to the level of 550 mm from the bottom plate.
3. The particles are shaped as a heap with critical angle of repose at the beginning of each test.
4. A special procedure is employed in order to provide better control of the test parameters and to avoid non-prototypic “water piston” effect (also noticed by Cheng et al.<sup>[85]</sup>). The effect is observed at the very beginning of gas injection when liquid (which initially fills the bed and the gas chamber) is pushed suddenly upwards (as a “piston”) by the gas causing instantaneous fluidization of the bed. Therefore, in the PDS tests the debris bed is held in its initial shape using a stiff stainless steel net before activation of gas injection.

- Gas injection is started and gradually adjusted to reach the desired flow rate. Then the net is quickly removed in upward direction allowing particles to start spreading process.

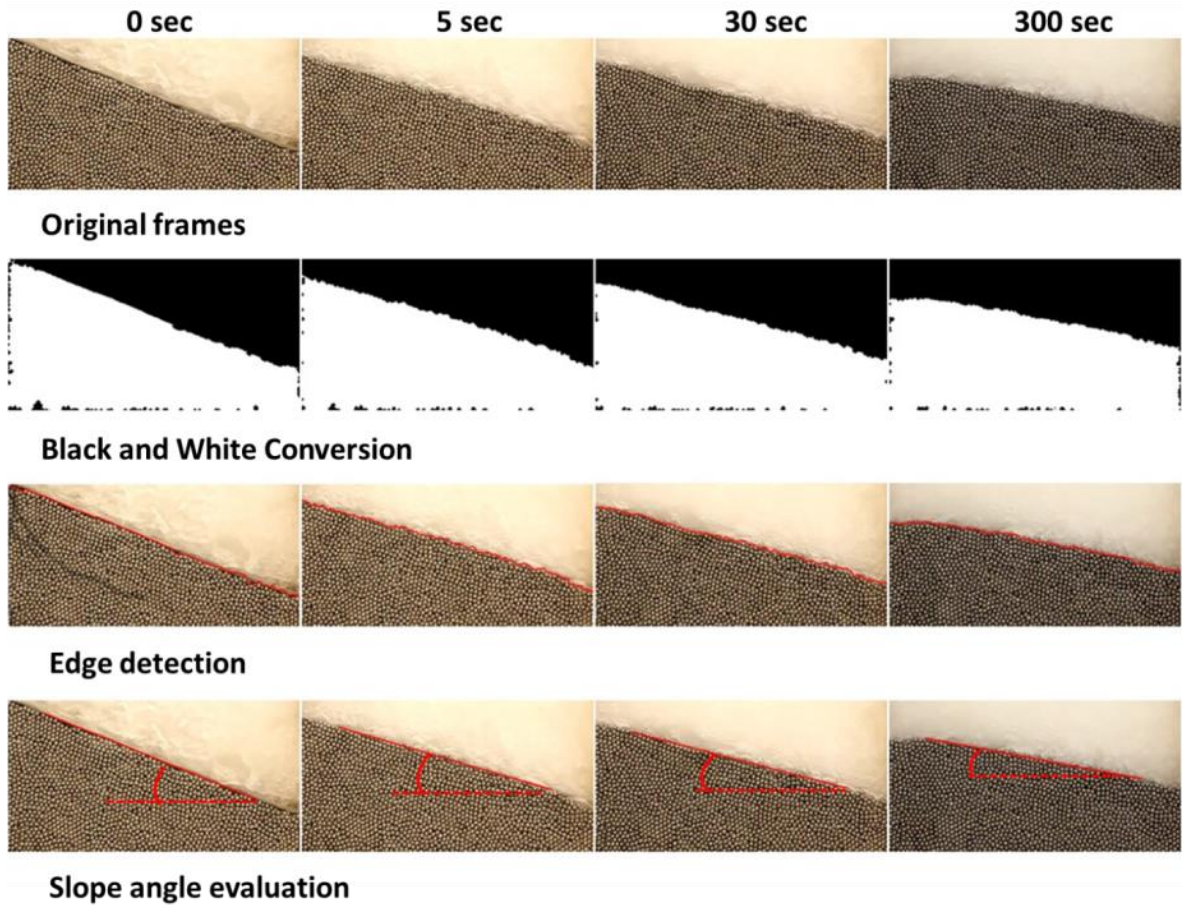


Figure 62: Examples showing post-processing technique applied to the video recorded during experiment PDS-C8.

Table 14: Particles properties

Particle	$d_p$ [mm]	$\rho_p$ [kg/m <sup>3</sup> ]	$\theta_{rep}(U_g = 0)$ [degree]	$\varepsilon$	$U_{mf}$ m/s
Stainless steel cylinders	3.4	7800	33	0.35	2.61
Stainless steel spheres	6	7800	22	0.38	3.55

The runtime of experiments was up to 5 minutes. The entire test is recorded by a video camera and subsequently individual frames are extracted and analyzed using standard Matlab© image processing technics. First, noise reduction is applied and frames are converted to black-white picture. Heap shape is found through Sobel edge detection function. Linear interpolation of the

edge coordinates is used to obtain the heap slope angle for each analyzed frame (see examples in Figure 62).

### Superficial Gas Velocities in PDS-C Facility

In order to provide comprehensive assessments of efficacy of the particulate debris spreading, as one of the SA mitigation strategy, we have to reach air superficial velocities comparable with prototypic steam velocities. Here we perform rough estimation of the steam superficial velocities which can be achievable with steam simulant (air) in PDS-C facility. Another words, we would like to answer the question: what part of the debris bed we can simulate in the PDS-C facility in terms of superficial velocities?

Velocity of the steam flowing out at the debris bed top is a crucial parameter for the debris bed spreading. Consider a steam generating (at atmospheric pressure) corium debris bed with properties chosen within the typical ranges considered in [8], [7].

Table 15: Steam generating debris bed properties.

Debris volume	Initial bed length, $L$	Initial bed height, $h$	Porosit $y, \varepsilon$	Slope angle, $\theta$	Specific heat release, $W$	Particle density, $\rho_p$	Steam density, $\rho_s$	Latent heat of evaporation, $H_e$
20 m <sup>3</sup>	4 m	2.8	0.5	35°	240 W/kg	8000 kg/m <sup>3</sup>	0.59 kg/m <sup>3</sup>	2.258 MJ/kg

Assuming uniform heat generation in the debris bed, the heat flux to be removed from the bed with local height  $h$  is:

$$Q_{HF}(h) = \rho_p \cdot (1 - \varepsilon) \cdot W \cdot h \quad (4.1)$$

Then the steam superficial velocity  $v_{steam}$  as function of the bed height  $h$  can be estimated as:

$$v_{steam}(h) = \frac{Q_{HF}(h)}{\rho_s \cdot H_e} \quad (4.2)$$

Here we assume saturated water and only vertical steam velocity.

In the experiment we use air as steam simulant. In order to achieve similar conditions for particulate spreading we normalize the superficial velocity  $v_{gas}$  to the corresponding minimum fluidization velocity of the debris bed  $u_{mf}^{gas}$ . The  $u_{mf}^{gas}$  is independent of the geometry and dimensions of the bed. We estimate the  $u_{mf}^{air}$  and  $u_{mf}^{steam}$  at atmospheric pressure conditions assuming identical properties of the coolant and debris bed particles. The  $u_{mf}$  can be calculated as:

$$u_{mf} = \frac{\mu_g \cdot Re_{mf}}{\rho_g \cdot d_p}, \quad (4.3)$$

where  $\mu_g$  is the dynamic viscosity of the flowing gas and the Reynolds number  $Re_{mf}$  for the three-phase fluidization [9]:

$$Re_{mf} = \sqrt{33.7^2 + 0.0406 \cdot Ar_{lg}} - 33.7, \quad (4.4)$$

where the gas-phase Archimedes number with liquid-buoyed solids is

$$Ar_{lg} = \rho_g \cdot (\rho_p - \rho_c) \cdot g \cdot d_p^3 / \mu_g^2. \quad (4.5)$$

Due to higher gas density, the bed fluidization by air requires lower injection velocities than for the steam. Results of calculations of minimum fluidization velocity are presented in Table 16 for spherical particles with diameters of  $d_p = 3.43$  mm (corresponds to 3x3 mm stainless steel (SS) cylinders used in PDS tests), particle material and coolant densities  $\rho_p = 8000$  kg/m<sup>3</sup>,  $\rho_c = 1000$  kg/m<sup>3</sup> respectively. Eq. (4.3) suggests that in our laboratory conditions we can fluidize the debris bed by air flow at 2.6 m/s.

Table 16: Minimum bed fluidization velocities by air and steam for the stainless steel 3x3 mm in size cylindrical particles.

Gas	$\rho_g$ (kg/m <sup>3</sup> )	$\mu_g$ (Pa·s)	$u_{mf}$ (m/s)
Water steam	0.590	$1.2 \cdot 10^{-5}$	3.78
Air	1.225	$1.85 \cdot 10^{-5}$	2.61

Normalizing steam velocity  $v_{steam}(h)$  with respect to minimum fluidization steam velocity we get:

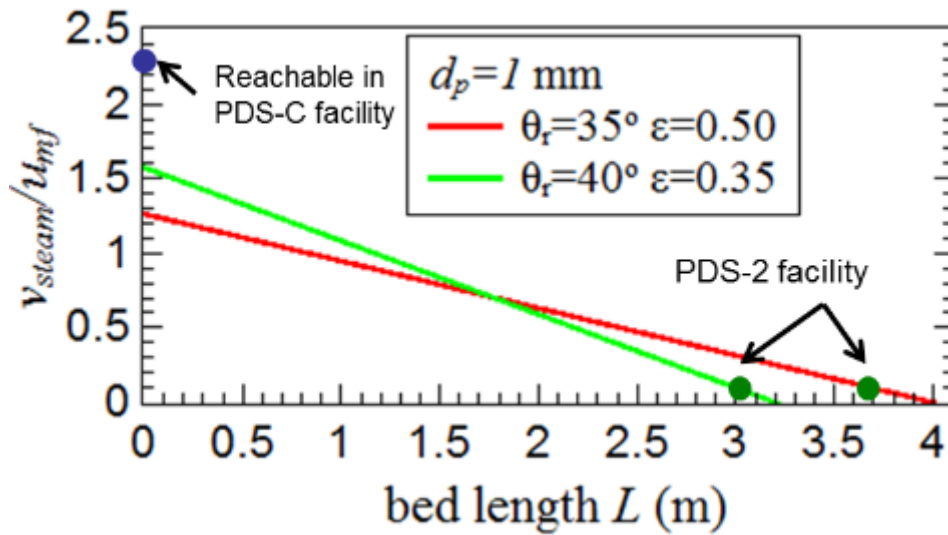
$$\frac{v_{steam}(h)}{u_{mf}^{steam}} = \frac{\rho_p \cdot (1-\varepsilon) \cdot W \cdot d_p}{H_e \cdot \mu_g \cdot Re_{mf}} \cdot h \equiv \frac{\rho_p \cdot (1-\varepsilon) \cdot W \cdot d_p \cdot \tan \theta}{H_e \cdot \mu_g \cdot Re_{mf}} \cdot L. \quad (4.6)$$

The superficial velocity of the injected air in our PDS laboratory tests can be scaled down from the superficial velocity of generated steam in SA conditions according to the following (see Table 16):

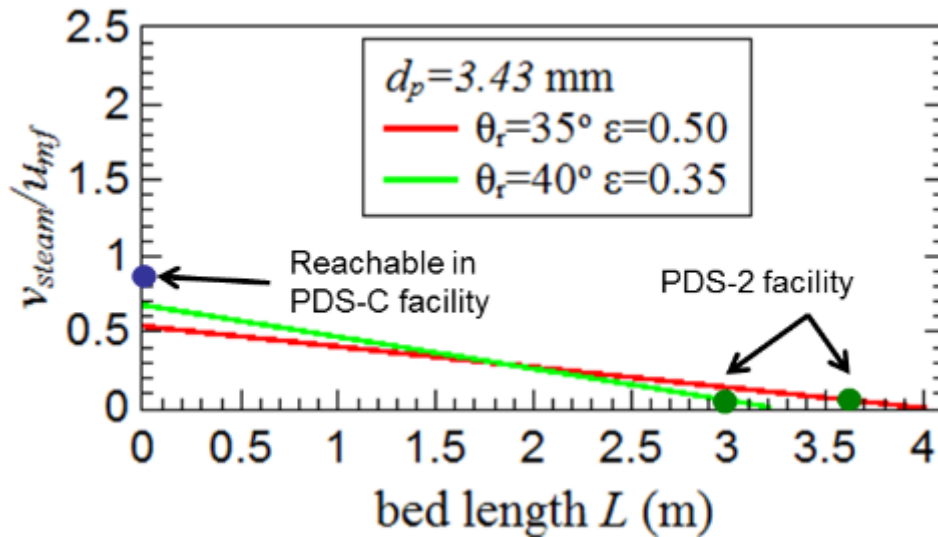
$$v_{air} = \frac{u_{mf}^{air}}{u_{mf}^{steam}} \cdot v_{steam} \cong 0.69 \cdot v_{steam}. \quad (4.7)$$

Normalized superficial steam velocity as a function of bed's length and height is plotted in Figure 63 for different particle size and bed porosities. As it can be seen in Figure 63a, with small 1 mm particles the bed is fluidized at the top, while for larger particles and the same gas velocity fluidization limit is not reached (Figure 63b).

The green and blue points in Figure 63 represent the normalized gas velocities achievable in PDS-2 and PDS-C facilities respectively. PDS-2 facility can be used to simulate particulate debris spreading with prototypic steam flow rate in the vicinity of the debris bed leading edge. PDS-C facility can provide high gas flow rate typical for a top part of a tall debris bed go up to fluidization limit.



a)



b)

Figure 63: Normalized superficial velocity of the steam as function of debris bed length with particles of different sizes: a) for 1 mm particles; b) for 3.43 mm particles. The green and blue points show air velocities reachable in PDS-2 and PDS-C facilities respectively.

### 4.2.2 Estimation of particulate flow rate

The heap slope angles, obtained from the recorded video data, are used to calculate the particle mass flow ( $Q_p$ ) at given local angle of the heap slope ( $\phi$ ) and normalized gas injection velocity ( $Q_g$ ) by using following expression as suggested in Doppler et al.[91]:

$$Q_p = -\rho_p \cdot (1 - \varepsilon) \cdot \frac{L^2}{8} \cdot \frac{d(\tan \phi)}{dt} \quad (4.8)$$

where  $\rho_p$  is the particle density,  $\varepsilon$  is the porosity and  $L$  the heap length.

The gas injection normalized velocity ( $Q_g$ ) is defined by the ratio between the gas superficial velocity ( $U_g$ ) and minimum fluidization velocity ( $U_{mf}$ ).

When superficial air velocity reaches  $U_{mf}$  the force exerted on the bed by the flowing fluid is equal to the weight of the entire bed. Minimum 3-phase fluidization velocity can be calculated according to Eq. (4.9), where  $Re_{gmf}$  is the gas Reynolds obtained according to the empirical correlation proposed by Zhang et al.[92] (Eq. (4.10)).

$$U_{mf} = \frac{\mu_g \cdot Re_{gmf}}{\rho_g \cdot d_p} \quad (4.9)$$

$$Re_{gmf} = \sqrt{33.7^2 + 0.0408 \cdot Ar_{lg}} - 33.7 \quad (4.10)$$

where  $Ar_{lg}$  is the gas phase Archimedes number with liquid-buoyed solids (Eq. (4.11));  $\mu_g$  and  $\rho_g$  are air dynamic viscosity and density respectively;  $d_p$  is equivolume sphere diameter and  $\rho_l$  is the liquid density.

$$Ar_{lg} = \rho_g \cdot (\rho_p - \rho_l) \cdot g \cdot d_p^3 / \mu_g^2 \quad (4.11)$$

### 4.2.3 Test conditions and results

The experimental matrix with test conditions and calculated  $Q_g$  is provided in Table 17. Particulate flow rate as function of the slope angle was calculated using Eq. (4.8) for each experiment performed at fixed gas flow rate. An example of such dependency is shown in Figure 64. Experimental observations suggest that spreading is much faster (especially at high air superficial velocity) at the initial stage of the test, when slope angle is large, and then it slows down. Similar observations also have been made by Cheng et al.[86].

Table 17 Experimental matrix

Experiment	Particle	Air Flow rate [L/s]	$U_g$ [m/s]	$Q_g$ [-]
PDS-E21 <sup>[90]</sup>	SS cylinders 3x3 mm	22	0.11	0.05
PDS-C1		10	0.34	0.13
PDS-C2		20	0.69	0.26
PDS-C3		30	1.03	0.39
PDS-C4		40	1.37	0.53
PDS-C5		50	1.72	0.66
PDS-C6	SS spheres 6mm	5	0.17	0.05
PDS-C7		10	0.34	0.10
PDS-C8		15	0.52	0.15
PDS-C9		20	0.69	0.20
PDS-C10		30	1.03	0.29
PDS-C11		35	1.20	0.34
PDS-C12		45	1.54	0.44
PDS-C13		50	1.72	0.49

A set of tests with the same particles and different gas flow rates are carried out in order to determine particulate flow rate  $Q_p = Q_p(Q_g, \phi)$ . It is instructive to note that (Figure 64) the particulate flow rate is (i) near-zero at low values of  $\phi$ , and (ii) rapidly increasing function at higher values of  $\phi$ .

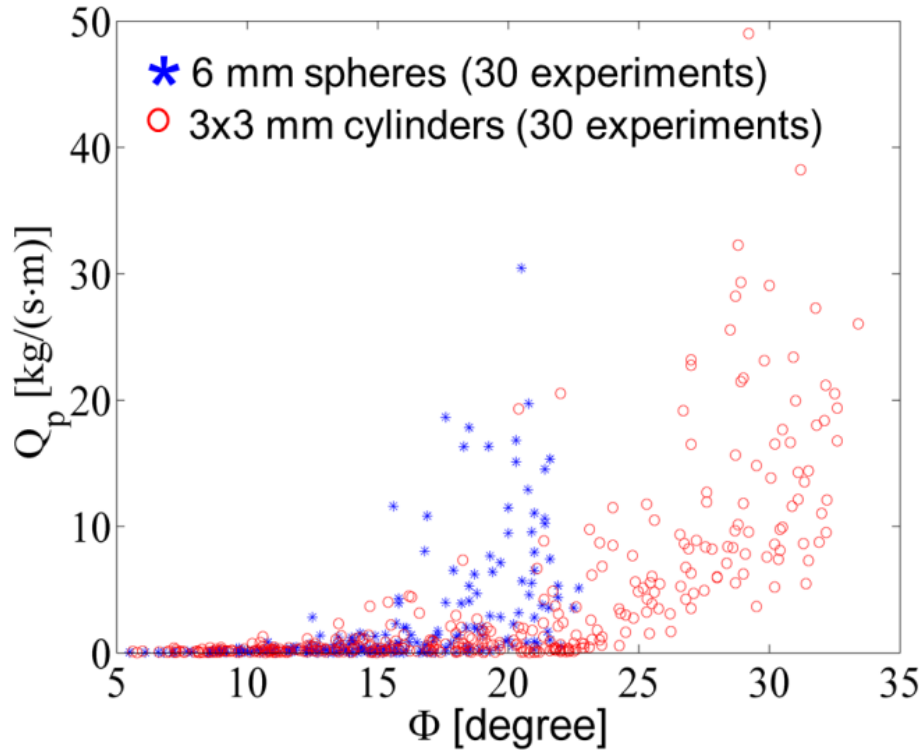


Figure 64: Particulate flow rate per unit width as function of heap slope angle obtained from different PDS experiments with stainless steel spheres and cylinders.

These observations lead us to suggestion of specific form of analytical fit to the experimental data. Analytical fit functions for SS 3x3 mm cylindrical particles and for SS 6 mm spheres are provided by Eq. (4.12) and Eq. (4.13) respectively.

$$Q_p(Q_g, \phi) = 2.6e^{-7} \cdot Q_g \cdot \tan \phi + 278.9 \cdot Q_g [\tan \phi - \tan(-14.5 \cdot Q_g + 15.0)]^2, \quad (4.12)$$

$$Q_p(Q_g, \phi) = 1.9e^{-8} \cdot Q_g \cdot \tan \phi + 251.4 \cdot Q_g [\tan \phi - \tan(-8.8 \cdot Q_g + 6.8)]^2, \quad (4.13)$$

As an example the fit function and experimental data for SS 3x3 mm cylinders are plotted in Figure 65.

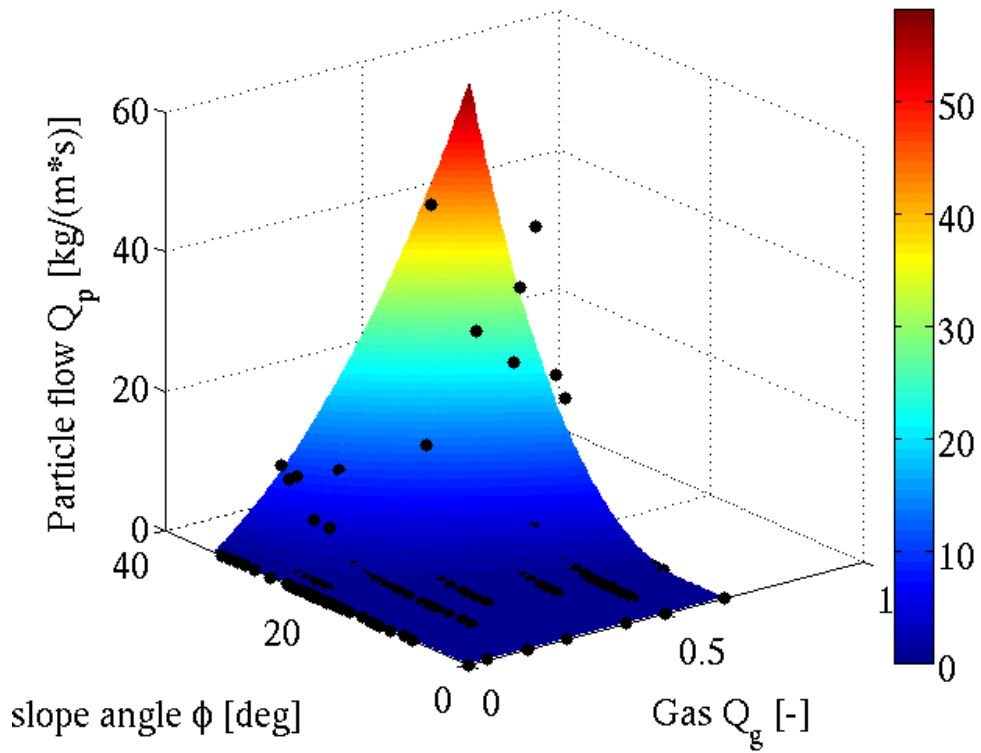


Figure 65: Example of the analytical fit applied to experimental closures for SS 3x3 mm cylindrical particles: experimental points (black dots) and fit surface (colormap).

### 4.3 Scaling Approach

The self-leveling phenomenon is a particular case of a more general problem of three phase gas–liquid–particle flow. In this work, our aim is to develop a simple scaling approach to predicting particle spreading rate and to use PDS-C empirical data to calibrate and validate it.

There are four main forces acting on the particles and determining spreading dynamics of the bed: (i) buoyancy ( $F_B$ ), (ii) aerodynamic drag ( $F_D$ ), (iii) gravity ( $F_G$ ), and (iv) inter-particle friction ( $F_{Fr}$ ). Given that average particle spreading velocity is relatively slow we neglect by inertia forces. We also do not consider capillary and cohesion forces, which can become important for small particles. In Figure 66 main forces acting on a particle are shown schematically.

The presence of the two-phase coolant flow increases drag, which effectively reduces gravity force and thus reduces the friction force. When the coolant velocity is below the minimum fluidization velocity the observable effect is a reduction of the repose angle as shown by Eames et al.[94].

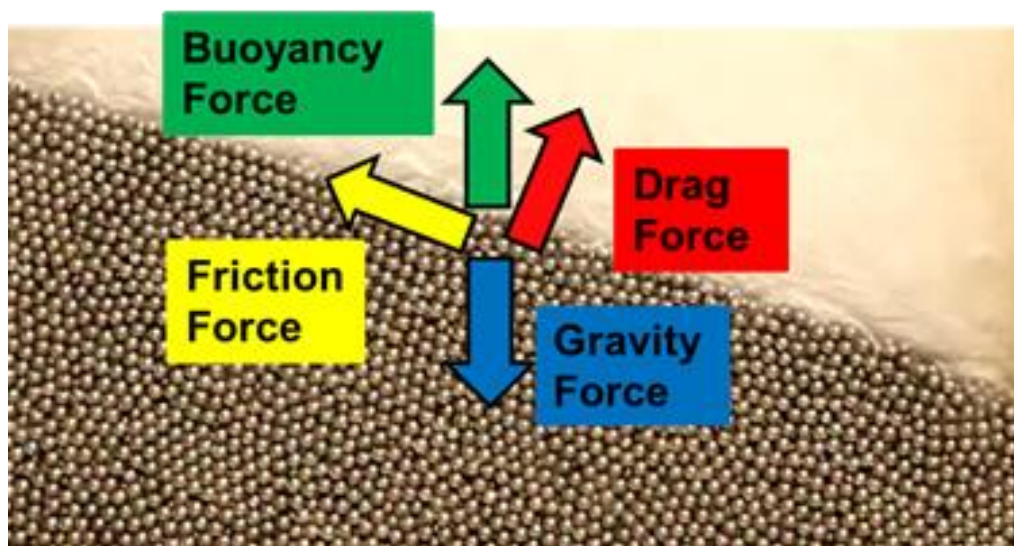


Figure 66: Schematic of the balance between main forces acting on a particle in the debris bed.

Particle flow rate can be expressed as a function of the forces

$$Q_p = f(F_D, F_B, F_{Fr}, F_G), \quad (4.14)$$

or parameters which determine the forces

$$Q_p = f(d_p, U_g, Q_g, \rho_p, \rho_l, \rho_g, \mu_g, g, \phi, k_{Fr}), \quad (4.15)$$

where  $k_{Fr} = \tan \theta_{rep}(Q_g)$  is friction coefficient which is a function of gas flow rate and for the coarse, cohesion-less materials is equal to the tangent of the repose angle [94].

Applying the Rayleigh's method of the dimensional analysis, formalized by Buckingham [93] one can find that relation Eq. (4.15) can be represented with only four independent non-dimensional combinations of the parameters Eq. (4.16).

$$F \left( \frac{Q_p(Q_g, \phi)}{\rho_p \cdot U_g \cdot d_p}, Ar_{lg}, \frac{\tan \theta_{rep}(Q_g)}{\tan \theta_{rep}^0}, \frac{\tan \phi}{\tan \theta_{rep}(Q_g)} \right) \quad (4.16)$$

Since the rate of particulate debris spreading is determined by the local gas flow rate  $Q_g$  and slope angle  $\phi$  of the bed [90], we propose following form of Eq. (4.16):

$$Q_p^*(\phi) = \frac{Q_p(Q_g, \phi) \cdot Ar_{lg}}{\rho_p \cdot U_g \cdot d_p \cdot \frac{\tan \theta_{rep}(Q_g)}{\tan \theta_{rep}^0}} \quad (4.17)$$

where  $Q_p^*$  is a normalized non-dimension particle spreading rate (to be determined based on the PDS-C data),  $\theta_{rep}^0 = \theta_{rep}(0)$  corresponds to critical repose angle of a particle heap[95] at  $U_g = 0$ , and

$$\phi = \frac{\tan \phi}{\tan \theta_{rep}(Q_g)} \quad (4.18)$$

is normalized slope angle. In eq. (4.17) the  $Ar_{lg}$  represents the effect of gravitational and buoyancy forces, while  $U_g$  and  $\frac{\tan \theta_{rep}(Q_g)}{\tan \theta_{rep}^0}$  describe the effect of drag and friction forces respectively.

The dimensionless relation Eq. (4.17) follows relative importance of different factors, which are intuitively well understood and can be expressed as follows

$$Q_p \sim \frac{F_D \cdot F_B}{F_{Fr} \cdot F_G} \quad (4.19)$$

I.e. larger gravity and friction forces (larger  $Ar_{lg}$  and smaller  $\tan \theta_{rep}(Q_g)/\tan \theta_{rep}^0$  in Eq. (4.17)) will reduce particle flow rate, and vice versa, higher drag force and buoyancy (larger  $U_g$  and smaller  $Ar_{lg}$  in Eq. (4.17)) will increase particulate flow rate.

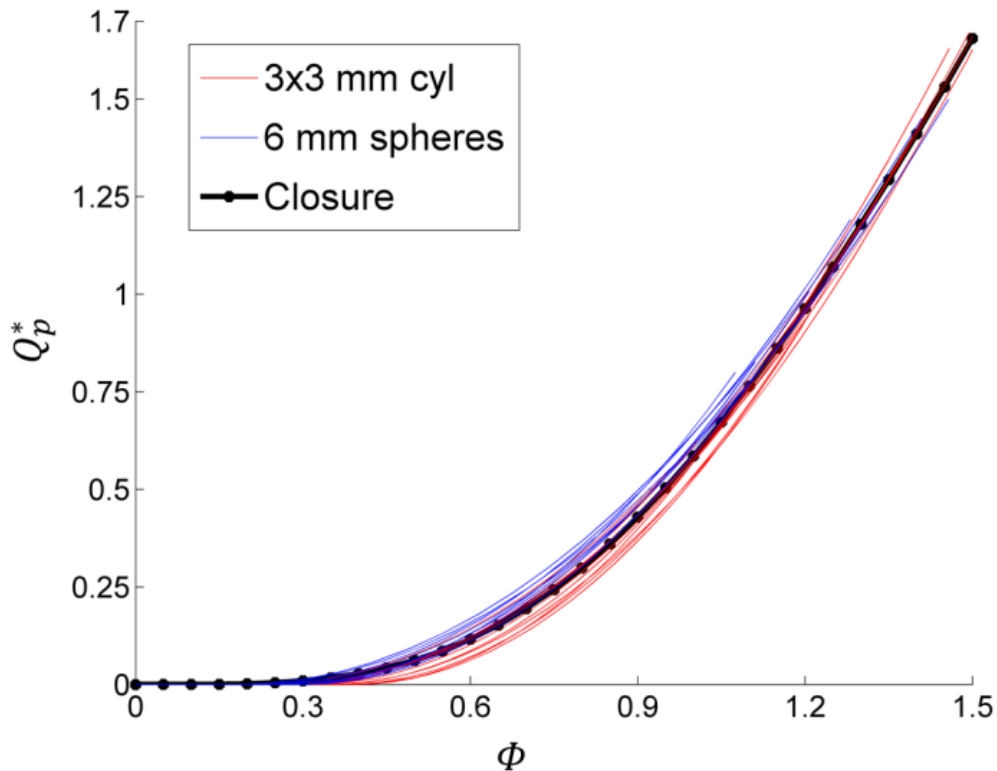


Figure 67: Non-dimensional representation of experimental closure curves. The red curves represent SS 3x3 mm cylinders while the blue are for SS 6 mm spheres. The black curve indicates the universal non-dimensional closure

The effect of particle density on  $Q_p$  has to be confirmed in the next series of experiments with different particles. Although, it is clear that larger particles made of denser material will be

more difficult to move (as suggested by Archimedes number in Eq. (4.17)) as it was observed by Cheng et al.[84].

The proposed dimensionless relation (4.17) has been applied to post process experimental data from the tests with stainless steel particles (3x3 mm cylinders and 6 mm spheres). The resulting fit curves built in the non-dimensional variables for different experiments with different particles and gas injection conditions essentially converge into a single dependency as shown in Figure 67.

This result suggests that the scaling approach captures most important phenomena and can be used to introduce a universal closure for non-dimensional particulate debris spreading rate independent on the particle properties and gas flow rate. Such closures can be introduced (see also Figure 67) as using polynomial fittings to the PDS-C data, e.g.

$$Q_{p1}^*(\Phi) = \Phi^4(0.2871 \Phi^2 - 1.234\Phi + 1.532),$$

or

$$Q_{p2}^*(\Phi) = \begin{cases} \left(\Phi - \frac{1}{4.5}\right)^2, & \Phi > 0.29293 \\ 0.017068 \Phi, & \Phi < 0.29293 \end{cases} \quad (4.20)$$

Obtained correlation can be used to predict evolution of the debris bed shape in time. An example of the application of the proposed model to simulation of the particulate debris spreading in reactor accident conditions and comprehensive sensitivity and uncertainty analyses are presented in Basso et al.[96].

#### **4.4 Summary**

A set of PDS-C experiments has been carried out with different stainless steel particles in order to quantify particle flow rate in debris bed self-levelling phenomenon. A scaling approach has been proposed in order to introduce a universal closure for non-dimensional particulate debris spreading rate independent on the particle properties, gas and coolant properties and gas flow characteristics. Application of proposed scaling approach to different PDS-C tests results in dense clustering of the non-dimensional data suggesting that the most important physical phenomena are captured properly in the approach. A universal closure has been proposed based

on the available data. More tests will be performed in the future with particles made of different material, mixtures of particles with different sizes and irregular shapes, etc. in order to extend empirical database for validation of the proposed closure.

## **4.5 Investigation of Particulate Debris Spreading: Possible Effect of the Heaters and Thermocouples in COOLOCE Facility**

### **4.6 Goals and tasks**

The goal of this task is to quantify time scale for particulate debris spreading. Experimental studies are performed at KTH in PDS-C facility with air injection from the bottom of the debris bed [35]:

- (i) to produce data for development and validation of the model for prediction of particulate debris spreading;
- (ii) to assess the influence of the heaters and thermocouples on spreading of the particles used in COOLOCE facility at VTT.

### **4.7 Experimental Approach and Procedure**

The geometry and total mass of the particle bed has no effect on the mass flux caused by the two-phase flow through the bed [3]. Until onset of fluidization, the bulk of the bed is immobile and the spreading is determined by relatively slow particle motion in a thin topmost layer of the bed. Thus the physical processes governing the spreading of the topmost layer are the same for any size of the bed. Therefore, there is no need to reproduce actual conical shaped of the bed used in COOLOCE test section. In the planar geometry of the PDS-C facility a slice of the COOLECE conical debris bed [1], [2] is considered. A few significant differences between the previous tests performed by VTT [2] and tests presented here are:

- VTT tests are focused on dryout of the non-movable conical bed;
- The geometry of the bed is realized by a conical net keeping the slope angle at about 45° well exceeding the critical angle of repose of spherical particles.
- In PDS tests air injection at the bottom of the bed is used to simulate steam flow.

#### **4.7.1 Experimental facility**

Experimental facility consist of the PDS-C test section and a mockup of the heaters and thermocouples (TC) used in COOLOCE tests performed by VTT [2].

#### **PDS-C test section**

PDS-C is a medium size experimental setup for separate effect tests on basic phenomena of particulate debris spreading at elevated gas-flow rates. It has been designed to provide closures for particulate debris spreading at different gas injection flow rates. The closures are necessary for particulate debris spreading model validation and development.

The scheme of the setup is given in the Figure 68, Figure 69 and Figure 70. It is a vertical rectangular in cross section container made of Plexiglas with the dimensions of the active zone 73x405x915 mm. The bottom plate through which the air is injected into the active zone has 287 orifices  $\varnothing 1.5$  mm evenly distributed over the surface. The bottom plate is a part of aluminum rectangular pressurized compartment allowing gas fluxes up to 2.4 m/sec (flow rate up to 70 liters per second). The minimum gas flux providing the uniform gas injection over the injection plate is about 0.17 m/s (~5 L/s of the flow rate). The tests section commonly accommodates debris mass around 30-40 kg or volume up to 10 liters.

As an addition to test section, there is also a top flange (not shown in figures) mounted on top of the acrylic water tank. The flange prevents water being splashed out of the water tank. The flange has geometry of the box without two opposite sides through which injected air escapes. It's front and back sides are made of 3 mm thick aluminum plates.

PDS-C Facility Design Parameters (see Figure 68) are:

1. Fixed parameters:

- Facility type: room temperature water/air facility.
- Facility tests section material: Plexiglas.
- Air injection provided through a perforated plate at the bottom.

2. Ranges of variable parameters:

- Debris particles material:
  - Sand and gravel
  - Stainless steel.
  - Zirconium-silicate, ceramic or glass.
- Volume of the debris bed (with porosity): up to 9 liters.
- Air flow rate up to 70 L/s or 2.4 m/s superficial air velocity
- Initial debris bed shape:
  - Right triangle
  - Isosceles triangle

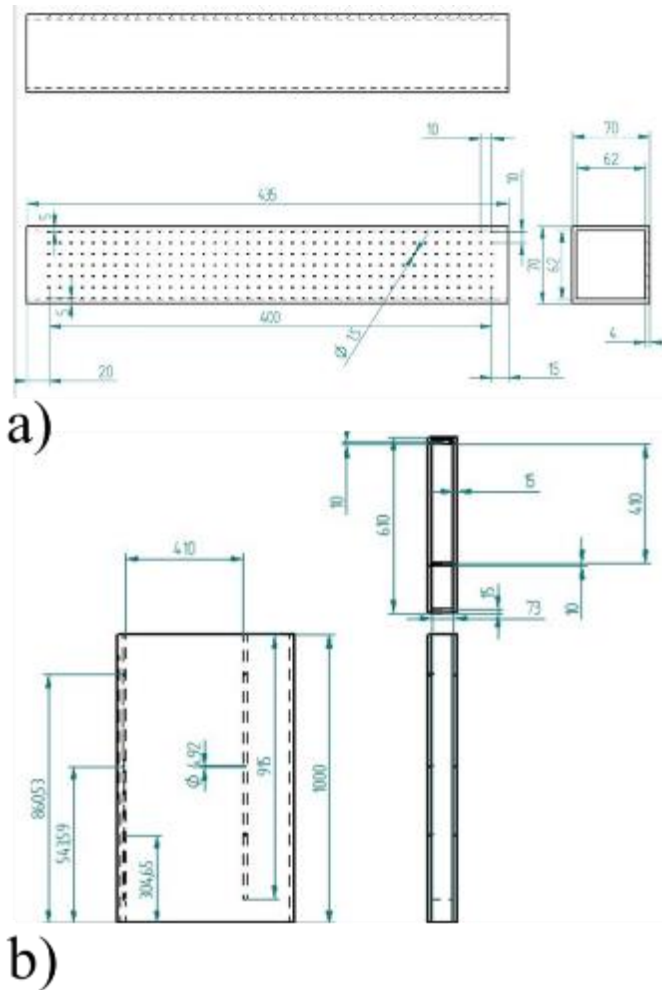


Figure 68: PDS-C drawings: air injection chamber (a) and acrylic body (b).

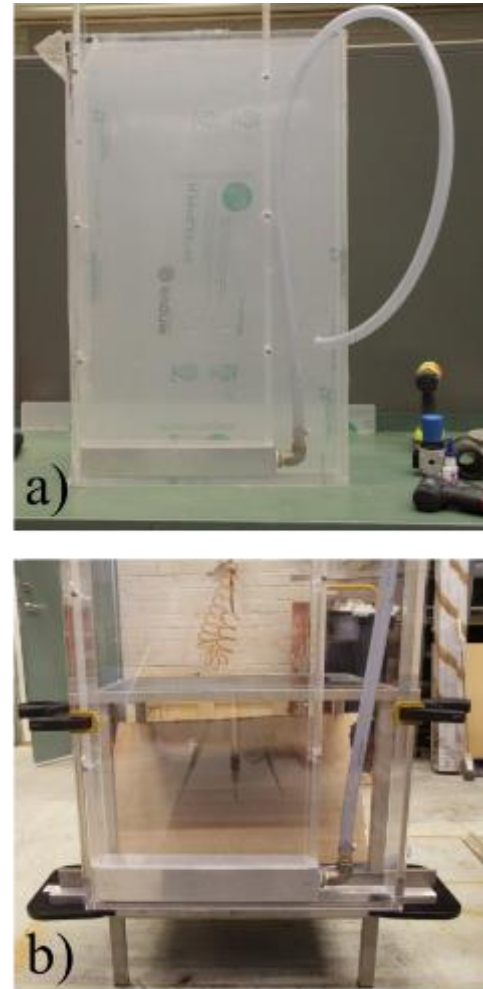


Figure 69: PDS-C facility: Manufactured (a) and installed (b).

### Mockup of the COOLOCE heaters and TCs

In order to design the mockup of the heaters and TCs pins we followed the original arrangement of the heaters and TCs in COOLOCE-1 facility provided in the VTT report [1]. The scheme and photographic image of the heaters and TCs in COOLOCE-1 is shown in Figure 71(a-b). The pitch size between the mockups of the heaters and TCs is 25 mm. The external diameter of the heaters and TCs mockups is 6 and 2 mm respectively. As seen from Figure 71(a), the locations of the heater and TC pins are almost regular. Therefore, the mockup has two regular meshes of the pins corresponding to the 6 mm thick heaters and 2 mm thick TCs. The schematic of the pins holding plate of the mockup is shown in Figure 71(c). The plate lateral dimensions correspond to the:

- Dimensions of the PDS-C facility and its air injection chamber;
- Length of the slope of the silica-zirconia bed having a critical angle of repose close to  $22^\circ$ ;

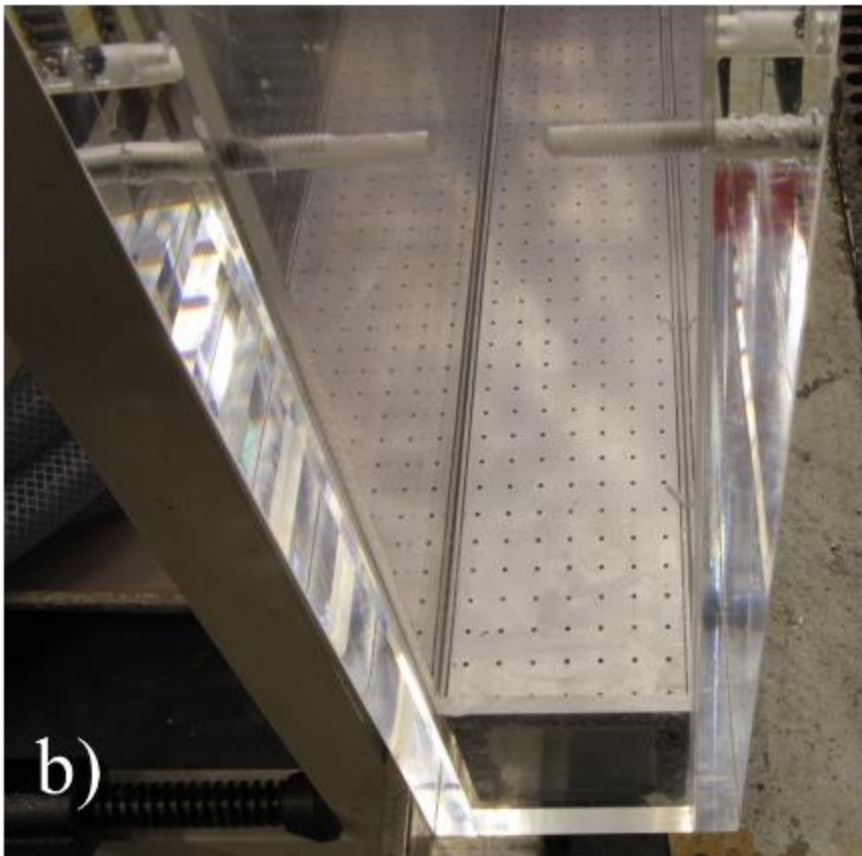


Figure 70: PDS-C test section (a) and its spreading plate (b).

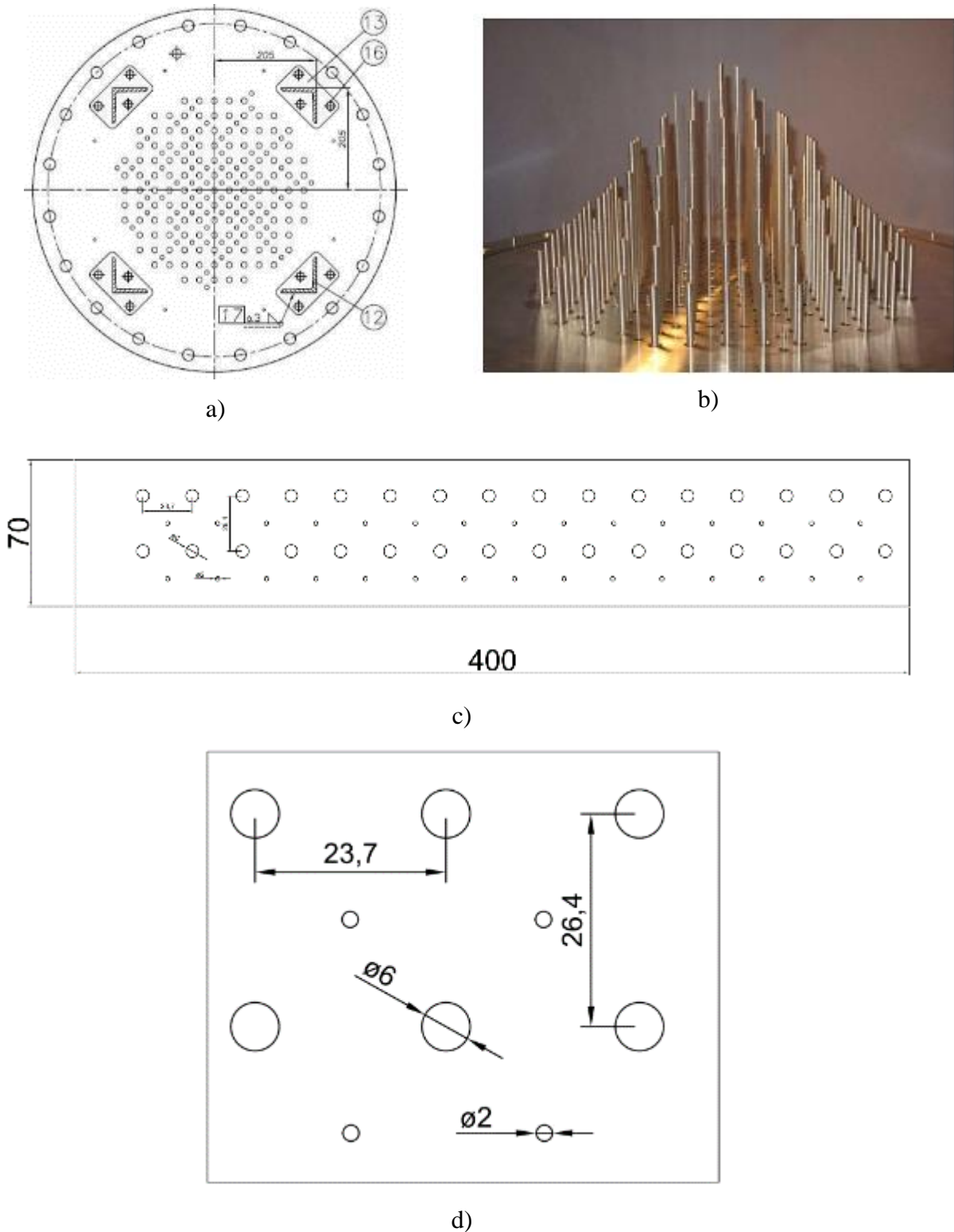


Figure 71: Schematics (a) and photographic image (b) of the heaters and TCs used in COOLOCE-1 facility [1]. Schematics of the pins arrangement in COOLOCE mockup: plate (c) and holes (d) dimensions together with pitch sizes.

The lateral pitch sizes for the pins are shown in Figure 71(d). As seen from Figure 71(d) the pitch sizes are different in transversal directions. This is due to inclined position of the pins

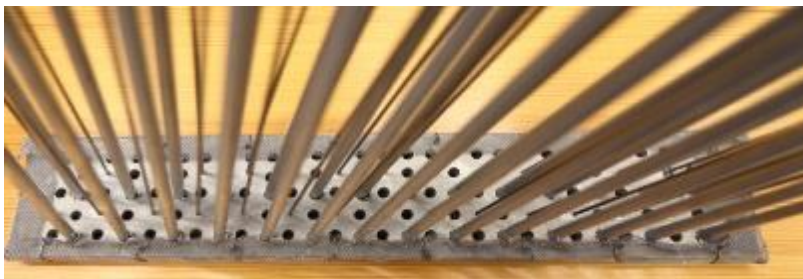
holding plate which is lying on top of the bed slope at angle close to critical angle of repose. When assembled, the pitch sizes of the vertically aligned pins in both lateral directions are the same. The assembled mockup is shown in Figure 72.



a)



b)



c)



d)

Figure 72: COOLOCE heaters and TCs mockup: top (a) and side (b) views; pins holding plate with inner (c) and outer (d) perforated surfaces as well net protecting the particle through flow.

As shown in Figure 72(b-d) the pins holding plate is perforated with additional holes. The fine stainless steel net Figure 72(d) limits the particle flow through the perforated plate allowing only gas flow through additional holes in between pins. Beside the pins holding function, the perforated plate serves as a heap-holder.

## **Debris simulants: properties and characterization**

As the debris simulants we use particles having different physical properties as well as size and morphology. Typical particulate debris used in PDS experiments are:

- Stainless steel cylinders, spheres and their mixtures;
- Sand gravel with size distribution and irregular morphology;
- Zirconium-silicate beads.

In this report we present the results performed with a latter particles, namely, the zirconium-silicate beads.

### ***Zirconium-silicate beads***

The VTT has performed series of tests with zirconium-silicate beads [1], [2]. For our tests we use the same beads purchased from the same supplier Alpine Hosokawa [4]. The main properties of the particles provided by supplier [4] are summarized in Figure 73(a). Size distribution of the beads in the ranges 0.8-1.0 mm is provided by manufacturer.

The size distribution of the beads has been analyzed by employing the image processing. The image (Figure 74a) of the 2001 particles has been filtered, color inverted (Figure 74b) and with MatLab image processing toolbox the average diameter of each recognized particles was estimated. The resulting statistics in beads size distribution is presented in Figure 75(a). For comparison, the size distribution of 960 beads analyzed by the VTT [5] is provided on the same graph. The cumulative fraction of the particles from both analyses is shown in Figure 75(b). A slightly larger fraction of the smaller particles in our analysis (vs VTT's) is an acceptable uncertainty and might be attributed to the measurement error. In either case the particles sizes are within the size distribution range specified by the supplier.

Data Sheet	Alpine Powerbeads SZS
Material	Zirconium Silicate sintered
Chemical Composition	ZrO <sub>2</sub> 55 % SiO <sub>2</sub> 35 % Al <sub>2</sub> O <sub>3</sub> 10 % Y <sub>2</sub> O <sub>3</sub> traces HfO <sub>2</sub> traces
Specific weight	4.1 g/cm <sup>3</sup>
Settled bulk density	2.5 g/cm <sup>3</sup>
Hardness Mohs	7.2
Hardness HV5	9.4 MPa
Fracture toughness K <sub>IC</sub>	2.8 MPam <sup>1/2</sup>
Crushing load (2.0 - 2.5 mm)	1370 N
Crystallite size (av.)	370 nm
Roundness	97 %
Open porosity	0 %
Colour	white
Surface	satin finished

a)



b)

Figure 73: Properties (a) and image (b) of the 0.8-1.0 mm zirconium-silicate Alpine Powerbeads provided by supplier [4].

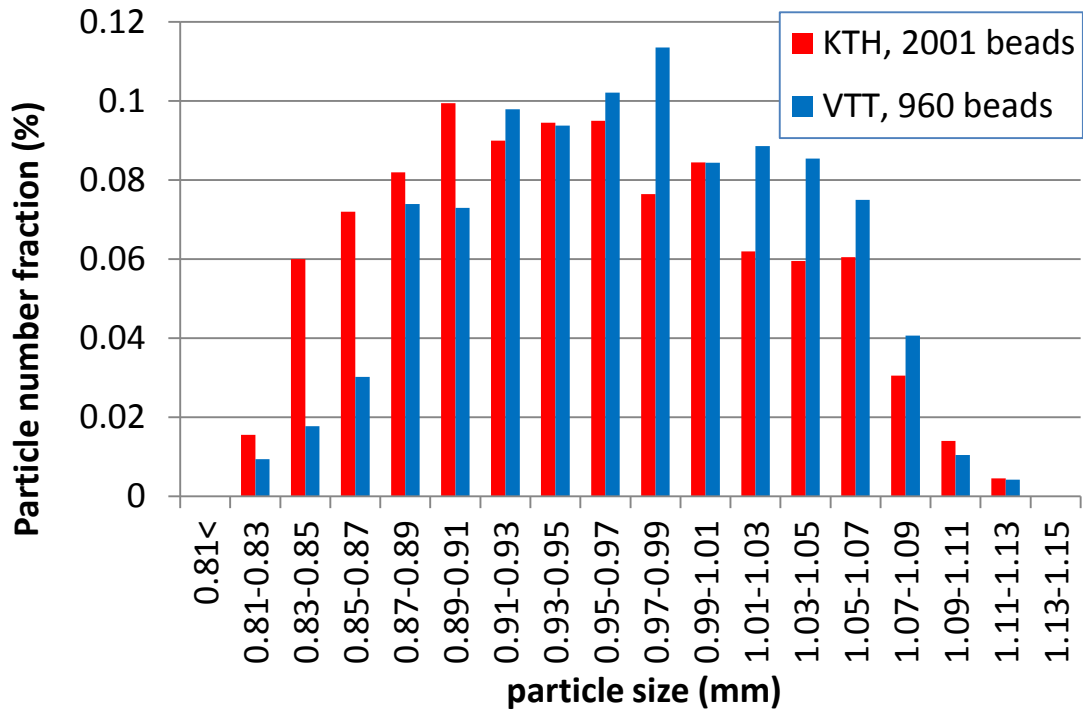


a)

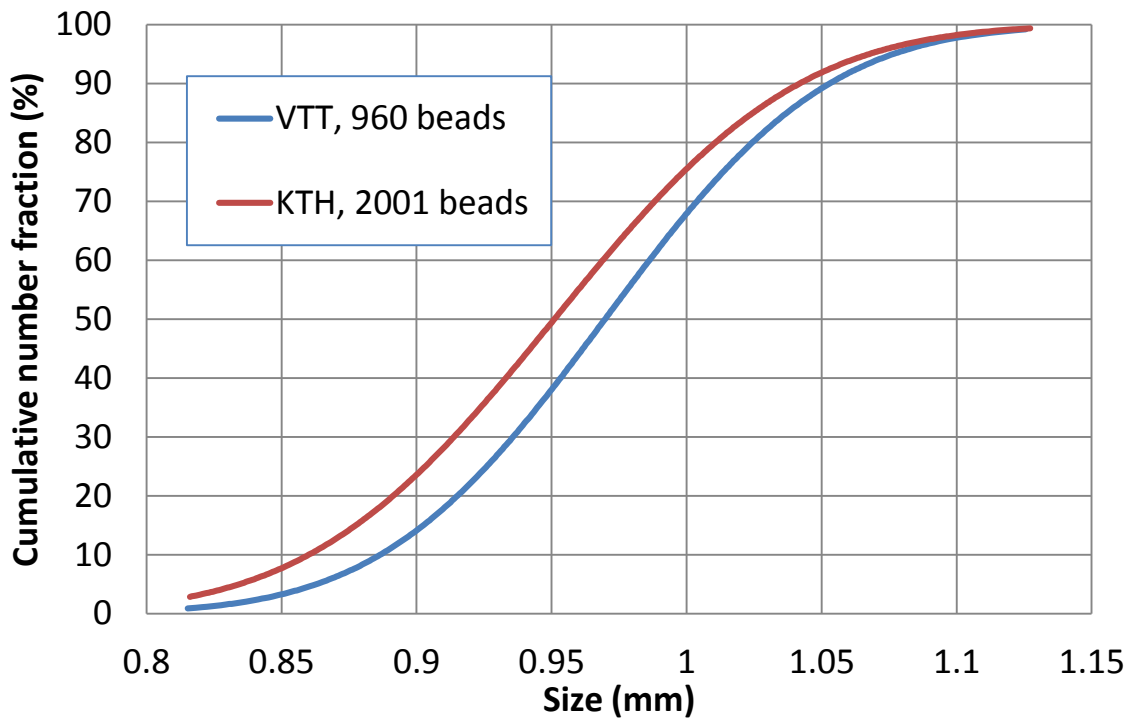


b)

Figure 74: Original (a), filtered and color inverted (b) images of the beads.



a)



b)

Figure 75: Size distribution of the zirconium-silicate beads.

The number averaged particles size estimated by VTT and KTH are 0.97 and 0.95 mm respectively.

## Experimental procedure

A typical measurement procedure used in PDS-C tests with and without (w/o) COOLOCE heaters and TC mockup is described in this section. Both procedures consist of two phases: (i) debris bed preparation and (ii) test execution. In Table 18 and Table 19 important steps in the experimental procedures are provided for both types of the tests.

Table 18: Experimental procedure for preparation of the tests with and w/o mockup.

No	Step	Tests w/o mockup	Tests with mockup
1.	Installation of the COOLOCE heaters/TC mockup	-	+
2.	Particle filling	+	Is performed through a 30x70 mm opening between mockup plate and wall of the test section.
3.	Bed shaping with critical angle of repose	+	Not needed because mockup plate is at the critical angle of repose already.
4.	Installation of the heap-keeper and top flange	+	The mockup provides function of the heap holder.
5.	Plugging the opening for particle filling.	-	+
6.	Water pouring into facility	+	+
7.	Installation of the rulers for bed geometry measurements	+	+
8.	Installation of the video recording equipment	+	+

Table 19: Experimental procedures for running the tests with and w/o mockup.

No	Step	Tests w/o mockup	Tests with mockup
1.	Activation of the video recording equipment, photographing bed and test section prior test.	+	+
2.	Activation of the gas injection at the desired flow rate	+	+
3.	Removal of the heap-keeper or lift of the mockup	Heap-keeper is removed from facility.	The mockup is lifted by ~20cm above the bed top surface.

The aforementioned (Table 18) *heap-keeper* is a perforated plate wrapped in a thin stainless steel net having the mesh size smaller than a particle size being used. The purpose of the heap-keeper is to prevent occurrence of so called *water piston effect* influencing the debris bed when gas injection is rapidly turned on. Prior the gas flow activation the porous volume of the debris bed is filled with water. Sudden gas flow activation leads to a fast momentum transfer from the gas to the water in the porous media. Since the porous media is a pile of particles (heap) the momentum is further transferred to them from the accelerated water flow. This process is far from being a prototypic to boiling and steam production in the corium debris bed caused by the decay heat at reactor scale. Therefore it has to be avoided. Such effect has been also observed by Cheng et al. in [6]. As a countermeasure authors proposed (i) gas pre-charge and (ii) pressure-adjustment approaches. The first method is discussed below. The second method requires significant modification of the test section complicating the design and operation of the facility.

A simplest solution would be to turn on gas injection controlling valve gradually from zero to a desired flow rate (pre-charge method used in [6]). In practice however, the time scale of the gas flow settling (slow process of the valve opening) can be much longer than the characteristic time scale of the particle self-leveling process. Essentially, this is valid for the high gas fluxes and low particle densities. Therefore, another method of the avoiding of the piston effect and its influence is to use the heap-holder allowing no particle flow when gas injection is activated. After the establishment of the necessary gas flow the heap-holder is removed manually indicating the beginning of the measurements.

The main difference between operational procedures (given in Table 18) of the test with and without COOLOCE heaters/TCs mockup is that unlike to the heap-holder function described above, the mockup is not completely removed from the facility when experiment starts; instead, it is lifted-up above the debris bed while the pins (heaters/TCs mockup) remain inside the bed. In this way, we simulate the effect of the COOLOCE heaters and thermocouples resisting the particle flow. The effect of this resistance has been evaluated in our tests and results are presented in the following chapter.

#### 4.8 Results and Observations

In total 13 tests were performed: ten without the COOLOCE heaters/TC mockup and three with mockup. The test conditions and results are summarized in Table 20.

Table 20: Results from tests with- and without COOLOCE heaters/TCs mockup performed in PDS-C facility on self-leveling of the 0.8-1 mm zirconium-silicate beads.

Total air flow rate (L/s)	Superficial velocity (m/s)		Self-leveling time (s)						
	Air	Steam (assessed)	Experiments with mockup	Experiments w/o mockup					
			Tests 1-3	Tests 4-6	Tests 7-9	Tests 10-12	Test 13	mean	Standard deviation $\sigma$ (s)
5	0,17	0,25	<b>19,2</b>	21,9	21,8	20,8	-	<b>21,50</b>	0,50
10	0,34	0,50	<b>4</b>	3,6	8,1	4,2	3,6	<b>4,88</b>	1,88
15	0,52	0,77	<b>3,9</b>	4	4,4	3,8	-	<b>4,07</b>	0,25

As seen from Table 20 the total air flow rate is fixed to 5, 10 and 15 L/s which correspond to the superficial velocity of the air ranging from 0.17 up to 0.52 m/s. As estimated in APPENDIX 1 the fluidization velocity of the bed consisting 0.95 mm large zirconium-silicate beads is about 0.62 m/s. The highest value of the air superficial velocity reached in our tests is 0.52 m/s. In our early studies with stainless steel particles [3] we found that the bed partial fluidization already takes place at the gas velocity equal to ~70% of the theoretical value estimated from Eq. (4.3) in APPENDIX 1. Indeed, for the zirconium-silicate particle pile we observed similar phenomenon. The top of the bed is near its fluidization limit at 15 L/s total flow (0.52 m/s). This fact may explain why at the highest superficial velocity the tests with- and without

COOLOCE heaters/TCs mockup show the same self-leveling time as presented in Figure 76. Note, the corresponding superficial velocity of the steam given in Table 20 and on upper axis in Figure 76 is calculated from expression (4.7) (APPENDIX 1).

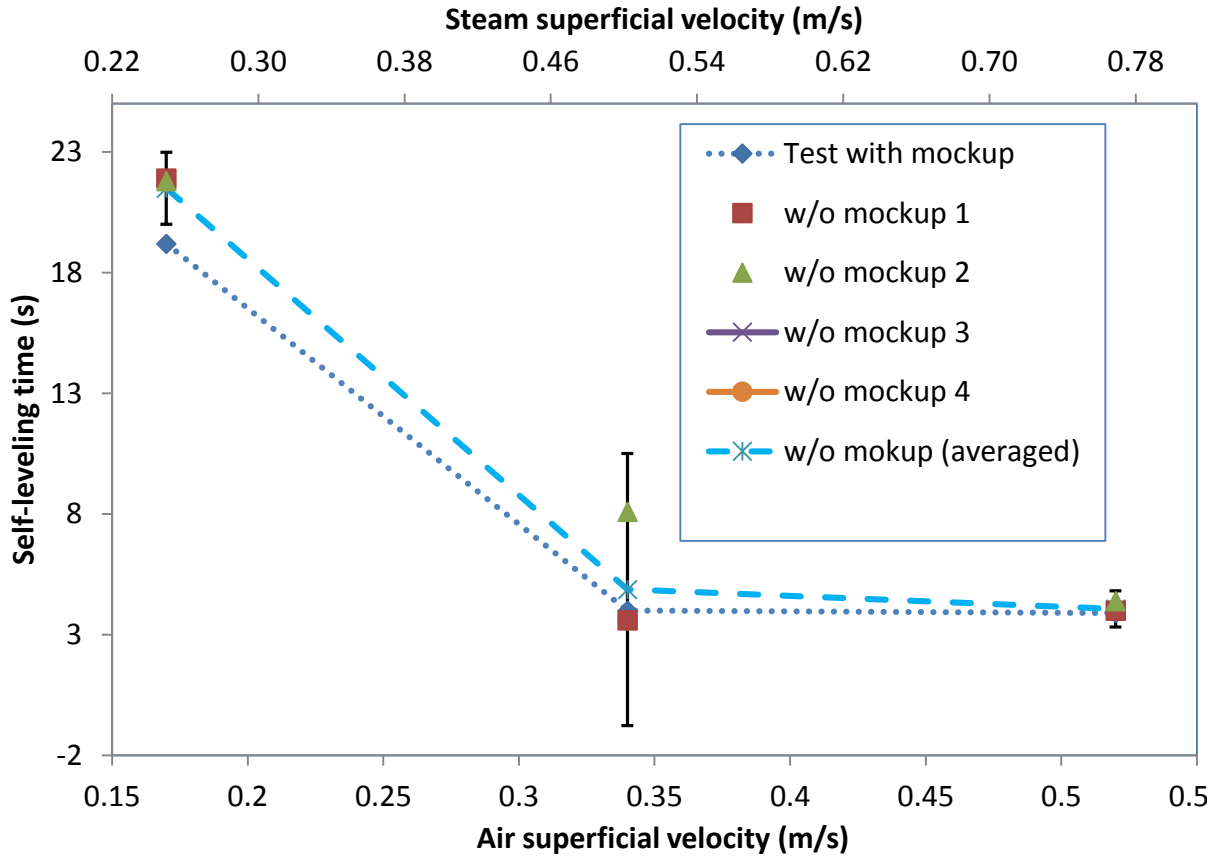


Figure 76: Results from the tests with zirconium-silicate beads: 3 tests with mockup and 10 tests w/o mockup are grouped in 4 groups. The error bars correspond to the tripled standard deviation  $\pm 3\sigma$  of the characteristic self-leveling time.

For the lowest 0.17 m/s superficial velocity of the air the effect of the COOLOCE heaters/TCs mockup is noticeable. Surprisingly, at this point the particle self-leveling process with presence of the mockup is slightly faster than w/o it. Possible explanations of the observed phenomenon are:

- The partial extraction of the COOLOCE heaters/TCs mockup from the bed (see “Experimental procedure”) may influence beads self-leveling by enhancing the downslope particle flux at the very beginning of the test.
- The heaters/TCs mockup pins may influence the local two-phase currents enhancing the turbulent flows which, again, might slightly increase particle flux.

Nevertheless, assuming that the measurement uncertainty of the test with and w/o mockup is the same, the self-leveling time for either case is almost the same. In other words, the light blue dashed line (single test per air velocity point, with mockup) and the blue dotted line (averaged between tests, w/o mockup) are both within the ranges of the experimental errors (Figure 76).

#### 4.8.1 Fluidization velocities of the zirconium-silicate bed

Following the approach presented in APPENDIX 1 we calculate the minimum fluidization velocities of the zirconium-silicate beads by air and steam. In these calculations properties of the bead are used as shown in Figure 73 and Figure 75, and gas properties are calculated at atmospheric pressure and temperature of 20°.

Table 21: Minimum fluidization velocities of the zirconium-silicate beds by air and steam.

Gas	Minimum fluidization velocity $u_{mf}$ (m/s)
Air	0.62
Steam	0.92

#### 4.8.2 Summary and Outlook

In total 13 exploratory tests were carried out to clarify the influence of the COOLOCE heaters and TCs mockups on particle self-leveling process. Results of the preliminary analysis suggest that there is no significant influence of the mockup pins on self-leveling, at least for the air superficial velocities ranging from 0.17 up to 0.52 m/s. There is a tendency, which might be within experimental error however, that the heaters and TCs pins may even enhance the particle self-leveling process at lower superficial velocities of the gas (<0.17 m/s for air and <0.24 m/s for steam). This finding is counterintuitive and need to be confirmed by performing more tests at even lower gas injection rates. For that, the gas injection chamber used in PDS-C facility must be redesigned in order to achieve uniform air injection below 0.17 m/s (see complete specs of the PDS-C facility in 4.7.1).

The PDS-C tests reported herein were carried out in a configuration when COOLOCE heaters/TCs mockup pins are extended over the debris bed top surface. In the previous VTT studies [1]-[2] the heaters and TCs tips are below the bed top surface. If the future self-leveling

tests will be performed in the same (VTT) configuration then there will be no influence of the heaters/TCs on self-leveling process, at least at the initial stage of spreading. As it was mentioned [3] the only top most layer of the pile of particles is movable while the bed bulk is immobile. This is valid for the case when gas superficial velocity is below bed's minimum fluidization velocity.

## 5 Application of MC3D and TEXAS-V to analysis of steam explosion in a BWR containment

Release of core melt from failed reactor vessel into a pool of water is adopted in several existing designs of light water reactors (LWRs) as an element of severe accident mitigation strategy. Corium melt is expected to fragment, solidify and form a debris bed coolable by natural circulation. However, energetic fuel-coolant interaction (steam explosion) can threaten containment integrity potentially leading to large early release of radioactive products to the environment.

The goal of this work is to develop a numerical computationally efficient tool for robust bounding assessment of steam explosion risk with application to a reference design of a Nordic BWR. The outcome of such assessment is foreseen as Steam Explosion Impact Map (SEIM), i.e. map that denotes containment failure probability in terms of input scenario parameters. The framework relies on the steam explosion analysis performed with NRC approved TEXAS-V code. Development of SEIM is a comprehensive problem that requires execution of the following tasks:

- develop data, full, and surrogate models (SMs) to bound ex-vessel steam explosion loads taking into account:
  - melt ejection mode
  - pool conditions (accident scenarios and operator actions)
  - code modelling uncertainty
- establish connection between ex-vessel steam explosion impulse, containment load, containment fragility and risk of containment failure.

Development of SEIM relies on a large number of calculations where for every vector of input parameters probability of failure must be estimated. Given large number of input parameters such assessment becomes computationally expensive, it can be accomplished only if TEXAS-V code will be substituted with a fast surrogate model (SM) that can reliably reproduce TEXAS-V calculations in terms of integral impulse and maximum dynamic pressure.

In order to reduce the number of uncertain parameters in SEIM a comprehensive sensitivity study of TEXAS-V must be performed. Results of sensitivity study can be used to (i) optimize framework performance, (ii) adjust ranges for input parameters and (iii) indicate parameters

that have high impact on the target functions (integral impulse, maximum pressure, failure domain) and therefore are the first candidates to reduce the uncertainty.

Ranges of the uncertain parameters are selected based on the available information about prototypic severe accident conditions in a reference design of a Nordic BWR. Both aleatory uncertainty in characteristics of melt release scenarios and water pool conditions, and epistemic uncertainty in modeling are considered.

Comparative analysis of TEXAS-V against MC3D in terms of impulse distribution is foreseen in the project. The objective of the comparison is to demonstrate reasonable conservatism of TEXAS-V against best estimate code. In addition MC3D is used to identify ranges of input parameters in TEXAS-V that cannot be otherwise specified.

In this report we present (i) brief overview of the TEXAS-V code and key constitutive equations, (ii) the methodology of the SEIM framework, (iii) details implementation of sensitivity study and SM development in conjunction with (iv) sampling and optimization approach required to suppress otherwise stochastic estimates of the explosion impulse by deterministic TEXAS-V code, and in the end provides (v) Morris sensitivity measures for a limited number of input parameters considered a priori as the most influential.

## 5.1 TEXAS-V code

The Texas-V is a 1D 3-field transient code with Eulerian fields for gas and liquid and Lagrangian field for fuel particles. It comprises two modules: one for calculation of premixing and another one for calculation of steam explosion.

The **premixing model** is based on conservation equations and two key constitutive models: the *fragmentation model for mixing* and the *phase change model*. All of them are applied in three flow regimes: bubbly flow, droplet flow and transition flow.

The fuel fragmentation is due to the following mechanisms:

- Rayleigh-Taylor instability
- Boundary layer stripping
- Kelvin-Helmholtz instability

Kelvin-Helmholtz instability and boundary layer stripping are considered to have minor effect with vapor film present and are reduced rapidly with rise of void fraction.

The Rayleigh-Taylor instability model is thus the key constitutive relation in TEXAS describing fuel fragmentation. It was developed by Chu and Corradini [74] based on Pilch's [76] original concept of a multi-step fragmentation theory for liquid particles. The model considers the fuel particles to be deformed and dynamically fragmented into a discrete number of particles from its initial diameter to smaller sizes. The implemented equations are as follows:

$$D_f^{n+1} = D_f^n (1 - C_o \Delta T^+ We^{0.25})$$

$$We = \frac{\rho_c U_{rel}^2 D_f^n}{\sigma_f}$$

$$\Delta T^+ = \frac{U_{rel} (t^{n+1} - t^n)}{D_f^n} \left( \frac{\rho_c}{\rho_f} \right)^{1/2}$$

$$C_o = 0.1093 - 0.0785 \left( \frac{\rho_c}{\rho_f} \right)^{1/2}$$

where  $n$  is time iteration index;  $D_f$  is fuel particle diameter;  $\Delta T^+$  is dimensionless time step;  $U_{rel}$  is relative velocity;  $t$  is time;  $\sigma_f$  is fuel surface tension;  $\rho_f, \rho_c$  are densities of fuel and coolant respectively.

The melt jet is represented in the form of discrete master particles that fall into water pool sequentially. It is further assumed that coherent fuel jet will not breakup until the fuel particle at the leading edge exposed to the oncoming coolant is fragmented (and swept away from the interface), that is only master particle at the leading edge of the jet can be subject to fragmentation. Two alternative mechanistic approaches are implemented in TEXAS-V as driving the onset of leading particle breakup:

- Leading edge breakup.
- Trailing edge breakup.

*The trailing edge* algorithm forces leading master particle to fragment at the tail of the fragmented debris, i.e. at the beginning of the premixing region. *Leading edge* algorithm implies start of the leading master particle fragmentation at the leading front of the fragmented debris, i.e. at the end of the premixing region. The trailing edge regime provides very slow jet propagation (limited by sedimentation of fragmented particles) and high rate of primary breakup. It is intended to predict fragmentation rates of small jets prone to sinusoidal instability. Differences in the prediction of jet propagation and void generation (as an indicator of fragmentation rate) are provided in Figure 77.

Given characteristic scales of melt release in reactor case we consider leading edge regime to provide adequate prediction of jet breakup and propagation velocity; this is also in line with MC3D calculations of jet front propagation in water.

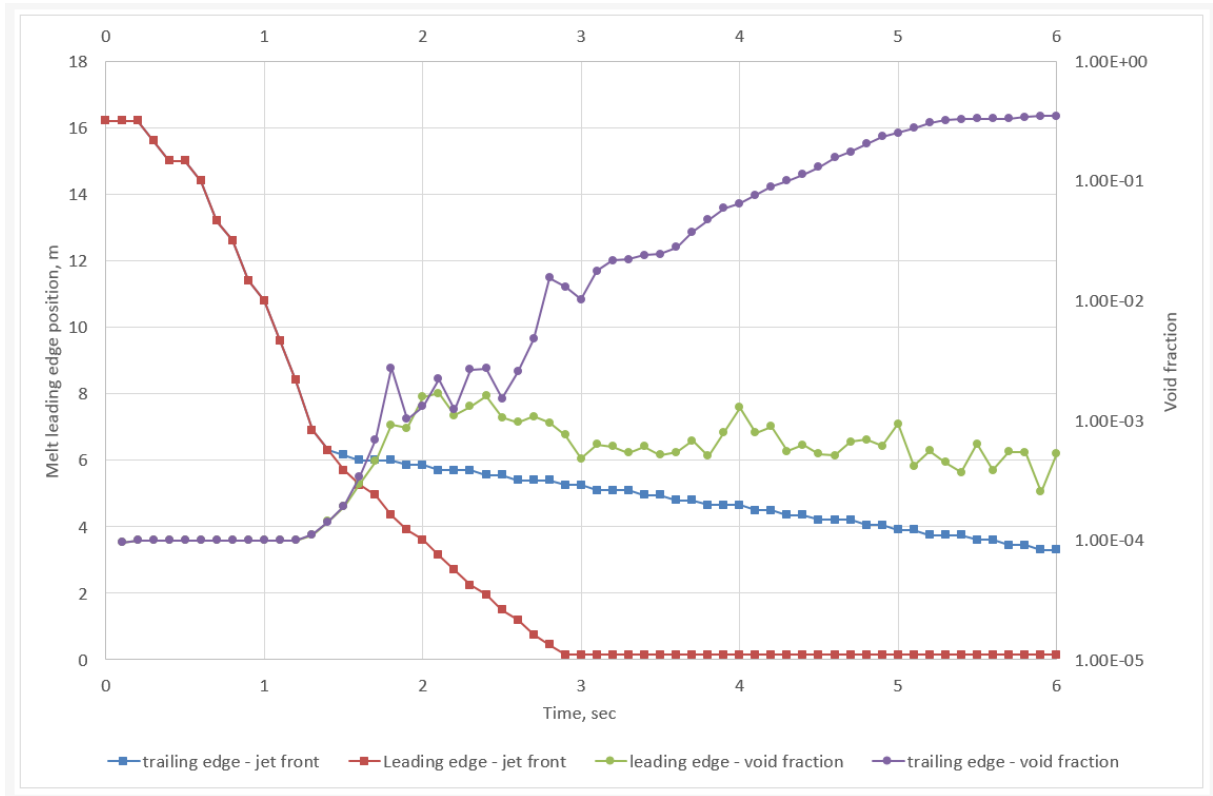


Figure 77: Trailing edge breakup vs leading edge breakup mechanisms.

The phase change model (in continuous liquid field) comprises of two primary equations that define:

1. Heat loss from fuel particles  $\dot{q}_{fuel}$ :

$$-\dot{q}_{fuel} = \pi D_f^2 h_{film} (T_f - T_{sat}) + \pi D_f^2 \sigma F (T_f^4 - T_{sat}^4),$$

where the first term (on the right hand side of the equation) describes convection heat transfer rate from fuel particle to the liquid vapor interface, and the second term is the radiation heat transfer rate from the fuel particle to the saturated liquid-vapor interface. Temperature profile inside a particle is solved in simplified way using steady state approach: it is assumed spatially constant in the bulk and linearly decreasing within a thin thermal layer  $\delta$ .

The corresponding steam generation rate  $\dot{M}_{s,p}$  is then expressed as:

$$-\dot{q}_{fuel} = \pi (D_f + 2\delta_{film})^2 h_{lg} (T_f - T_{sat}) + C_{rad} \pi D_f^2 \sigma F (T_f^4 - T_{sat}^4) + \dot{M}_{s,p} h_{fg},$$

where the first term on the r.h.s. is convection heat transfer rate from the liquid-vapor interface around the fuel particle to bulk liquid field and the second term is the fraction  $C_{rad}$  of radiation heat flux that is absorbed in the subcooled liquid;  $h_{fg}$  is the latent heat of steam.

2. Heat flux balance around steam bubbles and resulting steam generation rate  $\dot{M}_{s,b}$ :

$$A_{gL}K_g \frac{(T_g - T_{sat})}{\delta_g} = A_{gL}h_{L,sL}(T_{sat} - T_L) + \dot{M}_{s,b}h_{fg}$$

where the term on the left hand side of the equation is the vapor bubble-side heat transfer rate; the first term on the right hand side is the bulk liquid-side heat transfer rate;  $A_{gL}$  is the surface area of the interface between the liquid field and the vapor field as determined from the vapor bubble radius and the flow regime.

The net rate of steam generation  $\dot{m}_s$  per unit volume is thus can be expressed in terms of the net heat flux  $\dot{q}_{net,f}$

$$\dot{m}_s = \frac{\dot{q}_{net,f}}{h_{fg}V_{cell}}$$

$$\dot{q}_{net,f} = \dot{q}_{fuel} - \dot{q}_l - \dot{q}_v$$

where  $\dot{q}_l$  and  $\dot{q}_v$  are the heat received by coolant liquid and coolant vapor respectively, which becomes the internal energy of the coolant; and  $V_{cell}$  is cell volume.

The **dynamic fine fuel fragmentation** (upon steam explosion) is due to the fragmentation model proposed by Tang and Corradini [77] which is largely based on the original Kim's model [78]. It is a combination of thermal and hydrodynamic effects, which conceptually can be summarized as:

1. Film boiling around a molten fuel particle
2. Film collapse by external pressure pulse
3. Coolant micro-jets impingement on the surface of and possibly inside fuel particle
4. Rapid coolant expansion and fragmentation of the fuel into droplets

Being computationally expensive it is replaced in TEXAS with a semi-empirical equation where fragmentation rate  $\dot{m}_f$  expressed as:

$$\dot{m}_f = C m_p \cdot \left( \frac{P - P_{th}}{\rho_c R_p^2} \right)^{0.5} F(\alpha) g(\tau)$$

where  $m_p$  is mass of the initial particle;  $R_p$  is radius of the initial particle;  $P_{th}$  is the threshold pressure necessary to cause film collapse;  $P$  is ambient pressure;  $F(\alpha)$  is the compensation factor for coolant void fraction; and  $g(\tau)$  is the factor for available fragmentation time.

The factor  $F(\alpha)$  is introduced to keep the correlation consistent with mechanism of the model because film collapse and coolant jet impingement become less likely to occur as vapor fraction increases. The factor  $F(\alpha)$  decrease from 1 to 0 at  $\alpha = 0.5$ . In the TEXAS input file this limit is named ALPHAS.

The threshold pressure  $P_{th}$  is evaluated based on theoretical work by Kim and experimental data. At ambient pressure 1 Bar the threshold pressure is in the range from 2 to 4 Bars. As the ambient pressure increases threshold pressure also increases, however no definite quantitative values have been suggested. In the TEXAS input file this parameter is designated as POLD. *In this study we define threshold pressure as  $P_{th} = P + 1bar$ .*

The integral fragmentation mass depends on the duration of the fragmentation process which in case of the Kims model for a single droplet is of cyclic manner with sequential events of film collapse, fine fragmentation of drop surface, reestablishment of the vapor film followed again by film collapse etc. In reality due to concurrent fragmentation of many drops this process can continue only for a limited time. The factor  $g(\tau)$  is introduced as empirical approach to account for the characteristic fragmentation time  $\tau$  during which Kims mechanism is considered to be operative. The factor  $g(\tau)$  decreases from 1 to 0 as this characteristic time is exceeded. At ambient pressure (1Bar) the recommended value for it is 4 ms but often values on the order of 10 ms have been used. It is indicated that as ambient pressure increases the fragmentation limit time decreases. In the TEXAS input file this parameter is designated as TFRAGLIMT; we optimize its value between 10 to 0 ms during explosion calculations to obtain maximum explosion impulse.

The heat generated due to dynamic fine fragmentation is expressed in TEXAS as:

$$\dot{q}_{frag} = \dot{m}_f \cdot (C_{pf} \cdot (T_f - T_s) + i_f)$$

where  $i_f$  is fuel latent heat;  $T_f$  is fuel temperature;  $T_s$  is saturation temperature of the coolant;  $C_{pf}$  is specific heat for the fuel. Due to extremely fine fragmentation of the fuel the rate of heat transfer is so fast that it is assumed to generate steam only giving the following equation for steam generation rate  $\dot{m}_s$  per unit volume:

$$\dot{m}_s = \frac{\dot{q}_{net,f} + \dot{q}_{frag}}{h_{fg}V_{cell}}$$

It is stated in the Tangs thesis that the current model reflects the key features of the "chain-reaction" required for the rapid escalation and propagation of the vapor explosion, i.e.:

- The pressure shock wave directly contributes to rapid fuel fragmentation;
- The fragmented fuel is quenched by the coolant, generating more vapor;
- The increased vapor mass raises the local pressure and sustains the shock wave propagation to neighboring fuel-coolant mixture regions.

Further details on the implemented models in TEXAS can be found in the original thesis by Chu [74] for premixing model and by Tang [77] for propagation model.

TEXAS-V code generates two output files, one for the premixing and one for the explosion; each file contains 24 physical parameters specified for every cell and time step. For the assessment of the explosion energetics we use dynamic pressure data to provide integral impulse per area (and maximum pressure):

$$I = \max(P_{ij}\delta t_i),$$

where summation is performed over repeated index;  $P_{ij}$  is pressure in the cell  $j$  at the time instance  $i$ ;  $\delta t_i$  is the time step at the time instance  $i$ . The maximum impulse is commonly found in the second cell ( $j = 2$ ) from the bottom of the domain.

A number of standalone calculations have been performed using TEXAS-V in which energetics of steam explosion for the scenario of oxidic melt release as a function of jet diameter was investigated. The conclusions drawn from the results were as follows:

- Leading edge breakup model demonstrated somewhat smaller explosion impulses than similar cases with trailing edge breakup
- Cases with jet diameters <70 mm can generate explosive impulses exceeding 50 kPa·s
- Cases with jet diameters >300 mm can generate explosive impulses exceeding 200 kPa·s
  - such explosion can threaten integrity of the containment
- Standalone calculations provide valuable insights but results are not always consistent and do not allow straightforward interpretation:
  - It is not evident how representative results of a single calculation and whether they can be considered as conservative or “best estimate”.
  - Lack of knowledge on importance of input parameters prevents identification of the main sources of uncertainty.
  - Dependence of output on input deduced from a limited number of single calculations can be random.

## 5.2 SEIM framework

The top level of the Steam Explosion Impact Map (SEIM) framework is represented in the Figure 78. It comprises of four components that define containment failure likelihood due to steam explosion in case of lower head failure and melt release into the lower dry well filled with water:

1. melt ejection mode,
2. pool characteristics,
3. steam explosion load,
4. structural fragility.

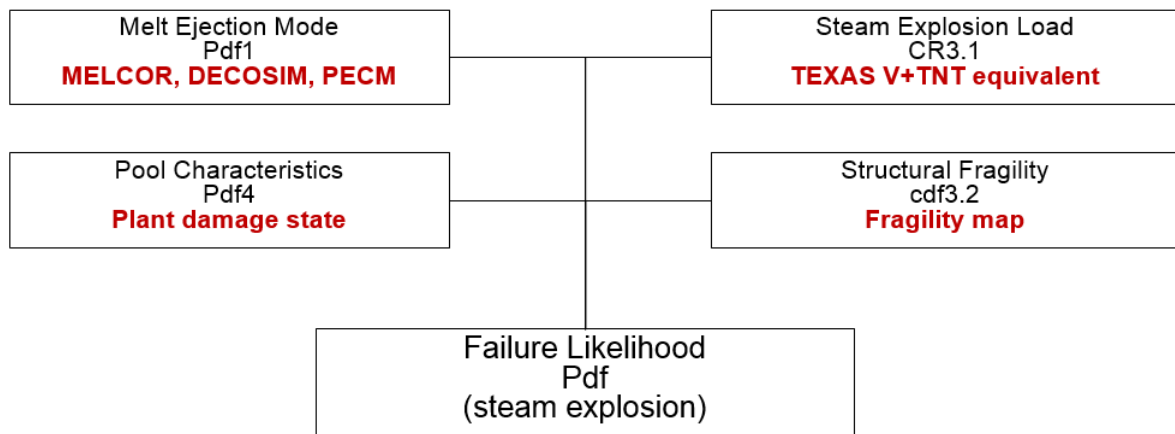


Figure 78: Top level of the SEIM framework

The deterministic model in the framework is Causal Relation 3.1 which is envisaged as a combination of the 1D FCI code TEXAS-V and a simplified approach to propagate predicted explosion impulses into actual containment loads (e.g. TNT equivalent method). The calculations with TEXAS-V code are complemented by MC3D 2D axisymmetric calculations for resolving spatial effects. Note that due to the 1D character of the developed here analysis phenomena related to the melt jet interaction with BWR LDW structures (forest of IGT / CRGT and their support under the lower head) are currently disregarded.

Melt Ejection Mode is defined as a limited number of vessel failure modes each characterized by a specific set of pdfs and intangibles. Those can be either an outcome of adequate modelling of lower head failure after reactor core reallocation and therefore characterized by epistemic uncertainty or defined in terms of ranges with uniform distributions based on state-of-the-art

knowledge. Among melt ejection parameters are melt composition, melt thermo-physical properties, release velocity, jet diameter etc.

Pool Characteristics are due to the accident scenario progression and plant damage state pdfs. Most of the parameters are considered as aleatory (not modelled) and dependent on the frequencies of related events that are random in nature: onset of flooding, operator actions, containment depressurization etc. Pool characteristic parameters include water pool depth, water temperature, containment pressure etc.

Another set of parameters that is not explicitly shown in the above diagram are code modelling parameters such as cell dimensions, coefficient used to fit implemented models to experimental data, model keys to activate different modelling approaches etc. Those are epistemic in nature and represent additional source of code epistemic (modelling) uncertainty.

Cumulative density function cdf<sup>3.2</sup> defines containment fragility and in general requires (i) addressing bounding failure criteria and (ii) deterministic analysis of failure mechanisms. It is dependent on the pool characteristics, for example, on the water level.

### 5.2.1 Surrogate model

The computational efficiency of the TEXAS-V code is not sufficient for the implementation of the SEIM framework (see next chapter). Therefore, the CR3.1 is replaced with a Surrogate Model (SM) – a numerically efficient substitute of TEXAS-V that can reliably reproduce TEXAS-V output. The SM development is demonstrated in the Figure 79. The approach is an iterative process. The initial list of input parameters is defined based on the actual variables in the TEXAS-V input file; ranges for the parameters are identified based on the state-of-the-art knowledge and MC3D calculations. The obtained dataset is then provided to the dedicated sampling, optimization and post-processing algorithms that builds a matrix of TEXAS runs and develops a database of steam explosion solutions: combinations of explosion integral impulse per area and maximum dynamic pressure as a function of input. This database is used either for the sensitivity study (Morris sampling method) or after filtering of failed cases for the training of Artificial Neural Networks (SOBOL sampling method). The trained ANN is the target SM for SEIM.

The results of the sensitivity study are used to reduce the number of input parameters and / or adjust input parameters ranges. In addition SM undergoes extensive numerical validation and, in case of inconsistent results, modifications to the sampling and optimization module are applied. With new dataset and processing module a new sensitivity study and new surrogate model are obtained. Such process is repeated until consistent physically sensible results are obtained. (Inconsistency of the results are due to appearance of stochastic phenomena in deterministic models: see explanation in chapter 5.3.2)

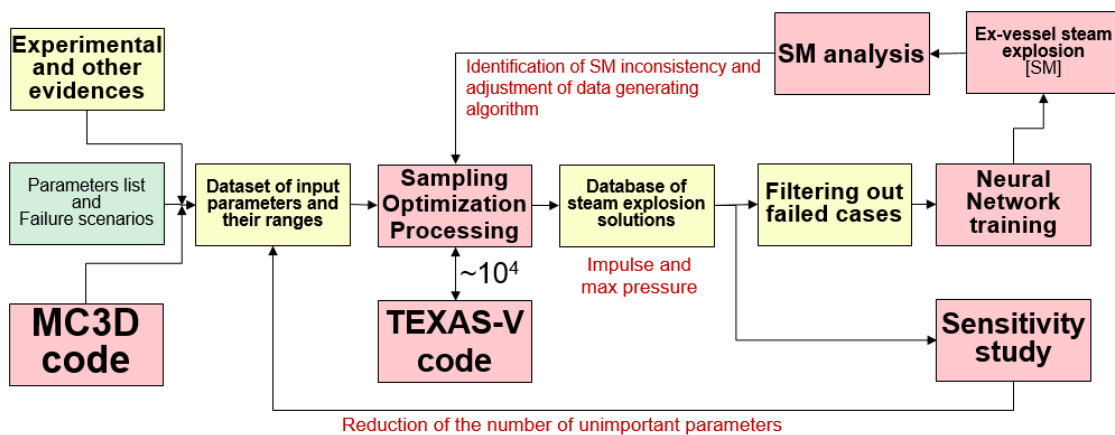


Figure 79: SM development methodology

The complete list of used parameters and applied ranges are the same as in the described later sensitivity study of TEXAS-V.

In practice the SM instead of predicting the actual impulse is trained to predict a range inside which the TEXAS-V estimated impulse will fall with a given confidence level. This naturally follows from the uncertainty of SM with respect to TEXAS. Implication of such approach are further detailed in the implementation of reversed analysis.

### 5.2.2 Implementation of the reversed analysis and results

SEIM framework is envisaged as a numerical tool to provide conditional failure probability (and failure domain) in terms of grouped and classified failure scenarios. In other words the objective of the analysis is definition of triplets: scenario, its frequency and containment failure probability. Currently grouping and classification of scenarios and respective dependent parameters is ongoing. Therefore, here we demonstrate implementation of SEIM framework where failure probability and failure domain are defined in terms of selected TEXAS input parameters only given their bounding ranges. The ranges for input parameters are defined based on the state-of-the-art knowledge applying uniform distribution for sampling. Such analysis is called reversed analysis, which is opposed to forward analysis where derived distributions of input parameters are propagated through the model to build the failure domain.

The input to the deterministic model in SEIM is classified in terms of three groups:

- **input modelled parameters:** epistemic, assumed to be modelled and dependent on the scenario; the group includes jet diameter, melt release velocity, melt composition etc.
- **scenario parameters:** aleatory, not modelled parameters; the group includes water level, containment pressure etc.
- **model deterministic parameters and intangibles:** model specific parameters that can be epistemic or aleatory; the group includes cell dimensions, model fit coefficients, model keys, triggering time etc. Note that aleatory model deterministic parameters are subject to optimization (see detail of sensitivity study implementation )

The classification is required for the SEIM framework execution and necessity to keep separated probability of failure from frequency of scenarios.

For any single vector of input parameters the SM is supposed to provide a single output. It was already mentioned that due to intrinsic uncertainty of SM with respect to TEXAS the actual output is a bounding range with known confidence level. The two bounding values are considered as initial values for pessimistic and optimistic analysis. These bounds can be further extended by distinguish of input parameters ranges between optimistic and pessimistic cases.

For simplicity hereafter we will refer to the output of SM as being a single integral impulse value, say, average of the bounds. The schematics of a single calculation in SEIM is demonstrated in the Figure 80a. If we further replace the vector of deterministic model parameters and intangibles  $(d_{N,i}, i_{N,i})$  with a distribution set  $pdf(d_{N,i}, i_{N,i})$  than for every vector of scenario  $(s_i)$  and input model parameters  $(P_{N-1,i})$  SEIM SM will provide instead of a single impulse value  $(P_{N,i})$  an impulse distribution  $pdf(P_{N,i})$  (refer to the Figure 80b).

The number of cases with impulses exceeding a threshold value define probability of failure. In other words for every single vector of scenario parameters and input modelled parameters  $(s_i, P_{N-1,i})$  SEIM can generate a single value of conditional failure probability  $P_f(s_i, P_{N-1,i})$ . Comparison of  $P_f(s_i, P_{N-1,i})$  with a screening frequency (formulated in ROAAM as physically impossible level, i.e. below 1/1000) identifies failure domain. Note that failure domain in the Figure 80c is built in terms of  $(s_i, P_{N-1,i})$ . In reversed analysis failure domain can be built in terms of any input parameters regardless classification or physical meaning. For example, in the Figure 80d the failure domain is built in terms of normalized system pressure, cell height and fuel temperature, i.e. in terms of scenario parameter, deterministic parameter and input modelled parameter respectively. Here the domain colored in red corresponds to the combination of input parameters for which failure probability exceeds the screening frequency (i.e. failure domain). These results are only for demonstrative purpose. Refined final data will be provided later.

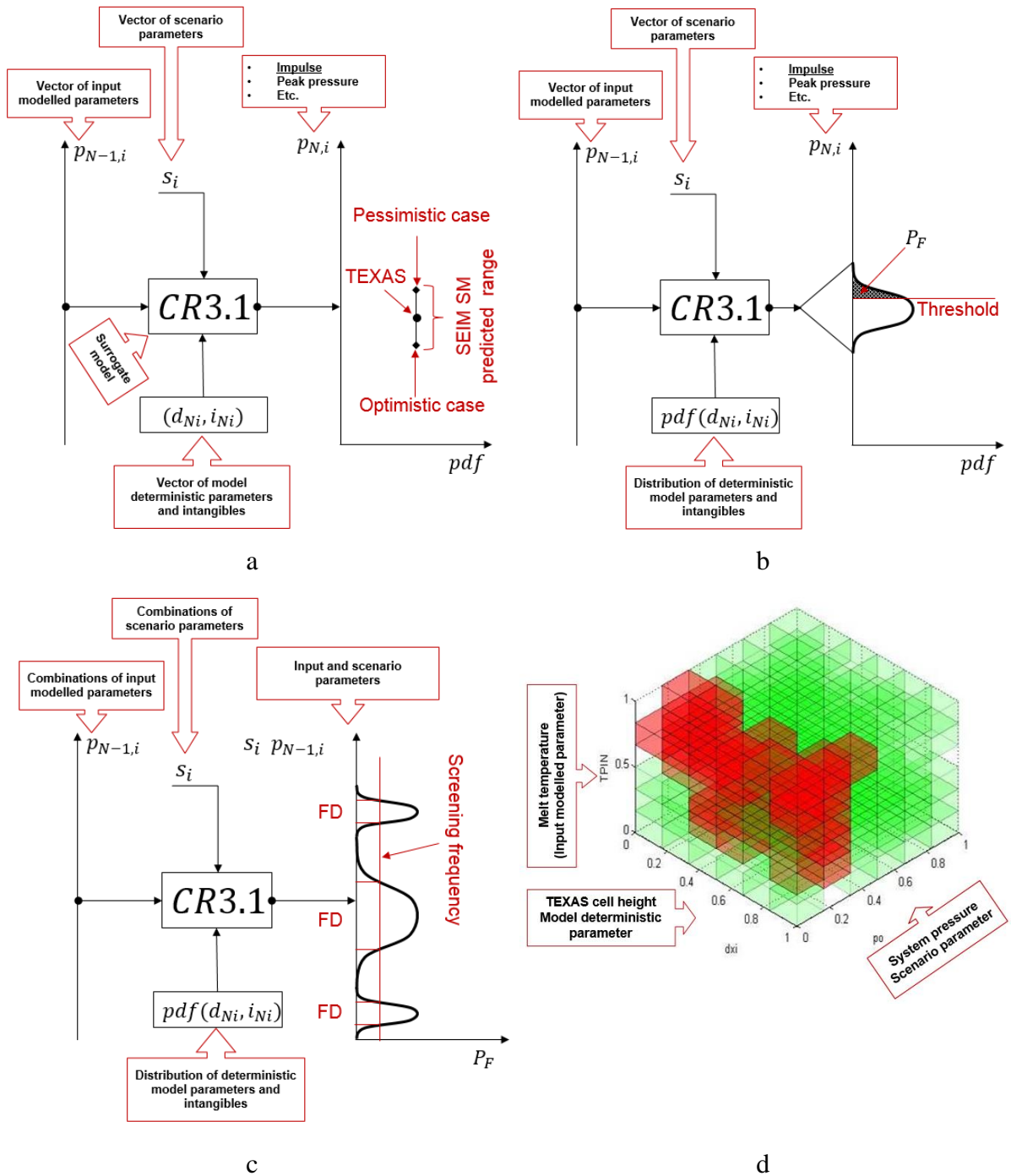


Figure 80: SEIM framework implementation

(a – deterministic output; b – failure probability; c – failure domain; d - example of failure domain in terms of three selected parameters for 300 mm jet diameter)

### **5.3 Sensitivity study of TEXAS-V**

In the scope of the study two bounding cases are approached: release of oxidic melt and release of metallic melt. Each case is further classified into 4 sets according to jet release diameter: 70 mm, i.e. Instrumentation Guide Tube (IGT) failure; 140 mm, i.e. Control Rod Guide Tube (CRGT) failure; 300 mm, i.e. large break; and 600 mm, i.e. catastrophic failure. The necessity for the classification is dictated by TEXAS code: different ranges of cell diameter are required for different ranges of jet diameters making these two parameters dependent. Therefore sensitivity study to both cell diameter and jet diameter can only be possible if ranges of these two parameters are set small enough to make them independent.

#### **5.3.1 Choice and classification of input parameters**

In total TEXAS-V input file contains more than 200 parameters for premixing and explosion modules. Among them sensible and physically meaningful parameters can be limited to around 50. After consideration of dependencies between parameters we have selected 21 of them for application in SM development and as a subject to sensitivity study. The complete list of parameters is provided in the Table 22 arranged according to classification in chapter 5.2.2.

Table 22: List of TEXAS-V parameters used in sensitivity study

Parameter	Units	Description
<b>Scenario parameters</b>		
po	Pa	Initial pressure
tlo	K	Water temeparture
xpw	m	Water level in the containment
tgo	K	Cover gas temperature
two	K	Wall temperature
<b>Input modelled parameters</b>		
RPARN	m	Fuel injection radius
CP	J/kg·K	Fuel capacity
RHOP	kg/m <sup>3</sup>	Fuel density
PHEAT	J/kg	Fuel latent heat
TMELT	K	Fuel melting temperature
TPIN	K	Fuel injection temperature
UPIN	m/sec	Fuel injection velocity
KFUEL		Fuel thermal conductivity
C(32)	J/m <sup>2</sup>	Fuel surface tension
<b>Deterministic parameters</b>		
dxl	m	Cell height
ariy	m <sup>2</sup>	Cell cross-section area
TMAX	sec	Premixing time
cfr	-	Proportional constant for rate of fuel fine fragmentation
rfrag	m	Initial size of fragmented particles
pold	Pa	Threshold pressure for film collapse
tfraglimt	s	Fuel fragmentation time interval

### 5.3.2 Implementation and results

The sensitivity study uses Morris method [79]; DAKOTA code [80] is applied to generate input dataset and Morris measures. Runs of TEXAS-V are performed automatically with a dedicated script. Two target functions are used for Morris measures estimation: (i) maximum pressure and (ii) integral impulse. The ongoing study implies cases containing up to 15000 of TEXAS-V runs.

One of the key guidance in the sensitivity study of a complex numerical model is necessity to identify possible sources of model stochastic behavior and minimize it in order to obtain

physically sensible results. The stochastic behavior of a deterministic model stems from the discrete and random treatment of the input in data sampling. This effect is demonstrated in the Figure 81. Here an explosion impulse from a single premixing case is built as a function of premixing duration (or triggering time). While the overall span of resulting impulses is large 10-25 kPa·s it is important to note that even for rather small deviation in premixing time about 100 ms the corresponding impulse can change from 16 to 25 kPa·s, i.e. by 36%. If triggering time is not optimized, the time dependence of the premixing conditions will most likely overwhelm effects of any other parameter and render the results of sensitivity study to physically senseless. The same is true in case of SM development and ANN training.

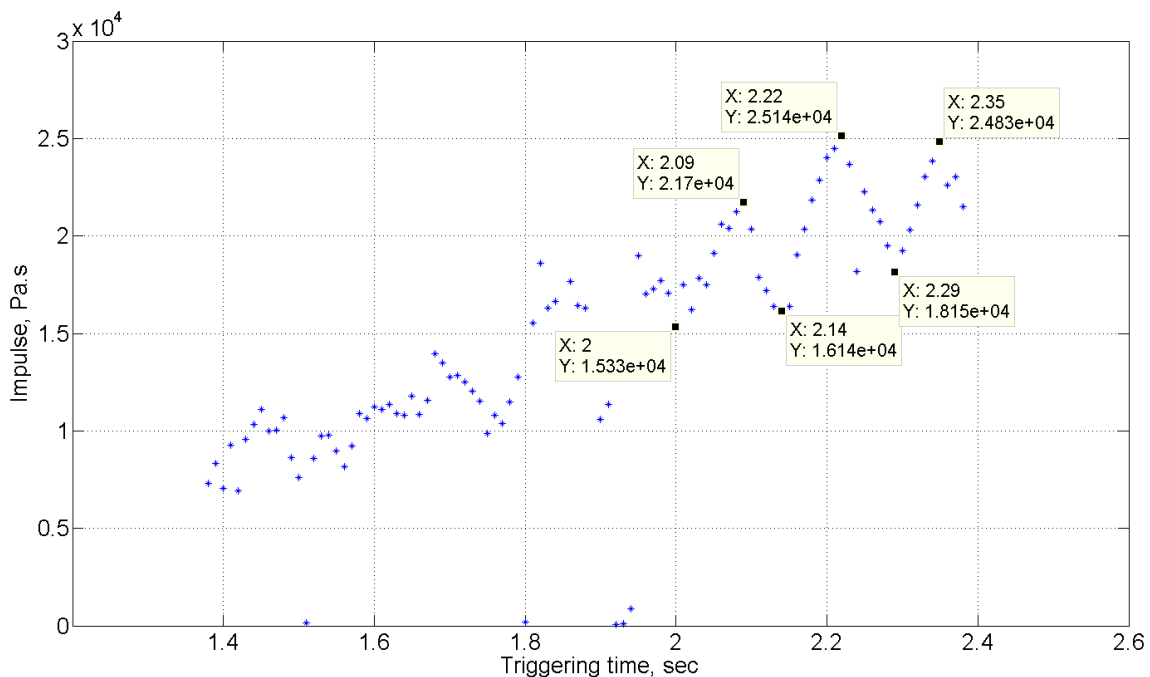


Figure 81: Explosion impulse predicted by TEXAS-V as a function of triggering time

In order to avoid such effects and to provide conservative assessment, optimization of parameters with respect to the impulse was applied. There are two TEXAS input parameters that require such optimization:

- Premixing time (TMAX, or time of the trigger)
- Time of fine fragmentation (TFRAGLIMT)

The latter, already mentioned in the chapter describing TEXAS-V, affects code failure behavior. Optimization of both parameters aims to obtain the maximum explosion impulse from a given premixing input list of TEXAS-V parameters and corresponding ranges used in the

sensitivity study is given in the below Table 23 and Table 24. These were identified for reference Nordic BWR based on available literature data and separate calculations by MELCOR for reallocated core mass and composition, FLUENT and PECM for thermal load and ANSYS for structural fragility and lower head failure.

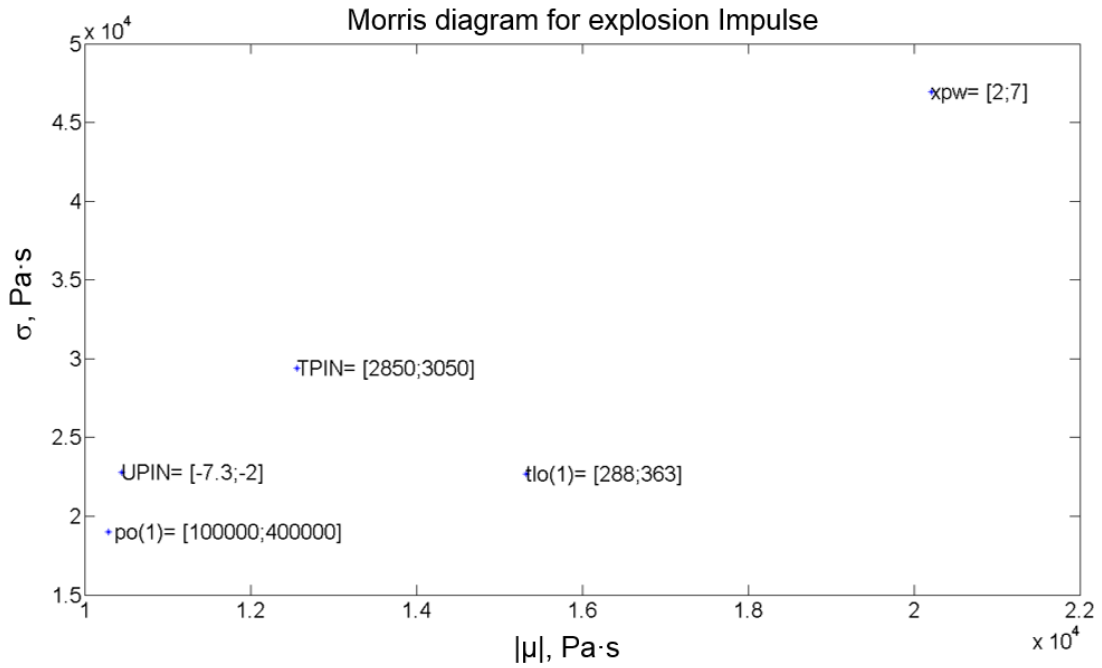
Table 23: List of scenario dependent parameters used in the sensitivity study

Parameter	units	Scenario I		Scenario II		Scenario III		Description
		max	min	max	min	max	min	
'ariy(1)='	m <sup>2</sup>	3	0.7	4.0	8.0	6.0	12.0	Cell cross-section area
'RPARN='	m	0.0735	0.0665	0.14	0.16	0.285	0.315	Fuel injection radius

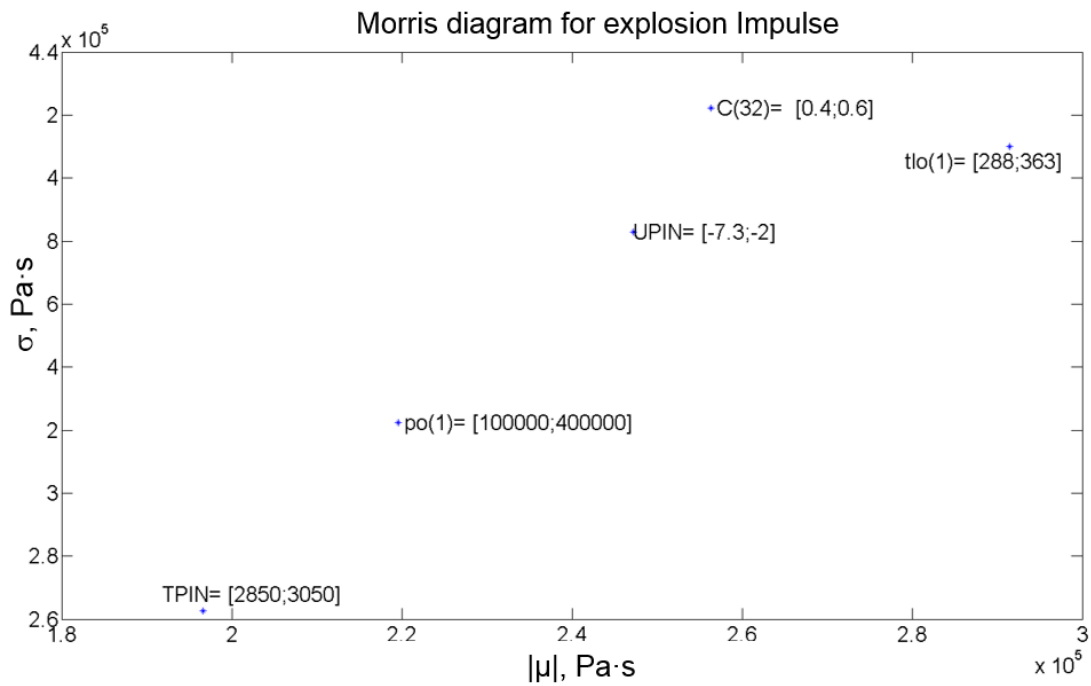
Table 24: List of scenario independent parameters used in the sensitivity study

Parameter	units	max	min	Description
'dxi(1)='	m	0.6	0.5	Cell height
'po(1)='	Pa	400000	100000	Initial pressure
'tlo(1)='	K	363	288	Water temperature
'CP='	J/kg·K	700	500	Fuel capacity
'RHOP='	kg/m <sup>3</sup>	8600	7600	Fuel density
'PHEAT='	J/kg	400000	280000	Fuel latent heat
'TMELT='	K	2800	2800	Fuel melting temperature
'TPIN='	K	30500	2850	Fuel injection temperature
'UPIN='	m/sec	-1.5	-7.4	Fuel injection velocity
'KFUEL='		2.0	7.0	Fuel thermal conductivity
'C(32)='	J/m <sup>2</sup>	0.6	0.4	Surface tension
'rfrag='	m	12E-05	8.0E-05	Initial size of fragmented particles
'cfr='	-	0.003	0.0015	Proportional constant in fine fragmentation model
'xpw='	m	7	2	Water level

Here we report results of sensitivity study only for two cases of melt jet release diameters: 300 and 500 mm and for the limited number of input parameters. Results for a complete set of parameters will become available later.



a

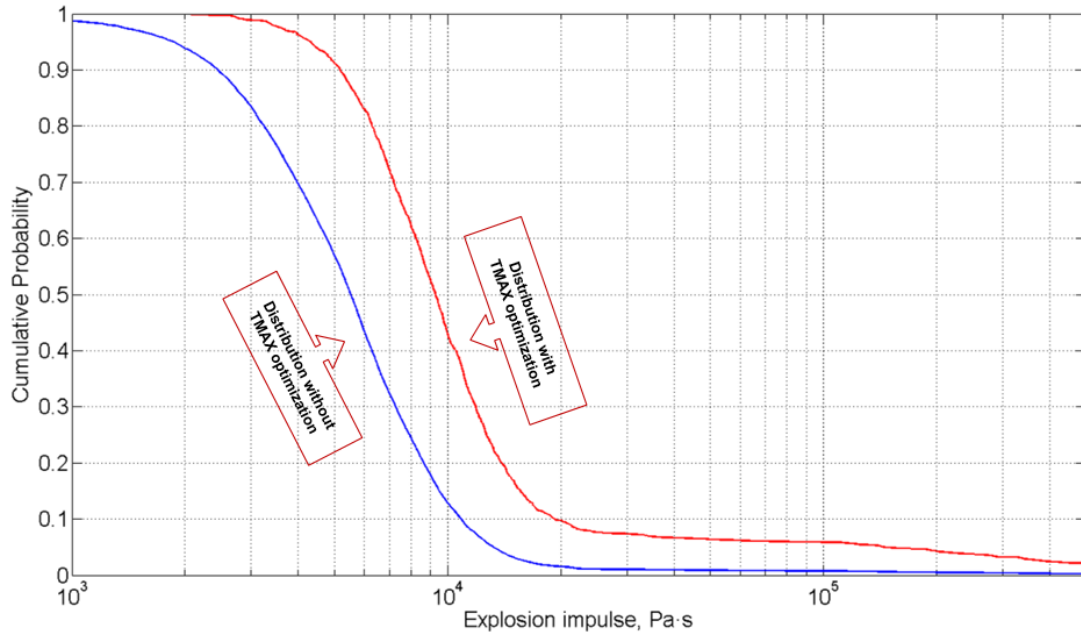


b

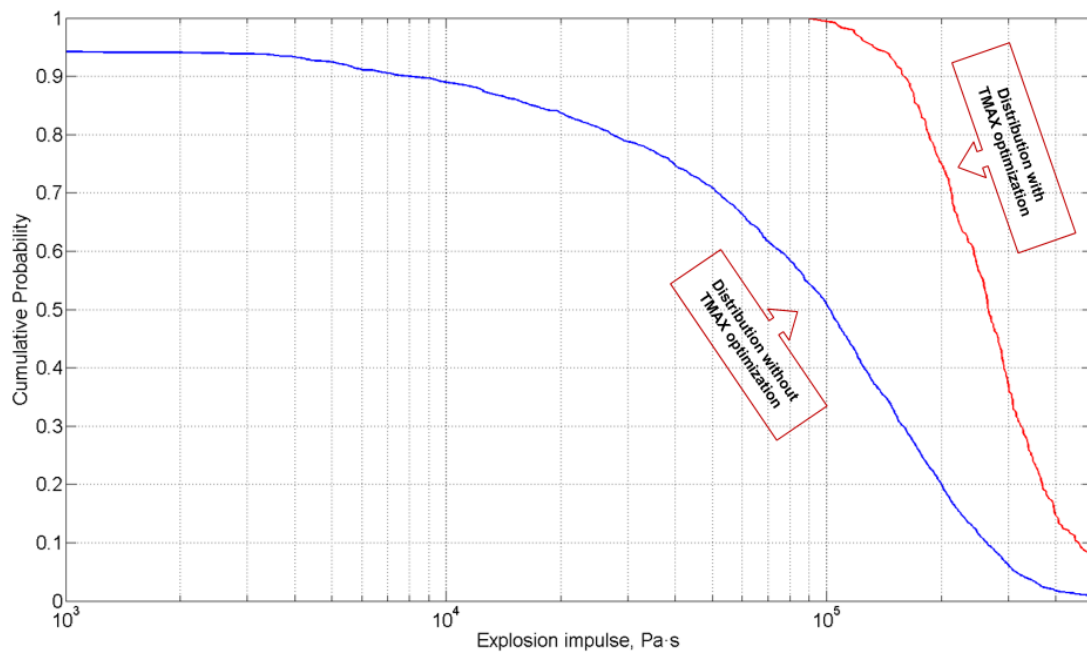
Figure 82: Morris diagrams for explosion impulse  
(a – 300 mm jet diameter; b – 500 mm jet diameter)

The two studies are different in terms of used parameters: in the 500 mm case water level was replaced with water surface tension. The effect of water level has been proved to be the most influential parameter out of considered in the first study and therefore it was replaced in the

following one. Other parameters are water temperature, melt inlet velocity, ambient pressure, and melt inlet temperature.



a



b

Figure 83: Cumulative density function for explosion impulse: a – 140 mm jet diameter; b – 500 mm jet diameter.

According to the results two most influential parameters are water level and water temperature. The former affects the total size of the premixture and system confinement, while the latter defines void condensation rate making both measures physically meaningful. Other parameters do not behave consistently between the cases and therefore require further clarifications.

It is valuable to further consider actual distribution of impulses provided by TEXAS-V for two bounding cases: 140 mm jet diameter and 500 mm jet diameter. Those are demonstrated in the Figure 83. Every plot contains 2 curves: one obtained without optimization of TMAX and another one with such optimization. Notice further that there is a large range of impulses spanned between the cases. For  $\varnothing 140$  mm jet, 10% of cases are characterized by impulses exceeding 20 kPa·s; for the 500 mm jet diameter this value is 450 kPa·s.

## **5.4 Summary and Outlook**

A robust algorithm has been developed to perform sensitivity study with TEXAS code. First data indicate that the most influential parameters are water level and water temperature, other potentially important parameters are melt superheat and melt surface tension. Some input parameters are not included yet in the analysis: emissivity, hydrogen generation. More work is to be done on assessments of the parameter ranges and their (sometimes hidden) dependencies.

Obtained database of impulse and pressure as a function of input TEXAS parameters is used for development of the SEIM surrogate model. The current work has demonstrated plausibility of the SEIM framework and its implementation.

Further work will be directed towards: (i) finalization of the sensitivity study aiming to cover completely all cases of melt ejection mode and vessel failure scenarios; (ii) refinement and generalization of the surrogate model; (iii) development of robust approach to demonstrate failure domain in a multidimensional space of input parameters; (iv) development of automatic methodology to group and classify failure scenarios based on the failure domain analysis and dependences between scenario and input modelled parameters.

## 6 Summary and Outlook

This work is motivated by the severe accident management strategy adopted in Nordic type BWRs. The goal of the project is to reduce uncertainties in assessment of (i) debris bed properties and coolability, (ii) steam explosion impact. In the experimental part of the project we investigate key physical phenomena of the debris bed formation and coolability, and producing experimental data for validation of simulation tools. Analytical approaches are employed to assess the uncertainties in modelling of debris bed coolability and steam explosion impact.

### **Investigation of debris agglomeration**

Confirmatory series of the DEFOR-A tests is carried out with high melting temperature simulant ( $ZrO_2-WO_3$ ) material. We consider the effects of the melt material, melt superheat, initial jet velocity on the (i) fraction of agglomerated debris, (ii) particle size distribution, (iii) ablation and plugging of the nozzle for the melt release. Several DEFOR-A (Debris Bed Formation – Agglomeration) tests have been carried out with melt release under water (DEFOR-A14 - A21). On average larger particles are obtained in the tests with melt release under water, than in the previous test series (DEFOR-A10 - A13) with melt release above water level, where we found no significant influence of the jet velocity on the particle size distributions. We also confirmed that there is no visible effect of the initial jet velocity on debris agglomeration. Melt superheat is the most important factor for the fraction of agglomerated debris. It also affects ablation and plugging phenomena of the nozzle made of lower melting temperature metals. Further tests would be needed to collect systematic experimental data necessary for validation of the models and codes.

### **Analysis of debris bed coolability**

In this work we further develop DECOSIM code to address (i) debris bed coolability in post-dryout regime; (ii) particulate debris spreading with possible feedbacks between dryout and spreading effectiveness. An analytical model is proposed based on the analysis of DECOSIM calculations for prediction of the maximum temperature of the debris if the size of the dry zone is known. Excellent agreement with the DECOSIM data is demonstrated.

The DECOSIM was validated against new COOLOCE data for different spatial configurations: (i) cylindrical debris bed with open side walls (COOLOCE-10), (ii) conical bed on a cylindrical

base (COOLOCE-12). The dependence of DHF on system pressure from COOLOCE experiments can be reproduced quite accurately if either the effective particle diameter or debris bed porosity is increased, which is consistent with MEWA simulation results reported in [70]. It is interesting to note that, despite the difficulty in predicting the absolute values of dryout heat flux due to high sensitivity of results to the values of debris bed porosity and particle diameter, the relative improvement of debris bed coolability for conical debris bed in comparison with flat (or cylindrical, behaving effectively as a flat) debris bed is captured quite well in the simulations. Further work would be necessary in order to utilize recently produced COOLOCE data for validation of the DECOSIM.

An analytical model based on observations of the solutions for the structure of the dry zone has been proposed in order to predict the maximum temperature reached at the top boundary of the debris bed. Comparison of the DECOSIM simulations carried out for conical and mound-shaped debris beds suggest that the analytical formula predicts quite well the maximum temperature rise in the debris bed. Importantly, the results are practically independent of debris bed shape and involve only few parameters, which reduce the uncertainties in the estimation of post-dryout behavior of debris beds. Further development and verification of the computationally efficient and sufficiently accurate simplified (surrogate) models would be necessary in order to employ the models in the uncertainty and risk analysis for different plant accident scenario conditions.

Empirical closure obtained in PDS-C experiments were implemented in DECOSIM in order to enable simulations of debris beds with evolving (due to particle spreading) geometry. Implementation of particle spreading algorithm in DECOSIM was verified against the 1D numerical model which solves the equation for debris bed height which is, essentially, a debris mass conservation equation. Good agreement between the maximum debris bed heights as functions of time calculated by DECOSIM and that from 1D model was demonstrated, as well as the shapes of debris bed at selected times were found to practically coincide. Few preliminary fully coupled DECOSIM simulations of debris bed were performed in which the superficial gas velocity and gas parameters involved in the correlation for the lateral particle flux were obtained from the two-phase flow model. Simulations were carried out and maximum temperatures of solid material were compared in the cases with and without particle spreading. Results suggest that spreading can enhance coolability for particles larger than 1.5 mm. Further studies are necessary in order to quantify the effect of the dry zone on debris bed spreading and coolability.

**Investigation of particulate debris spreading**

Boiling and two-phase flow inside the bed is a source of mechanical energy which can help to spread the debris bed by so called “self-leveling” phenomenon. The goal of this work is to quantify time scale for particulate debris spreading. Experimental studies have been carried out in PDS-C facility with air injection from the bottom of the debris bed. Based on the experimental data an analytical approach is developed by KTH to simulate particulate debris spreading.

Previously exploratory tests were carried out in PDS facilities in order to identify governing phenomena of particulate debris spreading. Also we addressed potential effect of the mockups of the COOLOCE heaters and TCs on the particle self-leveling process. Results suggested that there is no significant influence on the self-leveling for the considered ranges of the air injection velocities [35].

In this work a set of PDS-C experiments has been carried out with different stainless steel particles in order to quantify particle flow rate in debris bed self-levelling phenomenon. A scaling approach for particulate debris spreading has been proposed. Application of proposed scaling approach to generalization of the PDS-C tests results in dense clustering of the non-dimensional data suggesting that the most important physical phenomena are captured properly in the approach. Based on the scaling and on the PDS-C experimental data a universal semi-empirical closure has been developed for prediction of the debris mass flux as a function of local slope angle, gas flowrate, and debris bed properties. More tests would be necessary with particles made of different material, mixtures of particles with different sizes and irregular shapes, etc. in order to extend empirical database for validation of the proposed closure.

**Analysis of steam explosion in a Nordic BWR containment**

In this work we develop an approach for analysis of steam explosion sensitivity to the modeling and scenario parameters using TEXAS code. The approach is based on sampling of the input parameters within selected ranges in order to obtain statistical characteristics of the model response. Preliminary analysis helps to identify the most and the least important parameters. Obtained database of solutions for the impulse and pressure as a function of the TEXAS input parameters is used for development of a computationally efficient surrogate model. Further work is necessary for (i) selection and justification of the parameter ranges and clarification of

their potential inter-dependencies; (ii) continuation of the sensitivity study in order to cover remaining cases of melt ejection scenarios; (iii) refinement and generalization of the surrogate model; (iv) development of robust approach to demonstrate failure domain in a multidimensional space of input parameters; (v) development of methodology for grouping and classification of failure scenarios considering the failure domain and interdependences between scenario and input modelled parameters.

## 7 Nomenclature

$Ar_{lg}$	Air phase Archimedes number with liquid-buoyed solids, [-]
$d_p$	Equivolume sphere diameter, [mm]
$F_B$	Buoyancy force, [N]
$F_D$	Aerodynamic drag force, [N]
$F_{Fr}$	Inter-particle friction force, [N]
$F_G$	Gravity force, [N]
$k_{Fr}$	Friction coefficient [-]
$L$	Facility total length, [mm]
$Q_g$	Non-dimensional superficial gas velocity, [-]
$Q_p$	Particle mass flow per unit width, [kg/(m · s)]
$Q_p^*$	Non-dimensional normalized $Q_p$ , [-]
$Re_{gmf}$	Air Reynolds number at minimum 3-phase Fluidization, [-]
$U_g$	Superficial gas velocity, [m/s]
$U_{mf}$	Superficial gas velocity at minimum 3-phase fluidization, [m/s]
<i>Greek letters</i>	
$\varepsilon$	Bed porosity, [-]
$\mu_g$	Air viscosity, [Pa s]
$\rho_g$	Air density, [kg/m <sup>3</sup> ]
$\rho_l$	Liquid density, [kg/m <sup>3</sup> ]
$\rho_p$	Solid particle density, [kg/m <sup>3</sup> ]
$\theta_{rep}$	Repose angle, [degree]
$\phi$	Heap slope angle, [degree]
$\Phi$	Normalized slope angle [-]

## **8 Acknowledgement**

The work is carried out with support of the MSWI-APRI-8 project at KTH.

NKS conveys its gratitude to all organizations and persons who by means of financial support or contributions in kind have made the work presented in this report possible.

## **9 Disclaimer**

The views expressed in this document remain the responsibility of the author(s) and do not necessarily reflect those of NKS. In particular, neither NKS nor any other organization or body supporting NKS activities can be held responsible for the material presented in this report.

## 10 REFERENCES

- [1] Takasuo E., Kinnunen T., Pankkoski H. and Holmström S., “Description of the COOLOCE test facility – Conical particle bed”, VTT report VTT-R-08956-10 (2010).
- [2] Takasuo E., Kinnunen T., Pankkoski H. and Holmström S., reports VTT-R-07097-11 and VTT-R-02427-11 on experiments on coolability of conical particle bed, VTT (2011).
- [3] Konovalenko A., Basso S., Karbojian A. and Kudinov P., “Experimental and Analytical Study of the Particulate Debris Bed Self-leveling”, NUTHOS-9, N9P0305 (2012).
- [4] Alpine Hosokawa supplier of the powerbeads, <http://www.alpinehosokawa.com>
- [5] Private communication with VTT.
- [6] Cheng A. *et al*, “An experimental investigation on self-leveling behavior of debris beds using gas injection”, *Experimental Thermal and Fluid Science*, 48, pp. 110-121 (2013).
- [7] Yakush S., Lubchenko N., and Kudinov P., “Risk-Informed Approach to Debris Bed Coolability Issue,” *Proceedings of the 20th International Conference on Nuclear Engineering (ICONE-20)*, Anaheim, CA, USA, July 30 - August 3, Paper 55186 (2012).
- [8] Hofmann G., “On the location and mechanisms of dryout in top-fed and bottom-fed”, *Nuclear Technology*, 65, (1984).
- [9] Zhang J.-P., Epstein N., Grace J. R., “Minimum fluidization velocities for gas-liquid-solid three phase systems”, *Powder Technology*, 100(2-3), pp. 113-1118, (1998).
- [10] Yakush S., Lubchenko N., and Kudinov P., “Surrogate models for debris bed dryout”, *NURETH15-278*, (2013).
- [11] Britter R.E., “The spread of a negatively buoyant plume in a calm environment,” *Atmospheric Environment*, 13, pp. 1241-1247, 1979.
- [12] Budu A., “Debris Bed Formation at Low Temperature (DEFOR-LT experiment): Coolant flow influence on debris packing,” *SARNET mobility research report*, Division of Nuclear Power Safety KTH, Stockholm, 2008.
- [13] Dombrovsky L.A., Davydov M.V., Kudinov P., “Thermal radiation modeling in numerical simulation of melt-coolant interaction,” *Comp. Therm. Sci.* **1** (1) 2009, pp. 1-35.

- [14] Dombrovsky L.A., Davydov M.V., and Kudinov P., Thermal radiation modeling in numerical simulation of melt-coolant interaction, Proc. Int. Symp. Adv. Comput. Heat Transfer (CHT-08), May 11–16, 2008, paper 155.
- [15] Dinh T.N., Konvalikhin M.J., Sehgal B.R., “Core melt spreading on a reactor containment floor,” Progress in Nuclear Energy, 36 (4), pp. 405-468, 2000.
- [16] Frid W. and Kudinov P., “Ex-Vessel Melt Coolability Issue in BWRs with Deep Water Pool in Lower Drywell,” OECD/NEA MCCI Seminar 2010, Cadarache, France, 15th - 17th November, 2010.
- [17] Frost D.L., Brucker B., Ciccarelli P., “Effect of Boundary Conditions on the Propagation of a Vapor Explosion in Stratified Molten Tin/Water Systems,” Nuclear Engineering and Design 155, 311-333, 1995.
- [18] Fröhlich G., “Interaction Experiments between Water and hot Melts in Entrapment and Stratification Configurations,” Chemical Geology, 62, 137-147, 1987.
- [19] Herbert E., “The propagation of two-dimensional and axisymmetric viscous gravity currents over a rigid horizontal surface,” *J. Fluid Mech.*, **121**, pp. 43-58, 1982.
- [20] Huppert H., “Flow and instability of a viscous current down a slope,” *Nature*, **300**, pp. 427-429, 1982.
- [21] Karbojian A., Ma W.M., Kudinov P., Davydov M. and Dinh N., “A scoping study of debris formation in DEFOR experimental facility”, 15th International Conference on Nuclear Engineering, Nagoya, Japan, April 22-26, 2007, Paper number ICON15-10620.
- [22] Karbojian A., Ma W., Kudinov P., and Dinh T.-N., “A Scoping Study of Debris Bed Formation in the DEFOR Test Facility”, Nuclear Engineering and Design, **239**, 2009, 1653-1659.
- [23] Kudinov P. and Davydov M., “Approach to Prediction of Melt Debris Agglomeration Modes in a LWR Severe Accident,” Proceedings of ISAMM-2009, Böttstein, Switzerland, October 26 - 28, 2009.
- [24] Kudinov P. and Davydov M., “Development of Ex-Vessel Debris Agglomeration Mode Map for a LWR Severe Accident Conditions,” Proceedings of the 17th International Conference on Nuclear Engineering, July 12-16, 2009, Brussels, Belgium, Paper ICONE17-75080.
- [25] Kudinov P. and Davydov M., “Development and Validation of the Approach to Prediction of Mass Fraction of Agglomerated Debris,” The 8th International Topical Meeting on Nuclear Thermal-Hydraulics, Operation and Safety (NUTHOS-8), Shanghai, China, October 10-14, N8P0298, 2010.

- [26] Kudinov P. and Dinh T.-N., “A Computational Study of Debris Bed Formation,” ANS Transactions, 2008, paper 193463.
- [27] Kudinov P. and Dinh T.-N., “An analytical study of mechanisms that govern debris packing in a LWR severe accident”, The 12th International Topical Meeting on Nuclear Reactor Thermal Hydraulics (NURETH-12), Sheraton Station Square, Pittsburgh, Pennsylvania, U.S.A. September 30-October 4, 2007. Paper 247.
- [28] Kudinov P., Karbojian A., Ma W.M., Davydov M., and Dinh T.-N., “A Study of Ex-Vessel Debris Formation in a LWR Severe Accident”, Proceedings of ICAPP 2007, Nice, France, May 13-18, 2007, Paper 7512.
- [29] Kudinov P., Karbojian A., Ma W.M., Dinh T.-N., “*The DEFOR-S experimental study of debris formation with corium simulant materials,*” Nuclear Technology, **170**, 2010.
- [30] Kudinov P., Karbojian A., Ma W., and Dinh T.-N. “The DEFOR-S Experimental Study of Debris Formation with Corium Simulant Materials,” Nuclear Technology, 170(1), April 2010, pp. 219-230, 2010.
- [31] Kudinov, P., Karbojian, Tran, C.-T., Villanueva, W., 2013. Agglomeration and size distribution of debris in DEFOR-A experiments with Bi<sub>2</sub>O<sub>3</sub>-WO<sub>3</sub> corium simulant melt. Nuclear Engineering and Design, 263, pp. 284-295.
- [32] Kudinov P., Karbojian A., Tran C.-T., “Experimental Investigation of Melt Debris Agglomeration with High Melting Temperature Simulant Materials,” Proceedings of ISAMM-2009, Böttstein, Switzerland, October 26 - 28, 2009.
- [33] Kudinov P., Karbojian A., Tran C.-T., Villanueva W., “The DEFOR-A Experiment on Fraction of Agglomerated Debris as a Function of Water Pool Depth,” The 8th International Topical Meeting on Nuclear Thermal-Hydraulics, Operation and Safety (NUTHOS-8), Shanghai, China, October 10-14, N8P0296, 2010.
- [34] Kudinov P., Karbojian A., Ma W.M., and Dinh T.-N., “An experimental study on debris formation with corium simulant materials,” Proc. ICAPP’08, Anaheim, CA USA, June 8–12, 2008, paper 8390.
- [35] Kudinov P., Konovalenko A., Grishchenko D., Yakush S., Basso S., Lubchenko N., Karbojian A., “Investigation of debris bed formation, spreading and coolability.” NKS-DECOSE Project Report, 88p., June 2013.
- [36] Kudinov P. and Kudinova V., “Influence of Water Subcooling on Fracture of Melt Debris Particle,” ANS Transactions, 2009, paper 210646.

- [37] Kudinov P., Ma W.M., Tran C.-T., Hansson R., Karbojian A., Dinh T.-N. “Multiscale Phenomena of Severe Accident,” NKS-R and NKS-B Joint Summary Seminar, Armémuseum, Stockholm, 26th - 27th March 2009.
- [38] Kudinov P., “Decomposition, Validation and Synthesis in Multiscale Problems of Severe Accident Analysis,” Verification and Validation for Nuclear Systems Analysis Workshop, Center for Higher Education, Idaho Falls, ID, July 21 - July 25, 2008.
- [39] Kudinov P., Kudinova V., and Dinh T.-N., “Molten Oxidic Particle Fracture during Quenching in Water,” 7th International Conference on Multiphase Flow ICMF 2010, Tampa, FL USA, May 30-June 4, 2010.
- [40] Lundström P., Tuomisto H. and Theofanous T.G., “Integration of severe accident assessment and management to fulfill the safety goals for the Loviisa NPP,” International Topical Meeting on Probabilistic Safety Assessment, Park City, Utah, USA, September 29 - October 3, 1996.
- [41] Morris M. D., “Factorial sampling plans for preliminary computational experiments,” *Technometrics*, Vol. 33, No. 2, 1991, pp. 161–174.
- [42] PLINIUS FP6. Final Report. “Transnational Access to the Prototypic Corium Platform PLINIUS”, <http://www.plinius.eu>
- [43] Saltelli A., Tarantola S., Campolongo F., Ratto M., *Sensitivity Analysis in Practice*. John Wiley & Sons, Ltd, 2004, 94 p.
- [44] Shetty S. A. and Cerro R. L., “Spreading of a point source over inclined solid surfaces,” *Ind. Eng. Chem. Res.*, **34**, pp. 4078-4086, 1995.
- [45] Theofanous T. G., “On Proper Formulation of Safety Goals and Assessment of Safety Margins for Rare and High-Consequence Hazards,” *Reliability Engineering and System Safety* 54, pp. 243-257, 1996.
- [46] Theofanous T. G. and Dinh T.-N., “Integration of multiphase Science and Technology with Risk management In Nuclear Power reactors: Application of the Risk-Oriented Accident Analysis Methodology to the Economic, Simplified Boiling Water Reactor Design,” *Multiphase Science and Technology*, V20(2), Pages 81-211, 2008.
- [47] Vella D. and Huppert H. E., “Gravity currents in a porous medium at an inclined plane,” *J. Fluid Mech.*, **555**, pp. 353-362, 2006.
- [48] Yakush S. and Kudinov P., “Simulation of Ex-Vessel Debris Bed Formation and Coolability in a LWR Severe Accident,” *Proceedings of ISAMM-2009*, Böttstein, Switzerland, October 26 - 28, 2009.

- [49] Yakush S. and Kudinov P., “Transient Phenomena of Ex-vessel Debris Bed Formation in a LWR Severe Accident,” ANS Transactions, 2009, paper 210830.
- [50] Yakush S., Kudinov P., and Dinh T.-N., “Modeling of Two-Phase Natural Convection Flows in a Water Pool with a Decay-Heated Debris Bed,” Proc. ICAPP’08, Anaheim, CA USA, June 8–12, 2008, paper 8409.
- [51] Yakush S., Kudinov P., and Dinh T.-N., “Multiscale Simulations of Self-organization Phenomena in the Formation and Coolability of Corium Debris Bed,” Proc. The 13th International Topical Meeting on Nuclear Reactor Thermal Hydraulics (NURETH-13), September 27-October 2, 2009. Kanazawa City, Ishikawa Prefecture, Japan, Paper N13P1143.
- [52] Robb K., Corradini M., “Melt eruption modeling for MCCI simulations”, *The 14th International Topical Meeting on Nuclear Reactor Thermalhydraulics, NURETH-14 290*, Toronto, Ontario, Canada, September 25-30 (2011).
- [53] Yakush S., Lubchenko N., and Kudinov P., “Risk-Informed Approach to Debris Bed Coolability Issue,” Proceedings of the 20th International Conference on Nuclear Engineering (ICONE-20), Anaheim, CA, USA, July 30 - August 3, Paper 55186 (2012).
- [54] Yakush S. and Kudinov P., “Effects of Water Pool Subcooling on the Debris Bed Spreading by Coolant Flow,” ICAPP Proc., Paper 11416, 2011.
- [55] Hofmann G., “On the location and mechanisms of dryout in top-fed and bottom-fed”, *Nuclear Technology*, 65, (1984).
- [56] Zhang J.-P., Epstein N., Grace J. R., “Minimum fluidization velocities for gas-liquid-solid three phase systems”, *Powder Technology*, 100(2-3), pp. 113-1118, (1998).
- [57] Kubasch Jens H., “Bubble Hydrodynamics in Large Pools”, PhD thesis, ETH, Zurich, (2001).
- [58] Ergün S., “Fluid Flow through Packed Columns,” *Chemical Engineering Progress*, Vol. 48, 2, pp. 89-94 (1952).
- [59] Reed A.W., “The Effect of Channelling on the Dryout of Heated Particulate Beds Immersed in a Liquid Pool,” Ph.D. Thesis, Massachusetts Institute of Technology, Cambridge, 1982.
- [60] Bürger M., Buck M., Schmidt W., and Widmann W., “Validation and Application of the WABE code: Investigations of Constitutive Laws and 2D effects on Debris Coolability,” *Nuclear Engineering and Design*, Vol. 236, pp. 2164–2188 (2006).

- [61] Hu K. and Theofanous, T.G., “On the Measurement and Mechanism of Dryout in Volumetrically Heated Coarse Particle Beds,” *Int. J. Multiphase Flow*, Vol. 17, No. 4, pp. 519–532 (1991).
- [62] IAPWS, The International Association for the Properties of Water and Steam, <http://www.iapws.org>.
- [63] Thakre S., Ma W., Kudinov P., and Bechta S., “Study on Effective Particle Diameters and Coolability of Particulate Beds Packed with Irregular Multi-size Particles,” APRI-8, NKS-DECOSE Project Report, NKS-288, 2013.
- [64] Takasuo E., Kinnunen T. Pankakoski P.H., Holmström S., “The COOLOCE particle bed coolability experiments with a cylindrical geometry: Test series 3–5,” Research Report VTT-R-07099-11. Espoo, 2011. 27 p.
- [65] Takasuo E., Kinnunen T. Pankakoski P.H., Holmström S., “The COOLOCE particle bed coolability experiments with a conical geometry: Test series 6–7,” Research Report VTT-R-07097-11. Espoo, 2011. 26 p.
- [66] Takasuo E., Kinnunen T., and Holmström S., “COOLOCE particle bed coolability experiments with a cylindrical test bed: Test series 8–9,” Research Report VTT-R-07224-12. Espoo, 2012. 44 p.
- [67] Takasuo E., Holmström S., Kinnunen T., and Pankakoski P.H., “The COOLOCE experiments investigating the dryout power in debris beds of heap-like and cylindrical geometries,” *Nuclear Engineering and Design* 250 (2012), p. 687-700.
- [68] Takasuo E., Kinnunen T., Lehtikuusi, T., and Holmström S., “COOLOCE coolability experiments with a cylindrical debris bed and lateral flooding: COOLOCE-10,” Research Report VTT-R-00463-13. Espoo, 2013. 19 p.
- [69] Takasuo E., Kinnunen T., Lehtikuusi, T., and Holmström S., “COOLOCE-12 debris bed coolability experiment: cone on a cylindrical base,” Research Report VTT-R-07967-13. Espoo, 21 p.
- [70] Takasuo E., “Debris Coolability Simulations with Different Particle Materials and Comparisons to COOLOCE Experiments,” VTT report VTTOR-00257-13 (2013).
- [71] Tung, V.X. and Dhir, V.K., “A hydrodynamic model for two-phase flow through porous media,” *Int. J. Multiphase Flow* Vol. 14, No. 1, pp. 47–65 (1988).
- [72] Schmidt W., “Interfacial drag of two-phase flow in porous media,” *Int. J. Multiphase Flow*, Vol. 33, pp. 638–657 (2007).

- [73] Yakush S.E., Lubchenko N.T., and Kudinov P., “Surrogate Models for Debris Bed Dryout,” Proc. 15th International Topical Meeting on Nuclear Reactor Thermalhydraulics (NURETH-15), paper NURETH15-278, 16 pp.
- [74] Yakush S. and Kudinov P., “A Model for Prediction of Maximum Post-Dryout Temperature in Decay-Heated Debris Bed,” Proceedings of the 22th International Conference on Nuclear Engineering (ICONE-22), Prague, Czech Republic, July 7 –11, Paper 31214 (2014), 11 pp.
- [75] Chu, C.C., “One dimensional transient fluid model for fuel-coolant interaction,” 1986, university of Wisconsin-Madison.
- [76] Pilch, M., “Acceleration induced fragmentation of liquid drops,” 1981, University of Virginia.
- [77] Tang, J., “Modeling of the complete process of one-dimensional vapor explosions,” 1993, University of Wisconsin-Madison.
- [78] Kim, B.J., “Heat transfer and fluid flow aspect of small-scale single droplet fuel-coolant interaction,” 1985, University of Wisconsin-Madison.
- [79] Saltelli, A., et al., “Sensitivity analysis in practice: a guide to assessing scientific models,” 2004: John Wiley & Sons Inc. 219.
- [80] Adams, B.M., Bauman, L.E., Bohnhoff, W.J., Dalbey, K.R., Ebeida, M.S., Eddy, J.P., Eldred, M.S., Hough, P.D., Hu, K.T., Jakeman, J.D., Swiler, L.P., and Vigil, D.M., “DAKOTA, A Multilevel Parallel Object-Oriented Framework for Design Optimization, Parameter Estimation, Uncertainty Quantification, and Sensitivity Analysis: Version 5.4 User's Manual,” Sandia Technical Report SAND2010-2183, December 2009. Updated April 2013
- [81] S. Yakush, N. Lubchenko, and P. Kudinov, “Risk-Informed Approach to Debris Bed Coolability Issue”, *Proceedings of the 20th International Conference on Nuclear Engineering (ICONE-20)*, Anaheim, CA, USA, July 30 - August 3, Paper 55186 (2012).
- [82] B. Zhang, T. Harada., D. Hirahara, T. Matsumoto, K. Morita., K. Fukuda, H. Yamano, T. Suzuki, Y. Tobita, ”Self-Leveling Onset Criteria in Debris Beds”, *J. Nuclear Science and Technlogy*, **vol. 47**, 384 (2010).
- [83] B. Zhang, T. Harada., D. Hirahara, T. Matsumoto, K. Morita., K. Fukuda, H. Yamano, T. Suzuki, Y. Tobita, “Experimental investigation on self-leveling behavior in debris beds”, *Nuclear Engineering and Design*, **vol. 241**, 1, 366 (2011).
- [84] S. Cheng, H. Tagami, H. Yamano, T. Suzuki, Y. Tobita, B. Zhang, T. Marsumoto and K. Morita, “Evaluation of debris bed self-leveling behavior: A simple empirical approach and its validations”, *Annals of Nuclear Energy*, **vol. 63**, 188 (2014).

- [85] S. Cheng, H. Yamano, T. Suzuki, Y. Tobita, Y. Gonda, Y. Nakamura, B. Zhang, T. Matsumoto and K. Morita “An experimental investigation on self-leveling behavior of debris beds using gas-injection”, *Experimental Thermal and Fluid Science*, **vol. 48**, 110 (2013).
- [86] S. Cheng, Y. Tanaka, Y. Gondai, T. Kai, B. Zhang, T. Matsumoto, K. Morita, K. Fukuda, H. Yamano, T. Suzuki and Y. Tobita, “Experimental Studies and Empirical Models for the Transient Self-Leveling Behavior in Debris Bed”, *Journal of Nuclear Science and Technology*, **vol. 48**, 10, 1327 (2011).
- [87] D. Magallon, H. Hohmann, H. Schins, “Pouring of 100 kg scale molten UO<sub>2</sub> into sodium”, *Nuclear Technology*, **vol. 98**, 1, 79 (1992).
- [88] J.C. Hesson, R. H. Sevy, T. J. Marciniak, “Post- Accident Heat Removal in LMFBRs. In vessel consideration”, ANL-7859, Argonne National Laboratory, USA (1971).
- [89] J.D. Gabor, “Simulation Experiments for Internal Heat Generation, Reactor Development Program Progress”, ANL-RDP-32, Argonne National Laboratory, USA (1974).
- [90] A. Konovalenko, S. Basso and P. Kudinov, “Experimental and Analytical Study of the Particulate Debris Bed Self-leveling”, *The 9th International Topical Meeting on Nuclear Thermal-Hydraulics, Operation and Safety (NUTHOS-9)*, Kaohsiung, Taiwan, September 9-13, (2012).
- [91] D. Doppler, P. Gondret, T. Loiseux, S. Meyer and M. Rabaud, “Relaxation dynamics of water immersed granular avalanches”, *J. Fluid. Mech.*, **vol. 577**, 161 (2007).
- [92] J. Zhang, N. Epstein and J. Grace, “Minimum fluidization velocities for gas-liquid-solid three-phase systems”, *Powder Technology*, **vol. 100**, 113 (1998).
- [93] E. Buckingham, “On Physically Similar Systems; Illustrations of the Use of Dimensional Equations”, *Phys. Rev.*, **vol. 4**, 4, 345 (1914).
- [94] I. Eames and M. Gilbertson, “Aerated granular flow over a horizontal rigid surface”, *J. Fluid Mech.* **vol. 424**, 169 (2000).
- [95] D. Robinson and S. Friedman, “Observations of the effects of particle shape and particle size distribution on avalanching of granular media”, *Physica A: Statistical Mechanics and its Applications*, **vol. 311**, 1, 97 (2002).
- [96] S. Basso, A. Konovalenko and P. Kudinov “Sensitivity and uncertainty analysis for predication of particulate debris bed self-leveling in prototypic SA conditions”, *International Congress on Advances in Nuclear Power Plants (ICAPP)*, Charlotte, USA April 6-9 Paper 14329 (2014).

## **APPENDIX 1**

Title	Analysis of Debris Bed Formation, Spreading, Coolability, and Steam Explosion in Nordic BWRs
Author(s)	Pavel Kudinov <sup>1</sup> , Alexander Konovalenko <sup>1</sup> , Dmitry Grishchenko <sup>1</sup> , Sergey Yakush <sup>2</sup> , Simone Basso <sup>1</sup> , Nazar Lubchenko <sup>3</sup> , Aram Karbojian <sup>1</sup>
Affiliation(s)	<sup>1</sup> Division of Nuclear Power Safety (NPS), Royal Institute of Technology (KTH), Stockholm <sup>2</sup> Institute for Problems in Mechanics of the Russian Academy of Sciences, Moscow, Russia <sup>3</sup> Massachusetts Institute of Technology, Cambridge, Massachusetts, USA
ISBN	978-87-7893-397-3
Date	November 2014
Project	NKS-R / DECOSE
No. of pages	178
No. of tables	24
No. of illustrations	83
No. of references	96
Abstract	<p>The work is motivated by the need to assess effectiveness of severe accident management strategy adopted in Nordic type BWRs with melt ejection from the vessel into a deep water pool below the vessel. In this work we address phenomena relevant to the debris bed formation, coolability and steam explosion experimentally and analytically.</p> <p>A new series of DEFOR-A (Agglomeration) tests have been carried out in order to clarify the effect of the melt jet velocity on the particle size distribution and fraction of agglomeration. Ablation and plugging of the melt release nozzle is also addressed in this work.</p> <p>DECOSIM code was further developed to address debris bed coolability in post-dryout regime. An analytical model is proposed based on the analysis of DECOSIM calculations for prediction of the maximum temperature of the debris if the size of the dry zone is known. A model for prediction of particulate debris spreading has been implemented in the DECOSIM code. The code has been further validated against latest COOLOCE data for multidimensional debris bed configurations.</p> <p>A scaling approach for prediction of particulate debris spreading has been proposed in this work based on the PDS-C experimental data. A universal semi-empirical closure has been developed for prediction of debris spreading mass flux.</p> <p>An approach to steam explosion sensitivity analysis using TEXAS code has been developed. Obtained database of the impulse and maximum pressure as a function of TEXAS input parameters is used for development of the computationally efficient surrogate model.</p>
Key words	Nordic BWR, severe accident, debris bed formation, coolability, steam explosion